

STUDY OF THERMO-MECHANICAL PROPERTIES OF GRAPHENE-LIKE  
TWO DIMENSIONAL MATERIAL

by

Mohan Surya Raja Elapolu

A dissertation submitted to the faculty of  
The University of North Carolina at Charlotte  
in partial fulfillment of the requirements  
for the degree of Doctor of Philosophy in  
Mechanical Engineering

Charlotte

2021

Approved by:

---

Dr. Alireza Tabarraei

---

Dr. Yong Zhang

---

Dr. Youxing Chen

---

Dr. Russell Keanini

---

Dr. Xingjie Li



## ABSTRACT

MOHAN SURYA RAJA ELAPOLU. Study of thermo-mechanical properties of graphene-like two dimensional material. (Under the direction of DR. ALIREZA TABARRAEI)

Graphene is a layer of covalently bonded carbon atoms with a honeycomb lattice structure. It has exceptional properties, due to which it became prominent in a wide range of applications. The enormous success of graphene raised curtains to a new class of two dimensional materials. In this research we employed molecular dynamics simulations and machine learning methods to study thermo-mechanical properties of graphene-like two dimensional materials.

Reverse non-equilibrium molecular dynamics method has been employed to study the thermal transport properties of hexagonal-boron nitride (h-BN) nanoribbons, and  $C_3N$  nanotubes ( $C_3NNT$ ). Our results showed that effective thermal conductivity of h-BN nanoribbons is in the range of 75 - 160 W/m-K whereas Kapitza conductance of grain boundaries is in the range of 6 - 20 GW/m<sup>2</sup>-K. By increasing the misorientation angle the defect density at the grain boundaries increases due to which, the Kapitza conductance of the grain boundaries and the effective thermal conductivity of the h-BN nanoribbon decreases. Our MD simulations showed that a lower ballistic to diffusive transition length (72 - 80 nm) for  $C_3NNT$  compared to CNT (103 -107 nm). Due to the stiffer acoustic modes of CNT. Thermal conductivity of CNT is significantly higher than that of  $C_3NNT$  across the entire ballistic-diffusive range.

Molecular dynamics simulations are used to study the mechanical properties of graphene-like two dimensional material with focus on  $MoS_2$  and graphene. The toughness and strength of the  $MoS_2$  sheets are not significantly affected by increase in the number of layers from one to three. Griffith theory is not valid for nanoscale cracks of  $MoS_2$ . In comparison to Inglis theory, quantized fracture mechanics give better prediction for the fracture strength of  $MoS_2$  sheets when the crack tips are very sharp.

Environmental molecules like  $H_2$ ,  $O_2$ ,  $CO_2$ , and  $H_2O$  can react with material, and accelerate its failure. Hence, it is important to understand the environment-assisted cracking in two dimensional materials. The stress corrosion cracking in mono crystalline graphene in the presence of  $O_2$  molecules are studied. The strained graphene sheet is exposed to oxygen molecules. Our MD and density functional-based tight bonding simulations show that cracks in graphene can grow due to chemical reactions with environmental molecules. The results show that sub-critical crack growth can occur in graphene sheets when exposed to  $O_2$  molecules.

The mechanical and fracture properties of bicrystalline and polycrystalline graphene sheets with hydrogenated grain boundaries are studied. Molecular dynamics simulations are used to extract the traction-separation laws (TSL) of the hydrogenated grain boundaries of bicrystalline graphene. The adsorption site is an important factor for determining the level of the impact of hydrogenation on the fracture properties of the grain boundary. On the other hand, crack propagation path in the polycrystalline graphene sheet is affected by the hydrogenation of the grain boundaries. The crack prefers to grow along an intragranular path at lower hydrogenation percentage, whereas at higher hydrogenation percentage it changes to intergranular. Our results have showed that hydrogen embrittlement at grain boundaries is degrading the bicrystalline and polycrystalline graphene sheet due to which the strength and fracture toughness is decreasing.

Finally, A machine learning model has been developed to predict crack propagation path in polycrystalline graphene. The model is a combination of convolutional neural network, bidirectional recurrent neural network, and fully connected layers. The data set used to train the machine learning model is obtained using MD simulations. Fully trained ML model can predict the crack path in polycrystalline graphene sheet. The predicted crack path from the ML model is in close agreement with the one obtained from MD simulations.

## DEDICATION

To my family

## ACKNOWLEDGEMENTS

I would like to thank my advisor, Dr. Alireza Tabarraei, who provided his exceptional expertise and knowledge through out this process. I am grateful to University of North Carolina at Charlotte and National science foundations (NSF) for the financial support provided. I convey my sincere gratitude and thanks to dissertation committee members, Dr. Yong Zhang, Dr. Russell Keanini, Dr. Youxing Chen, Dr. Xingjie Li, and Dr. Alireza Tabarraei. I sincerely thank the collaborators, Dr. Xiaonan Wang, Dr. Douglas E. Spearot, Dr. Ali Ramazani, Amin Reihani, Md. Imrul Reza Shishir, and Dr. Alireza Tabarraei.

## TABLE OF CONTENTS

LIST OF TABLES	xii
LIST OF FIGURES	xiii
CHAPTER 1: INTRODUCTION	1
1.1. Two dimensional material	1
1.2. Fabrication Techniques of Two dimensional material	4
1.3. Experimental Studies of Properties	6
1.4. LAMMPS	6
1.4.1. Forcefields	7
1.4.2. Reverse Nonequilibrium Molecular Dynamics Method	9
1.4.3. Atomic stress	11
1.5. Machine learning	11
CHAPTER 2: Kapitza Conductance of Symmetric Tilt Grain Boundaries in Hexagonal–Boron Nitride	13
2.1. Introduction	13
2.2. The structure of nanoribbons and grain boundaries	15
2.3. Computational method	20
2.4. Results	23
2.4.1. Impact of misorientation angle on Kapitza conductance	23
2.4.2. Impact of misorientation angle on the effective thermal conductivity of ribbons	24
2.4.3. Effect of ribbons length on the Kapitza conductance and effective thermal conductivity of ribbons	27

2.4.4. Effect of temperature on Kapitza conductance and effective thermal conductivity of ribbons	28
2.5. Conclusion	29
CHAPTER 3: Phononic Thermal Transport Properties of $C_3N$ Nanotubes	30
3.1. Introduction	30
3.2. Structure of $C_3N$ nanotube	32
3.3. Computational method	32
3.4. Results	34
3.4.1. Thermal conductivity of $C_3NNT$ in comparison to CNT	34
3.4.2. Impact of length and chirality of $C_3NNT$ on its thermal conductivity	35
3.4.3. Impact of the diameter of $C_3NNT$ on thermal conductivity	38
3.4.4. Quantum correction of thermal conductivity	39
3.5. Phonon transport in $C_3NNT$	41
3.5.1. Dispersion relation and density of states	42
3.5.2. Phonon scattering in $C_3NNT$	43
3.6. Conclusion	48
CHAPTER 4: Fracture Mechanics of Multi-Layer Molybdenum Disulphide	49
4.1. Introduction	49
4.2. Structure of $MoS_2$	51
4.3. Computational method	53

	ix
4.4. Results	55
4.4.1. Crack propagation	55
4.4.2. Stress–strain relation and distribution	58
4.5. Conclusion	68
CHAPTER 5: An Atomistic Study of the Stress Corrosion Cracking in Graphene	70
5.1. Introduction	70
5.2. Molecular dynamics modeling using ReaxFF	72
5.3. Results	75
5.3.1. Stress–strain curves of graphene sheet	75
5.3.2. Graphene sheet in the absence of oxygen molecules	76
5.3.3. Chemisorption of O <sub>2</sub> molecules	77
5.4. Molecular dynamics modeling using DFTB	83
5.4.1. Results	84
5.5. Conclusion	88
CHAPTER 6: Atomistic Simulation-Based Cohesive Zone Law of Hydrogenated Grain Boudaries of Graphene	91
6.1. Introduction	91
6.2. The structure of grain boundary and bicrystal graphene	94
6.3. Cohesive zone model	97
6.4. Computational method	99
6.5. Results	101
6.5.1. Crack propagation	101

6.5.2.	Extraction of traction–separation law from MD	103
6.5.3.	Traction separation law of grain boundaries with no hydrogen atoms	105
6.5.4.	Impact of hydrogen adsorption site	109
6.5.5.	Hydrogen concentration at the grain boundary	112
6.5.6.	Temperature	112
6.6.	Conclusion	113
CHAPTER 7: Mechanical and Fracture properties of the polycrystalline graphene with hydrogenated grain boundaries		114
7.1.	Introduction	114
7.2.	Polycrystalline graphene sheet	117
7.2.1.	Generation	117
7.3.	Tensile loading	120
7.4.	Results	122
7.4.1.	Mechanical properties	122
7.4.2.	Fracture properties	127
7.5.	Conclusion	131
CHAPTER 8: A Novel Approach for Studying Crack Propagation in Polycrystalline Graphene Using Machine Learning Algorithms		132
8.1.	Polycrystalline graphene sheet	134
8.2.	Tensile loading	136
8.3.	Results	139
8.4.	Fracture process from Molecular Dynamics Simulations	139

	xi
8.5. Fracture process from Machine learning model	141
8.5.1. Data Preparation	143
8.5.2. Machine Learning Model	148
8.6. Conclusion	155
CHAPTER 9: Summary	156
REFERENCES	158

## LIST OF TABLES

TABLE 3.1: Ballistic to diffusive transition lengths of different nanotubes in nm	35
TABLE 3.2: Phonon MFP of different phonon modes of CNT	46
TABLE 3.3: Phonon MFP of different phonon modes of C <sub>3</sub> NNT	46
TABLE 4.1: Fracture toughness of MoS <sub>2</sub> ribbons with center crack	62
TABLE 6.1: Key parameters of TSL of grain boundaries with misorientation angle 21.9° and 38.4°	109

## LIST OF FIGURES

FIGURE 1.1: Graphite and graphene sheets	2
FIGURE 1.2: Hexagonal boron nitride sheets	3
FIGURE 1.3: MoS <sub>2</sub> sheet	3
FIGURE 1.4: C <sub>3</sub> N nanosheet and nanotube	4
FIGURE 1.5: Two-dimensional material with defects	5
FIGURE 1.6: RNEMD method	10
FIGURE 2.1: RNEMD method	15
FIGURE 2.2: Geometry of grain boundaries in a zigzag oriented h-BN nanosheets	16
FIGURE 2.3: Geometry of grain boundaries in an armchair oriented h-BN nanosheets	17
FIGURE 2.4: Geometry of grain boundaries in the transition zone of h-BN nanosheets	18
FIGURE 2.5: Temperature profiles of nanoribbons.	22
FIGURE 2.6: Kapitza conductance of grain boundaries in zigzag and armchair ribbons decreases with increase in their misorientation angle.	23
FIGURE 2.8: Defect density versus misorientation angle of grain boundaries. Grain boundary defect density increases almost linearly with increase in the misorientation angle.	25
FIGURE 2.7: Phonon vibrational spectral of grain and grainboundary atoms.	25
FIGURE 2.9: Effective thermal conductivity of zigzag and armchair ribbons decreases with increase in misorientation angle of grain boundaries.	26
FIGURE 2.10: Kapitza conductance of grain boundaries versus the ribbons length at 300 K.	26

FIGURE 2.11: Effective thermal conductivity of ribbons versus their lengths at 300 K.	26
FIGURE 2.12: Kapitza conductance of grain boundaries in zigzag and armchair ribbons at different temperatures.	28
FIGURE 2.13: Effective thermal conductivity of zigzag and armchair ribbons decreases with increase in temperature.	29
FIGURE 3.1: Structure of $C_3N$ nanotube	30
FIGURE 3.2: RNEMD in $C_3NNT$	33
FIGURE 3.3: Temperature distribution in $C_3NNT$	33
FIGURE 3.4: Comparison of thermal conductivity of $C_3NNT$ and CNT	35
FIGURE 3.5: Thermal conductivity of $C_3NNT$	36
FIGURE 3.6: Plot showing ballistic to diffusive transition in $C_3NNT$	37
FIGURE 3.7: Phonon density of states of $C_3NNT$	38
FIGURE 3.8: Acoustic phonon modes of $C_3NNT$ with different chirality	39
FIGURE 3.9: Quantum correction of thermal conductivity	39
FIGURE 3.10: Phonon dispersion curves and density of states of $C_3NNT$ and CNT	40
FIGURE 3.11: Comparison of acoustic modes of $C_3NNT$ and CNT	41
FIGURE 3.12: Comparison of phonon density of states of $C_3NNT$ and CNT	42
FIGURE 3.13: CNT phonon relaxation time at different polarizations	44
FIGURE 3.14: $C_3NNT$ phonon relaxation time at different polarizations	44
FIGURE 3.15: Acoustic phonon mean free path for CNT and $C_3NNT$	45
FIGURE 4.1: Bi-layer $MoS_2$ crystal in different views	51
FIGURE 4.2: $MoS_2$ sheet considered to run the simulations .	52

FIGURE 4.3: MoS <sub>2</sub> crack tips	52
FIGURE 4.4: MoS <sub>2</sub> crack propagation direction	54
FIGURE 4.5: MoS <sub>2</sub> crack path	54
FIGURE 4.6: Crack propagation in ACSC of length 7.51 nm at 300 K	56
FIGURE 4.7: Crack propagation in ACBC of length 7.87 nm at 300 K	57
FIGURE 4.8: Crack propagation in ZZC of length 7.61 nm at 300 K	57
FIGURE 4.9: Stress distribution in strained MoS <sub>2</sub> with center crack	59
FIGURE 4.10: Stress–strain relation of MoS <sub>2</sub> ribbons with center crack at 300 K	60
FIGURE 4.11: Stiffness of MoS <sub>2</sub> ribbons with center crack	61
FIGURE 4.12: Fracture strength of MoS <sub>2</sub> ribbons with center crack	62
FIGURE 4.13: Dependence of strength of MoS <sub>2</sub> on temperature	63
FIGURE 4.14: Griffith theory of MoS <sub>2</sub> ribbons	64
FIGURE 4.15: Cract tips with different radius in MoS <sub>2</sub>	65
FIGURE 4.16: Dependence of local stress on crack tip radius	67
FIGURE 4.17: Cracks with radius less than 0.7 nm	67
FIGURE 4.18: Quantized fracture mechanics in MoS <sub>2</sub>	67
FIGURE 5.1: Graphene sheet with edge crack	73
FIGURE 5.2: The initial distribution of oxygen molecules around the crack tip	74
FIGURE 5.3: The stress–strain curves of graphene sheet with cracks in the armchair and zigzag direction at 300 K	74
FIGURE 5.4: The atomic stress distribution ( $\sigma_{yy}$ ) in graphene sheets subjected to a strain of 0.076	75

FIGURE 5.5: The chemisorption process in a graphene sheet including a crack in the armchair direction subjected to a strain of 0.047 and exposed to 156 oxygen molecules	76
FIGURE 5.6: The chemisorption process in a graphene sheet including a crack in the zigzag direction subjected to a strain of 0.047 and exposed to 156 oxygen molecules	77
FIGURE 5.7: The atomic stress distribution ( $\sigma_{yy}$ ) in the graphene sheets subjected to a strain of 0.047 before and after chemisorption	78
FIGURE 5.8: The chain of chemical reactions between prestrained graphene sheets at 0.053 and 0.049 strain and oxygen molecules at 300 K	79
FIGURE 5.9: The atomic stress distribution ( $\sigma_{yy}$ ) in the graphene sheet before and after chemisorption	80
FIGURE 5.10: Subcritical crack growth in graphene sheets subjected to a strain of 0.076 when exposed to 156 oxygen molecules	80
FIGURE 5.11: Sub critical crack growth in graphene sheets subjected to a strain of 0.076 when exposed to 110 oxygen molecule	80
FIGURE 5.12: Subcritical crack growth in graphene sheets subjected to a strain of 0.076 when exposed to 72 oxygen molecules	81
FIGURE 5.13: The stress in the $y$ -direction ( $\sigma_y$ ) with respect to the simulation time during the chemisorption process in graphene sheets when cracks are exposed to 156 oxygen molecules	81
FIGURE 5.14: The circular domain used for modeling of stress corrosion cracking in graphene	85
FIGURE 5.15: Stress corrosion cracking in graphene sheet with zigzag edge crack	89
FIGURE 5.16: Stress corrosion cracking in graphene sheet with armchair edge crack	90
FIGURE 6.1: Bicrystalline graphene sheet with a grain boundary along the $x$ -direction	92

FIGURE 6.2: Out-of-plane deformation of bicrystalline graphene sheet along the grain boundaries	93
FIGURE 6.3: A schematic cohesive zone and its corresponding bilinear traction separation law	96
FIGURE 6.4: Crack propagation path along the grain boundary with misorientation angle $21.9^\circ$ without adsorbed hydrogen atom at 300 K	97
FIGURE 6.5: Crack propagation along the grain boundary with misorientation angle of $21.9^\circ$ with one hydrogen atom adsorbed at each pentagon-heptagon defect at 300 K	98
FIGURE 6.6: Crack propagation along the grain boundary with misorientation angle $38.4^\circ$ with no hydrogen atoms at 300 K	99
FIGURE 6.7: Crack propagation along the hydrogenated grain boundary with misorientation angle of $38.4^\circ$	100
FIGURE 6.8: The cohesive zone elements used to extract the TSLs	101
FIGURE 6.9: Traction-separation law of grain boundaries with no hydrogen atoms at 300 K	102
FIGURE 6.10: The adsorption site labels of the two GBs	103
FIGURE 6.11: TSL of GB with misorientation angle $21.9^\circ$ with one adsorbed hydrogen atom at 300 K	103
FIGURE 6.12: TSL of GB with $\phi_M = 38.4^\circ$ with one adsorbed hydrogen atom at 300 K	106
FIGURE 6.13: TSL of GB with $\phi_M = 38.4^\circ$ with one adsorbed hydrogen atom at 300 K	107
FIGURE 6.14: Fracture strength and toughness at GB with misorientation angle of $21.9^\circ$	108
FIGURE 6.15: Fracture strength and toughness at GB with misorientation angle of $38.4^\circ$	108
FIGURE 6.16: Fracture behavior at GB with misorientation angle of $38.4^\circ$	109

FIGURE 6.17: The adsorption site of hydrogen atom along the GB when the number of hydrogen atoms increases from one to three	110
FIGURE 6.18: Effect of hydrogen concentration on fracture properties	111
FIGURE 6.19: Impact of temperature on the fracture properties	111
FIGURE 7.1: Polycrystalline graphene with different grain sizes	115
FIGURE 7.2: Polycrystalline graphene sheet with an effective grain size of 4 nm after the annealing process	116
FIGURE 7.3: Mechanical properties of uncracked pristine graphene sheet	119
FIGURE 7.4: Mechanical properties of uncracked polycrystalline graphene sheet	121
FIGURE 7.5: Crack initiation and propagation in a polycrystalline graphene with average grain size 4 nm without hydrogenation	122
FIGURE 7.6: Crack initiation and propagation in a polycrystalline graphene sheet with average grain size 4 nm with 100% hydrogenation of its grain boundaries	123
FIGURE 7.7: Fracture properties of the precracked polycrystalline graphene sheet	125
FIGURE 7.8: Fracture process in polycrystalline graphene sheet with an average grain size of 6 nm	126
FIGURE 7.9: Fracture toughness and critical energy release rate of polycrystalline graphene sheet with hydrogenated grain boundaries	128
FIGURE 8.1: Graphene grains with different misorientation angles	135
FIGURE 8.2: Polycrystalline graphene sheets with initial edge cracks and average grain sizes changing from 3 nm to 9 nm	137
FIGURE 8.3: The fracture process in precracked polycrystalline graphene sheet	138
FIGURE 8.4: Crack growth in polycrystalline graphene sheets with average grain size 5 nm at strains	138

FIGURE 8.5: Crack growth in polycrystalline graphene sheets with average grain size 7 nm at strains	139
FIGURE 8.6: Initial configurations of polycrystalline graphene sheet	140
FIGURE 8.7: Polycrystalline graphene sheet showing the fully grown crack	141
FIGURE 8.8: The process used to generate output images with $128 \times 256$ pixels	142
FIGURE 8.9: Image of fully grown crack showing pixel values of crack	143
FIGURE 8.10: Process flow to predict fully grown crack in polycrystalline graphene sheet	144
FIGURE 8.11: Machine learning architecture used for processing a slice of the image	145
FIGURE 8.12: Bidirectional recurrent neural network showing the forward and backward recurrent neural network (RNN) cells.	147
FIGURE 8.13: Fully connected layer of the machine learning model	147
FIGURE 8.14: Comparison of crack lengths of MD and ML model	150
FIGURE 8.15: Crack propagation path obtained from MD simulations and machine learning model in polycrystalline graphene sheets	153
FIGURE 8.16: Crack propagation path obtained from MD simulations and machine learning model in polycrystalline graphene sheets	154

## CHAPTER 1: INTRODUCTION

Two-dimensional material is a layer of atoms covalently bonded together with thickness at the atomic scale. They are playing an important role in advancing various cutting edge technologies. Their unique structure gave them outstanding properties which are different from the bulk material. Characterizing thermal and mechanical behavior of two dimensional material is a challenging task due to the time and length scales involved. This research focuses on applying molecular dynamics (MD) and machine learning (ML) methods to study thermo-mechanical properties of graphene-like two dimensional material. The first part of this research focuses on understanding the thermal behavior of the h-BN nano ribbons and  $C_3N$  nanotubes [1, 2]. In the later part, the mechanical properties of the  $MoS_2$  sheets and graphene has been evaluated [3, 4, 5, 6]. Especially, MD simulations have been employed to understand environment assisted cracking in monocrystalline, bicrystalline and polycrystalline graphene in the presence of  $O_2$  molecules and H atoms. Finally, ML methods have been developed to predict crack propagation path in polycrystalline graphene [7]. Following sections of this introduction provides the details about the two dimensional materials considered and the numerical methods employed in this study.

### 1.1 Two dimensional material

Graphite is one of the stable crystalline allotropes of solid carbon (C) . As shown in Fig. 1.1a, it is a laminated material with weak Van der Waals force between the adjacent layers. The weak Van der Waals between the layers allows an easy isolation of a layer of graphite. The isolated layer of graphite is known as graphene. Graphene is the first two dimensional material to be successfully fabricated [8]. It raised curtains

to a new class of material known as two dimensional material. As shown in Fig. 1.1b, graphene is a layer of covalently bonded carbon atoms with a honeycomb lattice structure. Each carbon (C) atom in graphene is  $sp^2$ -hybridized forming bonds with three other carbon atoms leaving a free electron per each C atom. The combination of these factors gave exceptional mechanical [9, 10, 11, 12], thermal [13, 14, 15], and electronic [16, 17, 18] properties to graphene. Grapene has wide range of applications including field effect transistors [19, 20, 21], supercapacitors [22, 23, 24, 25], nano composites [26, 27, 28, 29, 30], electro mechanical sensors [31, 32, 33], and optical devises [34, 35]. On the flip side the zero band gap of graphene limited its applications. The phenomenal success of graphene made researchers to look for other two dimensional material. Hexagonal boron nitride (h-BN), nitrogen doped graphene and transition metal dichalcogenide (TMD) are some from the lot which showed promising results.

Hexagonal boron nitride is one of the stable crystalline allotrope of boron nitride. As illustrated in Fig. 1.2a it has layered structure similar to graphite. A monolayer of hexagon boron nitride has honeycomb lattice structure with equal number of covalently bonded boron (B) and nitrogen (N) at alternating sites as illustrated in Fig. 1.2b [36, 37, 38]. H-BN displays excellent optical properties [39, 40, 41], remarkable mechanical [42, 43, 44, 45] and thermal [46, 47, 48, 49] properties. Due to which it is finding applications in nanoscale electronics [50, 51, 52, 53], optoelectronic [54], and electrochemical sensing devices [55] and composite material [56, 57, 58, 59].

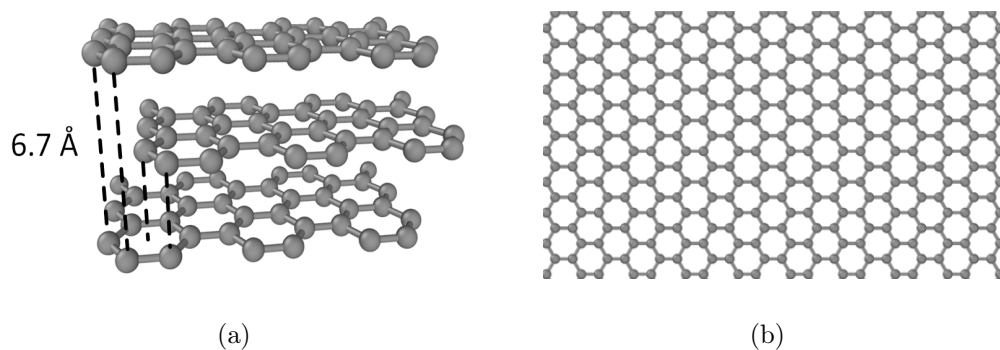


Figure 1.1: (a) Graphite , (b) Graphene (carbon atom shown in grey)

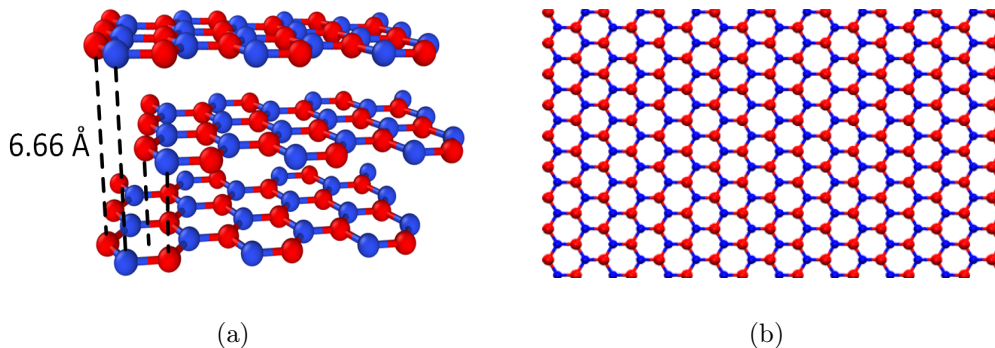


Figure 1.2: (a) Multi layer h-BN sheets, (b) Monolayer h-BN sheet (boron atom shown in red and nitrogen atom shown in blue)

Transition metal dichalcogenides are laminated material where each layer consists of a metal and chalcogen. Two-dimensional  $\text{MoS}_2$  is one of the most popular TMDs. As shown in Fig. 1.3,  $\text{MoS}_2$  sheet is made up of a layer of molybdenum sandwiched between two sulfur layers. It has unique physical, optical and electronic properties [60, 61, 62, 63]. Two-dimensional  $\text{MoS}_2$  has applications in microelectromechanical systems (MEMS) and nanoelectromechanical systems (NEMS) devices [64, 65, 66, 67, 68].

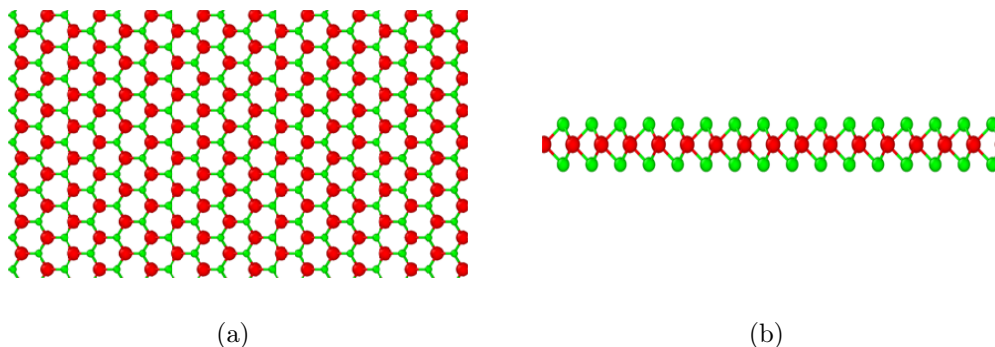


Figure 1.3: Molybdenum disulphide sheet (molybdenum atom shown in red and sulphur atom shown in green). (a) Top view, and (b) side view

Graphene has zero bandgap which limited its applications in digital circuits. Nitrogen doped graphene is proposed in an attempt to open band gap [69, 70, 71].  $\text{C}_3\text{N}$  sheets are one of the prominent two dimensional material obtained by doping nitrogen into the graphene sheets [72, 73]. As shown in Fig. 1.4, each hexagonal ring of

carbon atoms is surrounded by six nitrogen atoms which are covalently bonded.  $C_3N$  nanotubes are prepared by rolling  $C_3N$  sheets into tubes which are seamlessly welded at the joints.  $C_3N$  nanotube ( $C_3NNT$ ) is considered in applications like hydrogen storage [74].

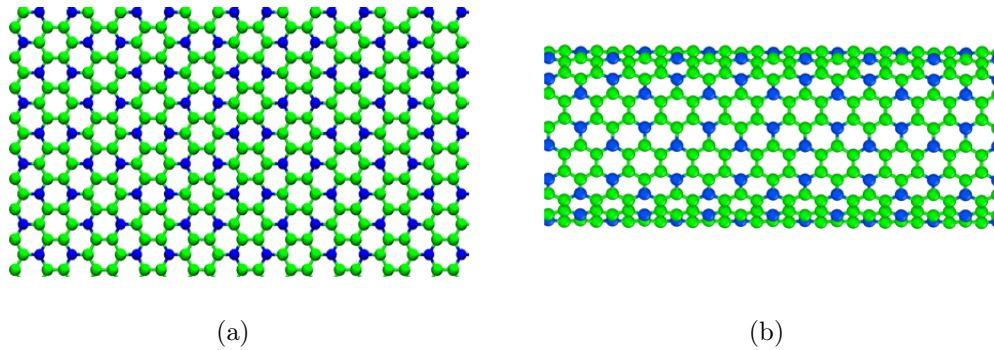


Figure 1.4: (a)  $C_3N$  sheet, and (b)  $C_3N$  nanotube (carbon atom is shown in green and nitrogen atom shown in blue)

## 1.2 Fabrication Techniques of Two dimensional material

Large scale production of two dimensional material without introducing defects is a challenging task. Some of the fabrication techniques of two dimensional material are mechanical exfoliation, and chemical vapor deposition (CVD). Mechanical exfoliation has been employed to fabricate graphene for the first time [8] . In this technique a peeling force is applied through material like scotch tape to exfoliate a single or few-atom-thick sheets of two dimensional material [75]. Mechanically exfoliated two dimensional material are of high quality with very limited efficiency [76]. On the other hand, CVD is widely used fabrication technique for large scale production of two dimensional material [76, 77, 78, 79]. In CVD technique chemical vapor, which contains the elements of material, is used to deposit the material on a catalytic metal surface. There will be several nucleation sites on the metal which grows through the atom-by-atom deposition of material obtained from chemical vapor. The sample obtained through CVD are polycrystalline which contains several grains stitched together at the grain boundaries. Polycrystalline graphene sheet is illustrated in Fig. 1.5c.

Two-dimensional material fabricated through exfoliation and CVD techniques are defected [80, 81, 82, 83, 84]. Fig. 1.5a shows the h-BN with grain boundaries containing Stone–Wales defects. Fig. 1.5b shows the bicrystalline graphene sheet with edge crack and hydrogenated grain boundary. Polycrystalline graphene sheet with grain boundaries made up of chain of Stone-Wales defects is illustrated in Fig. 1.5c. Defects alter the atomic arrangement of the two dimensional material. This in-turn alters the properties of the material significantly. Hence it is important to study the properties of the two dimensional material with the defects.

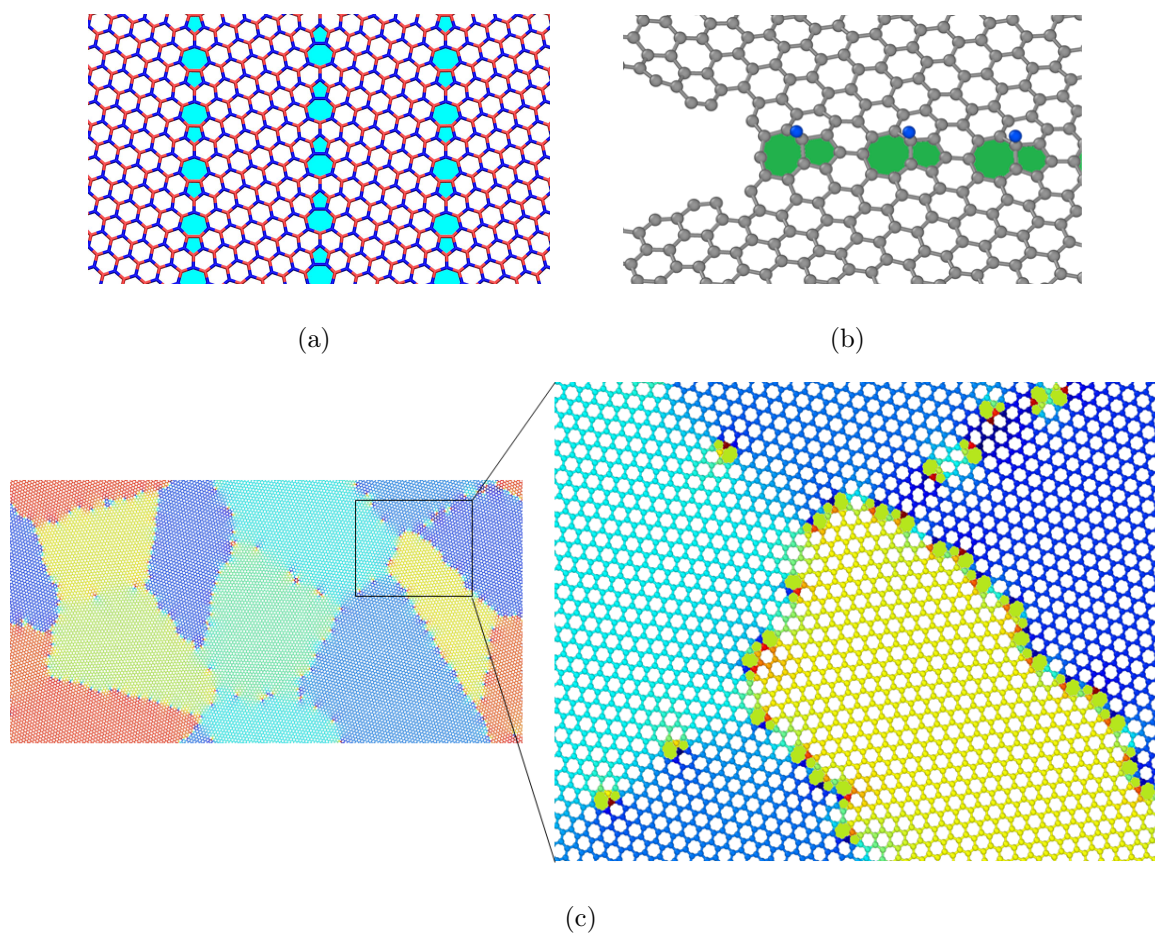


Figure 1.5: Two dimensional material with defects. (a) hexagonal boron nitride sheet containing grain boundaries, (b) graphene sheet with edge crack and hydrogenated grain boundary, and (c) polycrystalline graphene sheet

### 1.3 Experimental Studies of Properties

Prominent experimental techniques to study the properties of the two dimensional material are atomic force microscopy [85, 86, 87] and nanoindentation [88, 89, 90]. Due to the time and length scales involved are at nanoscales conducting the experiments is quite challenging. On the other hand numerical methods can be the best alternative to the experimental techniques. Molecular dynamics simulations can be used for the structures with atoms upto few millions. In this research, Large-Scale Atomic/Molecular Massively Parallel Simulator (LAMMPS) molecular dynamics package has been used to conduct the simulations.

### 1.4 LAMMPS

LAMMPS molecular dynamics package is based on the paper by Steve Plimpton [91]. It is one of the most popular package to implement classical molecular dynamics simulations. It utilizes three parallel algorithms namely atom decomposition, force decomposition and space decomposition. Atom decomposition divides the atoms to all the processors, force decomposition assigns each processor a fixed sub-set of interatomic forces to compute, space decomposition assigns a fixed spatial region. The parallelism allows the code to efficiently scale on the systems with few 100s of atoms to hundreds of millions of atoms.

In classical molecular dynamics simulations the system is described by Newton's laws of motion which is given by [91]

$$m \frac{dv_i}{dt} = \sum_j F_2(r_i, r_j) + \sum_j \sum_k F_3(r_i, r_j, r_k) \quad (1.1)$$

$$\frac{dr_i}{dt} = v_i \quad (1.2)$$

where  $m$  is the mass of the particle,  $r_i$  is the position vector of the system,  $v_i$  is the velocity of the particle,  $F_2$  is the force based on pairwise interactions between

atoms,  $F_3$  is the force based on three body interactions, and higher order terms in (1.1) defines the many body interactions. The force acting on the atoms is given by

$$F = -\frac{dE}{dr} \quad (1.3)$$

where  $r$  is the position vector of the atom,  $E$  is the energy contribution of the atom which is given by the interatomic potential.

#### 1.4.1 Forcefields

In molecular dynamics simulations the interatomic interactions are defined using interatomic potentials also known as forcefields. Forcefields are the empirical or semi-empirical formulation. In our simulations we used modified tersoff, modified REBO (reactive empirical bond order), REBO2+S, ReaxFF.

In this research, we conducted MD simulations to analyze the thermal properties of h-BN, C<sub>3</sub>N nanotubes and carbon nanotubes. We employed modified tersoff potential to define interatomic interactions between B-N, C-C and C-N atoms. It is based on the 3-body Tersoff potential [92, 93]. The energy of the system is given by [94, 95]

$$E = \frac{1}{2} \sum_i \sum_{j \neq i} V_{ij} \quad (1.4)$$

$$V_{ij} = f_C(r_{ij}) [f_R(r_{ij}) + b_{ij} f_A(r_{ij})] \quad (1.5)$$

$$f_R(r) = A \exp(-\lambda_1 r) \quad (1.6)$$

$$f_R(r) = -B \exp(-\lambda_2 r) \quad (1.7)$$

$$b_{ij} = (1 + \zeta_{ij}^\eta)^{-\frac{1}{2n}} \quad (1.8)$$

where  $V_{ij}$  is the bonding energy,  $f_A$  is three-body attractive potential term,  $f_R$  is the pairwise repulsive term,  $f_C$  is the modified cutoff function,  $r_{ij}$  is the distance between atoms  $i$  and  $j$ , and  $b_{ij}$  determines the strength of the bond between the atoms  $i$  and  $j$ .

In this study, the fracture properties of two dimensional MoS<sub>2</sub> has been determined through MD simulations. We used modified REBO to define interactions between Mo–S, Mo–Mo, and S–S. Reactive empirical bond order (REBO) potential is defined based on the repulsive and attractive forces [96]. The potential energy of the system is given by

$$E = \frac{1}{2} \sum_{i \neq j} f_{ij}^C(r_{ij}) [V_{ij}^R - b_{ij}V_{ij}^A] \quad (1.9)$$

$$V^R(r_{ij}) = \left(1 + \frac{Q}{r_{ij}}\right) A.e^{-\alpha r_{ij}} \quad (1.10)$$

$$V^A(r_{ij}) = B.e^{-\alpha r_{ij}} \quad (1.11)$$

$$b_{ij} = \left[1 + \sum_{k \neq i, j} f_{ik}^C(r_{ik}).G[\cos(\theta_{ijk})] + P(N_i)\right]^{-\frac{1}{2}} \quad (1.12)$$

where  $V^R$  is the repulsive term,  $V^A$  is the attractive term,  $b_{ij}$  determines the bond strength between atoms  $i$  and  $j$ ,  $f_{ij}^C$  is the cut-off term, and  $r_{ij}$  is the distance between atoms  $i$  and  $j$ . In this research, we studied the fracture properties of the bicrystalline graphene with hydrogenated grain boundaries using MD simulations. The interatomic interactions between C–C and C–H atoms are defined using REBO2+S potential. It is an improved version of REBO. The potential energy between the atoms is given by [97]

$$E = \sum_{i < j} [V_r(r_{ij}) + b_{ij}V_a(r_{ij})] f_c(r_{ij}) \quad (1.13)$$

$$f_c(r_{ij}) = f_c^{12}(r_{ij}) + [1 - f_c^{12}(r_{ij})] f_c^{34}(r_{ij})S_{ij} \quad (1.14)$$

where  $V_r$  is the repulsive term,  $V_a$  is the attractive term,  $f_c$  is the modified cut-off function,  $b_{ij}$  is the bond order,  $S_{ij}$  is the total screening function,  $f_c^{12}$  is the original cut-off function,  $f_c^{34}$  is the additional cut-off function, and  $r_{ij}$  is the distance between atoms  $i$  and  $j$ . We studied the stress corrosion cracking in graphene in the presence of oxygen molecules using MD simulations. Reactive ReaxFF potential is used to define

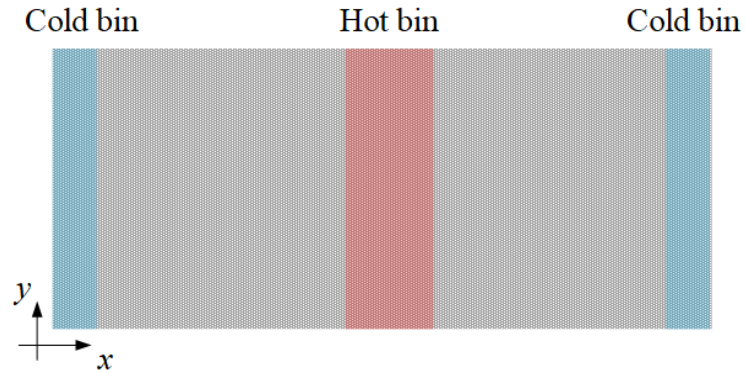
the interatomic interactions between C–C and C–O atoms [98, 99]. The potential energy of the system is given by

$$\begin{aligned}
 E = E_{bond} + E_{lp} + E_{over} + E_{under} + E_{val} + E_{pen} + E_{coa} + E_{C2} + E_{triple} \\
 + E_{tors} + E_{conj} + E_{H-bond} + E_{vdWaals} + E_{Coulomb}
 \end{aligned}
 \tag{1.15}$$

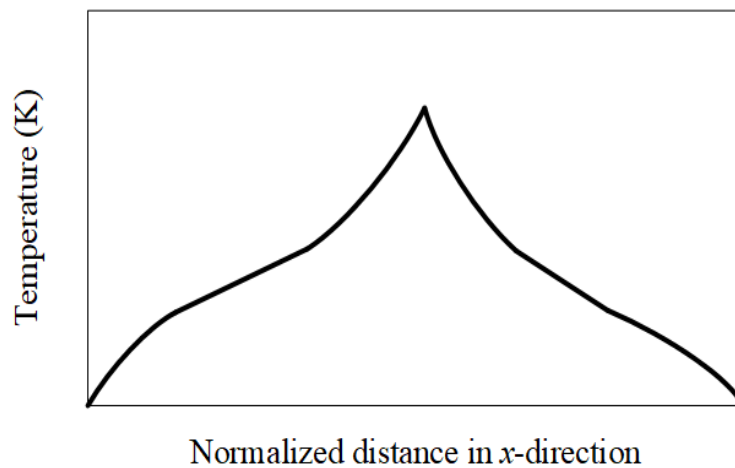
where  $E_{bond}$  corresponds to bond energy,  $E_{lp}$  is the lone pair energy,  $E_{over}$  is energy penalty on the system for an overcoordinated atom,  $E_{under}$  is energy contribution for an undercoordinated atom,  $E_{val}$  is the valence angle energy contribution,  $E_{pen}$  is the penalty energy,  $E_{coa}$  is the three-body conjugation term,  $E_{C2}$ ,  $E_{triple}$  is the triple bond stabilization energy,  $E_{tors}$  is the torsion energy,  $E_{conj}$  is the conjugation energy,  $E_{H-bond}$  is the hydrogen bond term,  $E_{vdWaals}$  is the energy due to van der Waals interactions,  $E_{Coulomb}$  is the energy due to Coulomb interactions

#### 1.4.2 Reverse Nonequilibrium Molecular Dynamics Method

Reverse nonequilibrium molecular dynamics (RNEMD) method [100] has been employed to study thermal transport in h–BN ribbons and C<sub>3</sub>N nanotubes. In this method a heat flux in the  $x$ -direction is imposed to create a temperature gradient  $\frac{\partial T}{\partial x}$  in the longitudinal direction of the simulation cell as shown in Fig. 1.6b. For this purpose, the simulation cell is divided into bins with the first bin is designated as the cold bin and the bin at the middle is designated as the hot bin, as shown in Fig. 1.6a. The heat flux is induced by a continuous transfer of energy from the cold bin to the hot bin.



(a)



(b)

Figure 1.6: (a) Simulation cell showing RNEMD method. The hot bin is at the middle and cold bins are at the two ends of the simulation cell. (b) The temperature profile of the simulation cell along the longitudinal direction.

The energy transfer is conducted by exchanging the kinetic energy of the coldest atom of the hot bin with the hottest atom of the cold bin. The swap of energy is continuously repeated until a steady state temperature profile is obtained. Due to the artificially induced heat flux between the hot and cold bin, a temperature gradient  $\frac{\partial T}{\partial x}$  in the  $x$ -direction between the hot and cold bin. The heat flux per unit time per unit area between the hot and cold bin is obtained using the exchanged kinetic energies

as

$$Q = \frac{1}{2tA} \sum_{ns} \frac{1}{2} (mv_h^2 - mv_c^2) \quad (1.16)$$

where  $ns$  is the number of kinetic energy swaps between the hot and cold bins,  $t$  is the length of simulation,  $v_h$  and  $v_c$  denote respectively the velocities of hot and cold atoms with alike mass  $m$  whose kinetic energies are exchanged, and  $A$  is the cross-sectional area of the simulation cell. The factor 2 in the denominator arises from the periodicity of the simulation cell which leads to the flux of heat from the middle bin in both directions along the  $x$ -axis. Thermal conductivity of the system is evaluated using the heat flux  $Q$  and temperature gradient  $\frac{\partial T}{\partial x}$ .

### 1.4.3 Atomic stress

The stress distribution in the system plays an important role in understanding the mechanical and fracture properties of nanomaterials. The virial definition has been employed to compute the stress tensor [101, 102, 103] which is given by

$$\sigma_{ij}^a = -\frac{1}{V^a} \left[ \frac{1}{2} m^a v_i^a v_j^a + \sum_{b=1}^n r_j^{ab} f_i^{ab} \right] \quad (1.17)$$

where  $\sigma_{ij}^a$  is the stress of atom  $a$ ,  $V^a$  is the volume of atom  $a$ ,  $m^a$  is the mass of atom  $a$ ,  $v_i^a$  and  $v_j^a$  are  $i^{th}$  and  $j^{th}$  component of the velocity of atom  $a$ ,  $n$  is the number of atoms in the neighborhood of atom  $a$ ,  $r_j^{ab}$  is  $j$ th component of the vector connecting atom  $a$  and atom  $b$  and  $f_i^{ab}$  is the  $i$ th component of interatomic force between atom  $a$  and atom  $b$ .

## 1.5 Machine learning

Studying the properties of nanomaterials often requires to accurately model atomic level interactions. Hence, atomistic modeling tools like first principle methods and MD simulations are employed. Computational cost of these simulations quickly grow with the system size. On the other hand, well-trained machine learning models can

make predictions or decisions instantaneously.

One of the well-known definition of machine learning is given by Tom M. Mitchell. The definition is "A computer program is said to learn from experience  $E$  with respect to some class of tasks  $T$  and performance measure  $P$  if its performance at tasks in  $T$ , as measured by  $P$ , improves with experience  $E$ ". Computer program develops machine learning models which can perform the given task. Performance of machine learning model on a given task improves with the experience obtained from the training data. A typical task for the machine learning model is to make predictions or decisions.

Machine learning is broadly divided into three categories based on the learning process. Supervised learning, unsupervised learning, and reinforcement learning. In supervised learning, the training data consists of input ( $X$ ) and the desired output ( $y$ ). Machine learning model obtained through the supervised learning is capable of predicting the output ( $\hat{y}$ ) based on the input ( $X$ ). The training data of unsupervised learning consist of only input ( $X$ ) and no information on the desired output is given. Machine learning model is expected to understand the hidden patterns in the data. In reinforcement learning computer program makes decision to achieve a given goal. A feedback is given for each decision it makes which improves its performance.

## CHAPTER 2: Kapitza Conductance of Symmetric Tilt Grain Boundaries in Hexagonal–Boron Nitride

### 2.1 Introduction

Monolayer hexagonal boron nitride (h–BN) is a graphene–like two–dimensional material which has a honeycomb lattice structure. As discussed in chapter 1, it has exceptional properties due to which it is finding applications in many industries. Chemical vapor deposition (CVD) is the prominent method used for large scale synthesis of nanomaterials such as h–BN [104, 105, 106]. Hexagonal boron nitride sheets obtained using CVD are polycrystalline consisting of individual grains stitched at grain boundaries [82]. Grain boundaries act as extended defects and their presence can significantly affect the properties of h–BN. The structure of grain boundaries and their impact on the thermal properties of bulk materials has been extensively investigated in the past [107, 108]. Studies on the effect of grain boundaries on the properties of two–dimensional materials are mostly limited to graphene [109, 110, 111] and the impact of grain boundaries on the properties of other two–dimensional materials are rarely studied.

High thermal conductivity of h–BN makes it important for diverse applications such as thermal management in electronics and thermal conductance enhancement of composite materials. Since grain boundaries are inevitably present in h–BN sheets, studying the impact of such defects on heat transport in h–BN is necessary. Such investigations not only reveal unique features regarding heat transport mechanism at nanoscale, but can provide insights on using defect engineering as a way for tailoring the thermal conductivity of h–BN.

Due to challenges in conducting experiments at nanoscale, computational methods

have become invaluable tools for studying properties of two-dimensional materials [112, 113, 114, 115, 116, 117, 12, 118, 119]. We use reverse nonequilibrium molecular dynamics (RNEMD) methods to study the impact of grain boundaries on the thermal conductivity of armchair and zigzag h-BN nanoribbons containing symmetric tilt grain boundaries. To understand the impact of the structure of grain boundaries on their thermal properties, grain boundaries with different misorientation angles are studied. Using phonon spectrum density of grains and grain boundaries we show that phonon scattering at grain boundaries is responsible for the thermal resistance at grain boundaries. By increasing the misorientation angle, Kapitza conductance of ribbons reduces which leads to a lower effective thermal conductivity of ribbons as well. The effect of temperature and grain size on the thermal properties of h-BN are studied. The modeling results predict that by increasing the length of grains the Kapitza conductance and effective thermal conductivity of ribbons increases. On the other hand, while the impact of temperature on the Kapitza conductance of grain boundaries is negligible, the effective thermal conductivity of ribbons reduces by increasing the temperature.

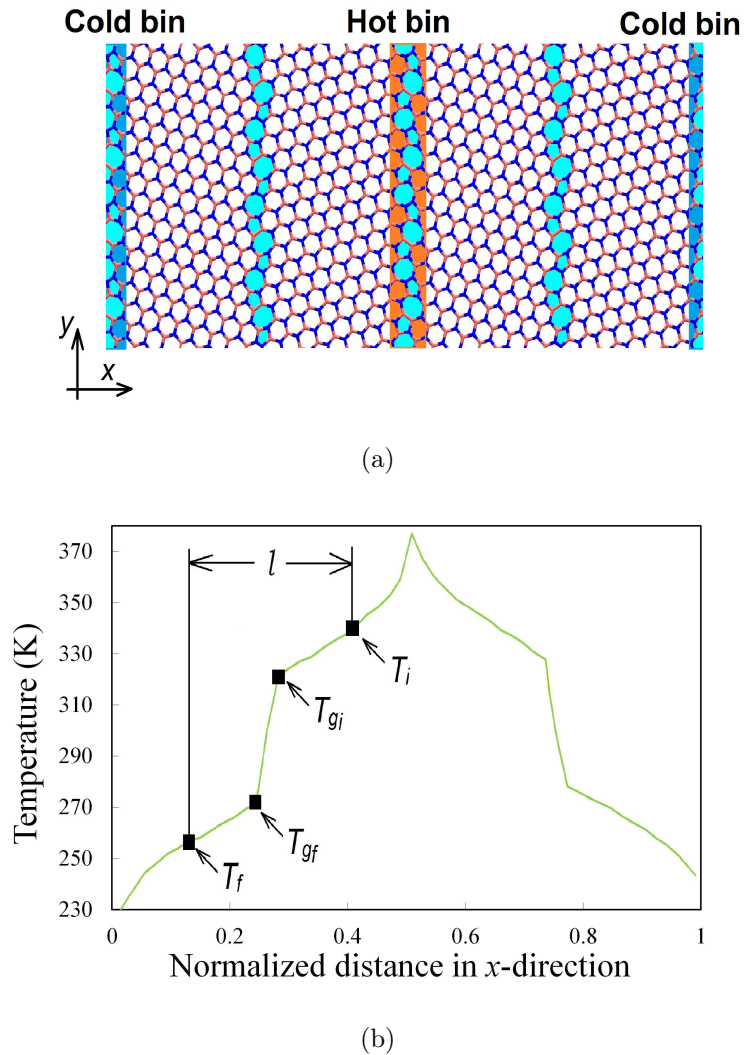


Figure 2.1: (a) A h-BN nanoribbon, containing four grain boundaries with same misorientation angle, used in the RNEMD simulations. The hot bin is at the middle and cold bins are at the two ends of the ribbon. (b) The temperature profile of the nanoribbon is shown schematically. The temperature profile includes a jump at the location of grain boundaries.

## 2.2 The structure of nanoribbons and grain boundaries

The structure of nanoribbons used in this chapter for RNEMD modeling is schematically shown in Fig. 2.1(a). The nanoribbons are periodic in the  $x$ -direction and each computational cell consists of four similar grain boundaries. As shown in Fig. 2.1(a) the grain boundaries are in the  $y$ -direction. All the four grains of the computational cell have the same size in the  $x$ -direction and their width in the  $y$ -direction is  $123 \text{ \AA}$ .

The lattice vectors  $\mathbf{a}_1 = \frac{a}{2}(3, \sqrt{3})$  and  $\mathbf{a}_2 = \frac{a}{2}(3, -\sqrt{3})$  are shown in Fig. 2.2(f) where  $a \approx 1.4457$  [120] is the boron–nitrogen bond length.

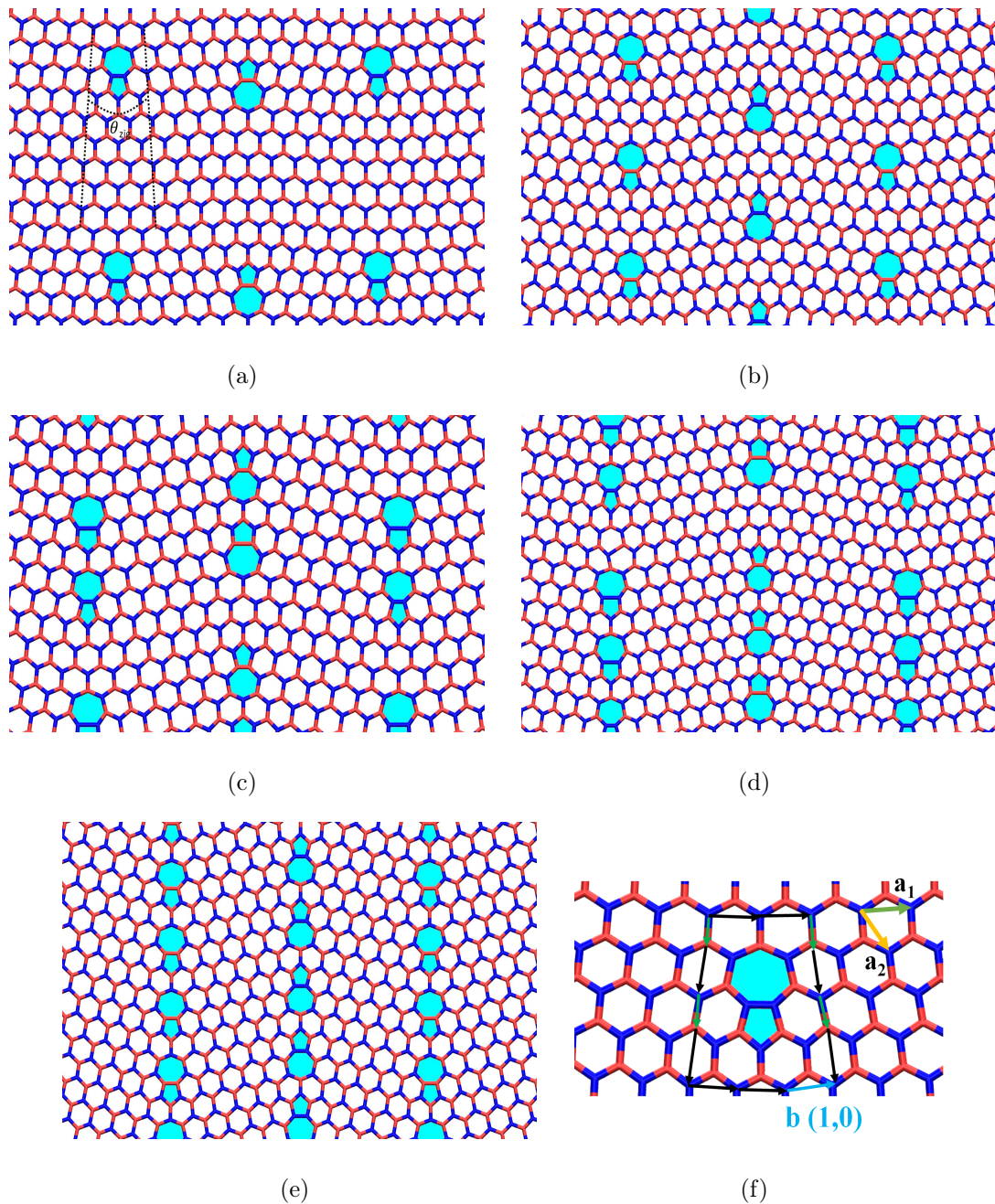


Figure 2.2: Geometry of grain boundaries in a zigzag oriented h-BN nanosheets. The misorientation angles of grain boundaries are (a)  $6.0^\circ$  , (b)  $13.17^\circ$  , (c)  $16.34^\circ$  , (d)  $17.87^\circ$  , and (e)  $21.73^\circ$ . (f) The Burger circuit at a dislocation core with a Burger vector  $\mathbf{b} = (1,0)$ . Nitrogen atoms are colored blue whereas red color represent boron atoms. (For interpretation of the references to color in this figure legend, the reader is referred to the web version of this article.)

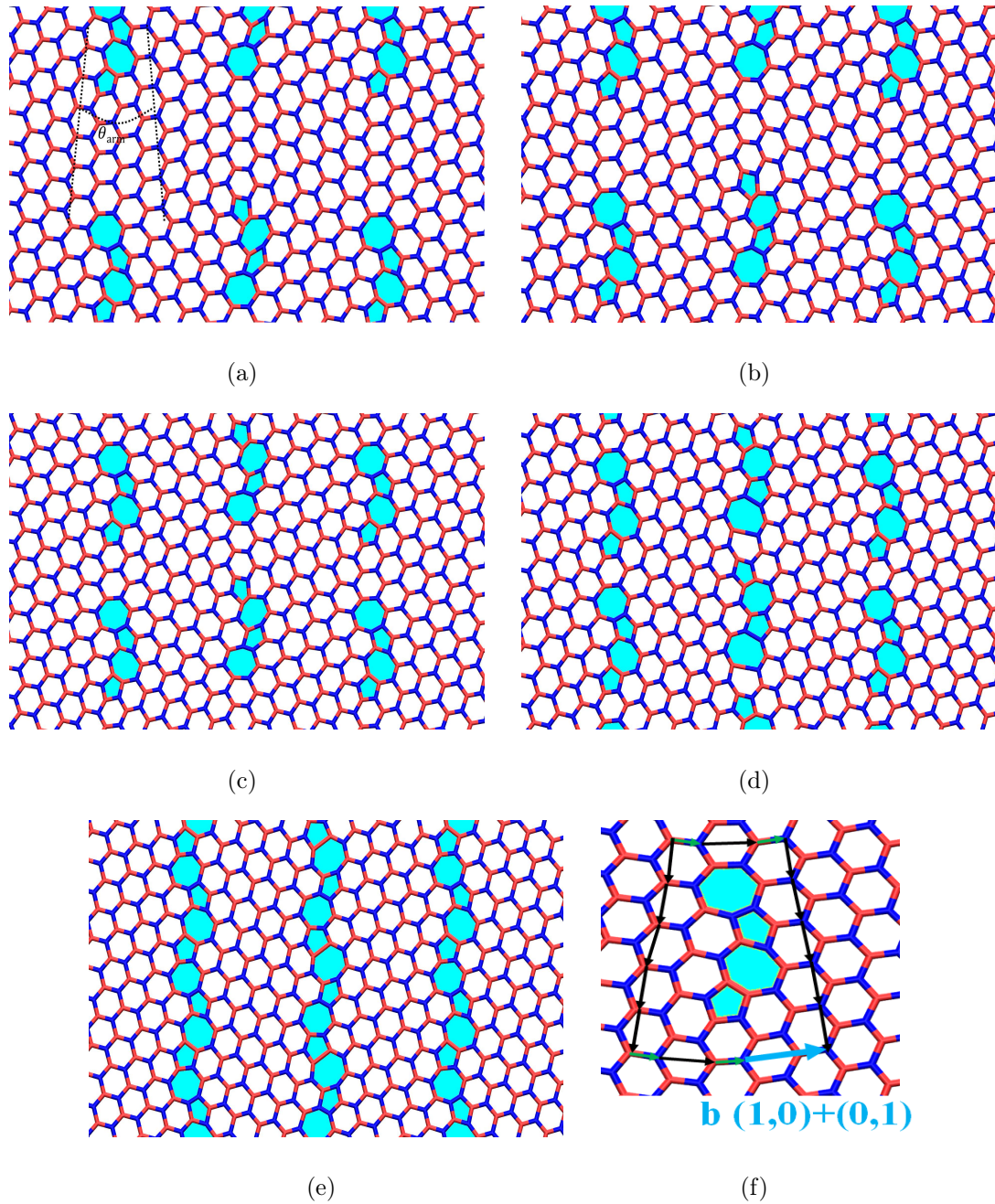


Figure 2.3: Geometry of grain boundaries in an armchair oriented h-BN nanosheets. The misorientation angle of grain boundaries are (a)  $13.08^\circ$  , (b)  $15.15^\circ$  , (c)  $17.97^\circ$  , (d)  $21.75^\circ$  , and (e)  $27.77^\circ$ . (f) The Burger circuit at a dislocation core with a Burger vector  $\mathbf{b} = (1,0) + (0,1)$ . Nitrogen atoms are colored blue whereas red color represent boron atoms. (For interpretation of the references to color in this figure legend, the reader is referred to the web version of this article.)

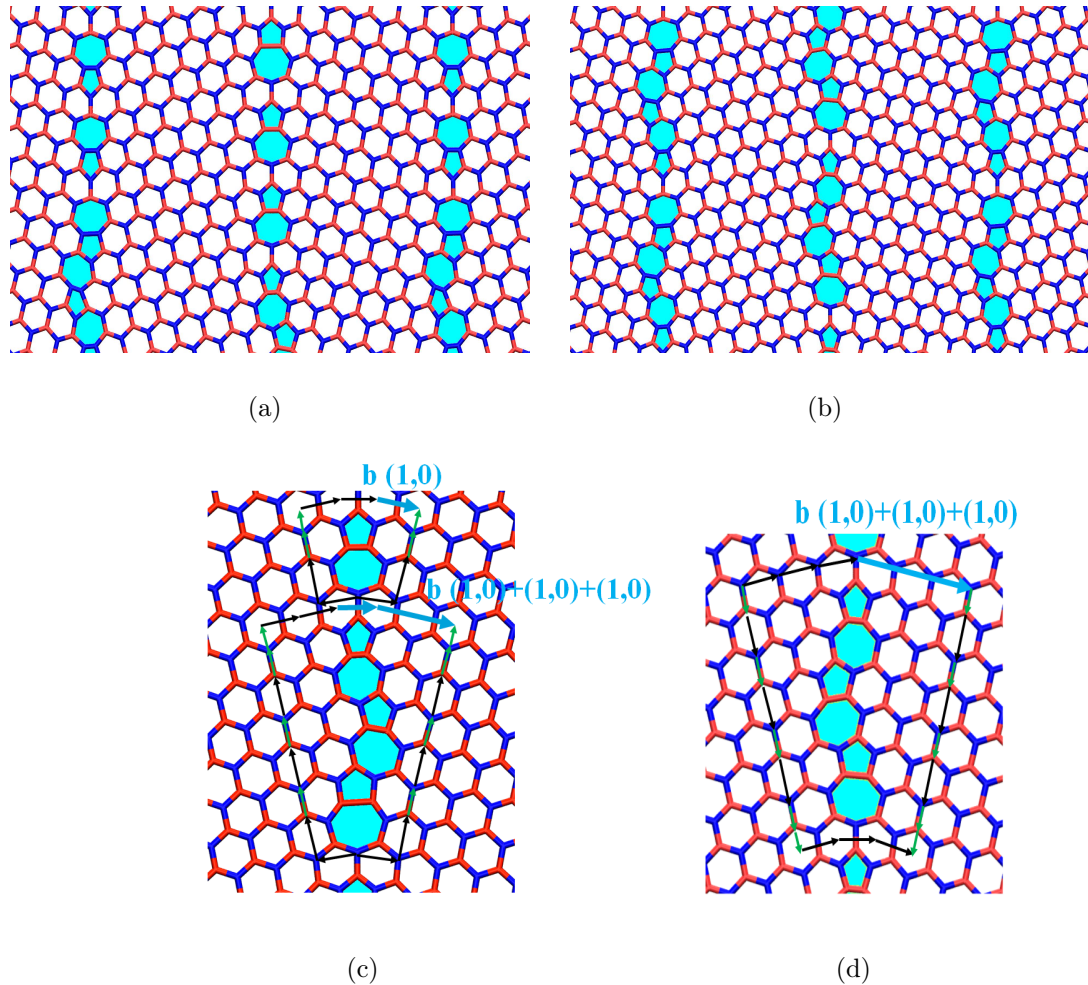


Figure 2.4: Geometry of grain boundaries in the transition zone. The misorientation angle of grain boundaries are (a)  $24.43^\circ$ , (b)  $27.79^\circ$ . (c) Grain boundaries with misorientation angle  $\theta_{zig} = 24.43^\circ$ , consists of two types of dislocations with burger vector  $\mathbf{b} = (1,0) + (1,0) + (1,0)$  and  $(1,0)$ , (d) grain boundaries with misorientation angle  $\theta_{zig} = 27.79^\circ$  consists of a dislocation with burger vector  $\mathbf{b} = (1,0) + (1,0) + (1,0)$ . Nitrogen atoms are colored blue whereas red color represent boron atoms. (For interpretation of the references to color in this figure legend, the reader is referred to the web version of this article.)

The grain boundaries considered in this chapter are shown in figures 2.2–2.4. As shown all the grain boundaries consist of repeating pentagon–heptagon (5–7) pairs [82]. Each 5–7 pair is known as Stone–Wales defect and represents the core of an edge dislocation corresponding to the removal of one chain of armchair atoms from the perfect lattice. Similar structures have been previously studied for the grain

boundary of graphene [121].

As depicted in Fig. 2.2, the grain boundaries of zigzag ribbons comprised of a regular array of 5–7 Stone–Wales defects separated by hexagonal rings [82]. Increasing the misorientation angle reduces the number of hexagonal rings between 5–7 pairs which is equivalent to increase in the dislocation density. At a misorientation angle of  $\theta_{\text{zig}} = 21.73^\circ$ , the 5–7 pairs are separated by only one hexagonal ring. Therefore, it is not possible to further increase the misorientation angle of grain boundaries while keeping the regular array of 5–7 defects. The Burger vector ( $\mathbf{b}$ ) of edge dislocations can be obtained by plotting Burger circuits around a 5–7 pair as shown in Fig. 2.2(f). Using the Burger circuit, the Burger vector of dislocations at each Stone–Wales defect of grain boundaries in zigzag ribbons is  $\mathbf{b} = \mathbf{a}_1$ .

As shown in Fig. 2.3, the grain boundaries in armchair ribbons are comprised of two pairs of 5–7 Stone–Wales defects. By plotting the Burger circuit around two 5–7 pairs, as shown in Fig. 2.3(f), the Burger vector of the dislocations are obtained as  $\mathbf{b} = \mathbf{a}_1 + \mathbf{a}_2$ . Similar to grain boundaries in zigzag ribbons, by increasing the misorientation angle, the number of hexagonal rings between two adjacent  $\mathbf{a}_1 + \mathbf{a}_2$  dislocations reduces. At a misorientation angle of  $\theta_{\text{arm}} = 27.77^\circ$  the Stone–Wales defects join each other and the hexagonal rings separating the dislocations disappear. Further increase in the misorientation angle will alter the Burger vector of dislocations.

To study the structure of grain boundaries with higher misorientation angle, we note that  $\theta_{\text{zig}} = 60^\circ - \theta_{\text{arm}}$ . Therefore, the maximum misorientation angle of armchair ribbons observed in Fig. 2.3, i.e.  $\theta_{\text{arm}} = 27.77^\circ$  is equivalent to  $\theta_{\text{zig}} = 32.23^\circ$ . Since the maximum misorientation  $\theta_{\text{zig}}$  in Fig. 2.2 is  $21.73^\circ$ , the range of  $\theta_{\text{zig}}$  between  $21.73^\circ$  and  $32.23^\circ$  is a transition zone where the grain boundary dislocations are a combination of those from armchair and zigzag ribbons.

The structure of grain boundaries in the transition zone for two misorientation angles of  $\theta_{\text{zig}} = 24.43^\circ$  and  $27.79^\circ$  are shown in Fig. 2.4. As shown in Fig. 2.4(c–d), the

structure of grain boundary in the transition zone is not made of just one type of dislocations. Instead the grain boundaries are comprised of (1,0) and (1,0)+(1,0)+(1,0) dislocations. When the misorientation angle is close to  $\theta_{\text{zig}} = 21.73^\circ$ , the density of (1,0) dislocations is higher than the density of (1,0)+(1,0)+(1,0) dislocations. When the misorientation angle approaches  $\theta_{\text{zig}} = 32.23^\circ$ , i.e, when the misorientation angle get closer to that of armchair ribbons, the (1,0) dislocations disappear and the grain boundary is made of an array of (1,0)+(1,0)+(1,0) dislocations.

In the rest of this paper, to ease the illustration of results, the data related to the grain boundaries in the transition zone, i.e  $21.73^\circ < \theta_{\text{zig}} < 32.23^\circ$ , are presented along with the results of grain boundaries of zigzag ribbons.

### 2.3 Computational method

In this chapter, we use reverse nonequilibrium molecular dynamics (RNEMD) method [100] to study thermal transport in h-BN ribbons containing symmetric tilt grain boundaries. Detailed description of RNEMD method is given in chapter 1. Fig. 2.1a shows the RNEMD method in h-BN ribbon with symmetric tilt grain boundaries. The temperature profile along the longitudinal direction of the ribbon is given in Fig. 2.1b. As discussed in chapter 1, in RNEMD method the simulation cell is divided into number of bins. In this chapter, the number of bins are chosen based on the length of the ribbons such that the width of bins does not change by the change in the ribbons length. As a reference point, we use 52 bins for ribbons with a length of 750 Å. The heat flux  $Q$  induced in the h-BN ribbons is calculated using Eq. (1.16). The cross-sectional area  $A$  in Eq. (1.16), is equal to the width times the thickness of nanoribbons. In our calculations we assume the thickness of the ribbons is 3.3306 Å [120] which is equal to the interlayer distance in bulk h-BN.

All the molecular dynamics simulations are conducted using LAMMPS molecular dynamics package [122]. Modified Tersoff potential [123, 124] is used to evaluate the interatomic interactions. To study the effect of temperature on the Kapitza conduc-

tance of nanoribbons, the simulations are performed at four different temperatures of 300 K, 500 K, 700 K and 1000 K. The velocity Verlet scheme is used to integrate the equations of motion using an integration time step of 0.1 fs. Total simulation time is at least 700 ps in which the system is equilibrated for a minimum of 200 ps and RNEMD scheme is implemented in the last 500 ps.

The equilibration stage consists of three steps. At first the optimized positions of the atoms are obtained by minimizing the energy of the system using the conjugate gradient method at zero temperature. Once the system energy is minimized, Berendsen thermostat is used in micro canonical ensemble (NVE) to raise the system temperature to the desired temperature for a minimum time period of 100 ps. Finally, to stabilize the system, the equilibration is carried out in canonical ensemble (NVT) for a time period of 100 ps. After the equilibration stage, the kinetic energy exchanges are conducted every 10 fs for 400 ps which is an enough time to induce a steady state temperature profile. After a steady state is reached, the simulation is conducted for another 100 ps and the temperature profile and heat energy exchanged data of the last 100 ps are used to evaluate the thermal conductivity of the grain boundaries and nanoribbons.

A typical steady state temperature profile of h-BN nanoribbons obtained using the above described method is shown in Fig. 2.1(b). As shown schematically, the thermal profile of nanoribbons includes a temperature jump at the grain boundary along with linear and nonlinear segments on each grain. The effective thermal conductivity of ribbons  $K_r$  can be calculated using the Fourier's law of heat conduction by

$$K_r = -\left(\frac{Q}{\partial T/\partial x}\right), \quad (2.1)$$

where  $\partial T/\partial x$  is the temperature gradient. The temperature gradient is evaluated using the linear segments of the temperature profile. Therefore the effective thermal

conductivity of the ribbon can be obtained using

$$K_r = -\frac{Q}{(T_f - T_i)/l} \quad (2.2)$$

where  $T_f$  and  $T_i$  are the end point values of the linear portion of temperature profile as shown in Fig. 2.1(b) and  $l$  is the distance between these two points.

The temperature jump at grain boundaries can be used to calculate the Kapitza conductance [125] of grain boundaries using

$$K_g = -\frac{Q}{\Delta T}, \quad (2.3)$$

where  $K_g$  is the Kapitza conductance and  $\Delta T$  is the temperature jump as shown in Fig. 2.1(b). The thermal resistance of grain boundaries  $R_g$  is the inverse of their Kapitza conductance

$$R_g = \frac{1}{K_g}. \quad (2.4)$$

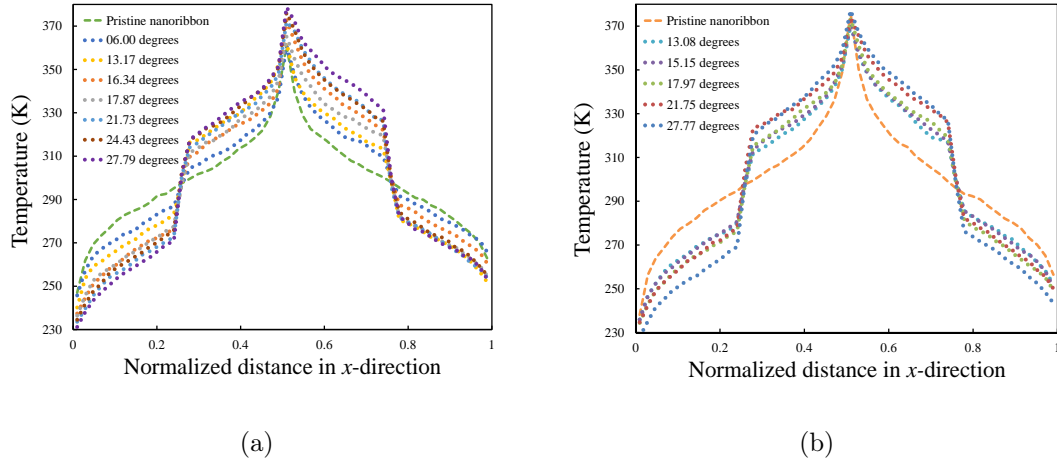


Figure 2.5: Temperature profiles of the nanoribbons containing grain boundaries show temperature jump in temperature profiles at the location of grain boundaries. The simulations are conducted at 300 K. (a) Zigzag oriented ribbons, (b) armchair oriented ribbons.

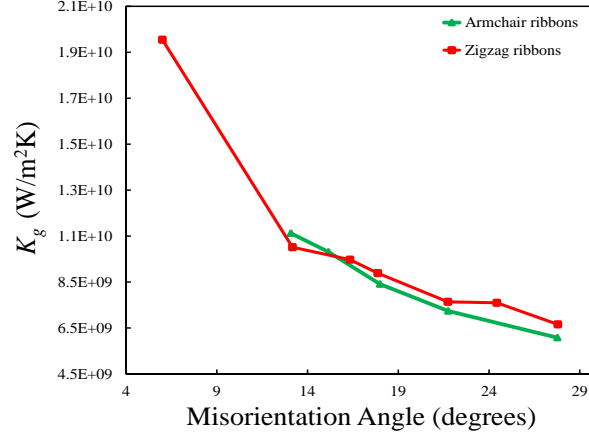


Figure 2.6: Kapitza conductance of grain boundaries in zigzag and armchair ribbons decreases with increase in their misorientation angle.

## 2.4 Results

### 2.4.1 Impact of misorientation angle on Kapitza conductance

The temperature profile of zigzag and armchair nanoribbons with a length of 750 Å at 300 K are shown in Fig. 2.5(a) and (b). The sharp temperature jumps at grain boundaries are characteristics of interface thermal resistance. The temperature jumps observed in these figures are used to find the Kapitza conductance of grain boundaries by employing Eq. (2.3). The Kapitza conductance of grain boundaries are plotted in Fig. 2.6. The Kapitza conductance of grain boundaries in zigzag ribbons is in between  $6.66 \times 10^9$  W/m<sup>2</sup>K and  $1.91 \times 10^{10}$  W/m<sup>2</sup>K and in armchair ribbons is in the range of  $6.08 \times 10^9$  W/m<sup>2</sup>K to  $1.06 \times 10^{10}$  W/m<sup>2</sup>K. The plots of Fig. 2.6 show that by increasing the misorientation angle the Kapitza conductance of grain boundaries reduces. In other words, the increase in the misorientation angle leads to an increase in the thermal resistance of grain boundaries. This is similar to the trend observed regarding the Kapitza conductance of the grain boundaries of graphene [109, 110]

To understand the mechanism leading to the thermal resistance of grain boundaries, we obtain the phonon spectra of the grain and grain boundary atoms. The phonon vibrational spectrum  $A(\omega)$  is calculated using the Fourier transform of the velocity

autocorrelation function (VACF) by

$$A(\omega) = \frac{1}{2\pi} \int e^{i\omega t} \left\langle \sum_{i=1}^N v_i(t)v_i(0) \right\rangle dt \quad (2.5)$$

where  $\omega$  is the phonon frequency,  $v_i(t)$  is the velocity of atom  $i$  at time  $t$  and  $N$  is the number of atoms in the system.  $\langle \dots \rangle$  denotes the ensemble average which in our calculations is replaced with time average. In our simulations, the time average is calculated in an NVE ensemble by recording the atoms velocity every 0.1 fs for 100 ps.

The phonon spectra of grains are shown in Fig. 2.7. As shown in Fig. 2.7(a), although the two grains have different orientations, but their phonon spectra are closely matching. Therefore, different misorientation of grains does not lead to a significant phonon scattering at the grain boundary.

As depicted in Fig. 2.7(b), the phonon spectrum of grain boundary atoms is not matching with phonon spectrum of grain atoms. The mismatch between the two spectra cause phonon scattering at the grain boundary which leads to interfacial thermal resistance at grain boundaries [110, 126]. As shown in Fig. 2.8 increasing the misorientation angle increases the defect density of grain boundaries. Larger defect density causes more phonon scattering which leads to a lower thermal conductivity of highly misoriented grain boundaries.

#### 2.4.2 Impact of misorientation angle on the effective thermal conductivity of ribbons

The effective thermal conductivity of the nanoribbons versus the misorientation angle of their grain boundaries are plotted in Fig. 2.9 for armchair and zigzag ribbons with a length of 750 Å. The effective thermal conductivity of both zigzag and armchair nanoribbons decreases by increasing the grain boundary misorientation angle. Zigzag ribbons have higher effective thermal conductivity than armchair ribbons. The

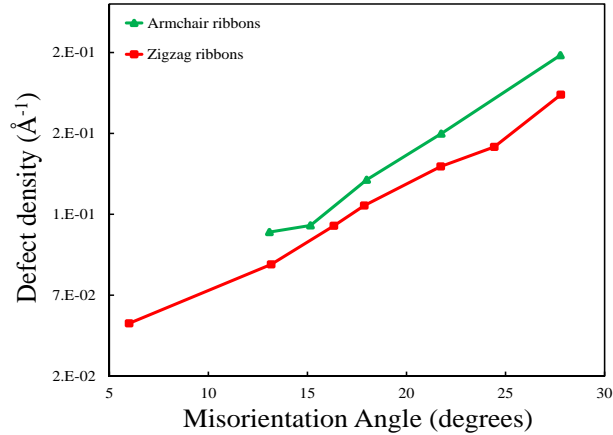


Figure 2.8: Defect density versus misorientation angle of grain boundaries. Grain boundary defect density increases almost linearly with increase in the misorientation angle.

effective thermal conductivity of zigzag nanoribbons is between 156.17 W/mK and 82.06 W/mK while for armchair nanoribbons it is between 106.64 W/mK and 76.03 W/mK. The reduction of thermal conductivity of ribbons is directly related to the reduction of Kapitza conductance of grain boundaries and is due to a higher defect density in such ribbons.

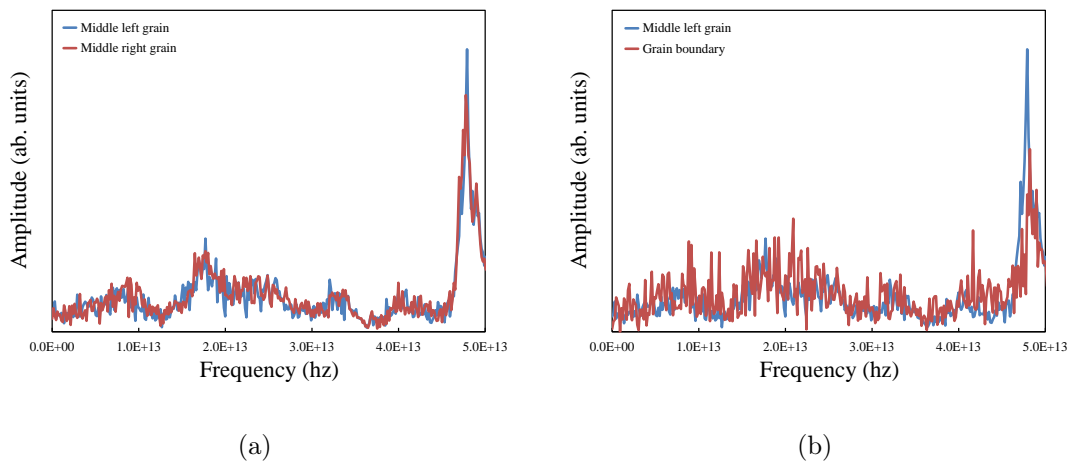


Figure 2.7: (a) Phonon vibrational spectra of two adjacent grains, (b) phonon vibrational spectra of grain atoms and grain boundary atoms.

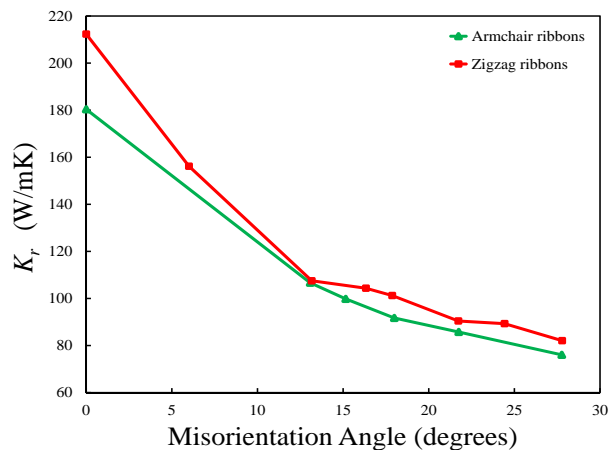


Figure 2.9: Effective thermal conductivity of zigzag and armchair ribbons decreases with increase in misorientation angle of grain boundaries.

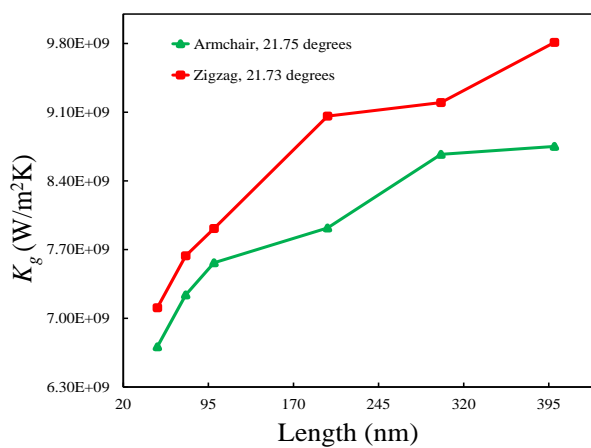


Figure 2.10: Kapitza conductance of grain boundaries versus the ribbons length at 300 K.

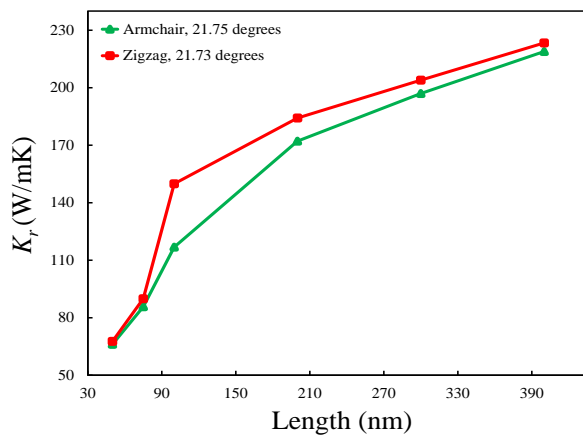


Figure 2.11: Effective thermal conductivity of ribbons versus their lengths at 300 K.

### 2.4.3 Effect of ribbons length on the Kapitza conductance and effective thermal conductivity of ribbons

The effects of grains length on the Kapitza conductance of grain boundaries are investigated by studying ribbons of different lengths. The Kapitza conductance of nanoribbons and effective thermal conductivity nanoribbons of different lengths at a temperature of 300 K are shown in Fig. 2.10 and Fig. 2.11, respectively. These plots are obtained for armchair and zigzag nanoribbon including symmetric tilt grain boundary with a misorientation angle of  $21.75^\circ$  and  $21.73^\circ$ , respectively. It can be observed that by increasing the length of grains, both the Kapitza conductance of grain boundaries and the effective thermal conductivity of ribbons increase. This is similar to the trend observed previously for other two-dimensional materials [110, 109, 114].

The higher thermal conductivity of longer ribbons is attributed to longer phonon mean free path in such ribbons. Thermal conductivity is directly related to phonon mean free path by

$$K_r = \frac{1}{3}C_p v l_{p-p} \quad (2.6)$$

where  $C_p$  is specific heat of the phonons,  $v$  is the group velocity and  $l_{p-p}$  is the effective phonon mean free path. The relationship between effective phonon mean free path ( $l_{p-p}$ ) and length of the nanoribbon ( $l$ ) is given by [127, 128]

$$\frac{1}{l_{p-p}} = \frac{1}{l_\infty} + \frac{1}{l} \quad (2.7)$$

where  $l_\infty$  is phonon mean free path of a infinite ribbon. Therefore, by increasing the length of nanoribbons the effective phonon mean free path increases which based on Eq. (2.6) leads to an increase in the Kapitza conductance of grain boundaries and effective thermal conductivity of ribbons.

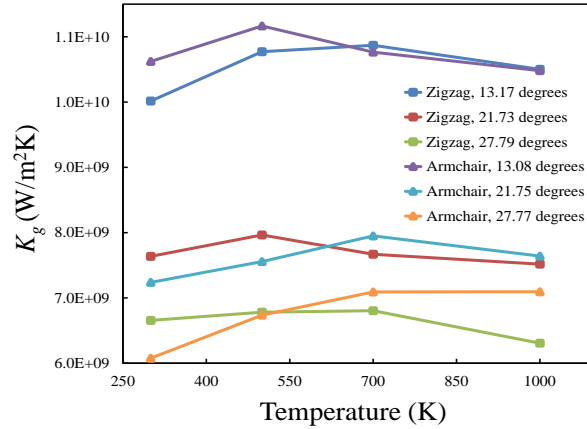


Figure 2.12: Kapitza conductance of grain boundaries in zigzag and armchair ribbons at different temperatures.

#### 2.4.4 Effect of temperature on Kapitza conductance and effective thermal conductivity of ribbons

The impact of temperature on the Kapitza conductance is studied by studying the Kapitza conductance of nanoribbons with a length of  $750 \text{ \AA}$  at temperatures of 300 K, 500 K, 700 K and 1000 K. The Kapitza conductance versus temperature for armchair and zigzag ribbons are shown in Fig. 2.12. These graphs show that temperature does not have a significant impact on the Kapitza conductance of grain boundaries of zigzag and armchair nanoribbons. By increasing the temperature, Kapitza conductance of grain boundaries initially increases slightly and then decreases with further increase in temperature. The reduction of Kapitza conductance at high temperatures can be attributed to increase in the thermal disorder in GB zone. Higher disorder leads to higher scattering which results in a lower Kapitza conductance [126, 129].

The effective thermal conductivity of zigzag and armchair ribbons with a length of  $750 \text{ \AA}$  as a function of temperature are shown in Fig. 2.13. It can be noticed that effective thermal conductivity decreases with increase in temperature. The effect of Umkalpp scattering increases with increase in temperature which results in decrease of effective thermal conductivity of the nanoribbon [130].

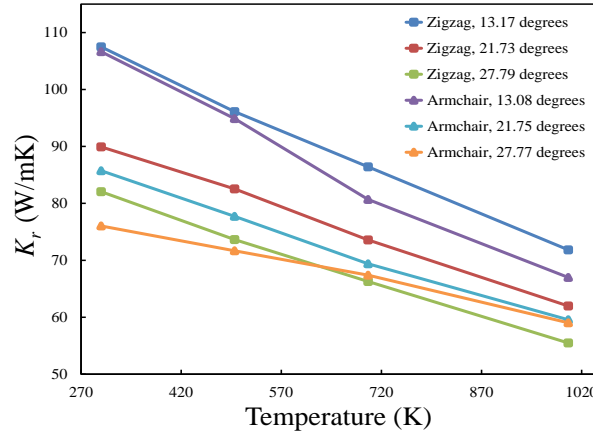


Figure 2.13: Effective thermal conductivity of zigzag and armchair ribbons decreases with increase in temperature.

## 2.5 Conclusion

In this chapter, we used reverse nonequilibrium molecular dynamics modeling to study the thermal properties of h-BN ribbon containing symmetric tilt grain boundaries. By increasing the misorientation angle of grain boundaries, their defect density increases. The increase in the defect density enhances phonon scattering at grain boundaries which results in lower thermal conductance of grain boundaries with higher misorientation angle. Kapitza conductance and effective thermal conductivity increases with increase in the length of nanoribbon which is due to larger phonon mean free path in longer ribbons. The temperature effects on the Kapitza conductance of grain boundaries is negligible whereas by increase in temperature the effective thermal conductivity of nanoribbons reduces.

## CHAPTER 3: Phononic Thermal Transport Properties of $C_3N$ Nanotubes

### 3.1 Introduction

Unique physical, chemical and mechanical properties of graphene [131, 132, 18, 133] make it an excellent candidate for the next generation of nano devices. A fundamental deficiency associated with using graphene in nanoelectronic devices is its zero band gap around the Fermi level. Because of its zero band gap, the electrical conduction cannot be modulated below a certain limit which makes it difficult to employ graphene in digital circuits where high ON/OFF ratios are necessary. Since a sizable band gap can greatly enhance the potential applications of graphene, intense research has been conducted toward band gap widening of graphene. Several techniques have been proposed to open a band gap in graphene including substrate-induced gap [134], electron confinement [135] and hydrogenization of graphene [136]. Although these techniques can be used to introduce a band gap in graphene, they face limitations in practice when their controllable implementation for large scale production is required.

Nitrogen doping is another method for opening band gaps in graphene [137]. De-

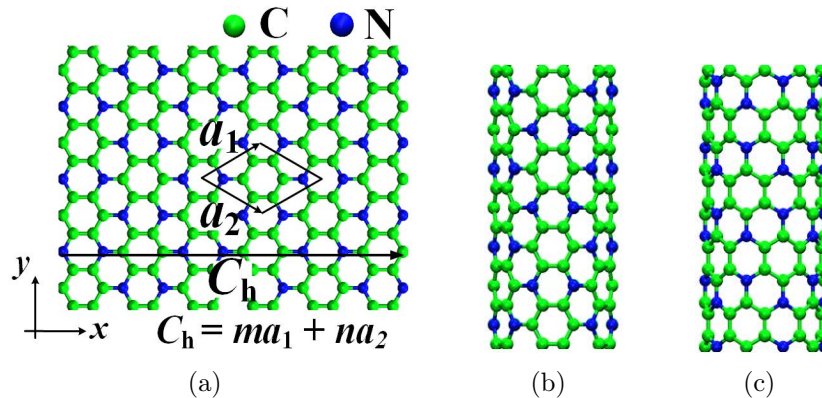


Figure 3.1: (a) Schematic of  $C_3N$  nanoribbon showing 8-atom unit cell, (b) armchair nanotube, and (c) zigzag nanotube.

pending on the synthesis procedure and nitrogen percentage various structures of N-doped graphene are generated. Monolayer  $C_3N$  is one of the most stable N-doped graphene materials which was first synthesized by the pyrolysis of single crystals of hexaaminobenzene trihydrochloride in solid state [72]. More recently large scale sheets of  $C_3N$  are fabricated via polymerization of 2,3-diaminophenazine [73].  $C_3N$  has a graphene-like atomic structure in which nitrogen (N) atoms are homogeneously and orderly distributed between the carbon (C) atoms as shown in Fig. 3.1. Each carbon phenyl ring is covalently bonded to six nitrogen atoms and both carbon and nitrogen atoms display a  $D_{6h}$  symmetry. The isolation of  $C_6$  rings leads to opening of an indirect band gap of 1.042 eV [138] which makes  $C_3N$  a semiconductor with strong polar covalent bonds.  $C_3N$  displays a high thermal conductivity of about 815 W/mK [139] and a high electrical conductivity of  $1.41 \times 10^3$  S/cm [72]. It has a Young's modulus of 1090.0 GPa which makes it stiffer than graphene [139]. Moreover, monolayer  $C_3N$  is very stable and can withstand temperatures as high as 2000 K.

Rolling up the  $C_3N$  nanosheets into nanotubes gives rise to other remarkable properties.  $C_3N$  nanotube ( $C_3NNT$ ) has been investigated for hydrogen storage [74, 140]. Hales and Barnard [141] used density functional theory to study the thermodynamic stability of  $C_xN$  nanotubes ( $x = 1, 2, 3, 5,$  and  $7$ ) and concluded that the relaxed structure of  $C_3N$  is independent of the nanotube chirality. Jalili et al. [142] studied the role of defects on the electronic properties of  $C_3NNT$  and concluded that  $C_3NNT$  with vacancy defects exhibit ferromagnetic spin ordering. Wang et al. [143] studied the mechanical and electronic properties of  $C_3NNT$  with various chiralities and showed that  $C_3NNT$  is semiconductor with high Young's modulus.

Computational methods have been proved to be promising in studying the properties of nanomaterials [144, 145, 146, 113, 147, 1, 148, 114, 149, 150, 151, 117, 152, 153, 12, 119, 154, 155, 3]. In this chapter we use reverse nonequilibrium molecular dynamics simulations to study the thermal properties of  $C_3NNT$ . The impact of chirality

and length of nanotubes on their thermal conductivity is studied. Furthermore, using the phonon dispersion curves and relaxation times, the lower thermal conductivity of C<sub>3</sub>NNT with respect to carbon nanotube (CNT) is explained. The transition length of C<sub>3</sub>NNT at which the heat energy transfer is changing from ballistic to diffusive mode is calculated. The reason for lower transition length of C<sub>3</sub>NNT than CNT is explained.

### 3.2 Structure of C<sub>3</sub>N nanotube

Fig. 3.1a illustrates the monolayer C<sub>3</sub>N nanoribbon in which each hexagonal carbon ring is covalently bonded to six nitrogen atoms. The C–C and C–N bonds have similar atomic bond lengths of 1.44 Å. C<sub>3</sub>N crystal involves a monoclinic unit cell with equal lattice constants  $a = b = 4.95$  Å containing six carbon atoms and two nitrogen atoms. C<sub>3</sub>NNT is closed cylinder constructed by rolling the monolayer C<sub>3</sub>N nanoribbon. C<sub>3</sub>N can be rolled in different angles with respect to its lattice. The atomic structure and electrical, mechanical and optical properties of nanotubes are affected by the rolling direction. The rolling direction is defined by the chiral vector  $C_h = m\mathbf{a}_1 + n\mathbf{a}_2$  where  $\mathbf{a}_1 = a(\frac{\sqrt{3}}{2}, \frac{1}{2})$  and  $\mathbf{a}_2 = a(\frac{\sqrt{3}}{2}, -\frac{1}{2})$  are the lattice vectors of C<sub>3</sub>N sheet. The integer indices  $(m, n)$  fully defines the nanotube and are used in the literature to characterize nanotubes. For example, the special cases in which  $m = n$  gives the armchair oriented nanotube as shown in Fig. 3.1(b) whereas the case with  $m = 0$  gives the zigzag oriented nanotube as shown in Fig. 3.1(c). The diameter of nanotubes can be obtained using the magnitude of the chiral vector which is equal to the perimeter of the nanotube.

### 3.3 Computational method

We study thermal properties of the zigzag and armchair C<sub>3</sub>NNT with various chiralities and lengths ranging from 4 nm to 1,000 nm. All the simulations are conducted using LAMMPS molecular dynamics package [91]. The interatomic interactions are simulated using modified Tersoff potential [156, 157]. The equations of motion are in-

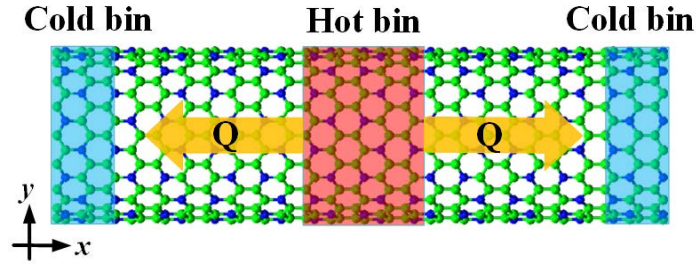


Figure 3.2: A schematic of C<sub>3</sub>N nanotube showing the hot bin and cold bin at the middle and two ends of nanotube, respectively.

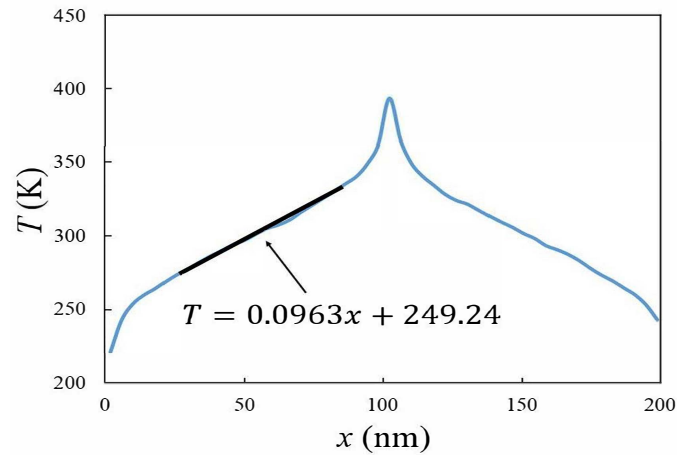


Figure 3.3: Temperature distribution along longitudinal axis of the nanotube.

egrated using velocity Verlet scheme with an integration time step of 0.1 fs. Periodic boundary conditions are considered along the longitudinal direction of the nanotube. The initial configuration of the system is relaxed by minimizing its potential energy using conjugate gradient method. The temperature of the system is slowly increased by scaling up the velocities of individual atoms using Berendsen thermostat [158] in a microcanonical ensemble (NVE) for a period of 50 ps. The system is further equilibrated and maintained at room temperature for 50 ps under canonical ensemble (NVT).

Thermal properties of C<sub>3</sub>NNT are evaluated using reverse nonequilibrium molecular dynamics (RNEMD) method [159]. Detailed description of RNEMD method is given in chapter 1. Fig. 3.2 shows the RNEMD method implemented in C<sub>3</sub>NNT. In this method a heat flux  $Q$  is imposed to the system which is given by Eq. (1.16). The

temperature gradient that develops as a result of the heat flux is calculated. For the purpose of imposing a heat flux, nanotubes are divided into slabs along the longitudinal direction. We divided 4 nm and 6 nm nanotubes into 20 slabs, 8 nm nanotubes into 40 slabs and nanotubes longer than 8 nm are divided into 50 slabs. In Eq. (1.16),  $A$  is the cross sectional area of the simulation cell.  $A$  of the nanotube is given by (circumference)  $\times$  (thickness of nanotube). Circumference is the magnitude of the chirality vector and thickness is taken the same as the interlayer distance of bulk  $C_3N$  which is 3.2 Å [139].

By repeating the exchange process, a steady state temperature profile similar to the profile shown in Fig. 3.3 is established. The slope of the linear portion of the temperature profile represents the temperature gradient  $\frac{\partial T}{\partial x}$  along the axis of nanotube. By taking the averages of the heat flux and temperature gradient and using the Fourier's law of heat conduction, the thermal conductivity  $K$  can be obtained from

$$K = -\frac{\langle Q \rangle}{\langle \partial T / \partial x \rangle}, \quad (3.1)$$

where  $T$  is temperature and brackets  $\langle \rangle$  denote average of the quantities with respect to time and the atoms in the domain. The averaging is taken over a period of 100 ps.

## 3.4 Results

### 3.4.1 Thermal conductivity of $C_3NNT$ in comparison to CNT

We compare the thermal conductivity of armchair and zigzag CNT with those of  $C_3NNT$  in Fig. 3.4. The armchair  $C_3NNT$  and CNT have a chirality of (5,5) and (10,10), respectively, with a similar diameter of 1.3 nm whereas the chirality of zigzag  $C_3NNT$  and CNT are (0,9) and (0,18), respectively, with a diameter of 1.49 nm.

The graphs of Fig. 3.4 show that thermal conductivity of CNT is higher than the thermal conductivity of their counterpart  $C_3NNT$  with the same length and diameter. By increase in the length, the difference between the thermal conductivities become

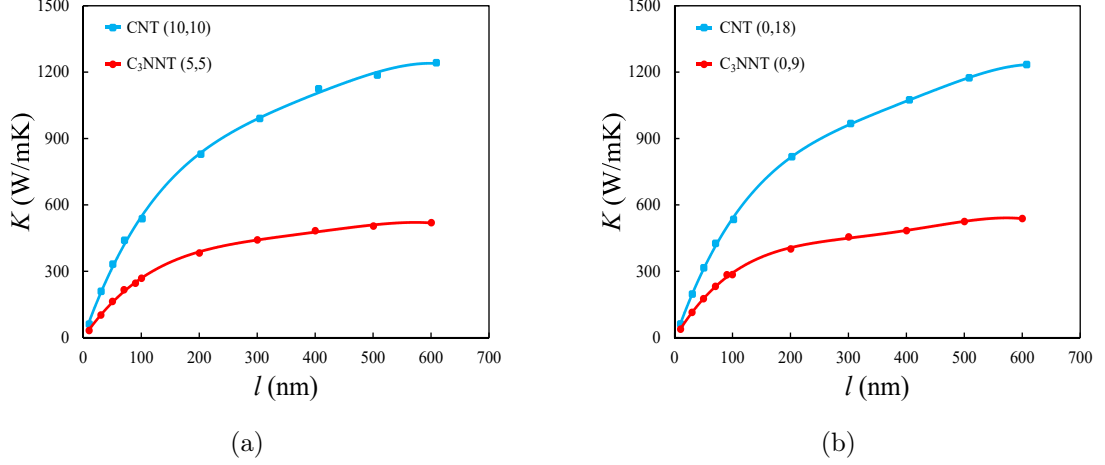


Figure 3.4: Comparison of thermal conductivity of C<sub>3</sub>NNT and CNT with varying length. (a) Armchair nanotubes, and (b) zigzag nanotubes. Thermal conductivities are not quantum corrected.

Table 3.1: Ballistic to diffusive transition length of different nanotubes in nm

Nanotube	length
CNT (10,10)	107.20
CNT (0,18)	103.32
C <sub>3</sub> NNT (5,5)	71.66
C <sub>3</sub> NNT (0,9)	79.95

more significant. At 600 nm the conductivity of (5,5) C<sub>3</sub>NNT is 519.8 W/mK which is considerably lower than the conductivity of the (10,10) CNT which is 1242.6 W/mK. Similarly, the thermal conductivity of (0,9) C<sub>3</sub>NNT is 538.3 W/mK which is considerably lower than the conductivity of the (0,18) CNT which is 1234.3 W/mK. The thermal conductivity of CNTs presented in this chapter is in good agreement with previous study in which the authors used nonequilibrium molecular dynamics [160].

### 3.4.2 Impact of length and chirality of C<sub>3</sub>NNT on its thermal conductivity

The impact of length and chirality of nanotubes on their thermal conductivity is studied by considering armchair nanotubes with chiralities of (5,5), (9,9) and (13,13) and zigzag nanotubes with chiralities of (0,9), (0,16) and (0,22) with lengths varying

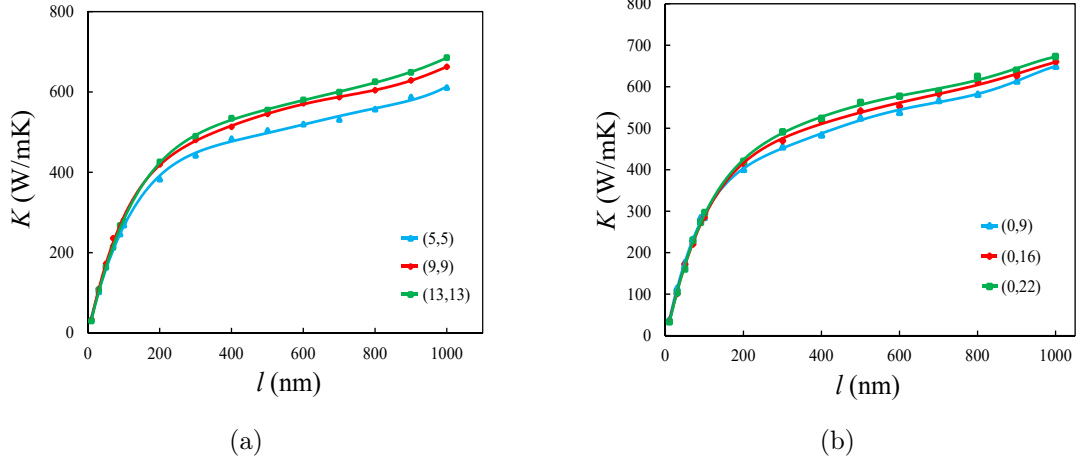


Figure 3.5: Thermal conductivity of  $C_3NNT$ . (a) Armchair nanotube, and (b) zigzag nanotube

from 4 nm to 1000 nm. The thermal conductivity of nanotubes of different chirality as a function of length are shown in Fig. 3.5. It can be observed that by increasing in the diameter, the thermal conductivity of both armchair and zigzag  $C_3NNT$  increases. The graphs of Fig. 3.5 also show that by increasing the length of nanotubes their thermal conductivity increases. This is not surprising since thermal conductivity  $K$  depends on the length via a power law relation

$$K = \alpha L^\beta. \quad (3.2)$$

When the nanotubes lengths are much smaller than phonon mean free path (MFP)  $l_0$ , i.e  $l_0 \gg L$ , heat flows ballistically and  $\beta = 1$ . On the other hand, when the MFP is much smaller than the nanotubes length,  $l_0 \ll L$ , heat flows diffusively and thermal conductivity is given by the Boltzmann-Peierls relation. In the diffusive regime  $\beta < 1$ . There is a transition length at which the transfer of heat energy changes from ballistic to diffusive. The transition length can be found by using the log-log plot of conductivity versus length as shown in Fig. 3.6. The log-log plot has a slope of  $\beta \approx 1$  at short lengths and a slope of  $\beta < 1$  for longer nanotubes. The

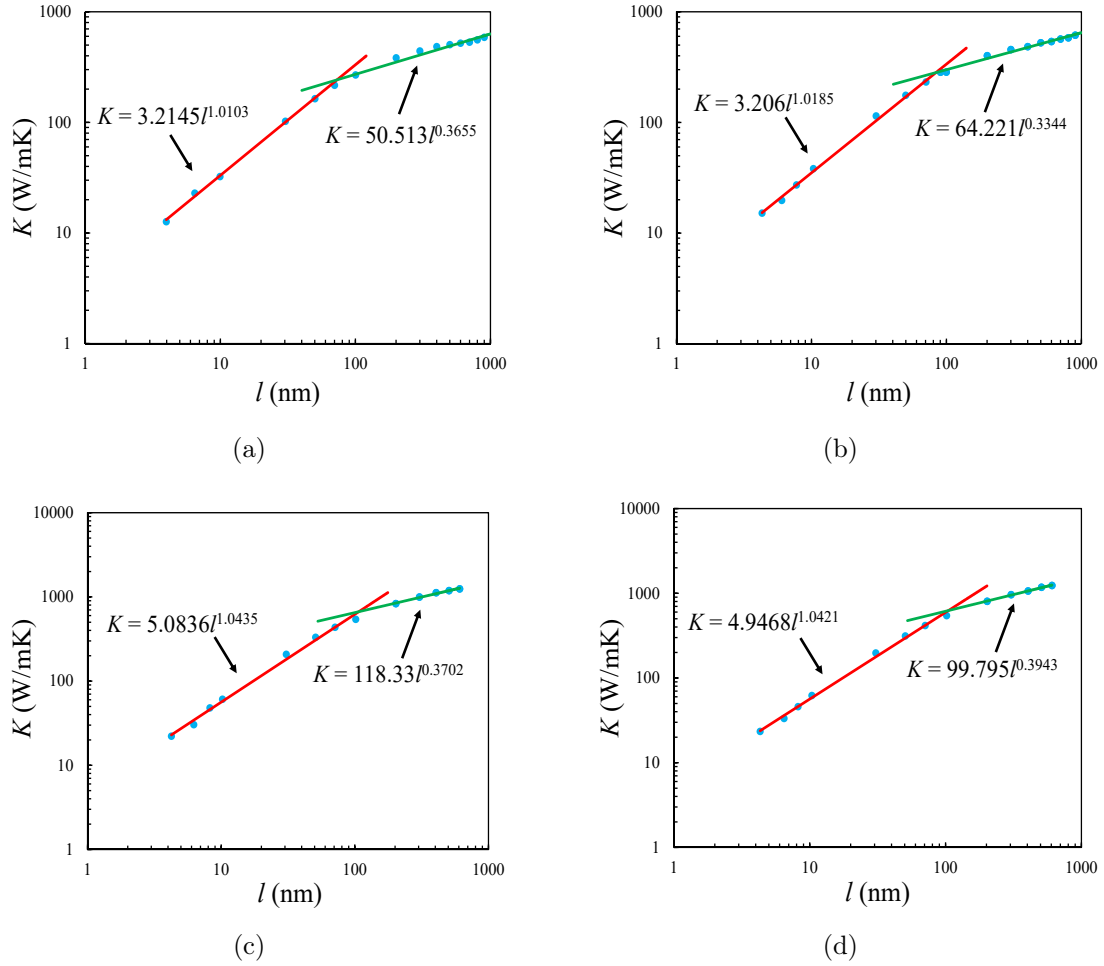


Figure 3.6: Log-Log plot of nanotube length versus conductivity showing the diffusive to transition length. (a)  $C_3$ NNT with chirality (5,5), (b)  $C_3$ NNT with chirality (0,9), (c) CNT with chirality (10,10), and (d) CNT with chirality (0,18).

transition length is the length at which the two tangent lines intersect. As given in Table 3.1, our results predict that the transition length of armchair and zigzag  $C_3$ NNT is approximately 71.66 nm and 79.95 nm respectively and the transition length of armchair and zigzag CNT is 107.20 nm and 103.32 nm respectively. The lower transition length of  $C_3$ NNT is due to higher scattering rates of phonons due to the presence of nitrogen.

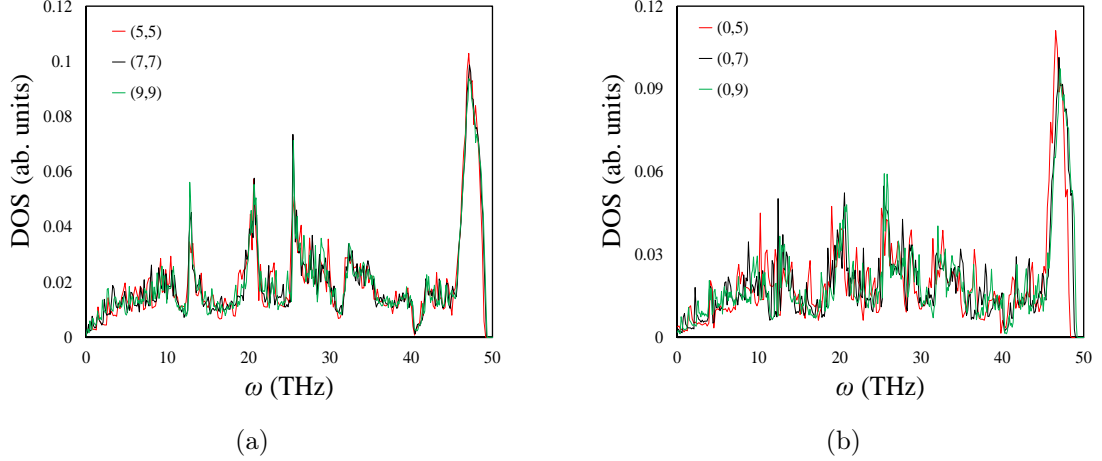


Figure 3.7: Phonon density of states of  $C_3NNT$  with different chirality. (a) Armchair nanotube, and (b) zigzag nanotube

### 3.4.3 Impact of the diameter of $C_3NNT$ on thermal conductivity

The graphs of Fig. 3.5 show that increase in the diameter of  $C_3NNT$  leads to an increase in their thermal conductivity. To understand the impact of diameter on thermal conductivity, the density of states and dispersion curves of  $C_3NNT$  with different chiralities are compared in Figures 3.7 and 3.8. As shown in Fig. 3.7, increase in the diameter of nanotubes results in blueshift of the peaks of density of states. Phonon stiffening generally leads to increase in group velocity and enhances the thermal conductivity. Comparison of the acoustic branches of phonon dispersion curves show that the change in the diameter, does not have a significant impact on the longitudinal (LA) and torsional (ToA) branches. However, by increase in the diameter, the transverse acoustic (TA) modes move upward resulting in a large enhancement in frequency and increase in phonon group velocity. Based on Eq. (3.6), the increase in group velocity leads to enhancement of thermal conductivity. Therefore, the main mechanism responsible for higher thermal conductivity of larger diameter nanotubes is the stiffening of transverse acoustic modes.

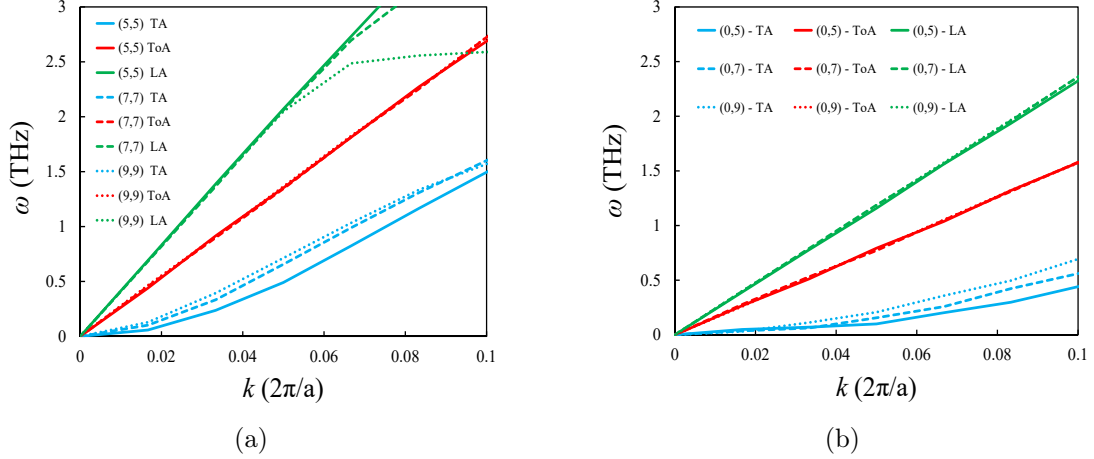


Figure 3.8: Acoustic phonon modes of C<sub>3</sub>NNT with different chirality. (a) Armchair nanotube, and (b) zigzag nanotube

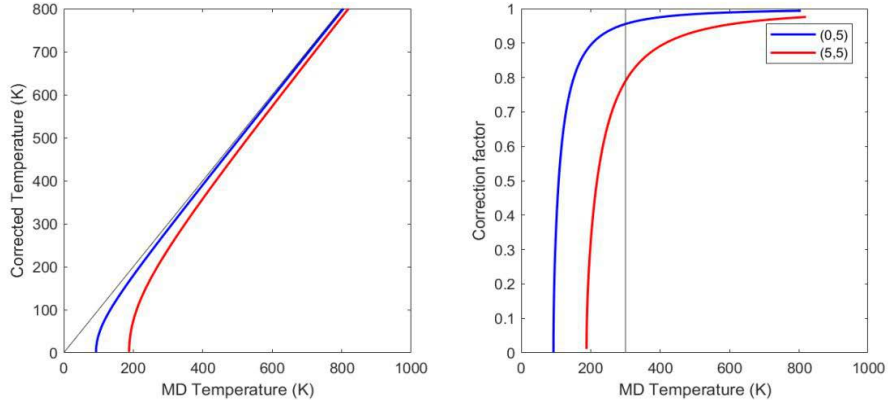


Figure 3.9: Quantum correction of thermal conductivity of armchair and zigzag C<sub>3</sub>NNTs with chiralities (5,5) and (0,5).

### 3.4.4 Quantum correction of thermal conductivity

Quantum effects can have a considerable effect on thermal transport at temperatures below Debye temperature [161]. This correction can be calculated by equating the total classical energy at a given temperature where the MD simulation are carried out ( $T_{MD}$ ), to the total phonon energy at temperature  $T$  as shown in Eq. (3.3). Where  $\omega_D$  is the Debye frequency corresponding to Debye temperature  $T_D$ , and  $D_N(\omega)$  is the density of states [162].

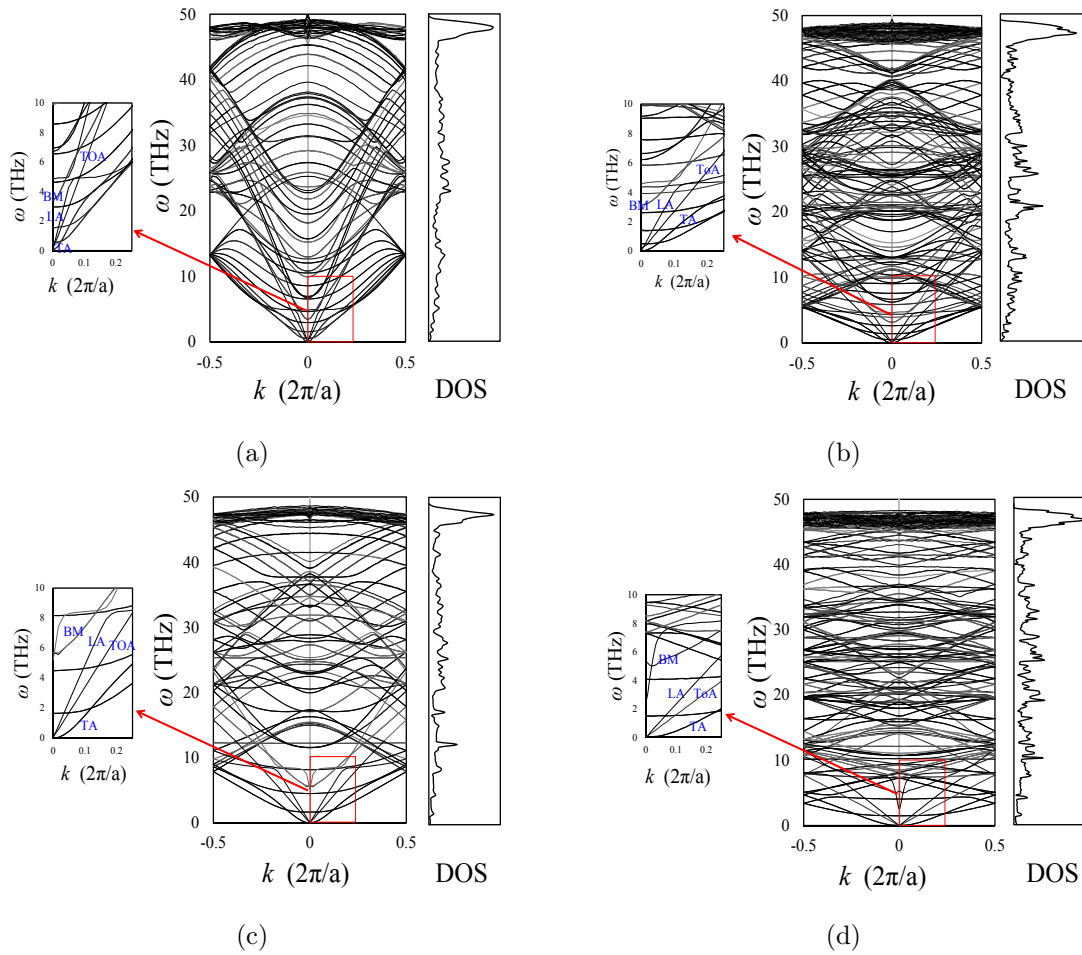


Figure 3.10: Phonon dispersion curves and density of states of CNTs and C<sub>3</sub>NNTs. (a) CNT with chirality (10,10), (b) C<sub>3</sub>NNT with chirality (5,5), (c) CNT with chirality (0,10), and (d) C<sub>3</sub>NNT with chirality (0,5)

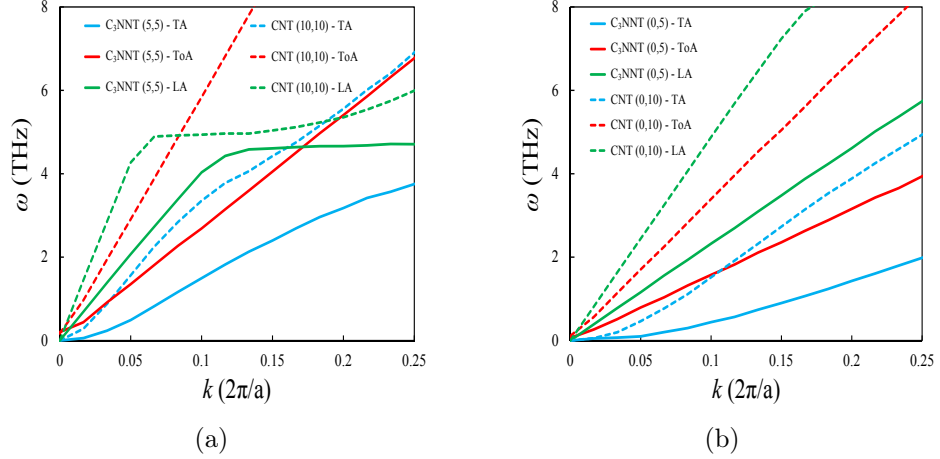


Figure 3.11: Comparison of acoustic modes of dispersion curves of C<sub>3</sub>NNT and CNT. (a) Armchair nanotube, and (b) zigzag nanotube

$$\frac{3}{2}k_B T_{MD} = \int_0^{\omega_D} D_N(\omega) \left( \frac{1}{2} + \frac{1}{\exp(\hbar\omega/k_B T) - 1} \right) \hbar\omega d\omega \quad (3.3)$$

Using Eq. (3.3) the MD temperatures can be corrected using Eq. (3.4). Therefore, the thermal conductivity obtained from MD simulations can also be corrected using a Eq. (3.5), where  $\frac{dT_{MD}}{dT}$  is the quantum correction factor.

$$T_{MD} = \frac{T^2}{T_D} \int_0^{\frac{T_D}{T}} \frac{x}{e^x - 1} dx + \frac{T_D}{4} \quad (3.4)$$

$$k_{qc} = \left( \frac{dT_{MD}}{dT} \right) k_{MD} \quad (3.5)$$

Fig. 3.9 shows the relation of MD temperature and corrected temperature, as well as the correction factor for thermal conductivity for (5, 5) and (0,5) C<sub>3</sub>NNT's.

### 3.5 Phonon transport in C<sub>3</sub>NNT

A phonon state can be described by wavevector,  $k$ , polarization  $p$ , which is transported by group velocity  $v$ , and has a relaxation time  $\tau$ . The phonon contribution to

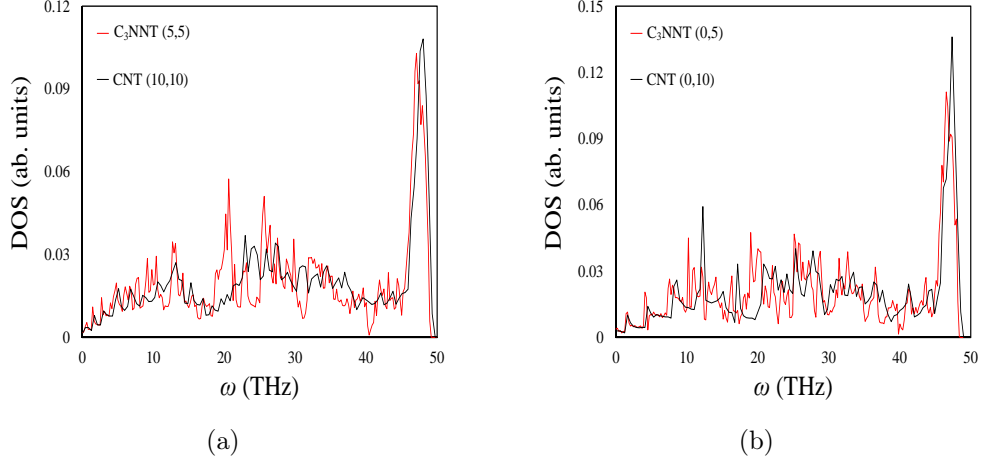


Figure 3.12: Comparison of phonon density of states of  $C_3NNT$  and CNT. (a) Armchair nanotube, and (b) zigzag nanotube

thermal conductivity can be calculated using Eq. (3.6) [163].

$$K = \int_0^{\omega_{\max}} C v l d\omega = \int_0^{\omega_{\max}} C v^2 \tau d\omega \quad (3.6)$$

where  $\omega$  is phonon frequency,  $C$  is the specific heat.

### 3.5.1 Dispersion relation and density of states

The impact of nitrogen atoms on thermal transport of  $C_3N$  nanotubes is further studied by comparing the phonon dispersion curves and density of states of  $C_3NNT$  with those of CNT. The phonon dispersion curves and density of states are constructed using the *fix phonon* [164] command in LAMMPS [91]. In this approach the dynamical matrix is constructed using molecular dynamics simulation by following the motion of atoms and employing the fluctuation–dissipation theory. For this purpose, first the Green’s coefficient function is obtained by taking the second moment of atomic displacements [165, 166, 167]. The force constant of individual atoms are then calculated using the Green’s coefficient function. Finally, the dynamical matrix of the unit cell is estimated from the force constants.

To extract the phonon dispersion curves, periodic boundary conditions are applied

in all directions with vacuum in the  $x$  and  $z$  directions to avoid unwanted interactions between neighboring images. The system temperature is increased to 300 K using Langevin thermostat [168, 169] under micro-canonical ensemble. Once the equilibration is reached, the dynamical matrix of the crystal is extracted using the *fix phonon* command [164]. The post-processing software *phana* is used to extract the dispersion curves and density of states from the dynamical matrix [164].

The phonon dispersion curves and density of states (DOS) of (5,5) and (0,5) C<sub>3</sub>NNT along with (10,10) and (0,10) CNT are shown in Fig. 3.10. These figures show that the phonon dispersions of nanotubes depends on the indices  $(m, n)$  or equivalently on the chirality and diameter of nanotubes. As shown in Fig. 3.10, for small values of  $k$  the dispersion relations of the longitudinal and torsional acoustic modes of all nanotubes is linear whereas it is nonlinear for transverse acoustic mode. The acoustic modes of C<sub>3</sub>NNT and CNT are compared in Fig. 3.11. It is observed that all the acoustic modes of C<sub>3</sub>NNT are depressed in comparison with CNT resulting in a reduction in the slope of the dispersion curve and significant reduction in the phonon group velocity of acoustic branches.

To further elucidate the reason for the difference between the thermal conductivity of CNT and C<sub>3</sub>NNT, their phonon DOS are compared in Fig. 3.12. The phonon DOS of armchair and zigzag CNT show a strong peak at about 48 THz ( 1600 cm<sup>-1</sup>) whereas the strong peak of armchair and zigzag C<sub>3</sub>NNT occurs at about 46 THz ( 1533 cm<sup>-1</sup>). Therefore, the DOS of C<sub>3</sub>NNT is redshifted with respect to CNT. Furthermore, as phonons with fixed number of frequencies gather in a narrower frequency range, the probability for phonon scattering enhances which leads to a lower phonon relaxation time.

### 3.5.2 Phonon scattering in C<sub>3</sub>NNT

Based on Eq. (3.6), thermal conductivity is directly related to phonon mean free path (MFP). For each phonon mode the MFP can be calculated using  $\lambda = v\tau$ . The

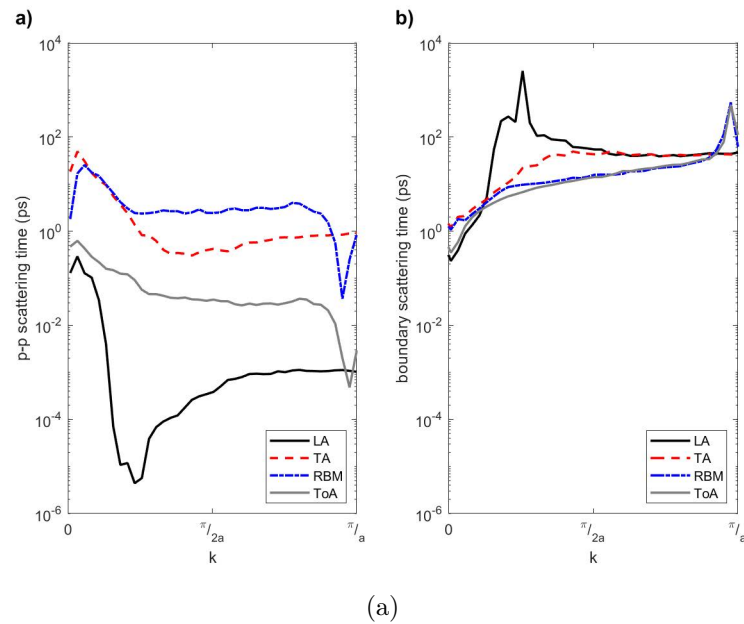


Figure 3.13: CNT phonon relaxation time at different polarizations with (a) phonon-phonon Umklapp scattering, (b) boundary scattering

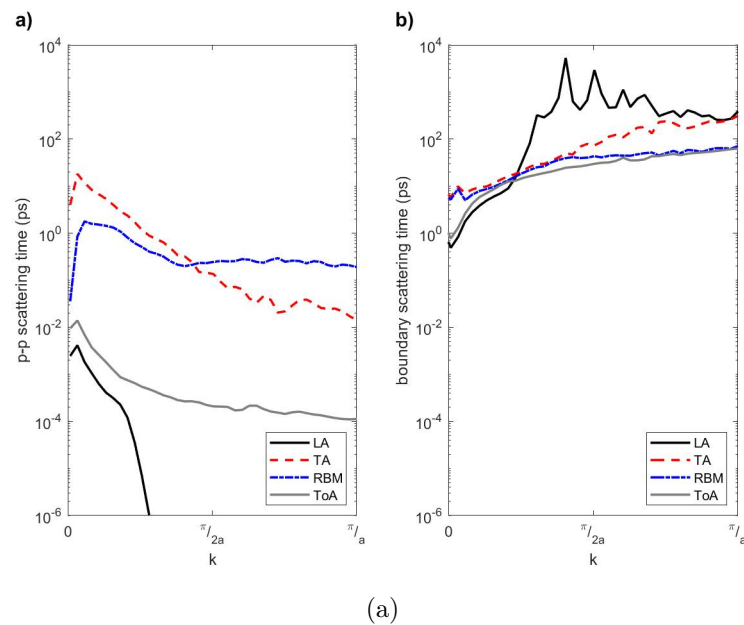


Figure 3.14: C<sub>3</sub>NNT phonon relaxation time at different polarizations with (a) phonon-phonon Umklapp scattering, (b) boundary scattering

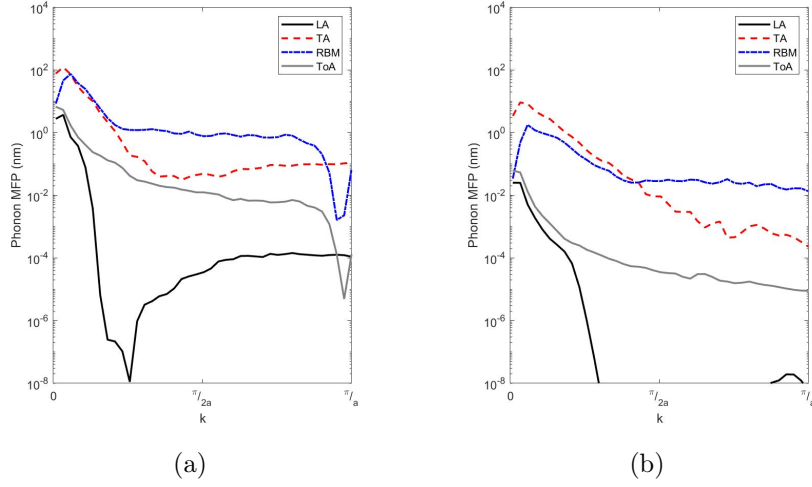


Figure 3.15: Acoustic phonon mean free path for (a) CNT, (b) C<sub>3</sub>NNT

group velocity can be obtained from dispersion curves as  $v = d\omega/dk$ . For independent scattering events the scattering probabilities are additive; therefore, one can obtain the total scattering rate as the sum of phonon-phonon (p-p), defect, and boundary scattering as shown in Eq. (3.7)

$$\frac{1}{\tau} = \frac{1}{\tau_{pp}} + \frac{1}{\tau_d} + \frac{1}{\tau_b} \quad (3.7)$$

where  $\tau_{pp}$ ,  $\tau_d$ , and  $\tau_b$  are the phonon-phonon, defect, and boundary scattering time constants. The boundary relaxation time was estimated using the relation,  $\tau_b = \frac{FL}{|v_g|}$ , where  $F = 1/2$  is the geometric factor used for nanotubes [170]. Here we have calculated the p-p scattering rate by considering three phonon processes, where in each scattering event either a phonon decays into two, or two phonons combine to generate a third phonon. The momentum and energy selection rules govern these scattering events and are shown in Eq. (3.8) and 3.9 respectively, where in case of a normal (N) scattering process  $G = 0$  and in case of an Umklapp process  $G$  is equal to a reciprocal lattice vector. The rate of a three-phonon Umklapp process was calculated based on first order perturbation theory using Eq. (3.10) where  $k$  is the wavevector

Table 3.2: Phonon MFP of different phonon modes of CNT with chirality (10,10) in nm

Phonon mode	at $k=0$	maximum
LA	2.766	3.695
ToA	6.716	6.716
RBM	8.436	74.56
TA	76.99	123.1

Table 3.3: Phonon MFP of different phonon modes of C<sub>3</sub>NNT with chirality (5,5) in nm

Phonon mode	at $k=0$	maximum
LA	0.025	0.025
ToA	0.062	0.062
RBM	0.034	1.772
TA	3.430	9.189

of a given phonon,  $M$  is the average atomic mass of the lattice,  $\gamma$  is the Gruneisen parameter shown in Eq. (3.11) Where  $C_p$  is the specific heat and  $\alpha$  is the volumetric thermal expansion coefficient.

$$k \pm k' = k'' + G \quad (3.8)$$

$$\hbar\omega \pm \hbar\omega' = \hbar\omega'' \quad (3.9)$$

$$\frac{1}{\tau_U} = \sum_{k'} \frac{8\gamma^2 \hbar\omega\omega'\omega''}{3n_a v_g^2 M} \pi \delta(\omega \pm \omega' - \omega'') (N'_0 - N''_0) \quad (3.10)$$

$$\gamma = V \left( \frac{dP}{d\epsilon} \right)_V = \frac{\alpha v_g^2}{C_p} \quad (3.11)$$

In order to calculate the p-p scattering rate of a phonon mode with wavevector

$k$ , in Eq. (3.10) the sum is taken over all possible  $k'$  modes using the dispersion relation while satisfying the selection rules listed in Eq. (3.8) and Eq. (3.9) [171]. Fig. 3.13 shows the acoustic phonon relaxation time of phonon modes (wavevector and polarization) based on p-p scattering in CNT lattice and boundary scattering of a 100 nm CNT. It can be seen that TA and radial breathing bands (RBM) indicate the lowest phonon scattering rates that exceeds the boundary scattering time at lower wavevector modes indicating ballistic phonon transport in these regions. In contrast, the LA and ToA bands have much higher scattering rates and indicate diffusive transport. Fig. 3.14 shows similar results of phonon scattering times of C<sub>3</sub>NNT, where the p-p scattering times are shorter than the case of CNT in all bands indicating higher scattering rates. This higher scattering rate can be attributed to presence of nitrogen atoms which can be treated as mass fluctuation or defects in the C<sub>3</sub>NNT lattice. On the other hand, the boundary scattering times are longer than the case of CNT due to mostly smaller values of phonon group velocity in C<sub>3</sub>NNT lattice. The higher rate of phonon scattering is also clearly reflected on the shorter phonon mean free path,  $\lambda = \tau.v_g$ , of C<sub>3</sub>NNT compared to CNT in all bands as shown in Fig. 3.15. Table 3.2 and Table 3.3 shows the MFP of different nanotubes. This analysis explains the lower thermal conductivity of C<sub>3</sub>NNT based on higher phonon scattering rates caused by presence of nitrogen atoms in the lattice; in addition, it indicates shorter ballistic-diffusive transition length in case of C<sub>3</sub>NNT.

The study of phonon transport in C<sub>3</sub>NNT in comparison with CNT, provides insight into the scattering mechanisms, and energy dissipation in nanoscale materials. Specifically, the observation of significant reduction in thermal conductivity and increased phonon scattering rates, by introduction of N atoms in the CNT lattice, signifies the role of mass fluctuation and phonon-impurity scattering in crystalline or organic nanomaterials. As a result, this large effect on thermal transport, which is also reported in highly-doped semiconductors [172, 173, 174], must be considered in de-

vice design process to prevent the generation of local hot-spots and large temperature gradients.

### 3.6 Conclusion

Thermal properties of the C<sub>3</sub>NNT are studied using RNEMD simulations. Our results indicate that thermal conductivity of C<sub>3</sub>NNT increases with increase in the length and chirality of the nanotubes. Thermal conductivity of C<sub>3</sub>NNT is significantly lower than the CNT. This is due to the lower group velocities and relaxation times of C<sub>3</sub>NNT. The ballistic to diffusive transition length for armchair C<sub>3</sub>NNT is 71.66 nm, for zigzag C<sub>3</sub>NNT is 79.95 nm, for armchair CNT is 107.20 nm and for zigzag CNT is 103.32 nm. The lower transition length for C<sub>3</sub>NNT is attributed to the higher phonon scattering rate occurring in C<sub>3</sub>NNT due to the presence of nitrogen atoms. Our calculations indicate a lower MFP of C<sub>3</sub>NNT than CNT which is consistent with the higher scattering rate in C<sub>3</sub>NNT than CNT.

## CHAPTER 4: Fracture Mechanics of Multi-Layer Molybdenum Disulphide

### 4.1 Introduction

The discovery of the fantastic properties of graphene such as high mechanical strength [131, 132] and excellent electronic properties [18, 133] has stimulated interests in exfoliating other two-dimensional graphene-like materials. Laminated materials composed of stacked layers with van der Waals force between adjacent sheets and strong covalent bonds within each layer have received the most attention toward exfoliation of two-dimensional materials. In laminated materials the weak bonding between layers allows an easy isolation of free-standing single or few-atom-thick sheets. The isolated free-standing sheets form stable two-dimensional materials which exhibits exotic properties distinct from their corresponding three-dimensional bulk materials.

Transition metal dichalcogenides (TMDs) are an important class of laminated materials which are formed by triatomic sheets anchored together by van der Waals forces. Each sheet can be isolated to form a stable two-dimensional material composed of hexagonal layers of metal atoms (M) sandwiched between two layers of chalcogen atoms (X) with an  $\text{MX}_2$  stoichiometry. The typical metals in TMDs are Mo, W, Nb, Re, Ni or V and the typical chalcogens are S, Se or Te; thereby providing more than 40 different combinations for the two-dimensional TMDs [175, 176].

Two-dimensional molybdenum disulfide ( $\text{MoS}_2$ ) is one of the most attractive TMDs. Opposed to graphene which shows a zero band gap, few layer  $\text{MoS}_2$  displays a direct band gap [64]. The presence of a direct band gap along with high mechanical strength [177] and other unique physical, optical and electrical properties make two-dimensional  $\text{MoS}_2$  an ideal candidate for a variety of applications including microelectromechanical systems (MEMS) and nanoelectromechanical systems (NEMS) devices

[64, 65, 66, 67, 68].

Understanding the mechanical and fracture properties of MoS<sub>2</sub> is essential in predicting its behavior upon incorporation into electromechanical devices. Ideally, the mechanical and fracture properties of two-dimensional materials should be characterized experimentally e.g. using uniaxial tensile test. Although recently some progress has been made in conducting experiments at nanoscales [178, 177, 179, 180, 181], however, still designing and performing experiments at nanoscales is very complicated. Currently, the most common techniques for measuring the mechanical properties of two-dimensional materials are atomic force microscopy and nanoindentation [182, 183, 184, 185]. However, factors such as indenter radius, indenter location and nonuniform stress and strain in the tested two-dimensional specimen make it challenging to extract the intrinsic mechanical properties using these experiments.

Computational studies, on the other hand, can provide valuable insights about the behavior of two-dimensional materials [144, 147, 186, 148, 151, 119, 146, 12, 114, 187, 1]. Cooper et al. [188] used density functional theory (DFT) to study the nonlinear response of MoS<sub>2</sub>. Wang et al. [117] used molecular dynamics modeling to study fracture properties of single layer MoS<sub>2</sub> under mixed mode loading. Bao et al. [189] studied the effects of crack configuration, length and angle on the fracture stress of MoS<sub>2</sub>. Wang et. al [179] used aberration-corrected transmission electron microscope and molecular dynamic simulations to study structure and dynamics of cracks in monolayer MoS<sub>2</sub>.

The studies on mechanical and fracture properties of MoS<sub>2</sub> have been mostly limited to monolayer molybdenum disulfide. In this chapter, we use molecular dynamics simulations to study the fracture properties of multilayer MoS<sub>2</sub>. Since the applicability of continuum concepts of fracture mechanics in systems of reduced dimensionality is an open debate, we use atomistic simulations to investigate whether Griffith and Inglis theory of brittle fracture [190] is applicable to multilayer MoS<sub>2</sub> sheets. Quan-

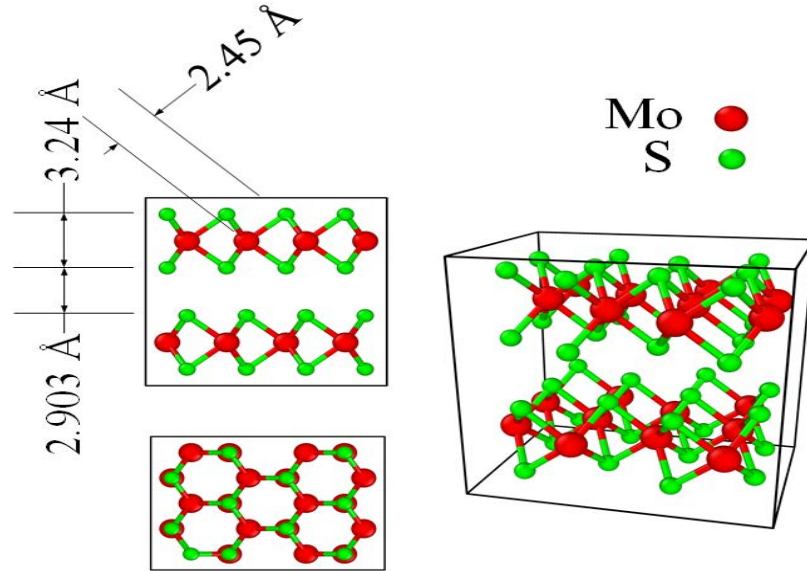


Figure 4.1: Bi-layer  $\text{MoS}_2$  crystal in different views

tized fracture mechanics theory which is developed more recently to overcome the issues associated with using continuum-based fracture theories at nanoscale is also investigate. The impacts of number of layers, crack configuration and crack orientation on the fracture stress and stiffness of few-layer  $\text{MoS}_2$  sheets are also studied.

## 4.2 Structure of $\text{MoS}_2$

Molybdenum disulfide can exist in two phases; the stable H phase (H- $\text{MoS}_2$ ) with semiconducting properties or metallic T-phase (T- $\text{MoS}_2$ ) which is not stable at ambient conditions [191]. In this chapter we study the fracture properties of H- $\text{MoS}_2$ . The atomic structure of H- $\text{MoS}_2$  is shown in Fig. 4.1. Each layer of  $\text{MoS}_2$  consists of a sublayer of molybdenum (Mo) atoms sandwiched between two sublayers of sulfur (S) atoms. Each Mo atom is covalently bonded to six S atoms (three bonds with the three S atoms on the top and three bonds with the three S atoms on the bottom layer). Each sulfur atom is covalently bonded to three Mo atoms. The stacking of sublayers of each layer of H- $\text{MoS}_2$  is ABA.

In multilayer  $\text{MoS}_2$ , the adjacent layers are bonded together by weak van der Waals

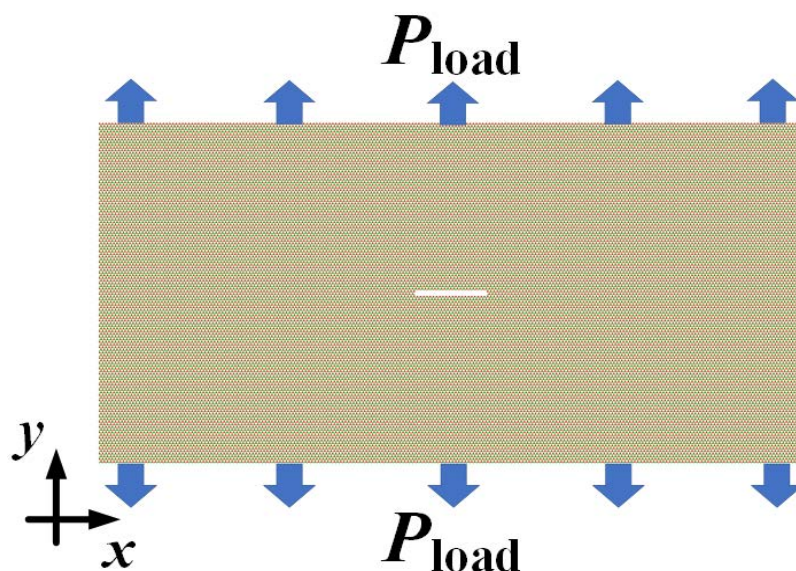


Figure 4.2: MoS<sub>2</sub> sheet considered to run the simulations .

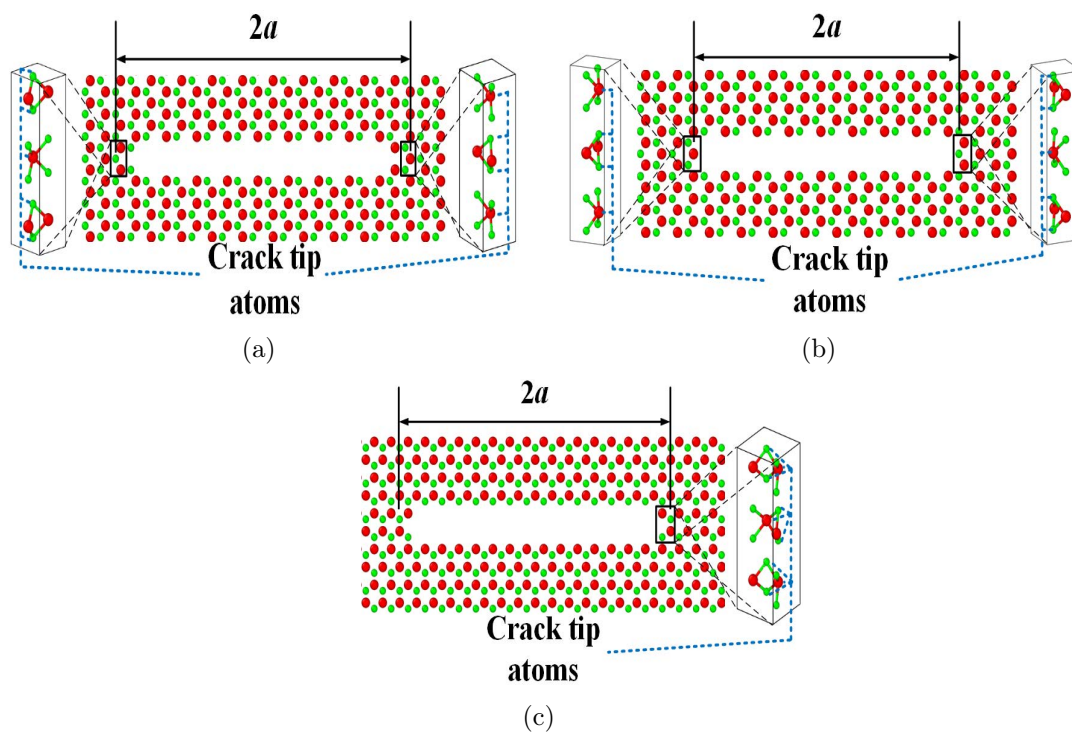


Figure 4.3: MoS<sub>2</sub> sheet crack tips (a) Armchair crack with sharp tip (ACSC), showing crack length and three-layer crack tip, (b) Armchair crack with blunt tip (ACBC), showing crack length and three-layer crack tip, and (c) Zigzag crack (ZZC), showing crack length and three-layer crack tip.

forces. When the number of layers are more than one, the S atoms of one layer are directly above the Mo atoms of the other layer and vice versa. The interlayer distance and bond lengths used to create the initial atomic structure of MoS<sub>2</sub> for our molecular dynamics simulations are shown in Fig. 4.1.

### 4.3 Computational method

The fracture properties of multilayer MoS<sub>2</sub> sheets are studied using rectangular MoS<sub>2</sub> samples which include crack at their centers as shown in Fig. 4.2. To remove the surface effects, the domain length parallel to crack is at least 10 times larger than the crack length. The width of the domain is 350 Å. MoS<sub>2</sub> sheets with one, two and three layers are considered.

Cracks with different sizes and configurations are created by removing layers of Mo and S atoms. The effect of crack configuration on fracture properties are studied by considering samples with cracks in the armchair direction (AC cracks) and zigzag direction (ZZ cracks) as shown in Fig. 4.3. The effect of crack tip configuration are investigated by studying cracks in the armchair direction with sharp (ACSC) and blunt tips (ACBC) as shown respectively in Fig. 4.3a and b. Each of the cracks with armchair edges contain two crack tips with dissimilar atomic configurations. For example as shown in Fig. 4.3a and b, in monolayer MoS<sub>2</sub>, one crack tip contains a Mo atom while the other tip is composed of two sulfur atoms. In multilayer MoS<sub>2</sub>, the two tips are composed of both Mo and S atoms but as shown in Fig. 4.3a and b, Mo and S atoms of the two tips do not appear in the same layer.

On the other hand, although the tip structure of the cracks with zigzag edges is same, opposed to the cracks in the armchair direction, the atomic structures of the two edges of the ZZ cracks are different from each other. In monolayer MoS<sub>2</sub>, one edge has Mo atoms at its outermost layer while the other edge has S atoms at its outermost layer. Such a difference in the atomic structures of the edges exists in multilayer MoS<sub>2</sub> as well where the order in which Mo and S atoms appear at the

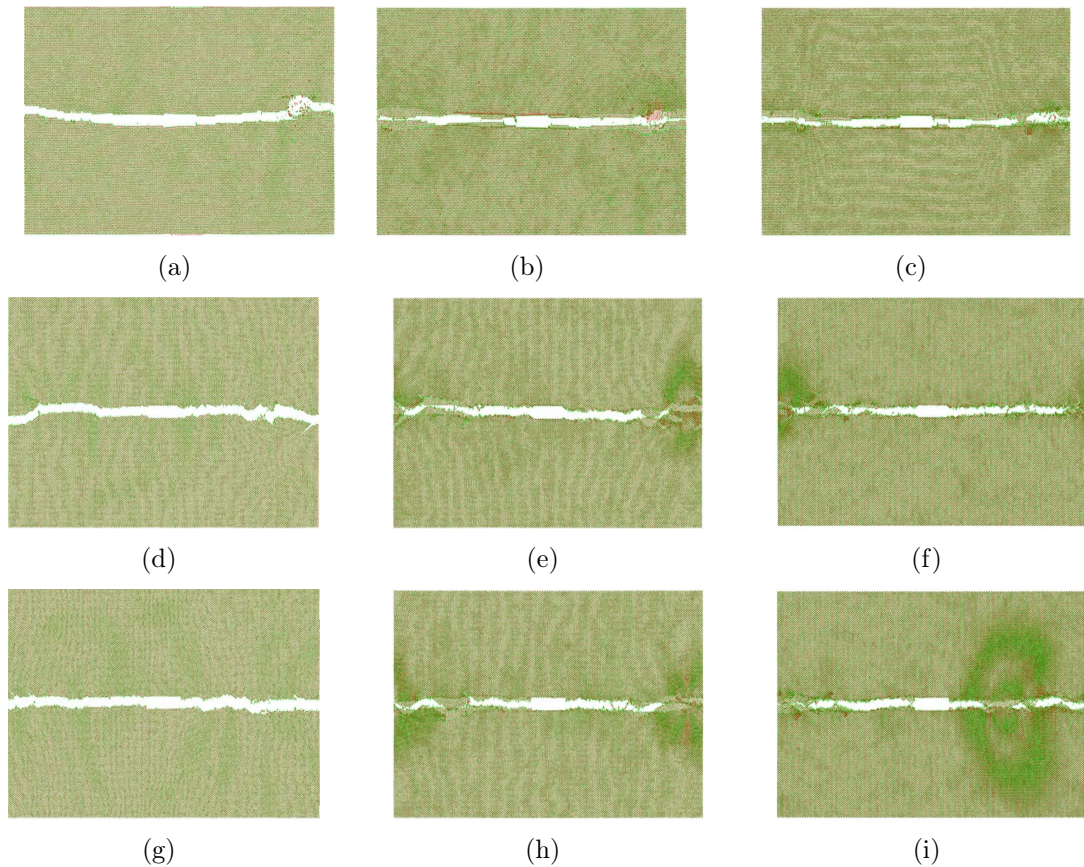


Figure 4.4: Crack propagation direction in multilayer  $\text{MoS}_2$  under Mode-I loading at 300 K. (a) One layer with ZZC, (b) two layers with ZZC, (c) three layers with ZZC, (d) one layer with ACSC, (e) two layers with ACSC, (f) three layers with ACSC, (g) one layer with ACBC, (h) two layers with ACBC, and (i) three layers with ACBC.

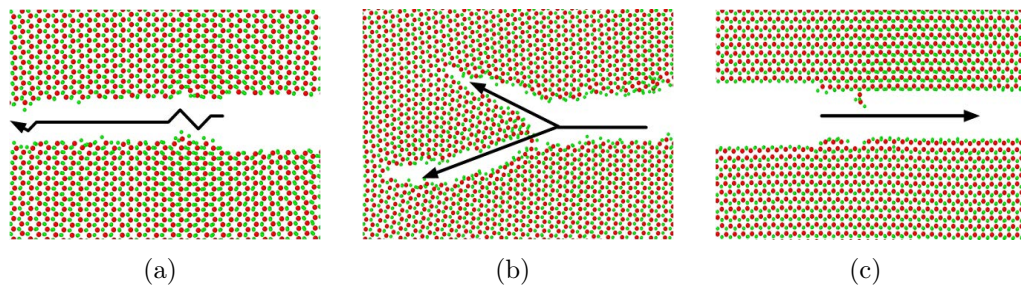


Figure 4.5: Crack propagation path in  $\text{MoS}_2$  under mode-I loading at 300 K (a) Armchair crack propagates along a straight path, (b) branching in the armchair crack, and (c) zigzag crack propagates in straight path.

outermost layer is different between the two crack edges.

The molecular dynamics simulations are conducted using LAMMPS molecular dynamics package [91]. Interatomic interactions between atoms are considered using modified reactive empirical bond order (REBO) potential [96, 179]. We use a maximum cut off distance of 2.85 Å for Mo–S interactions and 2.8 Å for S–S interactions. The equations of motion are integrated using the velocity Verlet scheme with a time increment of 1 fs. Loading is applied perpendicular to the crack by applying tensile strain in the  $y$ -direction of the MoS<sub>2</sub> sheet. The strain is applied to the domain in increments of 0.4 % or less. After every increment the energy of the system is minimized. After minimization the temperature of the system is increase to 300K using an NVE ensemble employing a Berendesn thermostat followed by equilibration within an NPT ensemble for a total of 15 ps. Therefore, the strain is applied at maximum rate of  $2.67 \times 10^8 \text{ s}^{-1}$ . The two edges parallel to the loading direction are free to relax while the top and bottom edges are clamped. After the equilibration of the system, the stress corresponding to the applied strain is calculated using the virial definition of stress [101, 102, 103] . All the images are generated using Ovito visualization software [192].

## 4.4 Results

### 4.4.1 Crack propagation

The propagation paths of armchair and zigzag cracks in MoS<sub>2</sub> sheets are shown in Fig. 4.4. Both armchair and zigzag cracks propagate perpendicular to the applied load. By increasing the number of layers, branching occurs along the propagation path of armchair cracks and some of the branchings are not through the thickness cracks. Although at a macro level both armchair and zigzag cracks grow in a straight path perpendicular to the load, however at a micro level the propagation path of armchair and zigzag cracks are different. As shown in Fig. 4.5, at the micro level both armchair and zigzag cracks tend to propagate along a zigzag direction. Since

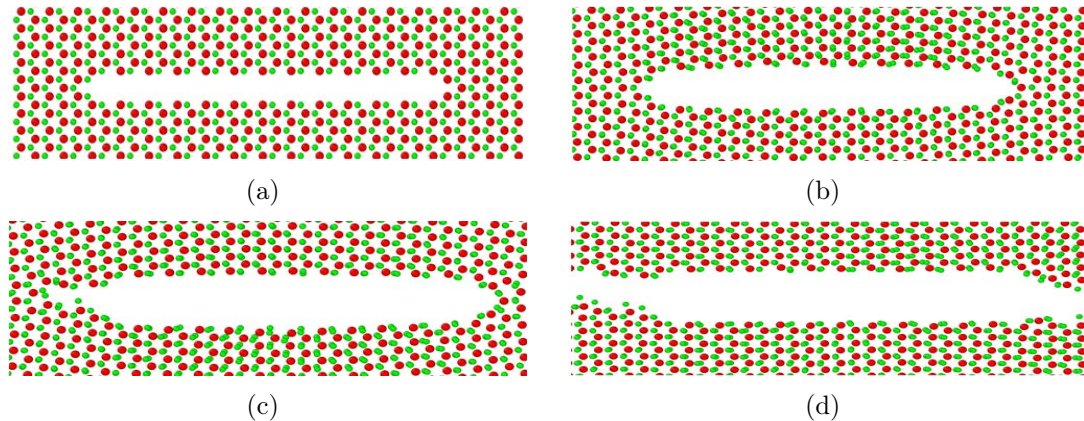


Figure 4.6: Crack propagation in MoS<sub>2</sub> sheet with ACSC of length 7.51 nm at 300 K. (a) Unstrained sheet, (b) 2.8 % strain, (c) Crack starts propagating at crack tip with S atoms at 4.0 % strain, and (d) Nanoribbon separates into two halves at 4.2 % strain.

microscopically cracks tend to propagate in the zigzag direction, the propagation path of ZZ cracks is smooth and ZZ cracks propagate in a self-similar path. On the other hand, the fracture path of armchair cracks is rough since AC cracks propagate by kinking to alternate zigzag directions to form macroscopically straight paths. This observations are consistent with previous molecular dynamics [117] and experimental studies [179].

The configuration of the cracks in a monolayer MoS<sub>2</sub> sheet at different tensile strains are shown in Figures 4.6–4.8. Since the atomic structures of the tips of cracks with armchair edges are different from each other, cracks growth does not occur simultaneously at both tips. Our simulations results predict that AC cracks with sharp tips (ACSC) tends to grow at the tip which is composed of two sulfur atoms and crack propagation at the other tip occurs with delay as shown in Fig. 4.6(c). On the other hand, as shown in Fig. 4.7(c), AC cracks with blunt tips (ACBC) start growing at the tip which is composed of a Mo atom. Due to the symmetry of the tips of ZZ cracks, propagation of such cracks occurs simultaneously at both tips as shown in Fig. 4.8.

The surface energy (for 3D materials) and edge energy (2D materials)  $\gamma$  is an im-

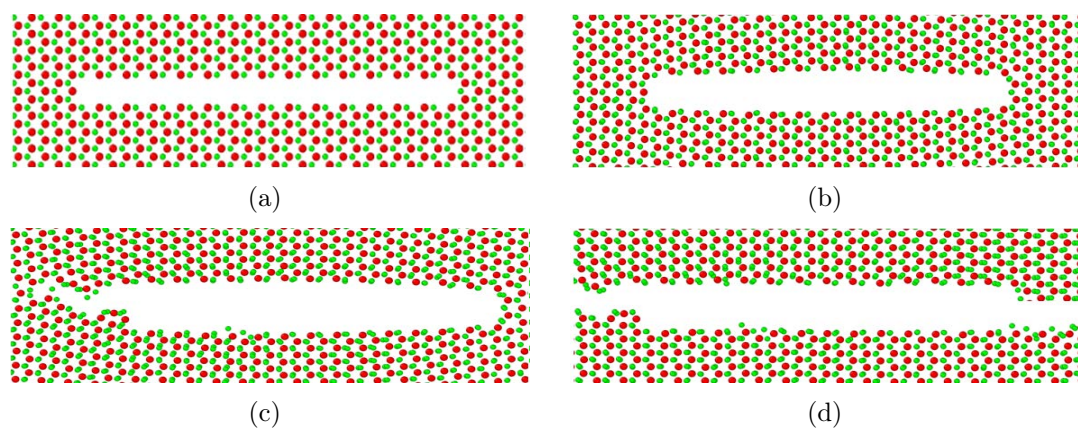


Figure 4.7: Crack propagation in MoS<sub>2</sub> sheet with ACBC of length 7.87 nm at 300 K . (a) Unstrained sheet, (b) 2.8 % strain, (c) Crack starts propagating at crack tip with S–Mo–S atoms at 4.0 % strain, and (d) Nanoribbon separates into two halves at 4.2 % strain.

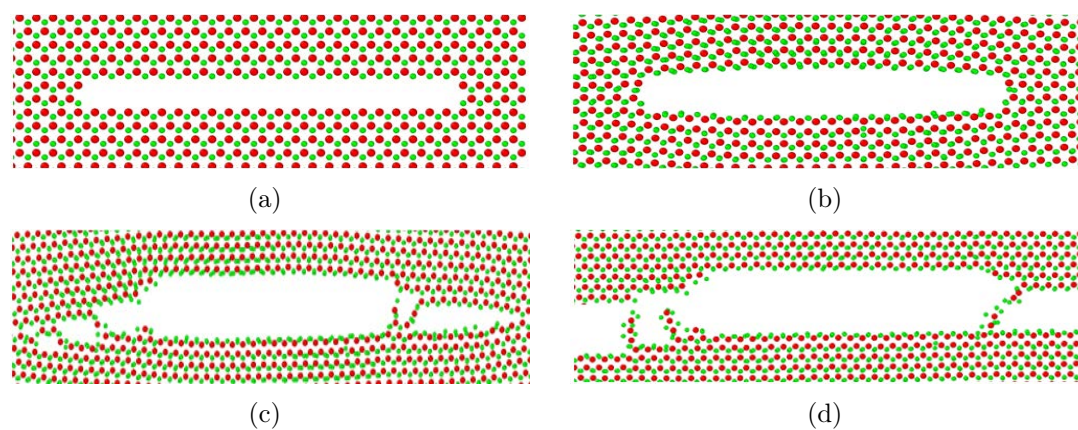


Figure 4.8: Crack propagation in MoS<sub>2</sub> sheet with ZZC of length 7.61 nm at 300 K . (a) Unstrained sheet, (b) 2.8 % strain, (c) Crack propagates at both crack tips at 4.1 % strain, and (d) Nanoribbon separates into two halves at 4.2 % strain.

portant parameter in the growth of cracks. It is defined as the energy requires to create one unit of new surface/edge and quantifies the amount of energy required to break the atomic bonds. The surface/edge energy density is a function of the difference between energy of the system before and after the creation of new surfaces/edges and can be obtained from

$$\gamma = \frac{U - U_0}{A} \quad (4.1)$$

where  $U$  is the energy of the system after the creation of new surfaces,  $U_0$  is the energy of the system without surfaces and  $A$  is the area of new surfaces.

To calculate the edge energies of monolayer MoS<sub>2</sub>, a model is created which is periodic in all the directions. The system is equilibrated to obtain the relaxed energy  $U_0$  of the system. Two new surfaces are created by splitting the system into two halves while still the periodic boundary conditions are applied in all the directions. The relaxed energy of the system  $U$  is obtained by minimizing the energy of the domain. The surface energy density can be obtained from Eq. (4.1) with  $A = 2lt$ , where  $l$  is the length of the edges and  $t$  is the thickness of monolayer MoS<sub>2</sub> and is equal to 6.143 Å. The factor of two is required because two new edges are created. The edge energies of monolayer MoS<sub>2</sub> for edges with zigzag chirality is  $\gamma_{ZZ} = 1.426 \text{ J/m}^2$  and armchair chirality is  $\gamma_{AC} = 1.464 \text{ J/m}^2$ , respectively. These are in agreement with the theoretical estimated values obtained using Morse-type bonding model [193]. The lower energy of zigzag edges makes zigzag direction a more favorable propagation path hence in the microscale both zigzag and armchair cracks intend to propagate in zigzag directions.

#### 4.4.2 Stress-strain relation and distribution

In characterizing the fracture properties of nanomaterials, the stress distribution of individual atoms in the vicinity of crack tip can be informative. To compute the stress tensor of each atom, the virial definition [101, 102, 103] is used, given by Eq. (1.17).

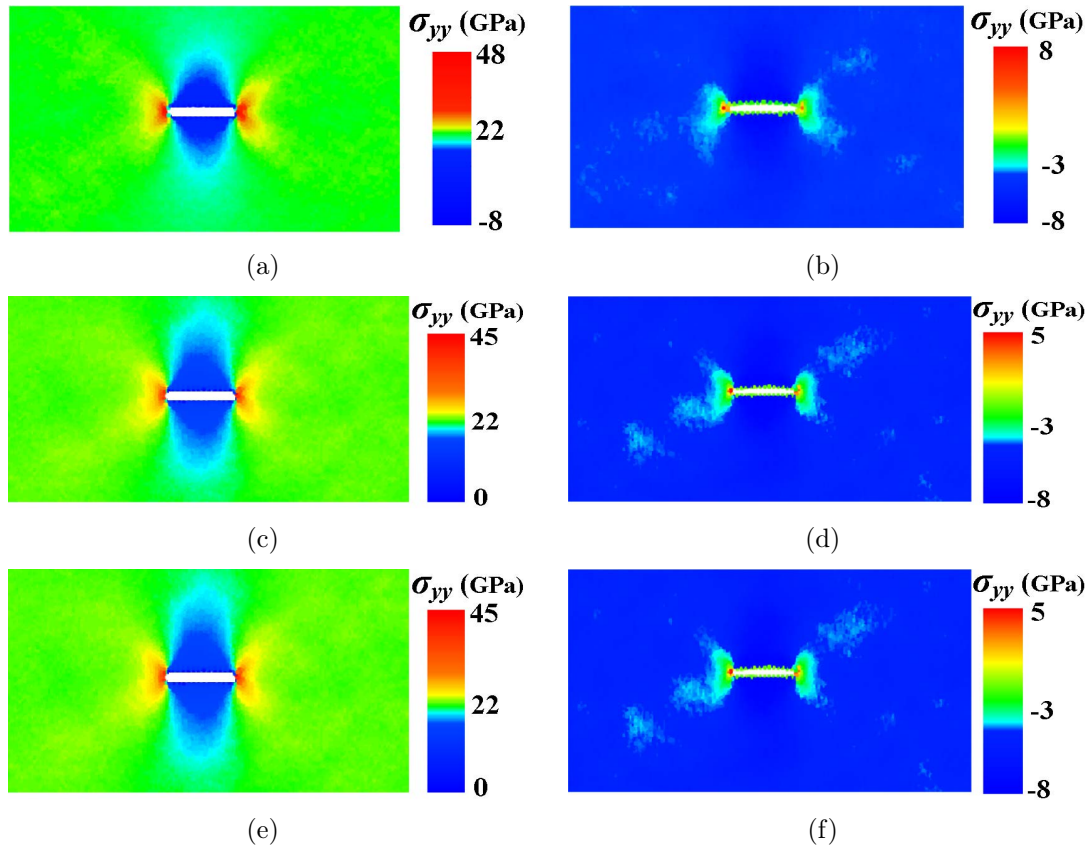


Figure 4.9: Stress ( $\sigma_{yy}$ ) distribution in cracked MoS<sub>2</sub> sheet at 300 K. (a) Mo layer of sheet with ACSC, (b) S layers of sheet with ACSC, (c) Mo layer of sheet with ACBC, (d) S layers of sheet with ACBC, (e) Mo layer of sheet with ZZC, and (f) S layers of sheet with ZZC.

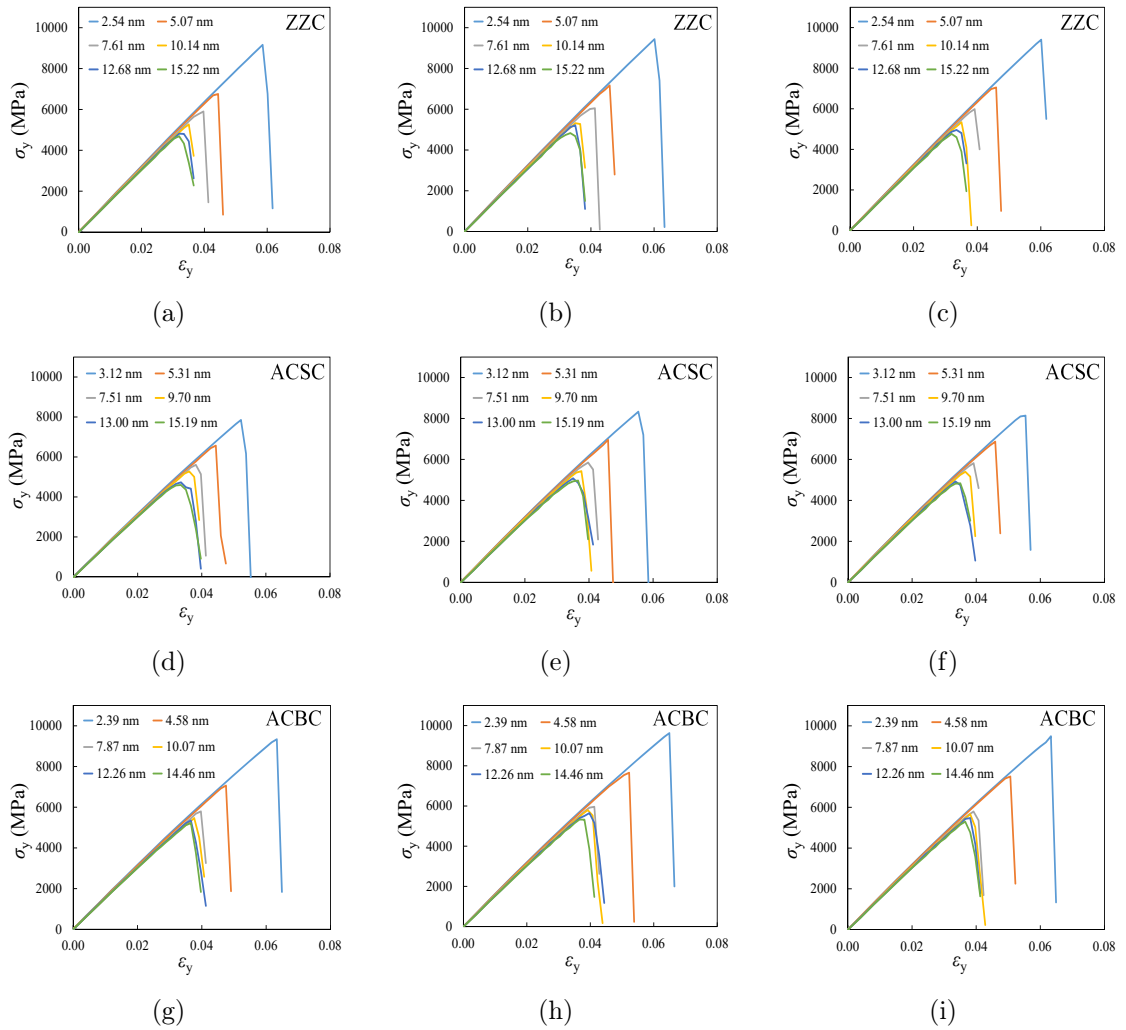


Figure 4.10: Stress–strain relation of MoS<sub>2</sub> ribbons consisting of different crack lengths at 300 K. (a) 1 layer, ZZC, (b) 2 layers, ZZC, (c) 3 layers, ZZC, (d) 1 layer, ACSC, (e) 2 layers, ACSC, (f) 3 layers, ACSC, (g) 1 layer, ACBC, (h) 2 layers, ACBC, and (i) 3 layers, ACBC.

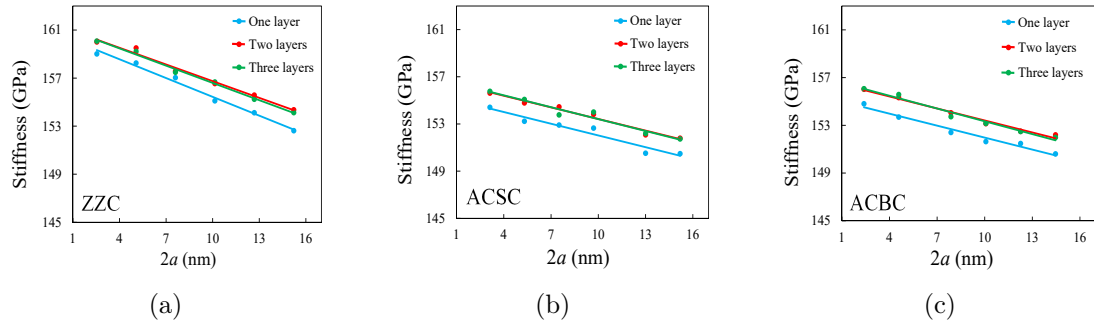


Figure 4.11: Stiffness of MoS<sub>2</sub> ribbons consisting of different crack lengths at 300 K. (a) ZZC, (b) ACSC, and (c) ACBC.

The atomic stress data is collected at the end of each NPT equilibration. To obtain a smooth atomic stress distribution across the sheet the stress data is time averaged over 2500 steps.

The normal stress distribution in the  $y$ -direction  $\sigma_{yy}$  in the molybdenum and sulfur layers of a monolayer MoS<sub>2</sub> sheet containing crack of about 75 Å under a tensile strain of 2.8 % are plotted in Fig. 4.9. A significant stress concentration close to the crack tip is observed. These figures show that the stress in the molybdenum layer is significantly higher than that in the sulfur layer. In addition, the stress concentration at the tip of AC crack with blunt tips (ACBC) is lower than other cracks.

The stress-strain curves of MoS<sub>2</sub> sheets containing crack with armchair and zigzag edges are plotted in Fig. 4.10. The crack sizes considered vary between 2.39 nm and 15.22 nm. Stress increases linearly with strain until reaching a critical stress after which the stress drops suddenly indicating a brittle crack growth in MoS<sub>2</sub>. The maximum stress is considered as the fracture strength of the material. The stiffness and strength of the MoS<sub>2</sub> sheets with different number of layers are plotted in Fig. 4.11 and 4.12, respectively. As shown in this figures, by increasing the crack length both strength and stiffness of the sheets reduces. The number of layers, on the other hand, does not have a significant impact on the stiffness, strength or fracture strain of MoS<sub>2</sub> sheets.

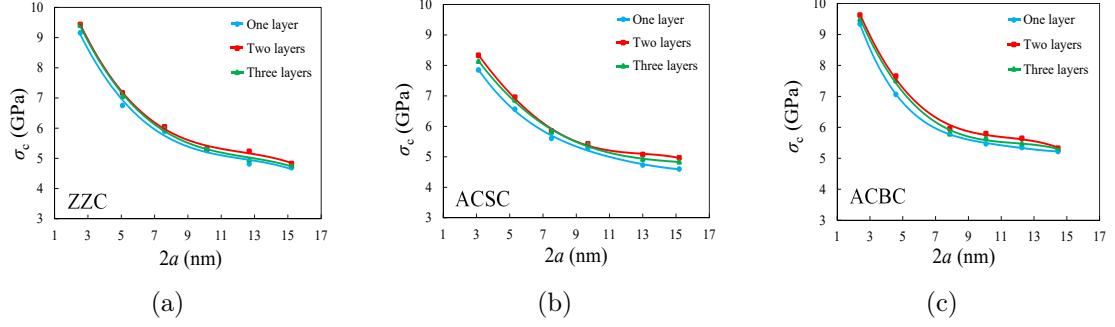


Figure 4.12: Fracture strength of MoS<sub>2</sub> ribbons consisting of different crack lengths at 300 K. (a) ZZC, (b) ACSC, and (c) ACBC.

Table 4.1: Fracture toughness ( $K_{IC}$ ) of MoS<sub>2</sub> with various cracks

No. of layers	Orientation	$K_{IC}$ (MPa $\sqrt{m}$ )
One	ZZC	$0.6531 \pm 0.050$
Two	ZZC	$0.6794 \pm 0.054$
Three	ZZC	$0.6683 \pm 0.048$
One	ACSC	$0.6410 \pm 0.060$
Two	ACSC	$0.6782 \pm 0.069$
Three	ACSC	$0.6661 \pm 0.064$
One	ACBC	$0.6803 \pm 0.083$
Two	ACBC	$0.7116 \pm 0.083$
Three	ACBC	$0.6972 \pm 0.082$

Fracture toughness describes the ability of materials to resist fracture and provides an indication of the strength of the material. For brittle materials, fracture toughness is characterized by the critical stress intensity factor for fracture  $K_c = \sigma_c \sqrt{a\pi} F(\phi)$ . Using the values of critical stress ( $\sigma_c$ ) given in Fig. 4.12, the fracture toughness of MoS<sub>2</sub> sheets are calculated and presented in Table 4.1. These results are in agreement with theoretical estimated value of 0.605 MPa $\sqrt{m}$  using Morse-type bonding model [193]. Results show that bi-layer and tri-layer MoS<sub>2</sub> sheets have a higher fracture toughness than monolayer MoS<sub>2</sub>. Moreover, the MoS<sub>2</sub> sheets which include a crack with ACSC have a lower fracture toughness than other cracks.

The impact of temperature on fracture strength of MoS<sub>2</sub> sheets is studied. The fracture strength of MoS<sub>2</sub> in a temperature range of 100–500 is plotted in Fig. 4.13.

Increasing the temperature in this range leads to a reduction in the fracture strength of monolayer MoS<sub>2</sub> sheets by about 34%.

Importantly, the stress–strain curves are used to address whether the Griffith theory of fracture is valid for MoS<sub>2</sub> sheets. According to the Griffith theory, brittle fracture occurs when the reduction in the potential energy of the system exceeds the energy required to create new crack surfaces. The Griffith theory is one of the pillars of continuum fracture mechanics, but its validity for predicting fracture of nanoscale systems composed of a few number of atoms should be verified.

Using Griffith theory, the critical stress  $\sigma_c$  at the onset of fast fracture for a strip with a central crack of length  $2a$  under a tensile uniaxial loading perpendicular to the crack is given by

$$\sigma_c = \frac{1}{F(\phi)} \sqrt{\frac{2E\gamma}{\pi a}} \quad (4.2)$$

where  $E$  is the Young's modulus,  $\gamma$  is the edge/surface energy of the newly created edges/surface in 2D/3D materials, and  $F(\phi)$  is a geometrical factor given by

$$F(\phi) = (1 - 0.025\phi^2 + 0.06\phi^4) \sqrt{\sec\left(\frac{\pi\phi}{2}\right)}, \quad \phi = \frac{2a}{W} \quad (4.3)$$

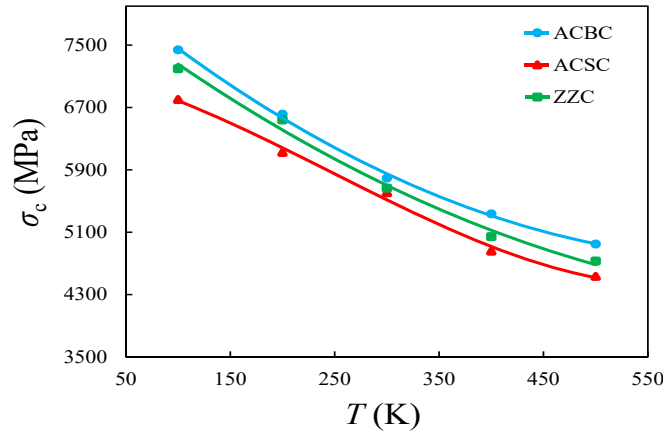


Figure 4.13: Dependence of strength of monolayer MoS<sub>2</sub> on temperature with ZZC, length is 7.61 nm and ACSC, length is 7.51 nm and ACBC, length is 7.87 nm.

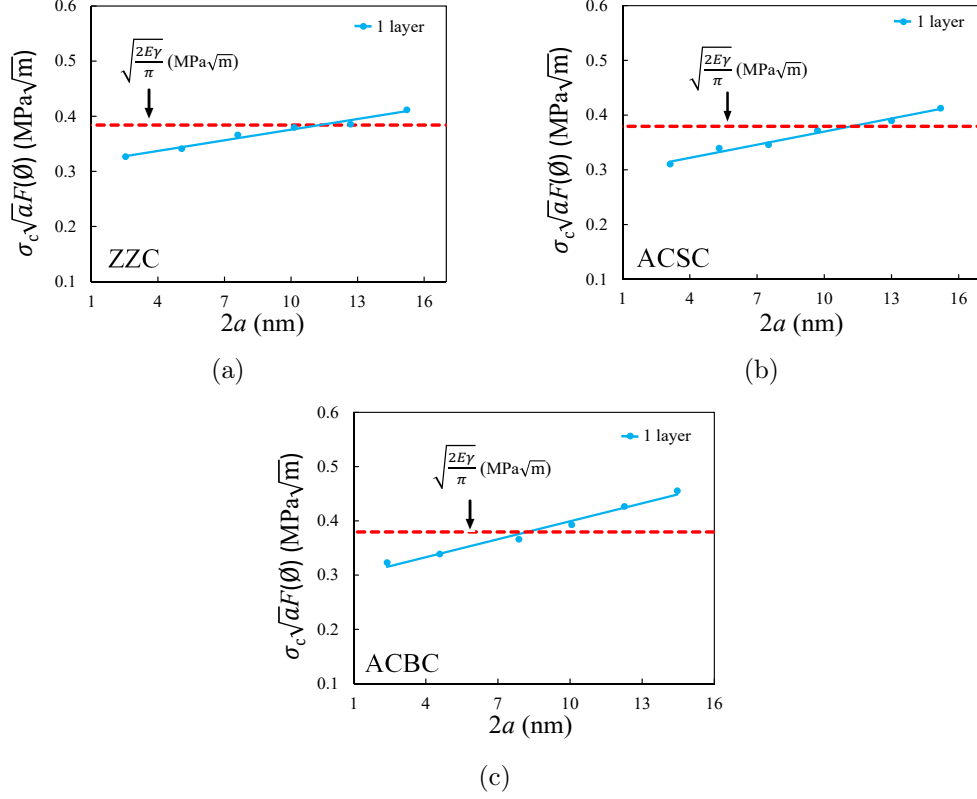


Figure 4.14: Griffith theory of MoS<sub>2</sub> ribbons consisting of different crack lengths at 300 K. (a) ZZC, (b) ACSC, and (c) ACBC.

where  $W$  is the width of the strip.

Griffith derived Eq. (4.2) by assuming that the central crack propagates along a self similar path. Therefore, according to the original Griffith theory,  $\gamma$  is the edge energy along the initial orientation of the crack. This means that according to the Griffith theory, for cracks in the armchair direction  $\gamma = \gamma_{AC}$  and for cracks in the zigzag direction  $\gamma = \gamma_{ZZ}$ . However, as shown in Fig. 4.5, both AC and ZZ cracks propagate along a zigzag direction. Therefore, the edge energy along the zigzag direction  $\gamma_{ZZ} = 1.426 \text{ J/m}^2$  is used as the value of edge energy of the newly created edges,  $\gamma$ , for both AC and ZZ cracks. By conducting molecular dynamics modelings of uniaxial tensile loading, the Young's modulus of pristine MoS<sub>2</sub> sheets in armchair and zigzag directions is approximately 159 GPa and 162 GPa.

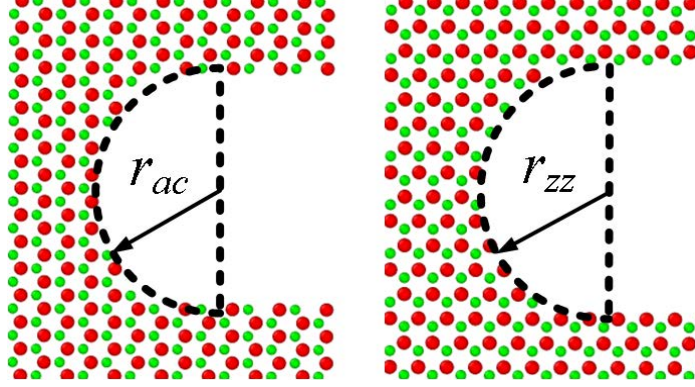


Figure 4.15: Crack tips with different radius considered to understand the effect of crack bluntness on fracture toughness. Zigzag crack tip radius ( $r_{zz}$ ) varied from 0.375 nm to 2.02 nm where as armchair crack tip radius ( $r_{ac}$ ) varied from 0.317 nm to 2.06 nm.

By rearranging the terms in Eq. (4.2), the Griffith criterion can be written as

$$\sigma_c \sqrt{a} F(\phi) = \sqrt{\frac{2E\gamma}{\pi}}. \quad (4.4)$$

Since the right hand side of the above equation depends only on the material properties, it is a constant which does not depend on the dimensions of the system and the crack size. Therefore, to validate the Griffith theory, two conditions should be satisfied. The first condition is to confirm that the product of the fracture stress  $\sigma_c$ , geometric factor  $F(\phi)$  and the square root of half the crack length  $a$  is a constant independent of the crack length,  $\sigma_c \sqrt{a} F(\phi) = const.$  The second condition is to confirm that the constant is indeed  $\sqrt{\frac{2E\gamma}{\pi}}$ .

To verify these conditions, the values of  $\sigma_c \sqrt{a} F(\phi)$  for monolayer MoS<sub>2</sub> strips including cracks in the armchair and zigzag directions are plotted in Fig. 4.14 and compared with  $\sqrt{\frac{2E\gamma}{\pi}}$ . As shown in Fig. 4.14, for the crack sizes considered,  $\sigma_c \sqrt{a} F(\phi)$  is linearly increasing while the values of  $\sqrt{\frac{2E\gamma}{\pi}}$  remain constant. The two values do not match with each other indicating that Griffith theory is not valid for cracks at nanoscale.

Using molecular dynamics simulation, the effect of crack tip blunting on the tough-

ness of monolayer MoS<sub>2</sub> sheets is studied. As shown in Fig. 4.15, blunt crack tips are created by removing a few atomic layers at the crack tip to obtain a notch with radius  $r$  at each tip. According to the Inglis theory, for a system with a center crack of length  $2a$  under mode-I loading, the local stress ( $\sigma_1$ ) at the crack tip is given by

$$\sigma_1 = \left(1 + 2\sqrt{\frac{a}{r}}\right) \sigma_y \quad (4.5)$$

where  $r$  is the radius of the crack tip and  $\sigma_y$  is the remotely applied tensile stress. This equation shows that by increasing the crack tip radius  $r$ , the local stress at the crack tip reduces. At the critical stress level  $\sigma_y = \sigma_c$  and the local stress  $\sigma_l$  required to break the atomic bond is equal to the bond strength  $\sigma_b$ . Therefore, at the fracture stress, Eq. (4.5) can be written as

$$\sigma_b = \left(1 + 2\sqrt{\frac{a}{r}}\right) \sigma_c \quad (4.6)$$

Since the bond strength  $\sigma_b$  is constant, the right hand side of Eq. (4.6) should be constant regardless of the crack size or tip radius.

To verify the Inglis theory at the nanoscale, the values of  $\left(1 + 2\sqrt{\frac{a}{r}}\right) \sigma_c$  for AC and ZZ cracks of lengths 7.87 nm and 7.61 nm as a function of their tip radius are plotted in Fig. 4.16. It can be observed that when the crack tip radius is larger than 1.15 nm, the values of  $\left(1 + 2\sqrt{\frac{a}{r}}\right) \sigma_c$  remain fairly constant which indicates that Inglis theory is valid for cracks with tip radius larger than 1.15 nm. On the other hand, when crack tip radius is smaller than 1.15 nm, the values of  $\left(1 + 2\sqrt{\frac{a}{r}}\right) \sigma_c$  increases quickly and deviate from the bond strength at the crack tip. Hence, the Inglis theory is not valid for cracks with sharp tips.

Quantized fracture mechanics is an energy-based fracture theory which was developed to resolve the issues of continuum-based fracture mechanics at the nanoscale [194]. According to quantized fracture mechanics, the fracture strength of MoS<sub>2</sub> sheets

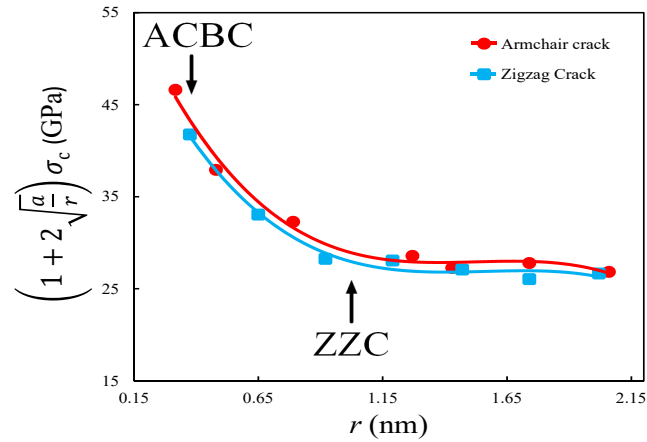


Figure 4.16: Dependence of local stress with change in crack tip at 300 K.

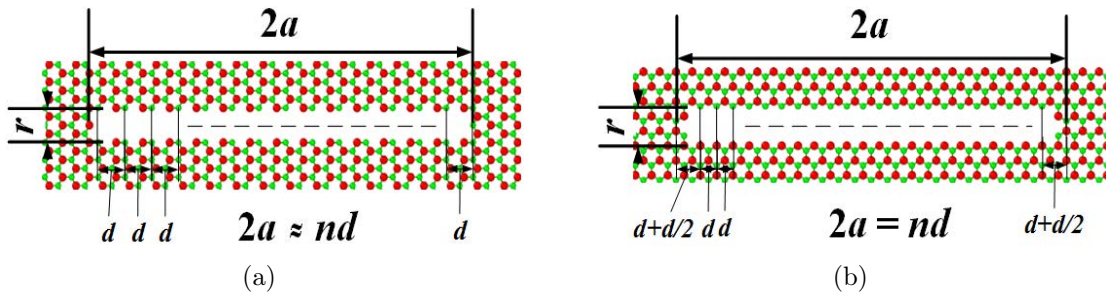


Figure 4.17: Cracks with radius less than 0.7 nm. (a) Armchair crack, and (b) Zigzag crack

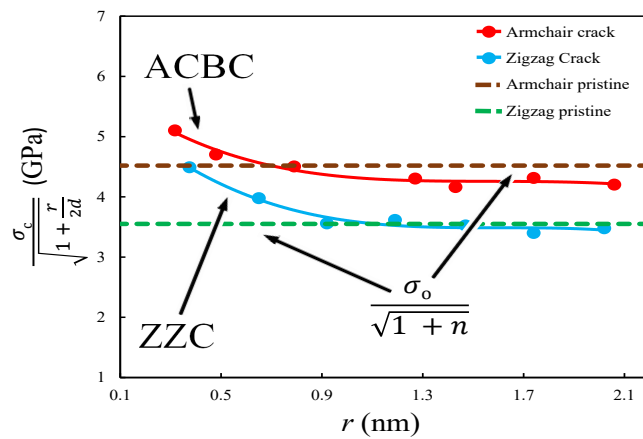


Figure 4.18: The values of  $\frac{\sigma_c}{\sqrt{1+\frac{r}{2d}}}$  plotted for cracks with different tip radii at 300 K.

can be obtained from

$$\sigma_c \approx \sigma_0 \sqrt{\frac{1 + \frac{r}{2d}}{1 + n}} \quad (4.7)$$

where  $\sigma_0$  is the strength of pristine MoS<sub>2</sub> sheets,  $r$  is the crack tip radius,  $d$  is fracture quantum parameter which is equal to lattice spacing and  $n$  is the number of vacancy defects along the length of the crack. The parameters  $d$  and  $n$  for AC and ZZ cracks are shown in Fig. 4.17.

By rewriting Eq. (4.7) as

$$\frac{\sigma_c}{\sqrt{1 + \frac{r}{2d}}} \approx \frac{\sigma_0}{\sqrt{1 + n}} \quad (4.8)$$

one can conclude that regardless of the crack tip radius, the value of  $\frac{\sigma_c}{\sqrt{1 + \frac{r}{2d}}}$  should remain constant for all the cracks with  $n$  vacancy defects. To verify if quantized fracture mechanics can predict the fracture strength of MoS<sub>2</sub>, we plot  $\frac{\sigma_c}{\sqrt{1 + \frac{r}{2d}}}$  for AC and ZZ cracks shown in Fig. 4.18. The values of  $n$  for these cracks are 14 and 24 for AC and ZZ cracks, respectively. Based on our MD simulations, the values of  $\sigma_0$  for AC and ZZ cracks are 17.68 GPa and 17.75 GPa respectively. As shown in Fig. 4.18, the values of  $\frac{\sigma_c}{\sqrt{1 + \frac{r}{2d}}}$  for AC and ZZ cracks are in close agreement with  $\frac{\sigma_0}{\sqrt{1 + n}}$  when crack tip radius is larger than 0.9 nm. For sharper cracks, the values of  $\frac{\sigma_c}{\sqrt{1 + \frac{r}{2d}}}$  increases and deviate from  $\frac{\sigma_0}{\sqrt{1 + n}}$ . However, this deviation is considerably smaller than what was observed for the Inglis theory. Therefore, in comparison with the Inglis theory, quantized fracture mechanics is in a better agreement with molecular dynamics simulations and can provide better prediction when the crack tip is sharp.

## 4.5 Conclusion

In this work the fracture properties of pre-cracked multi-layered MoS<sub>2</sub> subjected to mode-I loading is studied. Molecular dynamics results revealed that crack propagation path highly depends on the crack orientation. While zigzag crack propagate in a self-similar path, the armchair crack propagates by jumping between different zigzag directions. It is shown that Griffith theory is not applicable to determine the fracture strength of nanoscale MoS<sub>2</sub> sheets containing a center crack. Inglis theory can provide

reasonable predictions for all the cracks except for the sharpest AC and ZZ cracks. On the other hand, quantized fracture mechanics theory can provide a more accurate prediction than Inglis theory for the fracture strength of MoS<sub>2</sub> sheets with center cracks.

## CHAPTER 5: An Atomistic Study of the Stress Corrosion Cracking in Graphene

### 5.1 Introduction

In numerous cases environment interferes with the mechanical loadings in the initiation and propagation of damages. Environment assisted cracking (EAC) is a common damage problem in a variety of engineering materials such as metals, polymers, glasses and ceramics [195, 196, 197]; leading to the failure of materials well below their maximum strength. Although computational and experimental approach have been performed in the past to elucidate the environment assisted cracking process in three-dimensional materials [198, 199, 200, 201, 202, 196], the studies on the mechanism of environmental assisted cracking of two-dimensional materials are scarce. Since atomic structure of two-dimensional material are different than their three-dimensional counterpart, their physical and chemical properties are also significantly distinct from their three-dimensional counterparts. This necessitate a separate study of the environment assisted cracking process of two-dimensional materials.

Graphene is the first exfoliated two-dimensional material with a wide spectrum of potential applications. The mechanism of fracture in graphene under mechanical loading is studied in the past [203, 204, 205, 206], however the mechanism of environment assisted cracking of graphene occurring as an interplay between mechanical loading and chemical reactions is not yet completely understood. Although pristine graphene is inert and does not react easily with environment molecules, experiments conducted on chemical vapor deposited (CVD) graphene show that when polycrystalline graphene is exposed to ambient molecules its fracture strength and toughness significantly reduce [207] providing strong indication that environment assisted cracking occurs in graphene. In CVD-grown graphene sheet the dangling bonds formed by

the formation of point and line flaws allow the reaction between ambient molecules and carbon bonds. The charge transfer occurring by these adsorbates induces configurational changes by modifying the orbital hybridization from planar  $sp^2$  to distorted 3D  $sp^3$  hybridized geometry. Typical examples for graphene are hydrogenation (C–H bonds) [208, 119] and the formation of an oxidation-induced epoxy group (–O–) [209] by creating C–OH or C–O–C bonds. The configuration change from planar  $sp^2$  to 3D  $sp^3$  geometry alters the physical and chemical properties of graphene which leads to subcritical crack growth. The crack growth creates further dangling bonds which react readily with hydrogen and oxygen inducing further configuration change. This process repeats by initiating and growth of more cracks until the failure is reached.

The environment assisted cracking (EAC) can occur in two main forms: material embrittlement and stress corrosion cracking (SCC). The embrittlement is due to material degradation caused by the adsorption of environment molecules onto the graphene surface [210, 119] leading to the formation of different functional groups such as hydroxyl or epoxide at the graphene surface. Formation of such functional groups can lead to the stretch and rotation of graphene bonds which can eventually deteriorate the strength of the material. The SCC is due to material dissolution consisting of chemical reactions between the material atoms and ambient molecules such as  $H_2$ ,  $H_2O$ ,  $CO_2$  and  $O_2$ . Such chemical reactions can induce the failure of C–C bonds or can lead to an active removal of material from the defective sites such as crack tips [211]. The presence of mechanical stress can facilitate the chemical reactions leading to a faster crack nucleation and propagation. Chemomechanical conditions can also be employed to control the fracture path of graphene nano ribbons [212].

In this chapter, we use atomistic modeling to study the stress corrosion cracking of graphene. Stress corrosion cracking is a complex phenomenon [213]; many parameters impact the process, and taking into account the effects of all these parameters requires a huge number of experiments. Moreover, it is almost impossible to observe all the

affecting parameters during experiments, as the main cracking mechanism acts in a very tiny area at the vicinity of crack tip. On the other hand, molecular dynamics simulations provide a powerful tool to study the phenomena occurring in small time scales [214, 117, 186, 3, 215, 147, 148, 216, 151, 217, 1, 218, 219, 2, 220, 146, 221, 222, 114, 223]. Using molecular dynamics simulations we will study the subcritical crack growth of graphene in the presence of oxygen molecules. We first conduct molecular dynamics simulation using the reactive force-field (ReaxFF) interatomic potential to study crack growth under tensile loading when the graphene sheet is exposed to oxygen molecules. A second set of simulations are conducted by using molecular dynamics combined with density-functional-based tight binding (DFTB) [224] calculations to investigate a small zone in the vicinity of crack tip. These simulations are conducted to more accurately study the reaction occurring at the crack tip during the stress corrosion cracking process.

## 5.2 Molecular dynamics modeling using ReaxFF

We use molecular dynamics simulations to study the stress corrosion cracking of monolayer graphene sheets including an edge crack as shown in Fig. 5.1. The graphene sheets are under tensile loading applied by imposing tensile strains in the  $y$ -direction. Oxygen molecules are randomly distributed around the graphene sheet at a minimum distance of 2 Å from graphene surfaces. Since oxygen molecules do not readily react with pristine graphene, only the oxygen molecules around the crack are considered in the model.

The simulations of this section are conducted using LAMMPS molecular dynamics package [91]. The equation of motions are integrated using the velocity-Verlet scheme with a time step of 0.25 fs. ReaxFF interatomic potential [98, 99] is employed to describe the C-C and C-O interactions. ReaxFF is a bond order interatomic potential whose parameters are optimized based on quantum-mechanics training sets. ReaxFF can accurately simulate chemical reactions, bond breaking and forming of systems

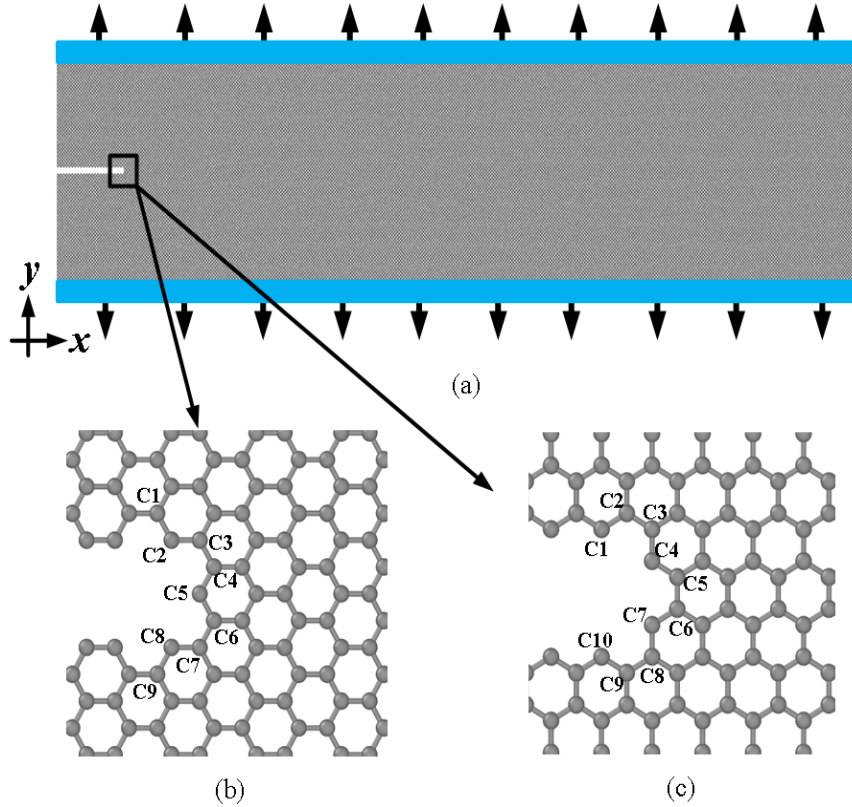


Figure 5.1: (a) A graphene sheet with an edge crack under tensile strain, (b) the configuration of crack in the armchair direction, (c) the configuration of crack in the zigzag direction.

consisting of C and O elements. In our simulations the C–C and C–O bonds are considered broken if their bond length exceeds  $1.9 \text{ \AA}$ .

The graphene sheet shown in Fig. 5.1 has dimensions of  $120 \text{ nm} \times 16 \text{ nm}$  and includes a  $10 \text{ nm}$  edge crack. Cracks are constructed in the armchair and zigzag directions by removing three and four rows of carbon atoms respectively as shown in Fig. 5.1b and c. The graphene sheet is subjected to a tensile loading along the  $y$ -direction as shown in Fig. 5.1. The loading is applied by imposing strain increments of  $0.2 \%$ , corresponding to a strain rate of  $5.33 \times 10^8 \text{ s}^{-1}$ , to the graphene sheet. The edges of graphene sheet perpendicular to the crack are free to relax. The displacement of the atoms located in the first few top and bottom layers are constrained in the  $y$  and  $z$ -direction while they are free to move in the  $x$ -direction. After every

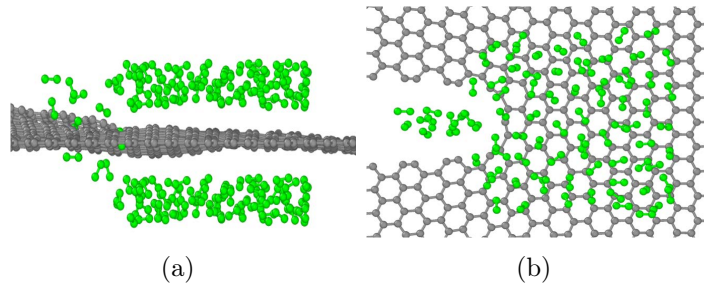


Figure 5.2: The initial distribution of oxygen molecules around the crack tip. (a) Side view (b) Top view

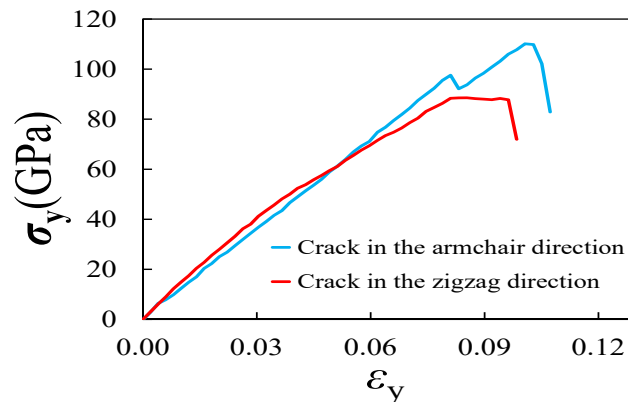


Figure 5.3: The stress–strain curves of graphene sheet with cracks in the armchair and zigzag direction at 300 K.

strain increment the energy of the system is minimized using the conjugate gradient algorithm. The system temperature is maintained at 300 K using the Berendsen thermostat [225] within a microcanonical ensemble for 1.25 ps. followed by equilibration within an NPT ensemble for 2.5 ps.

Oxygen molecules are randomly added around the crack tip at a strain level below the fracture strain  $\epsilon_f$  of graphene as shown in the Fig. 5.2. The initial separation between oxygen molecules and graphene surfaces or crack edges is more than 2 Å. The separation distance is chosen such that it is larger than the C–O cut off bond length and yet small enough that the O<sub>2</sub> molecules diffuse towards the C radical. After the addition of oxygen molecules, random velocities are assigned to the group of oxygen molecules at 300 K. Then the entire system is equilibrated within an NPT

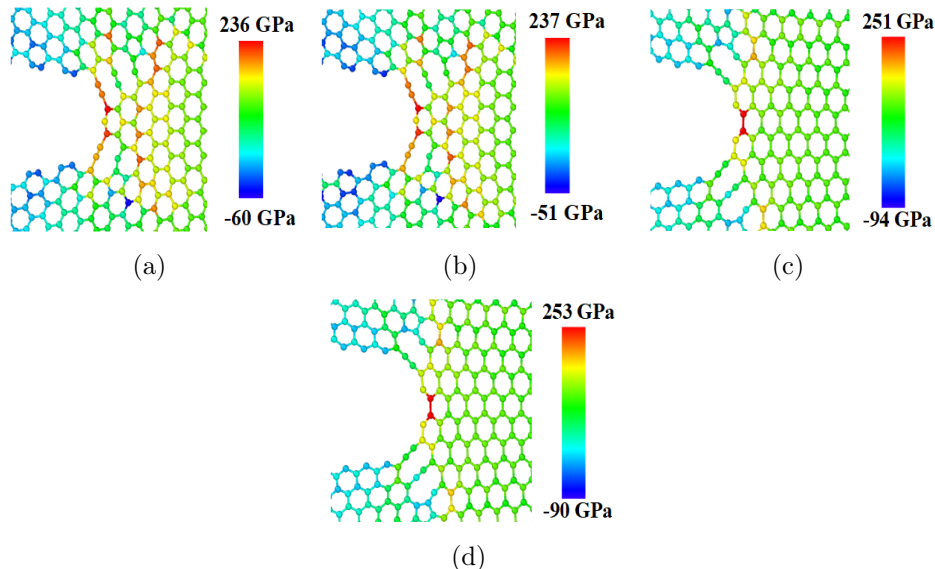


Figure 5.4: The atomic stress distribution ( $\sigma_{yy}$ ) in graphene sheets subjected to a strain of 0.076. (a) A graphene sheet with a crack in armchair direction, (b) the same sheet after equilibration for 55 ps. (c) a graphene sheet with a crack in zigzag direction, (d) the same sheet after 55 ps of equilibration.

ensemble at 300 K for 55 ps which allows the oxygen molecules to react with the crack tip.

The study of stress distribution in graphene sheet in the vicinity of crack tip, before and after chemisorption will provide better insight into this process. The stress tensor is computed using the virial definition [101, 102, 103] given by Eq. (1.17). To obtain a smooth atomic stress distribution across the sheet the stress data is time averaged over 2500 steps.

## 5.3 Results

### 5.3.1 Stress-strain curves of graphene sheet

The stress-strain response of graphene sheets with edge cracks subjected to mode-I loading at 300 K in the absence of oxygen molecules are shown in Fig. 5.3. Our results are in agreement with previous studies, in which authors employed ReaxFF potential to study the tensile properties of graphene [226]. It can be observed that the sheets with a crack in the zigzag and armchair directions fail respectively at strains of 0.085

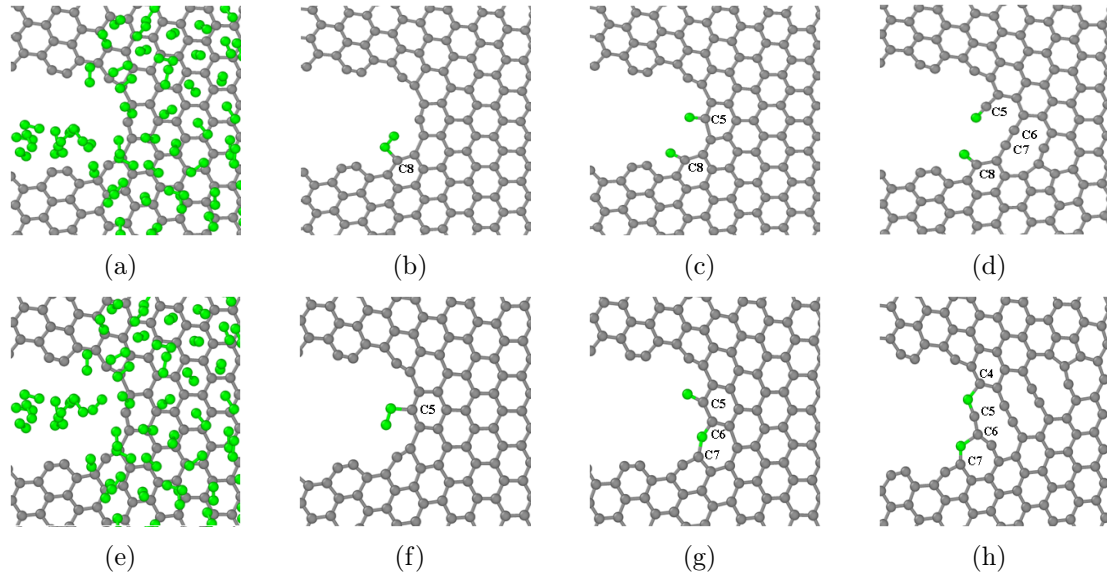


Figure 5.5: The chemisorption process in a graphene sheet including a crack in the armchair direction subjected to a strain of 0.047 and exposed to 156 oxygen molecules. (a)–(d) first example, (a) the initial distribution of oxygen molecules, 0 ps, (b) 0.15 ps, (c) 2.5 ps, and (d) 55 ps. (e)–(h) second example, (e) the initial distribution of oxygen molecules, 0 ps, (f) 0.125 ps, (g) 1.45 ps, and (h) 55 ps. Only the initial distribution oxygen molecules not adsorbed to graphene sheet are shown.

and 0.103. The flat portion of stress–strain response at the peak stress is due to the separation of the potential energy into high and low energy regions [226, 227]. We study the chemical reactions between graphene sheet and oxygen molecules at strains ranging from 0.047 to 0.076.

### 5.3.2 Graphene sheet in the absence of oxygen molecules

For the purpose of comparison, we conduct a tensile test modeling on graphene sheets with edge cracks in the absence of oxygen molecules. In these analysis, the graphene sheets are subjected to a tensile strain of 0.076 and equilibrate within an NPT ensemble at 300 K for 55 ps. As shown in Fig. 5.4, there is no change in the atomic arrangement and the stress distribution in the vicinity of crack tip during the 55 ps of equilibration. These results show that in the absence of oxygen molecules crack does not grow at a tensile strain of 0.076. On the other hand, the results presented in the following subsection demonstrate that the presence of oxygen molecule

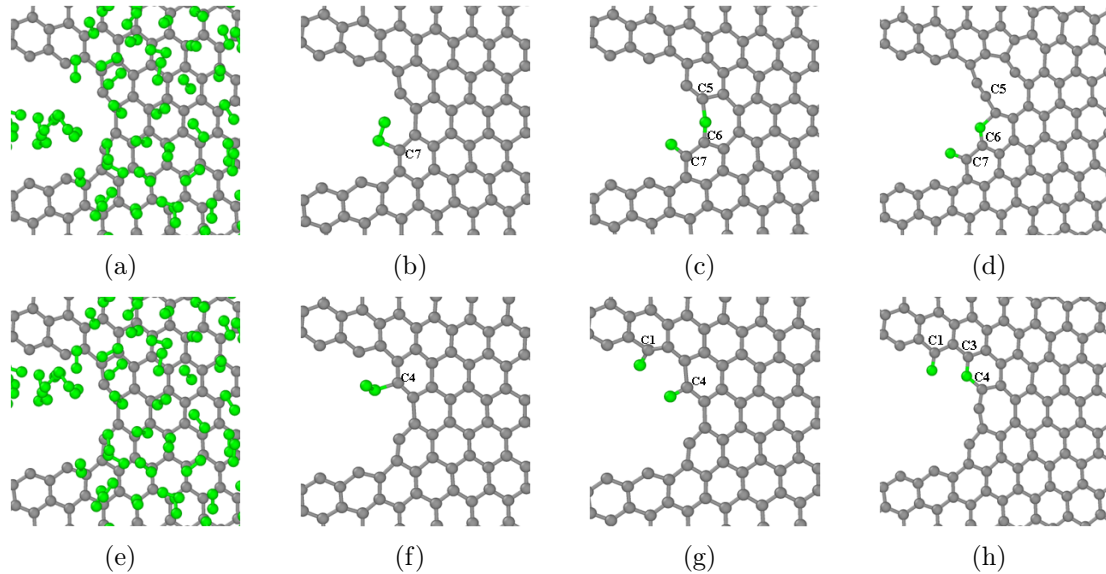


Figure 5.6: The chemisorption process in a graphene sheet including a crack in the zigzag direction subjected to a strain of 0.047 and exposed to 156 oxygen molecules. (a)–(b) first example, (a) the initial distribution of oxygen molecules, 0 ps, (b) 0.175 ps, (c) 0.525 ps, and (d) 55 ps. (e)–(h) second example, (e) initial distribution of oxygen molecules, 0 ps, (f) 0.325 ps, (g) 0.6 ps, and (h) 55 ps. Only the initial distribution oxygen molecules not adsorbed to graphene sheet are shown.

in the vicinity of crack tip leads to crack growth at strains of 0.076 or lower, hence the presence of oxygen molecules leads to subcritical crack growth in graphene.

### 5.3.3 Chemisorption of $O_2$ molecules

The cracked graphene sheet under a tensile strain of 0.047 exposed to 156 oxygen molecules are shown in Fig. 5.5 and 5.6. Various initial distribution of oxygen molecules around the crack tip are studied and two representative distributions for each crack orientation are shown in Fig. 5.5 and 5.6. While keeping the strain constant the system is equilibrated within an NPT ensemble at 300 K which allows the oxygen molecules to react with carbon atoms of graphene. In all the cases, the oxygen molecules are adsorbed to the carbon radicals located at the crack tip or in the vicinity of crack tip and as a results of this voids are formed around the crack tip. For example, for the crack in the armchair direction with an initial configuration shown in Fig. 5.5a, the  $O_2$  molecules react with carbon radicals C8 as presented in Fig. 5.5b.

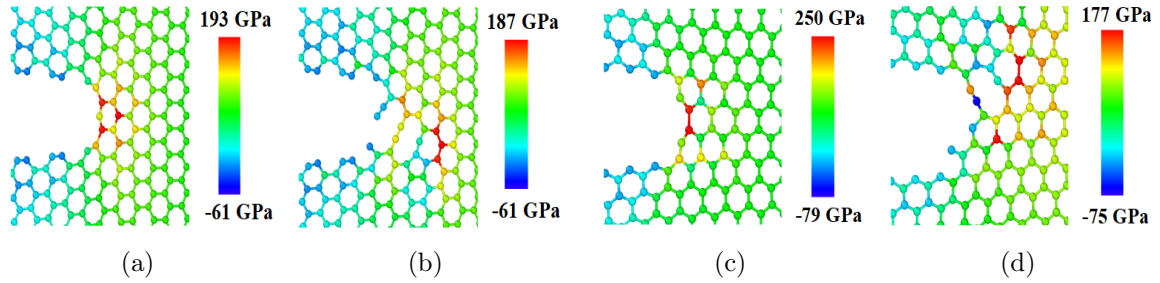


Figure 5.7: The atomic stress distribution ( $\sigma_{yy}$ ) in the graphene sheets subjected to a strain of 0.047 before and after chemisorption. (a) and (b) A graphene sheet including a crack in the armchair direction, (c) and (d) a graphene sheet including a crack in the zigzag direction.

The  $O_2$  molecules dissociates and the two oxygen atoms are adsorbed to C5 and C8 carbon atoms and form dangling bonds with them as shown in Fig. 5.5c. This leads to the failure of the C–C bond between C5 and C6 carbon radical as shown in Fig. 5.5d.

On the other hand, when graphene sheet is exposed to the  $O_2$  molecule distribution shown in Fig. 5.5e, one of the  $O_2$  molecules reacts with the C5 carbon radical as shown in Fig. 5.5f. The free oxygen atom in the peroxide forms a heptagon ring along with C6 and C7 carbon radicals as shown in Fig. 5.5g. For both cases, at the end of the simulation time voids and a 5–7 defect are formed around the crack tip as shown in Fig. 5.5(d) and (h).

A similar process is observed for the cracks in the zigzag direction as shown in Fig. 5.6. Similar to the cracks in the armchair direction, an oxygen molecule is first adsorbed to the carbon radicals around the crack tip. After the adsorption, the oxygen molecule dissociates leading to the formation of voids around the crack tip.

Cracks in both armchair and zigzag direction do not grow any further after the nucleation of initial voids and defects. During our simulation time period, a rapid crack growth is not observed at a strain of 0.047 when the graphene sheets are exposed to oxygen molecules. To understand the crack arrest behavior, the virial atomic stress distributions  $\sigma_{yy}$  around the crack tip before and after oxygen chemisorption are computed and shown in Fig. 5.7. The stress distributions of Fig. 5.7 show that the

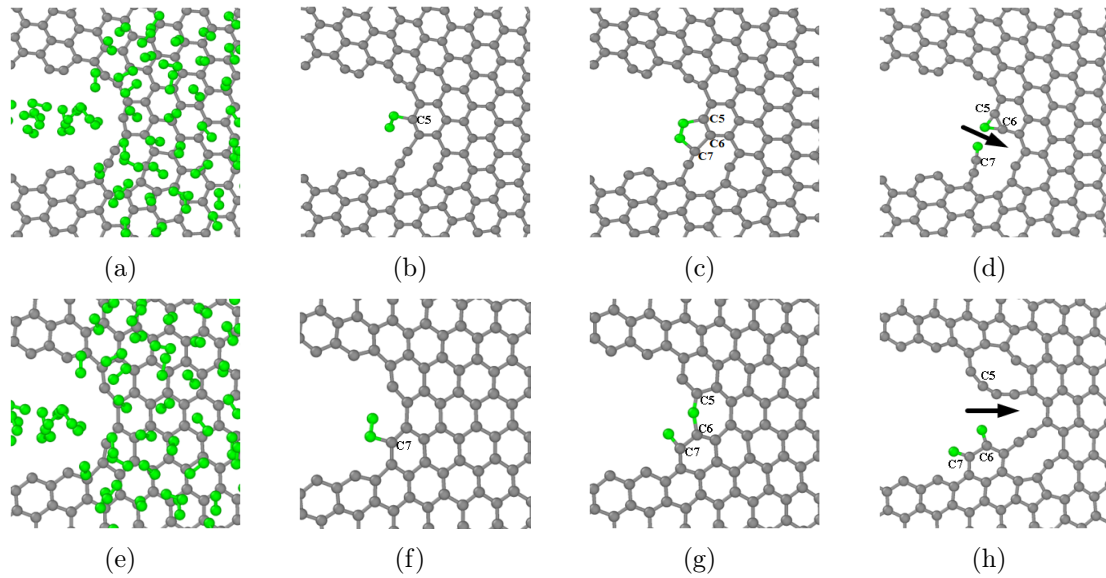


Figure 5.8: The chain of chemical reactions between graphene sheets and oxygen molecules at 300 K. (a)–(d) A graphene sheet including a crack in the armchair direction at a strain of 0.053 and exposed to 156 oxygen molecules, (a) initial distribution of oxygen molecules, 0 ps, (b) 0.075 ps, (c) 0.6 ps, and (d) 55 ps. (e)–(h) a graphene sheet including a crack in the zigzag direction at a strain of 0.049 and exposed to 156 oxygen molecules, (e) initial distribution of oxygen molecules, 0 ps, (f) 0.15 ps, (g) 0.275 ps, and (h) 55 ps. Only the initial distribution oxygen molecules not adsorbed to graphene sheet are shown.

nucleation of voids in the vicinity of crack tips leads to stress relaxation around the crack tip and reduces the stress concentration at the crack tip. Due to the reduction in the stress, chemical reaction between carbon radicals at the crack tip and oxygen molecules will require more time and energy, hence further chemical reactions are not observed during our simulation time of 55 ps.

The crack growth when the graphene sheets with cracks in the armchair and zigzag directions are respectively subjected to tensile strains of 0.053 and 0.049 and exposed to 156 oxygen molecules are shown in Fig. 5.8. The chain of chemical reactions between the graphene sheet including a crack in the armchair direction are shown in Fig. 5.8(a)–(d). The initial distribution of  $O_2$  molecules around the crack are shown in Fig. 5.8(a). During the simulation, as shown in Fig. 5.8(b) one of the  $O_2$  molecule attacks the carbon radical C5 forming a peroxide with a dangling peroxy atom. In

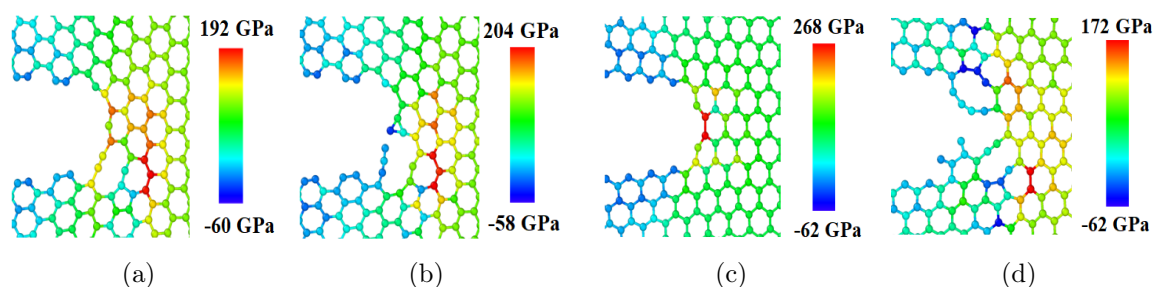


Figure 5.9: The atomic stress distribution ( $\sigma_{yy}$ ) in the graphene sheet before and after chemisorption. (a) and (d) a graphene sheet including a crack in the armchair direction at a strain of 0.053, (c) and (d) a graphene sheet with a crack in the zigzag direction at a strain of 0.049.

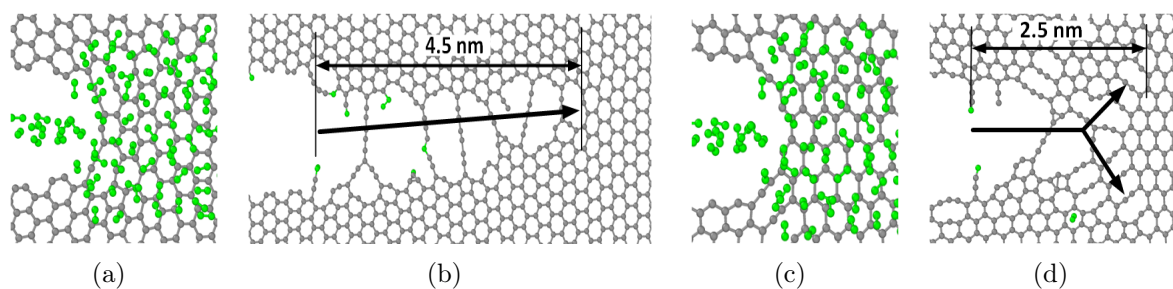


Figure 5.10: Subcritical crack growth in graphene sheets subjected to a strain of 0.076 when exposed to 156 oxygen molecules. (a) and (b) crack in the armchair direction, (c) and (d) crack in the zigzag direction before and after chemisorption process.

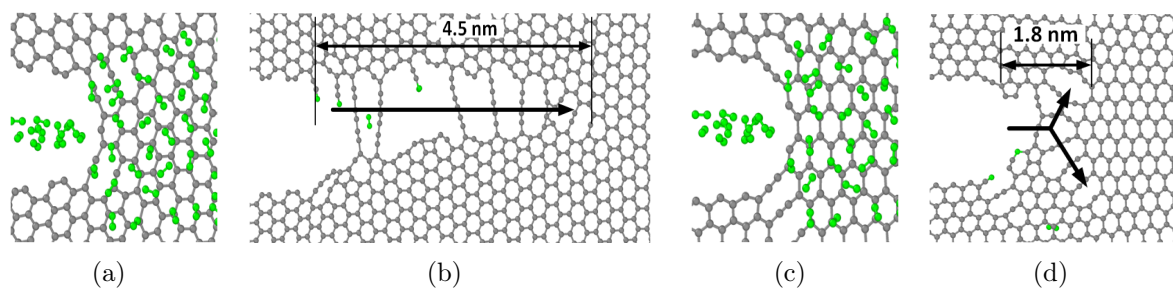


Figure 5.11: Subcritical crack growth in graphene sheets subjected to a strain of 0.076 when exposed to 110 oxygen molecules. (a) and (b) crack in the armchair direction, (c) and (d) crack in the zigzag direction before and after chemisorption process

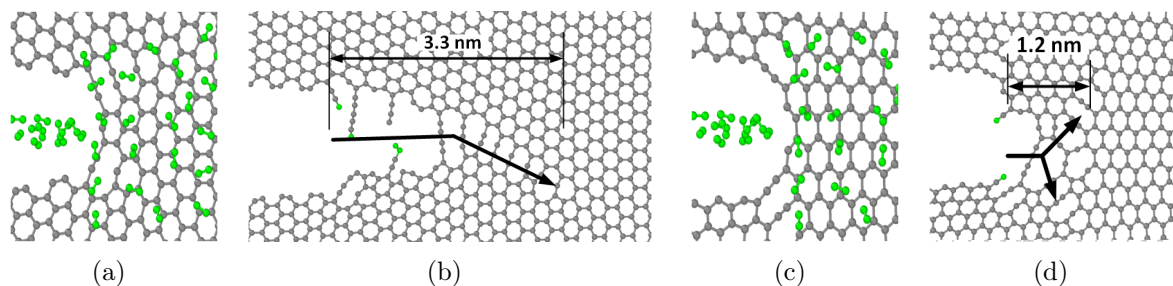


Figure 5.12: Subcritical crack growth in graphene sheets subjected to a strain of 0.076 when exposed to 72 oxygen molecules. (a) and (b) crack in the armchair direction, (c) and (d) crack in the zigzag direction before and after chemisorption process respectively

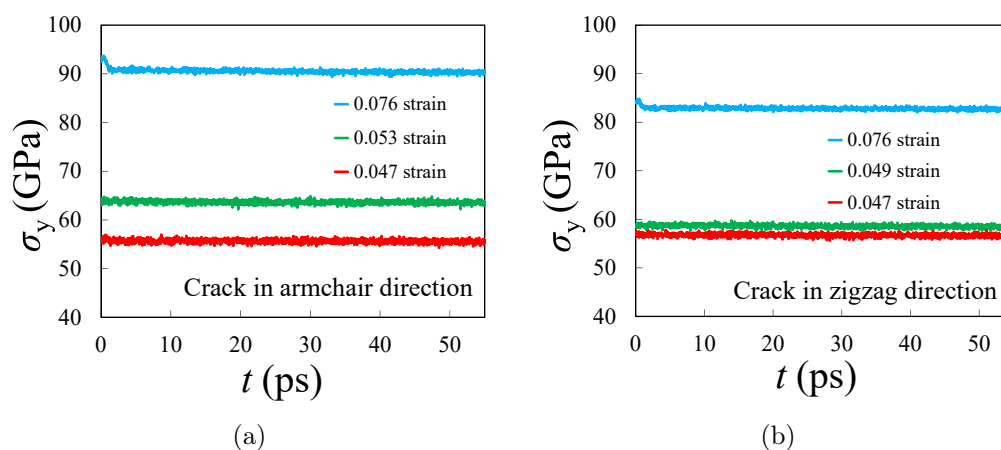


Figure 5.13: The stress in the  $y$ -direction ( $\sigma_y$ ) with respect to the simulation time during the chemisorption process in graphene sheets when cracks are exposed to 156 oxygen molecules. (a) crack in the armchair direction, (b) crack in the zigzag direction.

the next stage the peroxy radical reacts with carbon radical C7 and forms a pentagon ring as illustrated in Fig. 5.8(c) which consists of three carbon atoms C5, C6 and C7 and 2 oxygen atoms. As shown in Fig. 5.8(d), the O<sub>2</sub> molecule dissociate and leads to the breakage of the C–C bond between C6 and C7 carbon atoms.

The chemical reactions between graphene sheet with a crack in the zigzag direction are shown in Fig. 5.8(e)–(h). The O<sub>2</sub> molecule reacts with carbon radical C7 forming peroxide and the free oxygen atom in the peroxy radical reacts with C5 and C6 carbon radicals to form a heptagon ring which creates a ketone group at C7 as shown

in Fig. 5.8(g). In the next step the heptagon ring breaks which is followed by the failure of another C–C bond. This leads to the advancement of crack as shown in Fig. 5.8(h). A similar reactions between O<sub>2</sub> molecules and graphene [228] have been observed using density functional theory.

Although, in comparison with the graphene sheet with an armchair crack at 0.053 strain, more number of C–C bonds fail for the graphene sheet with a zigzag crack at a strain of 0.049, the crack does not grow further after the failure of the first few bonds. The stress distributions shown in Fig. 5.9 indicates that after the chemisorption, the stress at the bonds attached to the crack tip has reduced. This is more pronounced for the crack in the zigzag direction. Due to the stress relaxation at the crack tip, the chemical reactions between carbon radicals and oxygen molecules does not occur readily and crack does not grow during our simulations.

Finally, we study the chemisorption in graphene sheet exposed to 156, 110 and 72 oxygen molecules at a strain of 0.076. This strain is lower than the fracture strain of graphene sheets as shown in Fig. 5.4. The initial and final structure of the graphene sheets are shown in Fig. 5.10–5.12. A significant crack growth occurs for cracks in both armchair and zigzag directions. The cracks in the armchair and zigzag directions grow by 4.5 nm and 2.5 nm, respectively when graphene sheets are exposed to 156 oxygen molecules. On the other hand, the cracks in the armchair and zigzag direction grow by 4.5 nm and 1.8 nm when exposed to 110 oxygen molecules and by 3.3 nm and 1.2 nm when exposed to 72 oxygen molecules. In all cases, cracks have non-smooth edges and branching occurs for the cracks in zigzag direction. Also, the new edges of the cracks for all cases has a zigzag chirality.

The increase in the crack length leads to a reduction of the stiffness of the graphene sheet and as a result the stress in the  $y$ -direction reduces from about 93 GPa to 91 GPa and from 85 GPa to 83 GPa for the sheets with cracks in the armchair and zigzag direction and exposed to 156 oxygen molecules as shown in Fig. 5.13 . In case

of strains of 0.047, 0.049 and 0.053, as illustrated in Fig. 5.13, stress in the  $y$ -direction remains constant during the chemisorption process.

#### 5.4 Molecular dynamics modeling using DFTB

A fundamental issue of using molecular dynamics method is the adequate description of interatomic interactions, which should be as realistic as possible. In many cases, classical interatomic potentials cannot be used to model phenomena involving chemical reactions or interatomic bonds formation or breaking. To accurately model such problems, one needs to resort to self-consistent quantum mechanical methods. However, density functional (DF) or Hartree-Fock based self-consistent methods are computationally very demanding, imposing enormous limitations on the system size or the number of simulation steps that can be modeled using such techniques. In this section, as a compromise between accuracy and computational costs we use molecular dynamics combined with self-consistent-charge density-functional-based tight-binding (SCC-DFTB) [224] calculations. The SCC-DFTB method is a semiempirical method based on the density functional theory (DFT), which is an order of magnitude faster than DFT but maintains much of the accuracy of DFT. The abilities of DFTB in predicting and reproducing different properties of solids and molecules have been reviewed in Reference [229]. The abilities of DFTB in predicting C-H vibrations are examined in Reference [230] and it is shown that DFTB results are in good agreements with experimental values.

We investigate the stress corrosion cracking under pure mode I loading. Our atomistic domain is a circular zone cut around the crack tip as is shown in Fig. 5.14. Initial cracks in the zigzag and armchair directions are generated by removing four and three rows of carbon atoms, respectively. The radius of the domain is about 30 Å and it contains about 1000 carbon atoms. Mode I crack tip asymptotic displacement fields are applied to all the carbon atoms in the domain using the crack-tip asymptotic

displacement field given by [231]

$$u_x = \frac{K_I}{2\mu} \sqrt{\frac{r}{2\pi}} \cos \frac{\theta}{2} [\kappa - \cos \theta] \quad u_y = \frac{K_I}{2\mu} \sqrt{\frac{r}{2\pi}} \sin \frac{\theta}{2} [\kappa - \cos \theta] \quad (5.1)$$

where  $r$  is the distance between the boundary node and crack-tip,  $\theta$  is the polar angle,  $K_I$  is mode I stress intensity factor,  $\mu$  is the shear modulus, and  $\kappa = \frac{3-\nu}{1+\nu}$ , where  $\nu$  is the graphene Poisson's ratio which is taken equal to 0.165 [203].

After the imposition of the displacement field, the equilibrium configuration of the crack tip zone is obtained by relaxing the position of the interior atoms while the position of boundary atoms shown in red in Fig. 5.14 are kept fixed. Molecular dynamics (MD) combined with self-consistent-charge density-functional-based tight-binding (SCC-DFTB) [224] are employed to find the relaxed position of internal atoms. During this step, the chemical reactions occurring at the crack tip can be observed. All the modelings are conducted using DFTB+ package [232] which is a free and open source program.

All the simulations are conducted using a microcanonical (NVE) ensemble for a total simulation time of 1 ps. A Nosé-Hoover thermostat is used to maintain the temperature at 300 K. The velocity-Verlet algorithm with a time step of 1 fs is used for the purpose of time integration of atoms trajectory.

#### 5.4.1 Results

We have performed DFTB simulations to model stress corrosion cracking of both cracks in both armchair and zigzag directions when the graphene sheet is exposed to oxygen molecules. The modeling results for a domain with an initial crack in the zigzag direction are shown in Fig. 5.15. In this simulations, the graphene sheet is under mode I loading with a stress intensity factor of  $2.75 \text{ MPa}\sqrt{m}$ . Our DFTB modeling shows that under such loading and at a temperature of 300 K none of the C-C bonds break and crack does not propagate. We then place an oxygen molecule

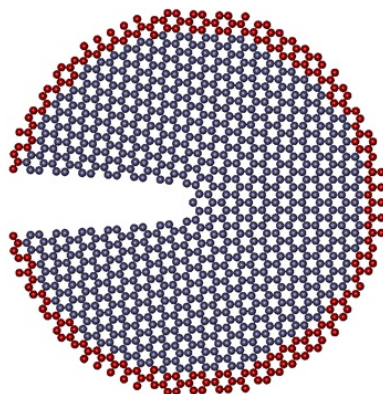


Figure 5.14: The circular domain used for modeling of stress corrosion cracking in graphene. Mode I crack tip asymptotic displacement field is applied on this domain. The position of interior atoms are relaxed while the boundary atoms shown in red are fixed.

at a distance of  $2 \text{ \AA}$  at the top of the graphene surface as is shown in Fig. 5.15a. The DFTB modeling predicts an immediate spontaneous dissociation of the oxygen molecule. As demonstrated in Fig. 5.15b, as a result of the presence of the oxygen molecule in the vicinity of the crack tip, the C–C bond located at the crack tip breaks and the crack advances a distance of  $\sqrt{3}r_0$ , where  $r_0$  is the graphene bond length. The two oxygen atoms are attached to the graphene carbon atoms and a C–O bond is formed behind of the crack tip with a C–O–C bridge generated at the crack tip. In the next step, another oxygen molecule is placed at a distance of  $2 \text{ \AA}$  above the graphene sheet (Fig. 5.15c) right on top of the C–O–C bridge. As is shown in Fig. 5.15d, opposed to the previous step, the oxygen molecule does not dissociate and the oxygen molecule is adsorbed to a carbon radical at the crack tip. The attachment of the oxygen molecule to the carbon radical leads to the rotation and stretch of the C–C bonds attached to the carbon radical.

In the third step shown in Fig. 5.15e an oxygen molecule is placed above the crack tip at a distance of  $2 \text{ \AA}$  from the graphene surface. The outcomes of the chemical reactions of the oxygen molecule with the graphene atoms are shown in Fig. 5.15f. This figure shows that in this step the oxygen molecule dissociates and one oxygen

atom is adsorbed to graphene forming a C–O–C bridge. This leads to the generation of a pentagon at the top edge of the crack. The other oxygen atom is attracted to the oxygen molecule introduced into the system in the previous step. This leads to the dissociation of this molecule and the formation of a new oxygen molecule. The newly formed oxygen molecule moves away from the crack tip.

In the fourth step, an oxygen molecule is placed in front of the C–O–C bridge and above the graphene surface as shown in Fig. 5.15g. As shown in Fig. 5.15h, during this step the oxygen molecule dissociates, the C–O–C bridge breaks and a new C–O–C bridge forms, i.e. the crack grows by about  $\sqrt{3}r_0$ . In the next step another oxygen molecule is placed ahead of the C–O–C bridge as illustrated in Fig. 5.15i. Similar to the previous step, the dissociation of the oxygen molecule breaks a C–O–C bond and another C–O–C bond is formed. However, as shown in Fig. 5.15j, in contrast to the previous step, the newly formed C–O–C bridge is not perpendicular to the crack path which results in the generation of a kink in the crack path. Finally, another oxygen molecule is added to the system as shown in Fig. 5.15k. The presence of a new oxygen molecule leads to the advancement of the crack by  $\sqrt{3}r_0$  as demonstrated in Fig. 5.15l.

To study the impact of crack chirality of corrosion process, we use DFTB modeling to study the corrosion when the initial crack is in the armchair direction. The simulations are conducted under a remote loading with stress intensity factor of  $2.75 \text{ MPa}\sqrt{m}$  which is less than its critical stress intensity factor. To study the crack propagation due to the corrosion, an oxygen molecule is placed at the top of the crack tip in a distance of  $2 \text{ \AA}$  from the graphene surface as is shown in Fig. 5.16a. The oxygen molecule dissociates and each oxygen atom is adsorbed to a carbon atom of the graphene sheet, as shown in Fig. 5.16b. The adsorption of oxygen molecule to the crack tip atom leads to a significant stretch of a C–C bond at the crack tip, however no C–C bond breaks during the simulation time of 1 ps in this step.

The initial configuration of the next step of the simulation is shown in Fig. 5.16c. In this step, the graphene sheet is exposed to another oxygen atom located 2 Å on top of the graphene sheet and behind the crack tip. As demonstrated in Fig. 5.16d, as a result of the chemical reactions between oxygen and graphene the bond stretched in the previous step breaks. Moreover, the oxygen molecule dissociates and its two oxygen atoms are attached to the graphene surface forming a C–O bond and a C–O–C bridge. The addition of another oxygen molecule to the system, as shown in Fig. 5.16d, results in the breakage of the C–O–C bridge and the adsorption of the two oxygen atoms to the graphene surface as illustrated in Fig. 5.16e.

In the fourth step shown in Fig. 5.16g another oxygen molecule is placed on top of the graphene sheet. As shown in Fig. 5.16h, as a result of the chemical reactions between oxygen molecules and carbon radicals, two carbon atoms are separated from the graphene surface generating two carbon monoxide (CO) molecules. In this step, crack does not propagate along its previous direction, however due to the separation of the carbon atoms, two C–C bonds on the crack edge breaks.

In the next step, another oxygen molecule is added to the system as shown in Fig. 5.16i. In contrast to the previous steps, the oxygen molecule does not dissociates but it is adsorbed to a carbon atom as shown in Fig. 5.16j. Due to bond rotation and stretching which occurs as a result of adsorption of an oxygen molecule to the graphene surface, a C–C bond at the crack tip breaks. Finally, another oxygen molecule is added at a distance of 2 Å below the graphene sheet as shown in Fig. 5.16k. In this step both of the oxygen molecules available in the system dissociate. A carbon atom is removed from the graphene sheet and a CO<sub>2</sub> molecule is formed. The other two oxygen atoms are adsorbed to the graphene sheet as shown in Fig. 5.16l.

Comparing the corrosion process demonstrated in Fig. 5.15 and Fig. 5.16 show that due to corrosion, both cracks tend to propagate along a zigzag direction, although the crack propagation can be associated with kinking along the crack path. The creation

of CO and CO<sub>2</sub> molecules show that material removal can play an important role in the corrosion of graphene.

## 5.5 Conclusion

Molecular dynamics modeling was used to study the mechanism of stress corrosion cracking in graphene. Cracked graphene sheets were exposed to oxygen molecules and the reaction of oxygen molecules with carbon atoms were studied. The first set of modelings employed molecular dynamics using ReaxFF interatomic potential. Large graphene sheets were exposed to oxygen molecules which were randomly distributed around the crack tip and edges. The results show that sub-critical crack growth can happen in graphene. At lower strains the voids and defects are generated ahead of the crack tip as a result of reactions between carbon and oxygen molecules. This can lead to stress relaxation at the crack tip which can prevent further crack growth.

Molecular dynamics simulations combined with DFTB calculations are conducted to more accurately study the reaction occurring at the crack tip. These MD modelings also show that sub-critical crack growth can occur in graphene. The results showed that crack growth in graphene can happen by two main mechanisms. These include atomic bond failure and material removal by forming CO or CO<sub>2</sub> molecules.

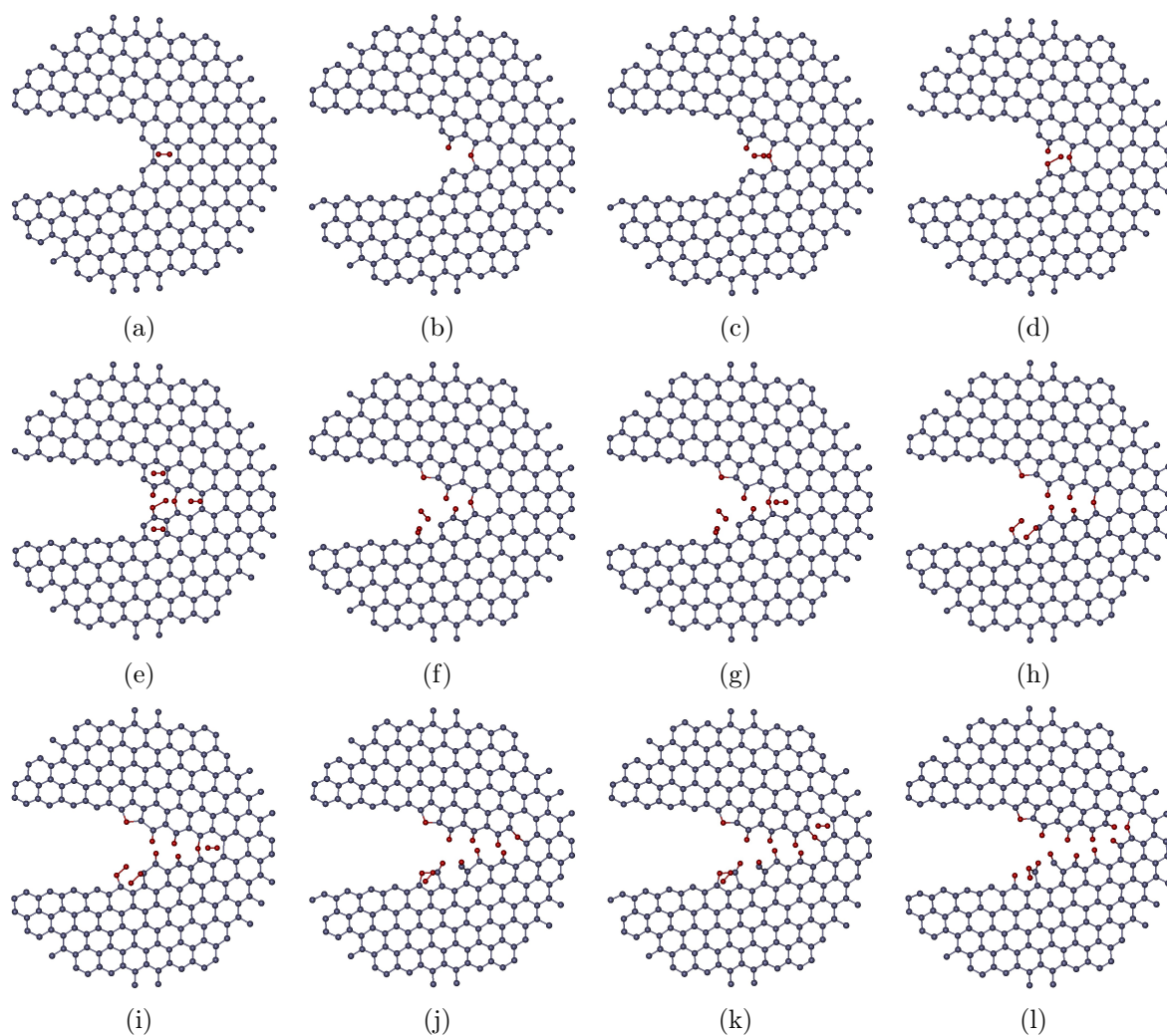


Figure 5.15: Zoom-in of the crack tip configuration showing the stress corrosion cracking of a zigzag crack under a stress intensity factor of  $2.75 \text{ MPa}\sqrt{m}$ . Oxygen molecules are added to the top of crack surface and in the vicinity of crack tip. The distance of oxygen atoms to graphene surface is at least  $2 \text{ \AA}$ .

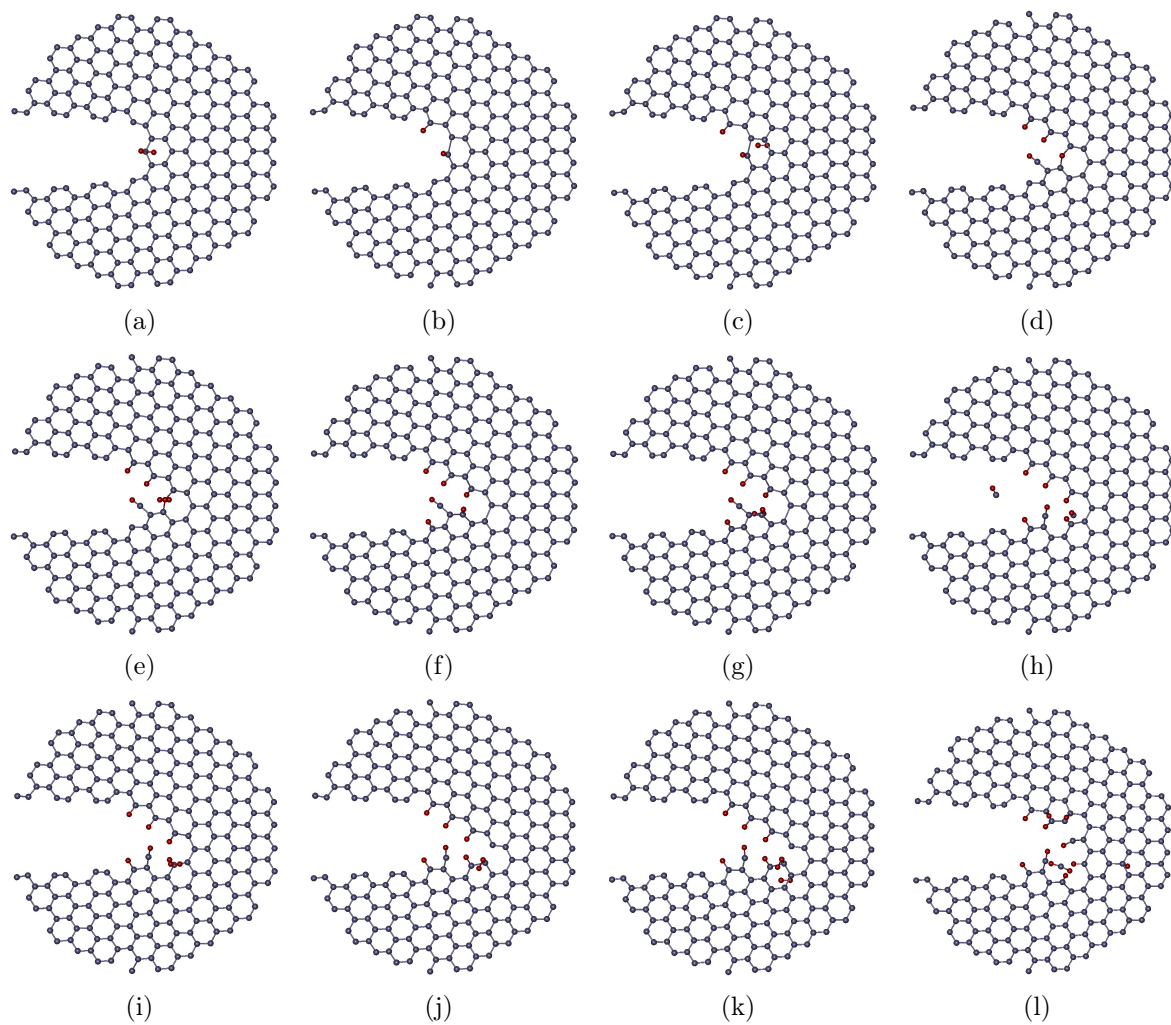


Figure 5.16: Stress corrosion cracking of an armchair crack under a stress intensity factor of  $2.75 \text{ MPa}\sqrt{m}$ . Oxygen molecules are added to the top of crack surface and in the vicinity of crack tip. The distance of oxygen atoms to graphene surface is at least  $2 \text{ \AA}$ .

## CHAPTER 6: Atomistic Simulation-Based Cohesive Zone Law of Hydrogenated Grain Boudaries of Graphene

### 6.1 Introduction

Due to the remarkable properties, graphene is finding applications in many industries. Chemical vapor deposition (CVD) is the most widely used technique for producing large graphene sheets. Graphene sheets generated by the CVD technique is polycrystalline [80, 81] composing of grains stitched together at grain boundaries. The high-resolution transmission electron microscopy data and molecular dynamics simulations indicate that grain boundaries are mainly composed of Stone-Wales defects [233, 80]. These defects are energetically favorable sites for chemisorption of extrinsic impurities such as hydrogen atoms [234, 235] which are abundant in the environment. Verma et al.[236] conducted molecular dynamics simulations to understand the mechanical properties and the failure morphology of bicrystalline graphene oxide. They concluded that epoxide functionalization of grain boundary atoms leads to the reduction in the tensile strength and boost the ductility of the bicrystalline graphene sheet. The adsorption of hydrogen atoms on the grain boundaries affect the mechanical properties of grain boundaries and thus alter the properties of polycrystalline graphene [119, 237]. In addition to the adsorption of environmental hydrogen molecules, deliberate hydrogenation of graphene can be used as a tool to alter the electronic, optical, mechanical and magnetic properties of graphene [238, 239]. Hydrogenated graphene exhibits ferromagnetism [240] and displays a band gap which can be tuned by the extent of hydrogenation [241, 242]. The reversible hydrogenation property of graphene can be exploited for hydrogen storage applications [238]. Understanding the impact of hydrogen adsorption on the strength and toughness of

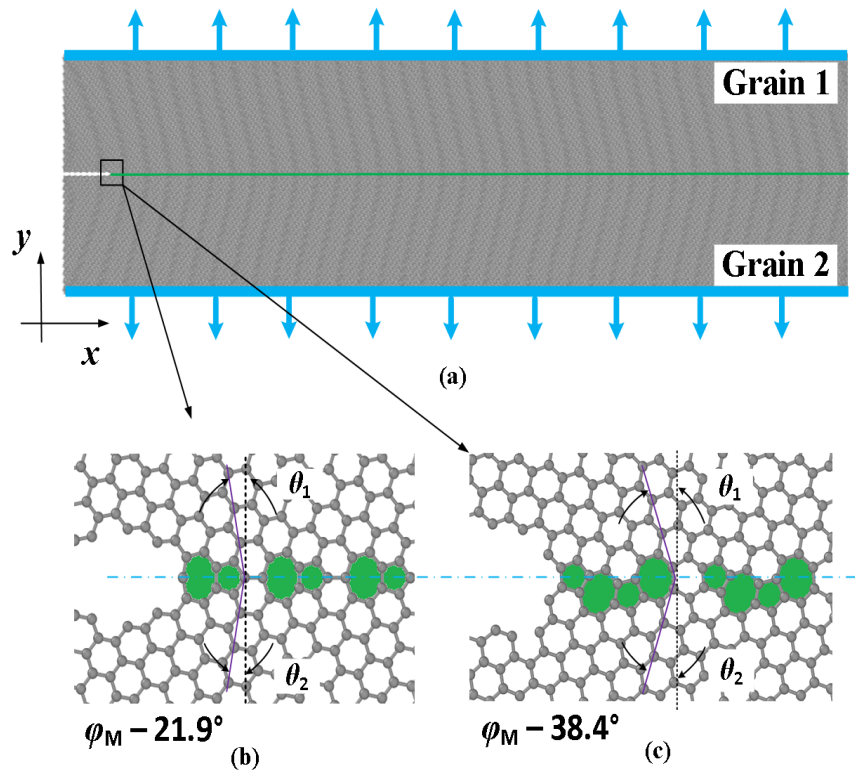


Figure 6.1: (a) Bicrystalline graphene sheet with a grain boundary along the  $x$ -direction, (b) a symmetric grain boundary with misorientation angle of  $21.9^\circ$ , (c) a symmetric grain boundary with misorientation angle of  $38.4^\circ$ .

graphene grain boundary is crucial in predicting the failure mechanism of polycrystalline graphene.

Herein, we conduct molecular dynamic simulations of the fracture of hydrogenated grain boundaries and express the results as continuum cohesive zone models (CZM) which embed concepts of the grain boundary toughness and strength. Cohesive zone models are developed to remove the stress singularity at the crack tip [243]. The CZM was proposed by Barenblatt [243, 244] and Dugdale [245] in studying the fracture of brittle materials [243] as an approximate representation of the crack tip fracture process zone. The cohesive zone is defined ahead of the crack tip as two virtual cohesive surfaces held together by cohesive traction. The cohesive traction between the two surfaces is a result of the interatomic interactions and constitutes resistance to crack propagation. A cohesive traction–separation law (TSL) is used to describe

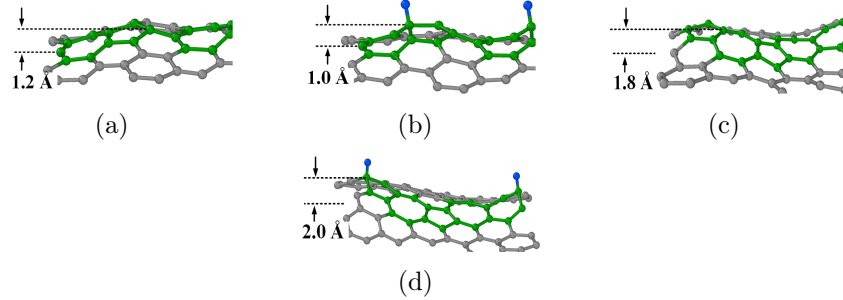


Figure 6.2: The out-of-plane deformation of bicrystalline sheet along the grain boundaries. (a) and (b) grain boundary with misorientation angle of  $21.9^\circ$  without and with adsorbed hydrogen atoms, (c) and (d) grain boundary with misorientation angle of  $38.4^\circ$  without and with adsorbed hydrogen atoms. The carbon atoms at the grain boundary are shown in green and the hydrogen atom is shown in blue.

the relation between cohesive traction and the separation displacement between the cohesive surfaces. The crack grows when the separation of the cohesive surfaces at the crack tip reaches a critical value.

The capability of cohesive zone model in providing more realistic features of failure mechanism has brought it significant attentions in the finite element modeling (FEM) of fracture problems. The development of a traction–separation law which realistically characterizes the collective features of failure process zone is essential in successful modeling of fracture using FEM. Several forms of the TSL have been proposed in the past including bilinear, exponential and trapezoidal [246, 247, 248, 249]. The functional form of such traction–separation laws is such that by increase in the separation of the cohesive surfaces the traction increases until it reaches a peak value and then decreases to zero at a critical separation value. Such models are often phenomenological laws derived from experiments [250, 251, 252] or trial–and–error finite element computations [253, 254, 255].

Atomistic simulations have become a valuable tool in studying properties of nanomaterials [256, 2, 144, 3, 147, 1, 257, 114, 139, 146, 258]. More recently, atomistic scale modeling of crack propagation is used for the extraction of traction–separation laws of cohesive zone. Yamakov et al. [259] used molecular dynamic simulations

to derive the traction–separation law of intergranular fracture of aluminum. Their bicrystal model includes a pre–existing crack along the grain boundary subjected to mode–I loading. Zhou et. al [260] extended this methodology to extract the cohesive law under mixed–mode loading conditions. Guin et. al [261] used molecular dynamics to derive the traction–separation law of intergranular fracture of graphene. Krull and Yuan [262] used quasi–static atomistic simulations of crack tip blunting to derive an exponential cohesive law of a single crystal specimen. Dandekar and Shin [263] used molecular dynamics simulations along with the Weibull distribution to parameterize the traction–separation law of the interface of  $\text{Al}_2\text{O}_3$ –Al composites. Paliwal and Cherkaoui [264] proposed a technique to derive the mixed–mode traction–separation law for non–planar crack growth using molecular dynamic simulation.

In this study, we use the basic concepts of the technique proposed by Yamakov et al. [259] to derive the traction–separation law of the symmetric tilt grain boundaries of graphene. The simulation is conducted on a bicrystalline graphene sheet under mode I loading with an edge crack along the grain boundary. The impact of hydrogenation percentage of grain boundary and adsorption site of hydrogen atoms on the traction–separation law of the grain boundary is studied.

## 6.2 The structure of grain boundary and bicrystal graphene

An essential step in studying the properties of grain boundaries (GBs) and extracting realistic traction–separation laws is the creation of models which mimic the structure of grain boundaries observed in experiments. The grain boundaries of graphene can be characterized by two angles  $\theta_1$  and  $\theta_2$  as shown in Fig. 6.1b and Fig. 6.1c . These two angles are the angles between the normal vector of the grain boundary and a particular crystallographic direction ( $0 \leq \theta_1, \theta_2 \leq 30^\circ$ ) (e.g. armchair or zigzag) of the adjacent grains.

The misorientation angle of the grain boundary is defined as  $\phi_M = \theta_1 + \theta_2$ . Due to the six–fold symmetry of the atomic structure of graphene, the misorientation angle

ranges from 0 to 60°. The grain boundary is symmetric if  $\theta_1 = \theta_2$  and  $\phi_L = |\theta_1 - \theta_2|$  defines the angle between the grain boundary vector and the symmetric tilt vector.

Theoretical studies and high-resolution images produced by transmission electron microscopy (HR-TEM) show that the GBs of graphene are mainly composed of pentagon–heptagon pairs [233, 80]. These pentagon–heptagon pairs are the edge dislocation cores, hence GBs of graphene can be considered as a one–dimensional chain of edge dislocations. The grain boundary misorientation angle is related to the dislocation spacing along the grain boundary by [265, 266]

$$\phi_M = 2 \arcsin \frac{|\mathbf{b}_{(1,0)}|}{2d_{(1,0)}} \quad (6.1)$$

where  $\mathbf{b}_{(1,0)}$  represents the Burgers vector of (1,0) edge dislocations and  $d_{(1,0)}$  represents the distance between dislocations. Based on this equation, small values of  $d_{(1,0)}$  lead to large misorientation angle. The closest possible value for  $d_{(1,0)}$  leads to a misorientation angle of  $\phi_M = 21.9^\circ$ . To construct grain boundaries with misorientation angle in the range of 21.9° and 60° it is necessary to use (1,1) dislocations. The misorientation angle in this case is obtained using [266]

$$\phi_M = 60^\circ - 2 \arcsin \frac{|\mathbf{b}_{(1,1)}|}{2d_{(1,1)}} \quad (6.2)$$

More complicated tilt grain boundaries can be constructed by using (1,0)+(0,1) dislocation or a combination of a (1,0) dislocation with (1,0) + (1,0) + (1,0) dislocation [233, 1, 266].

In this chapter, we create two bicrystalline graphene sheets by using (1, 0) and (1,0)+(0,1) dislocations to generate symmetric high–angle grain boundaries with misorientation angles of  $\phi_M = 21.9^\circ$  and  $\phi_M = 38.4^\circ$  as shown in Fig. 6.1. In graphene, zigzag and armchair directions represent two high–symmetry directions. Therefore, misorientation angles close to 0° and 60° are considered as small–angle grain bound-

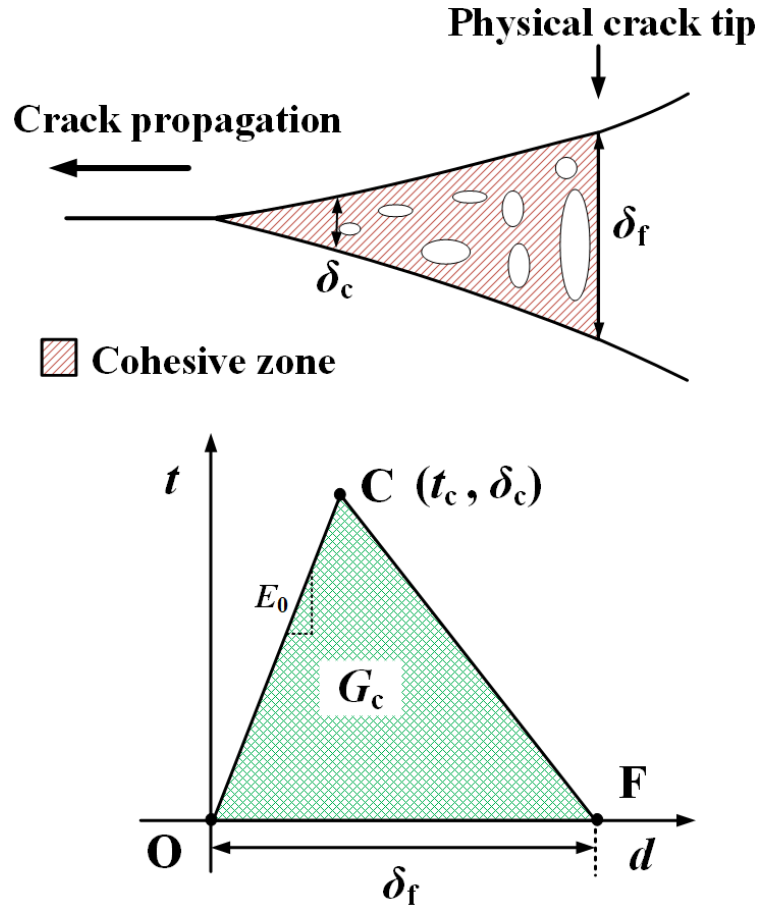


Figure 6.3: A schematic cohesive zone and its corresponding bilinear traction separation law.

aries in the zigzag and armchair directions, respectively.

The bicrystalline sheets have dimensions of  $140 \text{ nm} \times 35 \text{ nm}$  and include a  $5.4 \text{ nm}$  edge crack along the grain boundary as shown in Fig. 6.1. A vacuum of  $4 \text{ nm}$  in the  $x$  and  $z$  directions and  $2 \text{ nm}$  in the  $y$ -direction is prescribed to avoid interactions between the periodic images. An edge crack of length  $5.4 \text{ nm}$  and width of about  $0.7 \text{ nm}$  is created along the grain boundary by removing few layers of carbon atoms.

The bicrystalline sheets experience out of plane deformations at the location of grain boundaries as are shown in Fig. 6.2a and c. The adsorption of hydrogen atoms at the pentagon–heptagon defects of the GBs alter the configuration of grain boundaries as shown in Fig. 6.2b and d. This leads to a stretch of the C–C bonds at the adsorption

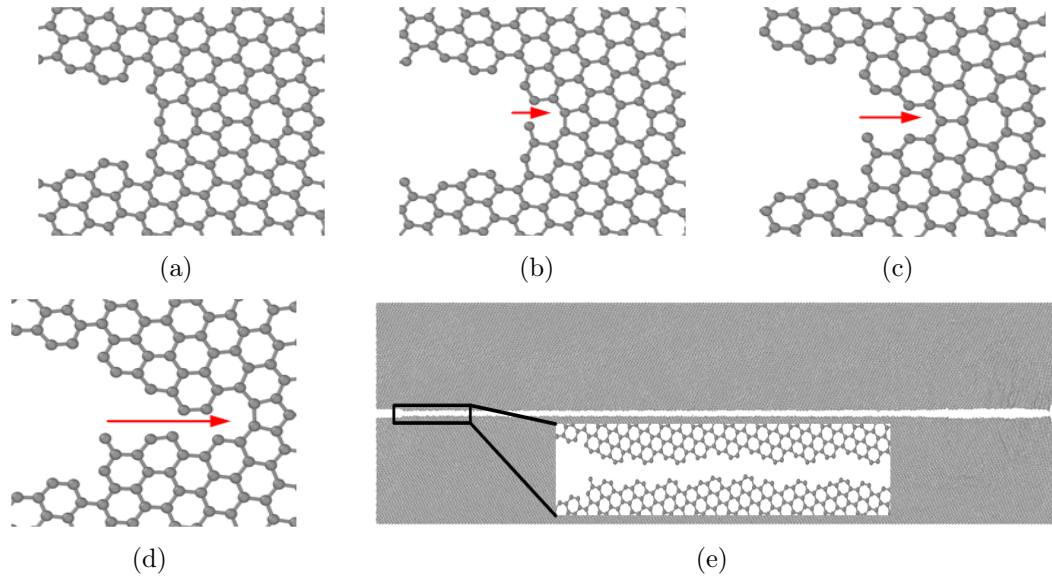


Figure 6.4: Crack propagation path along the grain boundary with misorientation angle  $21.9^\circ$  without adsorbed hydrogen atom at 300 K. (a) No strain, (b) at a strain of 3.08 %, (c) at a strain of 3.55 %, (d) at a strain of 3.58 % and (e) at a strain of 5.28 %.

site and alter the fracture and mechanical properties of grain boundaries. The impact of such structural alteration on the fracture properties of GBs are studied by obtaining the traction–separation laws of grain boundaries when hydrogen atoms are adsorbed to the pentagon–heptagon defects along the grain boundaries.

### 6.3 Cohesive zone model

Cohesive zone model was first introduced by Barenblatt [244, 243] by assuming the molecular cohesion exists near the crack surfaces. Dugdale [245] considered a process zone ahead of the crack tip and extended the concept to perfectly plastic materials. The implementation of the CZM in the framework of finite element formulation was first introduced by Hillerborg *et al.* [267] Cohesive zone models combine a strength based failure criterion for the prediction of damage initiation with an energy based fracture mechanics criterion to determine the crack propagation. Cohesive zone models employ a traction–separation law (TSL) to describe the material behavior within the cohesive zone. The TSL uses a softening constitutive equation relating the crack

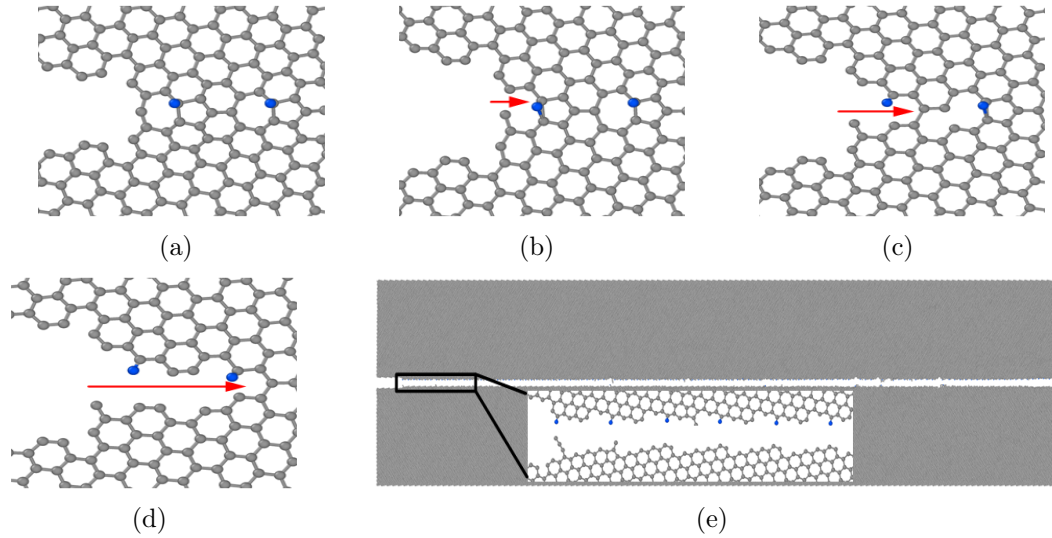


Figure 6.5: Crack propagation along the grain boundary with misorientation angle of  $21.9^\circ$  with one hydrogen atom adsorbed at each pentagon–heptagon defect at 300 K. (a) No strain, (b) at a strain of 2.88 %, (c) at a strain of 3.35 %, (d) at a strain of 3.38 % and (e) at a strain of 5.13 %.

surface traction to the material separation across the crack to represent the process of material deterioration occurring in the process zone ahead of the crack tip.

Trapezoidal, exponential and bilinear TSLs are used in the literature [268]. A bilinear traction–separation law is schematically shown in Fig. 6.3. In the bilinear TSL, the traction initially increases with the increase of separation until it reaches its peak value  $t_c$  at separation  $\delta_c$ . Further increase of separation leads to a reduction in the traction representing the irreversible damage in the process zone. The traction transfer across the crack surfaces reaches zero at a critical separation  $\delta_f$  when the crack is fully open.

The key parameters of this model are the initial stiffness of the cohesive zone  $E_0$ , peak traction  $t_c$  and fracture energy  $G_c$ . For the purpose of using a TSL in a finite element model, the initial stiffness of the cohesive model  $E_0$ , defined as  $t_c/\delta_c$ , should be chosen as high as possible to avoid the influence of CZM on the model compliance before the initiation of damage. However, the value of initial stiffness cannot be infinitely large otherwise it leads to numerical ill–conditioning. The peak traction  $t_c$

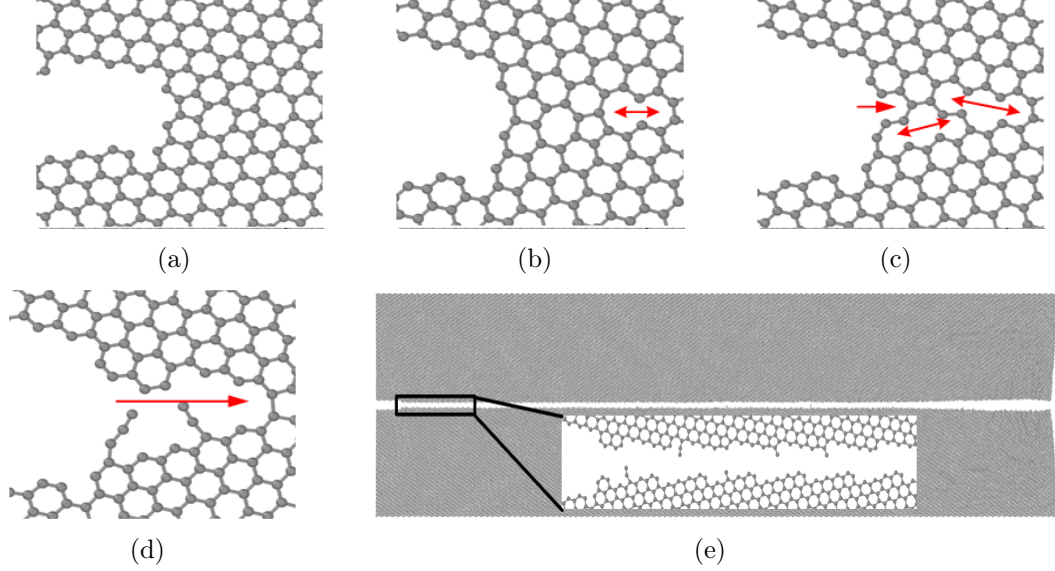


Figure 6.6: Crack propagation along the grain boundary with misorientation angle  $38.4^\circ$  with no hydrogen atoms at 300 K. (a) No strain, (b) strain of 3.23 %, (c) strain of 3.83 %, (d) strain of 4.13 % and (e) strain of 5.75 %.

represents the tensile strength of bulk material. A crack initiates when the maximum stress reaches  $t_c$ . The area under the traction–separation curve expressed by

$$S_e = \frac{1}{2} t_c \delta_f \quad (6.3)$$

represents the energy required to separate the two surfaces from each other. For the cohesive zone model to be consistent with the Griffith energetic approach for crack propagation, the area under the traction–separation curve should be equal to fracture energy  $G_c$  of the material [269, 268, 270], i.e.  $G_c = S_e$ .

#### 6.4 Computational method

The molecular dynamics simulations are conducted using LAMMPS molecular dynamics package [91]. The C–C and C–H interactions are defined using screened REBO2 (REBO2+S) potential [97] which is an improved version of reactive bond order potential (REBO). REBO2 potential is a screened environment–dependent potential which is capable of modeling fracture process in graphene accurately. For the

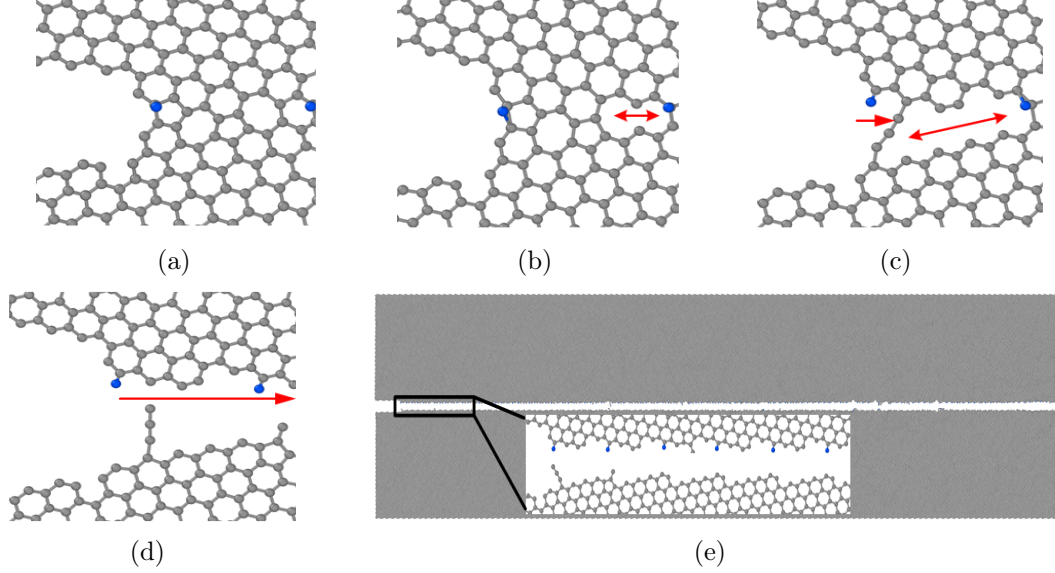


Figure 6.7: Crack propagation along the hydrogenated grain boundary with misorientation angle of  $38.4^\circ$  at 300 K. (a) No strain, (b) strain of 3.10 %, (c) strain of 3.88 %, (d) strain of 3.95 % and (e) strain of 5.48 %.

purpose of modeling crack growth the C–C bonds are considered broken when the bond length exceeds  $2.0 \text{ \AA}$ .

The equations of motion are integrated using the velocity Verlet scheme with a time step size of 0.1 fs. The initial configuration of the samples are optimized by minimizing their potential energy using the conjugate gradient technique. The sample temperature is scaled up to the desired value using the Berendsen thermostat within a time period of 5 ps followed by an equilibration stage within an NPT ensemble for about 5 ps. The model is subject to mode-I loading by applying a tensile strain in the  $y$ -direction at a rate of  $10^9 \text{ s}^{-1}$  as shown in Fig. 6.1. Each strain increment is followed by a step of equilibration within the NPT ensemble. The degrees of freedom of top and bottom layers of atoms are constrained in the  $y$  and  $z$ -directions while they are free to move in the  $x$ -direction. Images representing the atomistic structure of the bicrystalline graphene sheets are generated using the OVITO software [192].

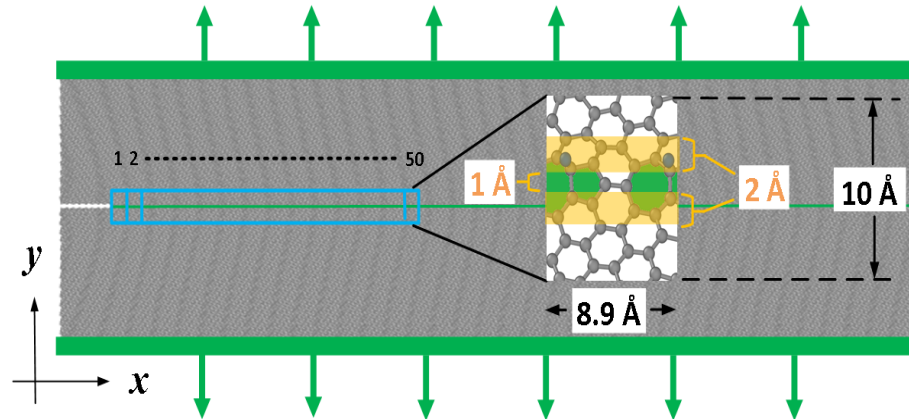


Figure 6.8: The cohesive zone elements used to extract the TSLs.

## 6.5 Results

### 6.5.1 Crack propagation

Regardless of the hydrogenation percentage of the grain boundary, the crack propagation path of the two bicrystalline structures considered in this study is along the grain boundary. Different stages of crack propagation with and without adsorbed hydrogen atoms are shown in Figures 6.4–6.7.

The crack growth along the grain boundary with misorientation angle of  $\phi_M = 21.9^\circ$  occurs by the failure of the C–C bond at the crack tip when the length of C–C bonds exceeds  $2.0 \text{ \AA}$ . As shown in Fig. 6.4b and Fig. 6.4c, the first C–C bond failure occurs at the heptagon located at the crack tip followed by the failure of the C–C bond at the pentagon. This process repeats by the failure of bonds in the next pentagon–heptagon pair until the bicrystal is split into two halves along the grain boundary, as shown in Fig. 6.4d and Fig. 6.4e. A similar trend is observed for this grain boundary when one hydrogen atom is adsorbed to each pentagon–heptagon pair as shown in Fig. 6.5. However, the strain at which the crack growth occurs is much lower than that of the same grain boundary without adsorbed hydrogen atoms.

The propagation mechanism of the crack along the grain boundary with misorientation angle of  $\phi_M = 38.4^\circ$  is shown in Fig. 6.6 and Fig. 6.7. Opposed to the previous

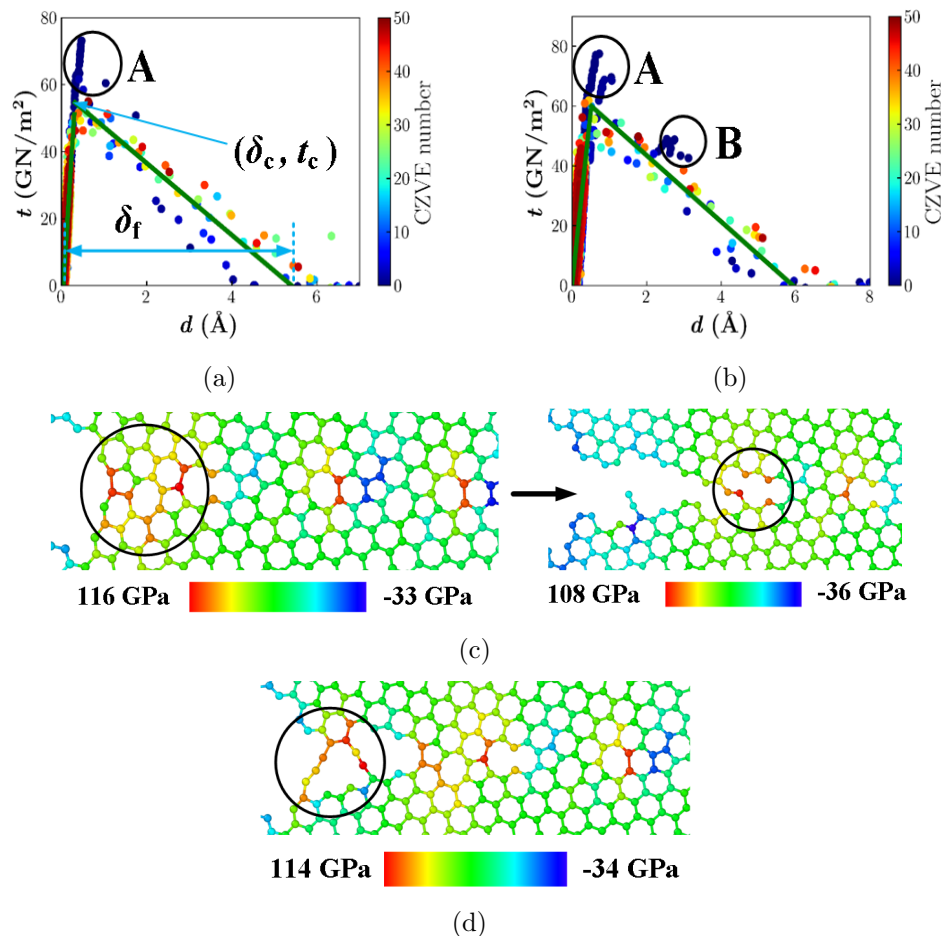


Figure 6.9: Traction–separation law of grain boundaries with no hydrogen atoms at 300 K (a) GB with  $\phi_M = 21.9^\circ$ , (b) GB with  $\phi_M = 38.4^\circ$ , (c) the stress distribution at the crack tip of the GB with misorientation angle of  $38.4^\circ$  before and after crack propagation. The stress concentration zone at the crack tip is encircled, (d) stress distribution at crack tip of the GB with misorientation angle of  $38.4^\circ$ . The chains of carbon atoms with high stresses are encircled.

case, the crack does not grow by the failure of the bond at the crack tip. Instead the bond shared between heptagon and the first hexagon ring along the grain boundary fails leading to the nucleation of a void on the grain boundary as illustrated in Fig. 6.6b. By increase in the tensile strain, more C–C bonds of the pentagon–heptagon pairs fail creating more voids of larger sizes as shown in Fig. 6.6c. Finally, the voids coalesce and the crack grows along the grain boundary as shown in Fig. 6.6d and Fig. 6.6e. A similar crack propagation mechanism is observed when one hydrogen

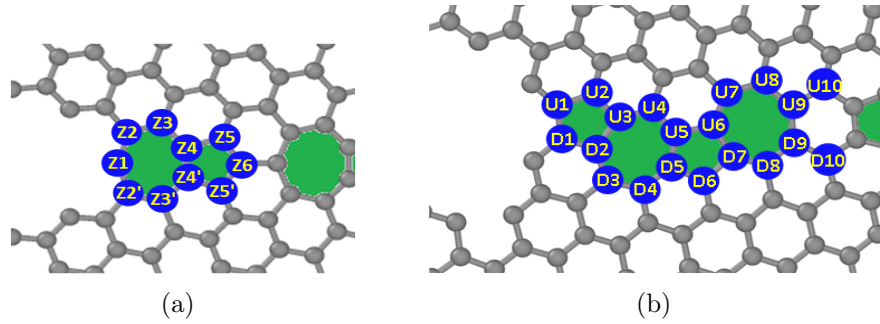


Figure 6.10: The adsorption site labels of the two GBs. a)  $\phi_M = 21.9^\circ$ , b)  $\phi_M = 38.4^\circ$ .

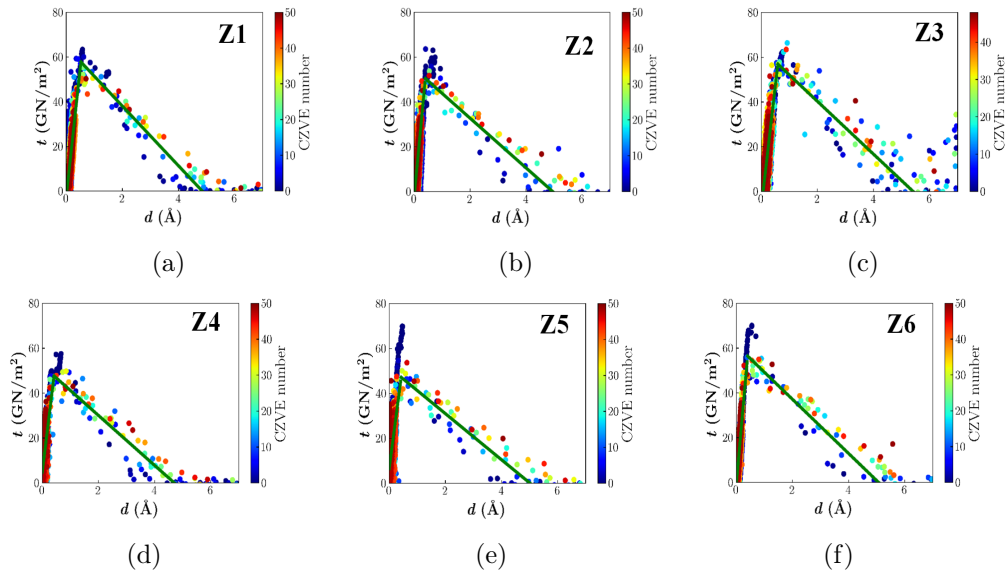


Figure 6.11: TSL of GB with misorientation angle  $21.9^\circ$  with one adsorbed hydrogen atom at 300 K. The adsorption sites are (a) Z1, (b) Z2, (c) Z3, (d) Z4, (e) Z5, (f) Z6.

atom is adsorbed to each pentagon–heptagon defect of the GB as shown in Fig. 6.7. However, for this bicrystalline sheet also the adsorption of a hydrogen atom to each pentagon–heptagon pair lowers the failure strain of the grain boundary.

### 6.5.2 Extraction of traction–separation law from MD

We follow a technique similar to the one proposed by Yamakov et al [259] to extract the traction–separation laws from the MD simulations. In this methodology the crack propagation path should be known a priori and a layer of atoms in the vicinity of the crack propagation path is used to extract the traction–separation laws. Since the crack propagation path of the two bicrystalline structures studied in this chapter is

along the grain boundary, a narrow horizontal layer of atoms ahead of the crack tip with height of  $\delta_y$  centered at the grain boundary line are employed to extract the cohesive laws. This horizontal layer is divided into bins with width of  $\delta_x$  as shown in Fig. 6.8. Each of the bins is known as a cohesive zone volume element (CZVE) and the atoms located within a CZVE in the reference domain are assigned to that element.

The virial formulation can be used to calculate the continuum stress from the MD simulations using Eq. (1.17). In Eq. (1.17),  $V^a$  is the volume of atom  $a$  in the reference configuration. For pristine graphene  $V^a = \frac{3\sqrt{3}}{4}r^2t$  where  $r = 1.42 \text{ \AA}$  is the C–C bond length and  $t$  is the thickness of graphene which is taken equal to  $3.35 \text{ \AA}$ .

The virial stress becomes equivalent of the Cauchy stress in the limit of time and volume averages [271, 272]. Thus, the stress of the  $n^{\text{th}}$  cohesive zone volume element is obtained by time and volume averaging of the atomic stresses belonging to the CZVE

$$\sigma^n = \frac{1}{N_t V^n} \sum_{t=1}^{N_t} \sum_{i=1}^N V^a \sigma^a(t) \quad (6.4)$$

where  $N$  is the number of atoms in the  $n^{\text{th}}$  cohesive zone volume element,  $V^n = NV^a$  is the volume of CZVE,  $N_t = 2500$  is the number of time steps at an interval of 0.25 ps over which the time averaging is conducted.

The non-zero component of the traction of each CZVE acting on the crack propagation path is calculated by calculating the  $y$ -component of stress from Eq. (6.4). The separation distance is calculated using the distance between centroids of upper and lower portions of CZVEs. For this purpose, the distance  $d_i$  between the  $y$  components of the centroids of each CZVE portions shown in the orange color in Fig. 6.8 is evaluated after every 0.25 ps. Separation distance  $d$  is given by  $d_i - d_0$  where  $d_0$  is the separation distance between  $y$  components of centroids before applying the strain. Similar to stresses, the separation distance is calculated by averaging over 2500 time steps.

Considering the high stress gradient in the vicinity of crack tip, the size of the CZVE should be small enough to capture the stress gradients. On the other hand, the size of CZVE should be large enough to ensure that the virial stress averaged over the CZVE converges to the Cauchy stress. In this chapter, the dimensions of the cohesive zones are  $\delta_y = 1$  nm and  $\delta_x = 0.89$  nm [261]. The height  $\delta_y$  is large enough to enclose the prestress field generated by the pentagon–heptagon defects. Using Hillerborg *et al.* [267] definition, the length of the cohesive zone of graphene is estimated to be 2.6 nm [261]. Therefore,  $\delta_x = 0.9$  nm is equivalent to having approximately three CZVE in the cohesive zone which is enough to resolve the stress gradient. The length  $\delta_x$  of CZVE affects the value of maximum traction  $t_c$  while does not impact the separation energy  $S_e$ . Since  $t_c$  represents the maximum stress sustainable by the grain boundary before a crack initiates, the value of  $\delta_x$  should be chosen such that the obtained value of  $t_c$  is consistent with the strength of grain boundary before defect. The chosen value of 8.9 Å for  $\delta_x$  is shown to satisfy this criterion [261].

### 6.5.3 Traction separation law of grain boundaries with no hydrogen atoms

The traction–separation points obtained using 50 CZVEs dispersed along the grain boundaries without any adsorbed hydrogen atoms at 300 K are shown in Fig. 6.9. It can be observed that with increase in the separation distance between the upper and lower halves of each CZVE the cohesive traction increases linearly until it reaches its peak value  $t_c$  after that it decreases linearly until it vanishes at separation  $\delta_f$ . The data points in Fig. 6.9 suggest that the traction–separation law is linear for this grain boundary. Two linear curves are fitted separately to the data, one before  $t_c$  and one after it, as shown in Fig. 6.9. The two curves meet at the traction  $t_c$ .

As shown in Fig. 6.9a and b, the traction of points in circle A exceeds  $t_c$ . This is due to the high atomic stress concentration at the crack tip before crack propagation occurs, as shown in Fig. 6.9c. The traction of points in circle B as shown in Fig. 6.9b is higher than the traction of other points with the same separation. This is due

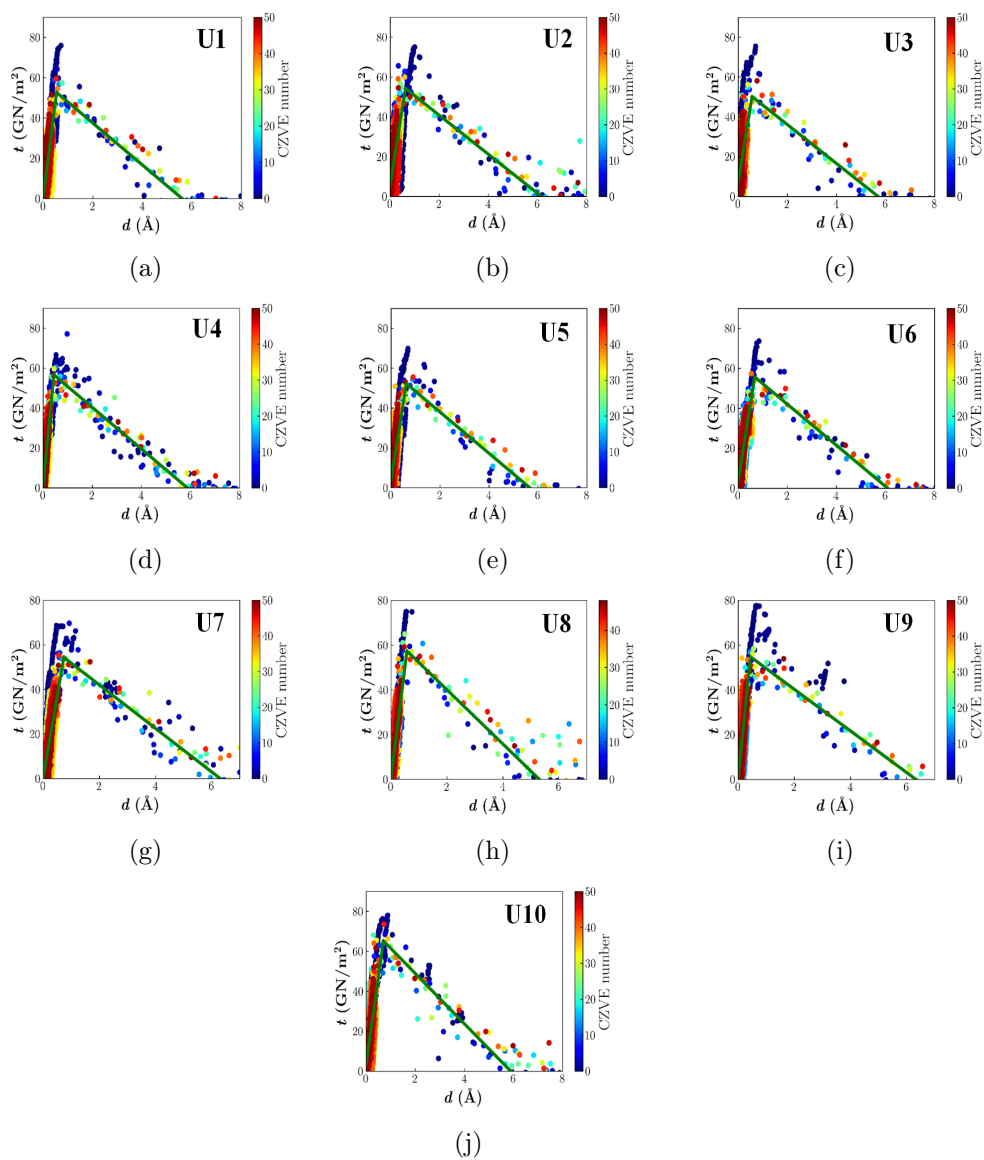


Figure 6.12: TSL of GB with  $\phi_M = 38.4^\circ$  with one adsorbed hydrogen atom at 300 K. The adsorption sites are (a) U1, (b) U2, (c) U3, (d) U4, (e) U5, (f) U6, (g) U7, (h) U8, (i) U9, (j) U10.

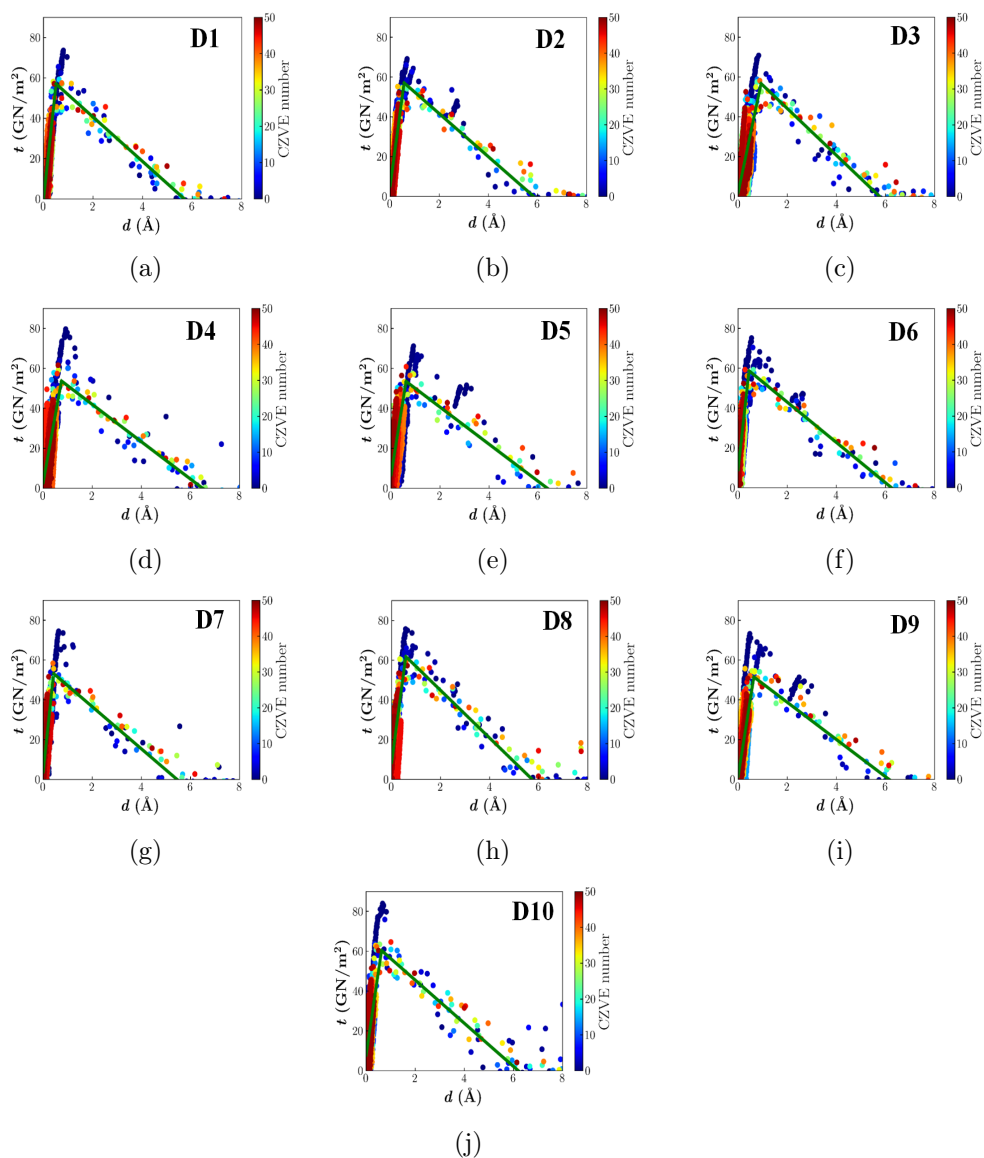


Figure 6.13: TSL of GB with  $\phi_M = 38.4^\circ$  with one adsorbed hydrogen atom at 300 K. The adsorption sites are (a) D1, (b) D2, (c) D3, (d) D4, (e) D5, (f) D6, (g) D7, (h) D8, (i) D9, (j) D10.

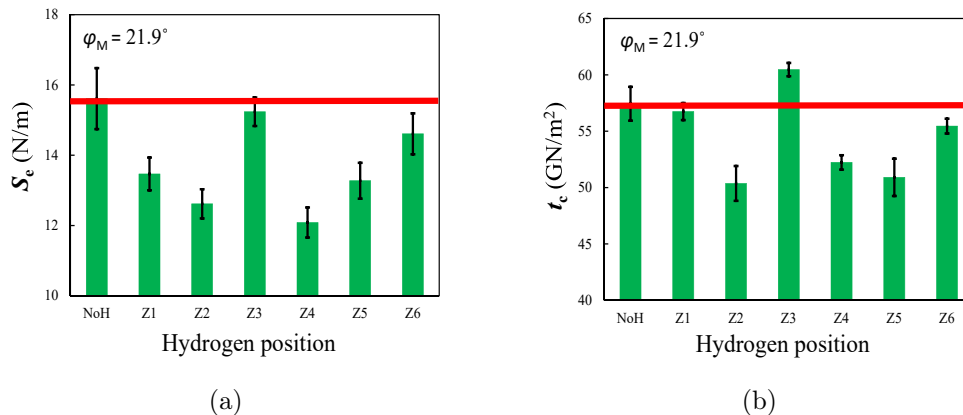


Figure 6.14: (a) Separation energy and (b) maximum traction of GB with misorientation angle of  $21.9^\circ$  as a function of hydrogen adsorption site.

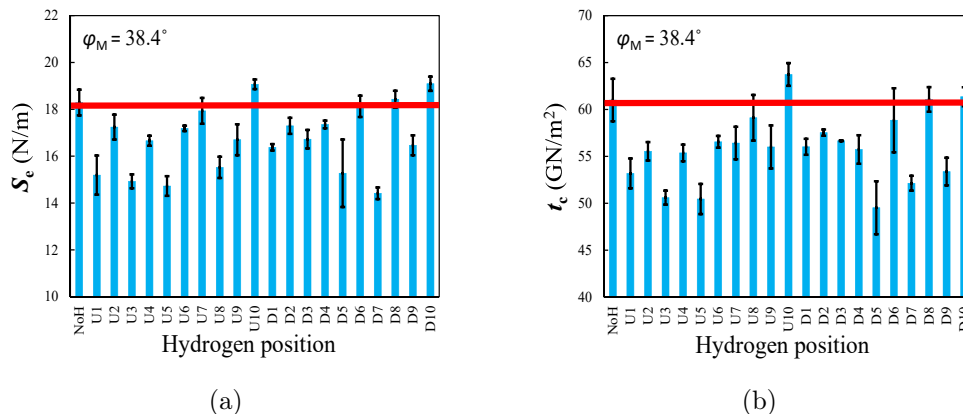


Figure 6.15: (a) Separation energy and (b) maximum traction of GB with misorientation angle of  $38.4^\circ$  as a function of a hydrogen adsorption site.

to the formation of chains of carbon atoms between the upper and lower halves of the cohesive zones as shown in Fig. 6.9d. The formation of these chains demands a higher stress for the crack to grow which appears as higher traction point in the traction–separation curves.

The values of  $t_c$ ,  $\delta_c$  and  $\delta_f$  for the two grain boundaries studied in this chapter are presented in Table 6.1. It can be observed that  $t_c$ ,  $\delta_c$  and  $\delta_f$  are higher for the grain boundary with misorientation angle  $38.4^\circ$ .

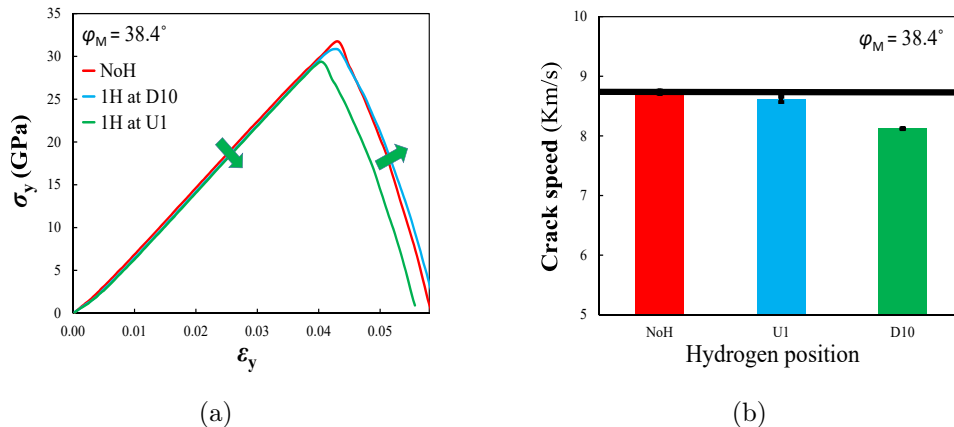


Figure 6.16: (a) Stress–strain plots and (b) crack velocities of GB with misorientation angle of  $38.4^\circ$  with and without an adsorbed hydrogen atom.

Table 6.1: Key parameters of TSL of grain boundaries with misorientation angle  $21.9^\circ$  and  $38.4^\circ$

$\phi_M$	$\delta_c$	$\delta_f$	$t_c$
$21.9^\circ$	$0.319 \pm 0.013$	$5.43 \pm 0.18$	$57.44 \pm 1.50$
$38.4^\circ$	$0.516 \pm 0.027$	$6.01 \pm 0.35$	$61.00 \pm 2.26$

#### 6.5.4 Impact of hydrogen adsorption site

The influence of hydrogenation of grain boundaries on the mechanical properties of graphene has been studied before [237, 273]. In this chapter, the impact of hydrogen adsorption site on the traction–separation law of each grain boundary is studied. For this purpose, the cohesive law of the grain boundaries when one hydrogen atom is adsorbed to each repeating pentagon–heptagon defects at 300 K is derived.

The hydrogen adsorption sites along the grain boundaries are labeled in Fig. 6.10. The repeating unit cell of the grain boundary with misorientation angle of  $21.9^\circ$  includes only one pentagon–heptagon pair. Due to its symmetry, six different adsorption sites are examined for this grain boundary. On the other hand, two pentagon–heptagon pairs exist in the unit cell of the grain boundary with misorientation angle of  $38.4^\circ$ . Due to the lack of symmetry, we examine the adsorption of hydrogen atoms to all the carbon atoms of both pentagon–heptagon defects. The traction–separation

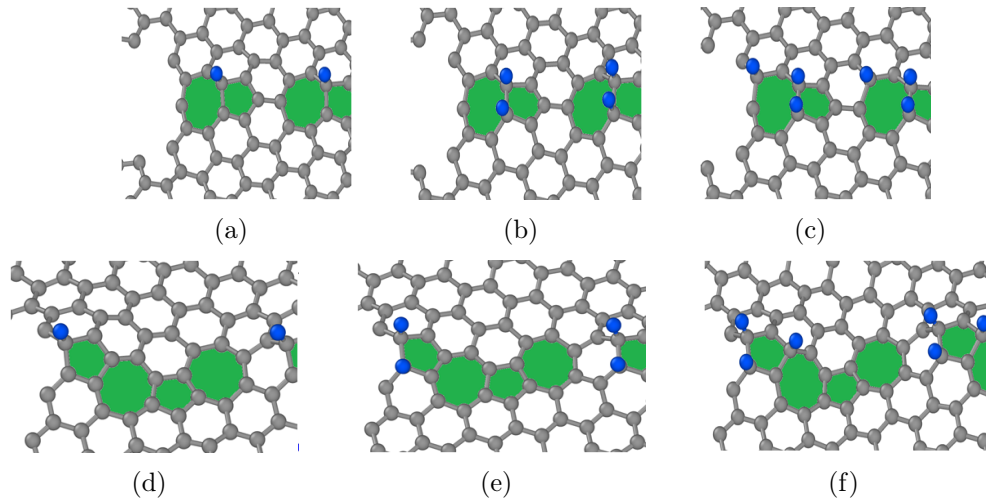


Figure 6.17: The adsorption site of hydrogen atom along the GB when the number of hydrogen atoms increases from one to three. (a–c) GB with misorientation angle of  $21.9^\circ$ , (d–f) GB with misorientation angle of  $38.4^\circ$ .

laws obtained for the grain boundary with misorientation angle of  $21.9^\circ$  is plotted in Fig. 6.11 whereas for the grain boundary with misorientation angle of  $38.4^\circ$  is plotted in Figures 6.12 and 6.13. The maximum traction and the fracture energy of each TSL is extracted and the results are compared with those obtained from pristine grain boundaries in Figures 6.14 and 6.15. It can be observed that in general the adsorption of a hydrogen atom reduces both the fracture strength  $t_c$  and fracture energy of the grain boundary. Therefore, the adsorption of a hydrogen atom leads to embrittlement of the grain boundary.

Based on the graphs of Fig. 6.14, for the grain boundary with misorientation angle of  $21.9^\circ$ , a hydrogen adsorption at the Z3 carbon atom does not significantly impact the fracture strength and energy of the grain boundary while hydrogen adsorption to all the other atoms lead to a reduction in the fracture energy of the grain boundary. This is because these atoms are attached to load carrying bonds and when a hydrogen atom is adsorbed to these atoms the bonds attached to them are stretched, hence these bonds fail more easily under the tensile stress.

The graphs in Fig. 6.15 show that a significant reduction in strength and fracture

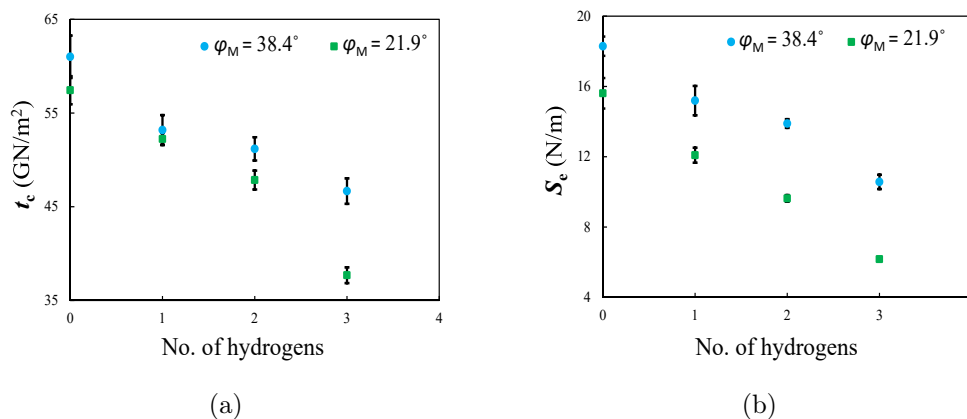


Figure 6.18: Effect of hydrogen concentration on the (a) strength and (b) separation energy of grain boundaries at 300 K.

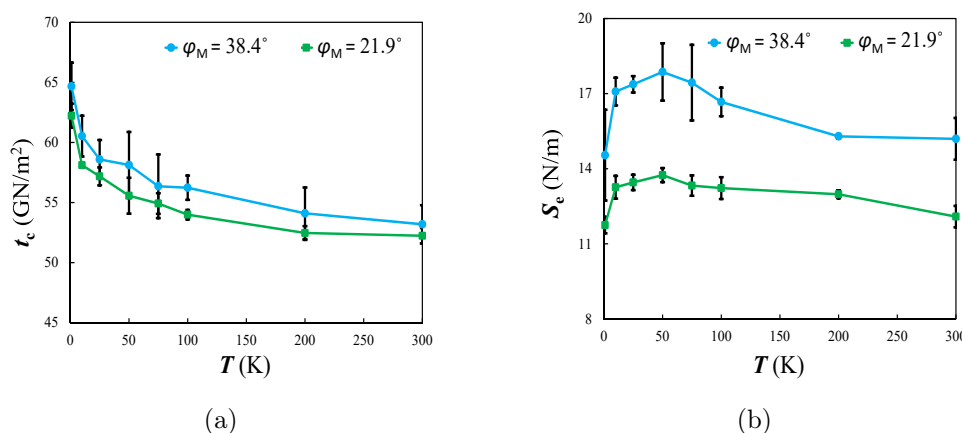


Figure 6.19: Impact of temperature on the (a) strength and (b) separation energy of GBs.

energy of the grain boundary with misorientation angle of  $38.4^\circ$  occurs when a hydrogen atom is adsorbed at U1, U3, U5, D5 and D7. These sites are all attached to critical load carrying bonds and an attachment of hydrogen atom causes these bonds to fail more easily. Although the adsorption of hydrogen atom to other atoms of the pentagon–heptagon pair also reduce the toughness and strength of GB, the adsorption of hydrogen atom to the U10 and D10 sites, which are the two atoms on the grain boundary not connected to pentagon–heptagon pairs, counter intuitively leads to a slight increase in the strength and fracture toughness of the grain boundary. To understand this behavior the stress–strain plots of this grain boundary with no

adsorbed hydrogen, one hydrogen adsorbed at D10 and one hydrogen adsorbed at U1 atom are plotted in Fig. 6.16a. The stress–strain plots clearly shows that the stiffness and strength of bicrystalline graphene sheet with a hydrogen atom at U1 is lower than those of bicrystalline sheet with no hydrogen atom. However, the adsorption of hydrogen atom at D10 has a negligible effect on the strength of the bicrystalline sheet. The crack growth speed of these three cases are shown in Fig. 6.16b. As shown, the crack speed of bicrystalline sheet with a hydrogen atom at U1 is close to that of bicrystalline sheet with no adsorbed hydrogen atom. On the other hand, the adsorption of hydrogen atom at D10 significantly reduces the crack speed. The lower crack speed gives time for the atomic stresses to build up in the vicinity of crack tip leading to a higher traction at the same separation distances. This in turn results in higher  $t_c$  and fracture toughness.

#### 6.5.5 Hydrogen concentration at the grain boundary

The effect of hydrogen concentration on the TSL is studied by increasing the number of hydrogen atoms per pentagon–heptagon pair from one to three. The hydrogen adsorption sites of the two grain boundaries are shown in Fig. 6.17. The chosen sites are those that have a more significant embrittlement effect based on the results of the previous section. As shown in Fig. 6.18, with increase in the hydrogen concentration the maximum traction and fracture energy decreases. The increase in the number of hydrogen atoms leads to a reduction of the fracture energies by 60% and 42% for GBs with  $\phi_M = 21.9^\circ$  and  $\phi_M = 38.4^\circ$ , respectively. These results show that hydrogen embrittlement can be severe in both grain boundaries studied in this chapter and can significantly reduce the strength and fracture energy of grain boundaries.

#### 6.5.6 Temperature

The impact of hydrogen on the strength and toughness of the GBs when one hydrogen atom is adsorbed per a pentagon–heptagon pair as shown in Fig. 6.17a and

d is studied. The temperature range studied is from 1 K to 300 K. The graphs of Fig. 6.19 show that with increase in the temperature the maximum traction uniformly decreases. The strength of both GBs at 300 K is smaller than that at 1 K. On the other hand, the graphs of Fig. 6.19b indicate that with increase in temperature the separation energy first increases and reaches its maximum at about 50 K and then decreases. With increase in temperature from 1 K to 300 K fracture strength decreases whereas critical separation increases. The interplay between these effects leads to the observed trend of separation energy, as illustrated in Fig. 6.19b. The fracture energy at 300 K is higher than that at 1 K, indicating that the grain boundaries are more ductile at the room temperature.

## 6.6 Conclusion

We have used molecular dynamics simulations to study how the adsorption of hydrogen atoms on the grain boundaries impact their fracture properties. We have extracted the traction–separation laws from molecular dynamics simulations for two high angle symmetric grain boundaries with and without adsorbed hydrogen atoms. The results show that in general the adsorption of hydrogen atom leads to a reduction in the strength and toughness of grain boundaries. The level of impact depends on the adsorption site. The impact is significantly higher if the adsorption site is attached to a critical load carrying bond. By increase in the number of hydrogen atoms the strength and fracture energy of the grain boundaries decrease significantly indicating that hydrogen embrittlement occurs in graphene grain boundaries. The impact of temperature on the strength and toughness of hydrogenated GBs were studied. The molecular dynamics results showed that by increase in the temperature the strength of GBs reduces, while the toughness first increases and then decreases.

## CHAPTER 7: Mechanical and Fracture properties of the polycrystalline graphene with hydrogenated grain boundaries

### 7.1 Introduction

Graphene multifunctionality which combines excellent properties such as large modulus of elasticity of 1 TPa [9, 10, 11, 12], high electron mobility in the room temperature ( $250,000 \text{ cm}^2 \text{ V}^{-1}\text{s}^{-1}$ ) [16], high thermal conductivity ( $5000 \text{ Wm}^{-1}\text{K}^{-1}$ ) [14], and large surface area of  $2630 \text{ m}^2/\text{g}$  [274] has made this 2D-atomic crystal an attractive material for use in a wide range of applications. The potential applications include electromechanical systems [31, 32, 33], electronics [275, 276], solar cells [277, 278, 279], hydrogen storage [280, 281], advanced composites [26, 27, 28, 29, 30], field-effect transistors [19, 20, 21], and supercapacitors [22, 23, 24, 25].

In addition to its intrinsic properties, another remarkable characteristic of graphene is its tunability. Different techniques including strain engineering [282, 283, 284, 285, 286], defect engineering [287, 288, 289, 290, 291, 150], chemical functionalization [292, 293, 294, 295, 296], and grain boundary engineering [297, 298, 299] are proposed to tune various properties of graphene such as its thermal conductivity [287, 300, 301, 302, 256, 303, 304, 305, 306, 307], electrical conductivity [308, 309, 310, 311], mechanical strength [312, 297, 313, 314, 315, 273, 316, 12, 317], fracture properties [119, 318, 4, 319, 320, 321, 5], and thermoelectrical properties [322, 323, 324, 325]. The most versatile tuning technique is functionalization the surface of graphene by the attachment of functional groups. This technique has become a focus of interest for manipulating the physical and chemical properties of graphene. For example, oxygen adsorption can significantly modify the thermoelectric properties of graphene [326, 327] and metal adatom deposition can induce a significant spin-orbit coupling

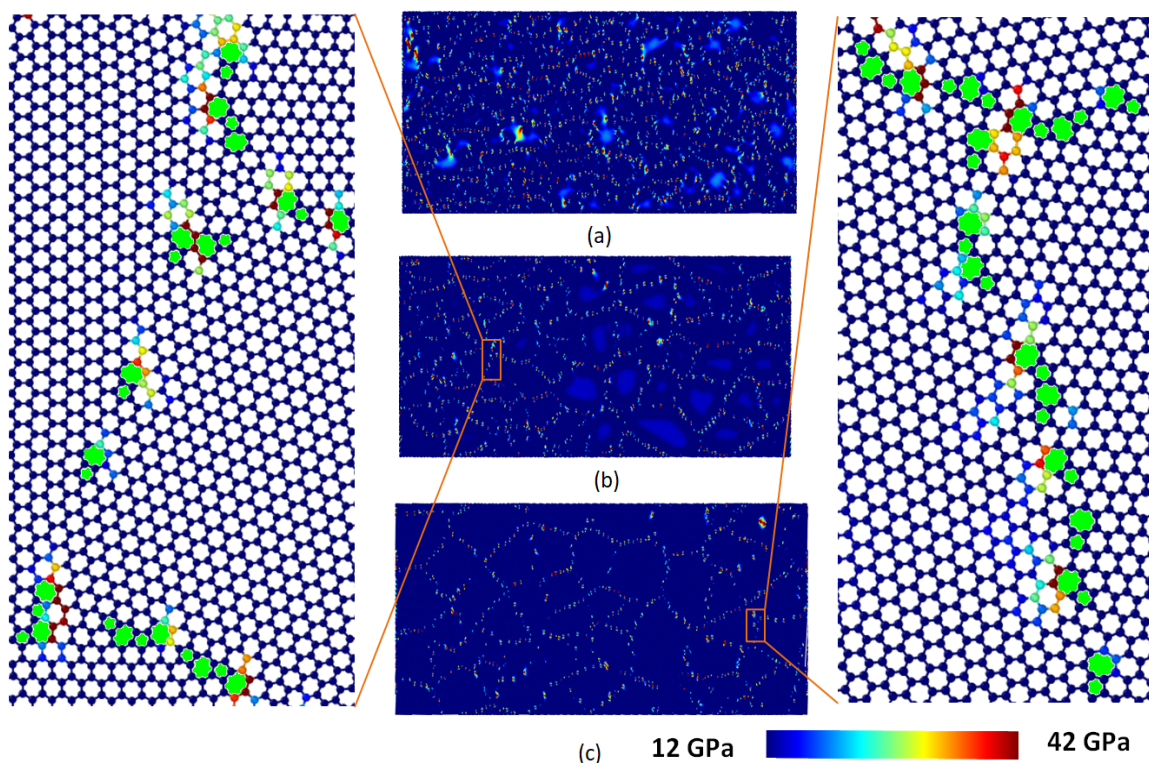


Figure 7.1: Polycrystalline graphene sheets with different grain sizes. (a) 4 nm (b) 6 nm, and (c) 8 nm.

in graphene [328, 329, 330].

Among various functional groups, hydrogen is of special interest. Hydrogen forms a covalent bond with a single carbon atom and induces a resonant impurity state around graphene Dirac point [331, 332]. This can significantly impact the electronic transport properties of graphene as is indicated by studying the impact of hydrogen density on the metal-insulator transition [333]. Experimental work has shown that localized magnetic moments are created around hydrogen impurities which can be important for graphene spintronics [334]. The high surface area of graphene has also made graphene a potential material for the development of an efficient solid-state hydrogen storage device.

In addition to intentional functionalization of graphene surface with hydrogen atoms, abundant presence of hydrogen atoms in the environment exposes graphene sheets to hydrogen molecules which can lead to the adsorption of hydrogen atoms to

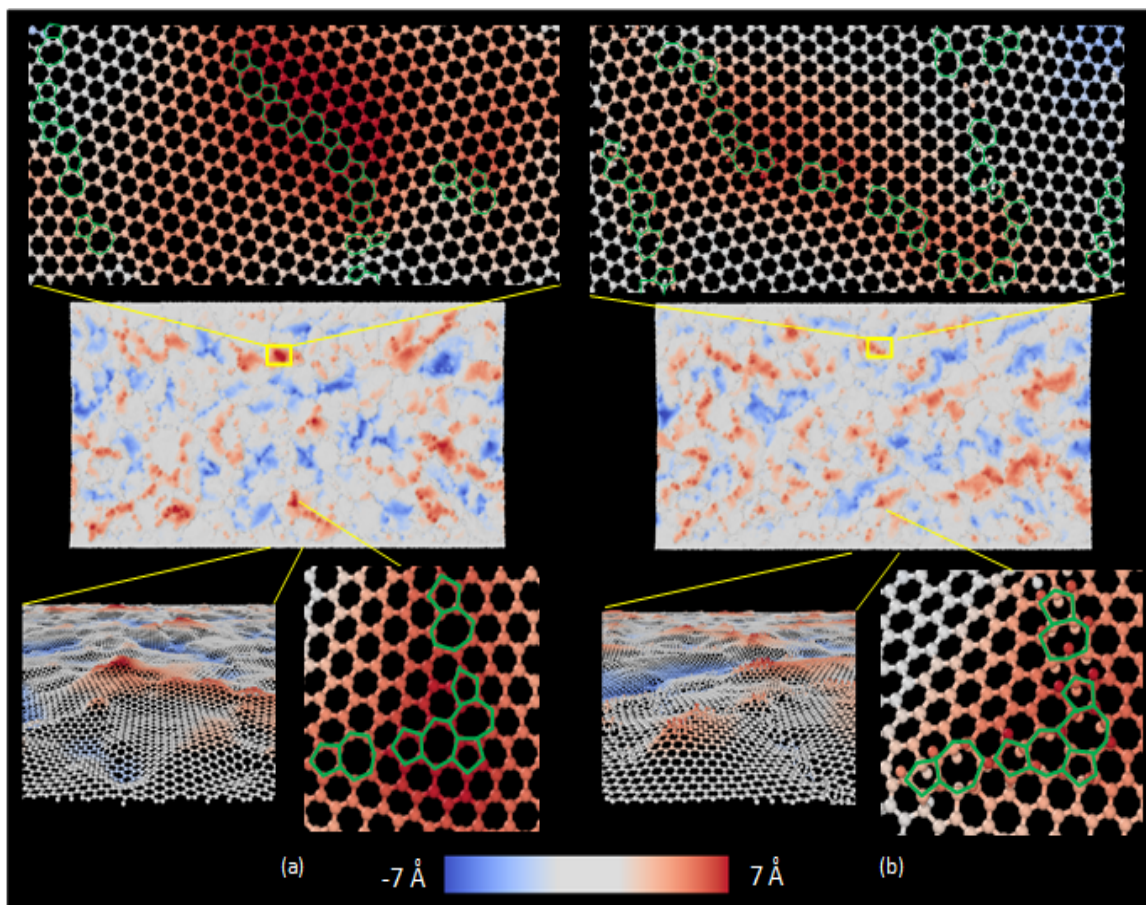


Figure 7.2: A polycrystalline graphene sheet with an effective grain size of 4 nm after the annealing process. The contour plot represents the out of plane deformation of atoms. a) Graphene sheet without hydrogenation, b) graphene sheet with 100% hydrogenation of grain boundary atoms.

the graphene surface. The presence of defect sites such as Stone–Wales defects, grain boundaries, vacancies, wrinkles, and sheet edges facilitate the physisorption of hydrogen atoms. The adsorption of hydrogen atoms to the graphene surface can alter the mechanical and fracture properties of graphene. Most of the studies on fracture and mechanical properties of hydrogenated graphene are limited to single grain graphene sheets [119, 335, 336, 337]. The impact of hydrogen adsorption on mechanical fracture properties of polycrystalline graphene with grain boundaries containing mostly Stone–Wales defects remain almost unexplored.

The large graphene sheets produced in industrial scales are polycrystalline sheets

composed of graphene grains seamed together at the grain boundaries. In polycrystalline graphene, the grain boundaries between misoriented grains are composed of a series of pentagon–heptagon rings (Stone–Wales defects) [81, 338, 233, 5]. Due to such defects, the properties of the polycrystalline graphene are different from the pristine graphene. Previous studies have investigated the thermal [339, 340, 341], mechanical [342, 222, 298], and fracture properties [343, 344, 19] of polycrystalline graphene and the impact of grain boundaries on properties of polycrystalline graphene.

The presence of pentagon–heptagon defects makes grain boundaries chemically more active than pristine graphene. Grain boundaries act as favorable adsorption sites for environmental atoms such as hydrogen atoms. Understanding the effect of hydrogen adsorption at grain boundaries on the mechanical, and fracture properties of polycrystalline graphene sheets is necessary for reliable use of polycrystalline graphene sheets in nanodevices. In this paper, we use molecular dynamic modeling to study the fracture properties of polycrystalline graphene when hydrogenation is confined to the grain boundaries. Considering the difficulties of conducting experiments at nanoscales, molecular dynamic modeling provides an invaluable tool to study phenomena occurring at short time and length scales [345, 146, 114, 171, 2, 346, 3, 347, 1, 222, 117, 348, 151, 220]. By conducting molecular dynamics on both pre–cracked and pristine polycrystalline graphene sheets, we investigate the effect of hydrogenation on both the mechanical and fracture properties of graphene sheets. The impact of polycrystalline grain size is also studied by considering polycrystalline sheets with different average grain sizes.

## 7.2 Polycrystalline graphene sheet

### 7.2.1 Generation

We have constructed polycrystalline graphene sheets with dimensions of 80 nm  $\times$  40 nm. The effective grain size  $l_e$  of the polycrystalline sheet is equal to  $\sqrt{\frac{A}{n_g}}$  where  $A$  is the surface area of the sheet and  $n_g$  is the number of grains in the sheet. We

have considered polycrystalline graphene sheets with average grain sizes of 4 nm, 6 nm, and 8 nm as illustrated in Fig. 7.1.

Experimental observations have indicated that the grain boundaries in graphene are mainly composed of pairs of 5 and 7 carbon atom rings [81, 338]. These pentagon–heptagon defects represent edge dislocation cores and have a low formation energy [233, 349]. In order for an atomistic model to be accurate, the atomic structure of the model should be similar to the experimental observations, e.g. the grain boundaries must be composed of mostly pentagon–heptagon defects. Constructing a polycrystalline sheet with grain boundaries composed mostly of pentagon–heptagon defects is challenging. Many previous studies on polycrystalline graphene were conducted by deviating from this motif by including voids and non pentagon–heptagon defects in the grain boundaries [342, 350, 90, 237].

The polycrystalline structure of multigrain graphene sheets is generated using the algorithm proposed in the previous study [344]. Using this algorithm, any two neighboring grains with different crystal misorientation are connected by a lattice that is composed by hexagon, pentagon, and heptagon defects and other kind of defects are not observed on the grain boundaries. In this methodology, the centers of each grain are randomly assigned and the boundary of each grain is chosen by constructing the Voronoi diagram associated with the grain centroids. A random crystalline orientation is also assigned to each grain. This leads to the generation of a structure with random misorientation angles varying from  $0^\circ$  to  $60^\circ$  between every two neighboring grains. The arrangement of carbon atoms in grains and along the grain boundaries are obtained by first generating a triangular lattice dual to the graphene lattice and then using centroidal Voronoi tessellation [351] to relax the atom positions along the grain boundaries. The grain boundaries obtained at this stage are made up of only pentagon–heptagon pairs (Stone–Wales defects). The position of the atoms are fine tuned by minimizing the energy of system using the conjugate gradient

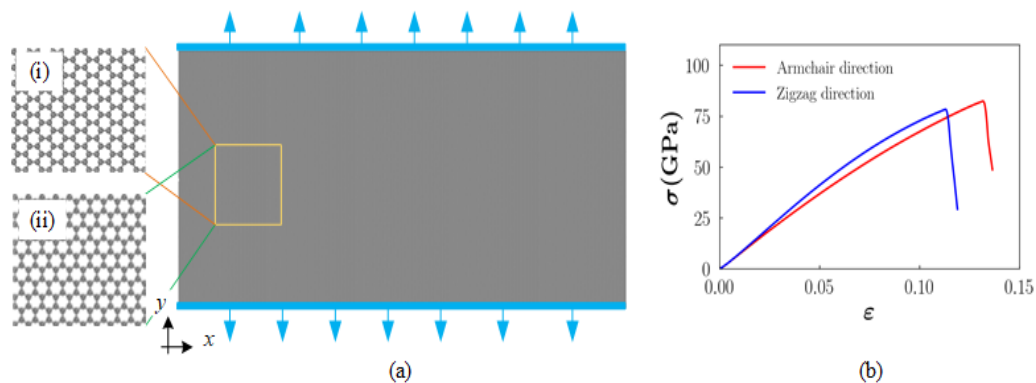


Figure 7.3: (a) Tensile loading on single crystal uncracked graphene sheet (i) grain oriented in armchair direction and (ii) grain oriented in zigzag direction, (b) stress-strain plots of the single crystal uncracked graphene sheets.

method and subjecting the polycrystalline graphene sheet to an annealing process. During annealing the polycrystalline graphene sheets are heated in such a way that the crystalline part of the sheet is unaffected but the grain boundary regions are allowed to break and reform C–C bonds. After cooling down, the polycrystalline sheet has a more stable structure at a lower energy [352] with grain boundaries composed of only pentagon–heptagon defects separated by hexagonal rings, as shown in Fig. 7.2.

The annealing process is conducted using the molecular dynamics by employing LAMMPS molecular dynamics package [91]. The REBO2 (REBO2+S) potential has been employed to describe C–C and C–H interactions [97]. REBO2 is a more advanced version of REBO potential which is capable of accurately modeling the fracture process in graphene sheet. Equations of motion of the system are integrated through velocity–Verlet algorithm with a time step size of 0.1 fs. The initial structure of graphene sheet is optimized by employing the conjugate gradient technique. The system is heated up to 250 K using Berendsen thermostat within a time period of 1 ps followed by equilibration within NPT ensemble for another 1 ps. Here on wards the heating and quenching is conducted within NPT ensemble. The graphene sheet temperature is increased up to 2500 K in steps of 250 K and each step lasts for a time period of 2 ps. After the heating stage, the system is quenched to 1 K for 15 ps.

Finally the system is further equilibrated at 1 K for a period of 10 ps. An Example of a polycrystalline graphene sheet obtained after the annealing process is shown in Fig. 7.2a. As can be seen, polycrystalline graphene is not a flat sheet and the presence of grain boundaries lead to out of plane deformation of graphene sheet.

After the annealing process, the grain boundaries are hydrogenated. Carbon atoms which act as adsorption sites are chosen randomly among the atoms of the pentagon–heptagon defects. Polycrystalline sheets with various grain boundary hydrogenation percentage between zero to hundred percent are generated; at zero percentage no carbon atom attached to pentagon–heptagon defects is hydrogenated while at 100 percent all the atoms of pentagon–heptagon defects are hydrogenated. The adsorption of hydrogen atoms changes the morphology of graphene sheet as is shown in Fig. 7.2b where the contour plot represents the out–of–plane deformation of the graphene sheet.

In this paper, to take into account the randomness of the polycrystalline structure, three polycrystalline graphene sheets are created for each grain size. Also, to take into account the randomness of the hydrogen adsorption sites, for each hydrogenation percentage three hydrogenated sheets are created for each of the polycrystalline sheets. The results reported for each grain size are the average of these nine simulations.

### 7.3 Tensile loading

After preparing the initial structure of graphene sheet, the temperature of the model is increased to 300 K. The graphene sheet temperature is scaled up to 300 K by using Berendsen thermostat within a time period of 5 ps. The system is equilibrated within an NPT ensemble for 5 ps at 300 K.

The graphene sheet is subjected to a tensile strain in the  $y$ –direction. To apply tensile loading on the graphene sheet, a few layers of atoms in the top and bottom edges are constrained in the  $y$  and  $z$ –directions while they are allowed to move in the  $x$ –direction. The tensile strain is applied in the  $y$ –direction in increments of  $10^{-7}$ . Each step of strain increment is accompanied by a step of NPT equilibration for 0.1 fs

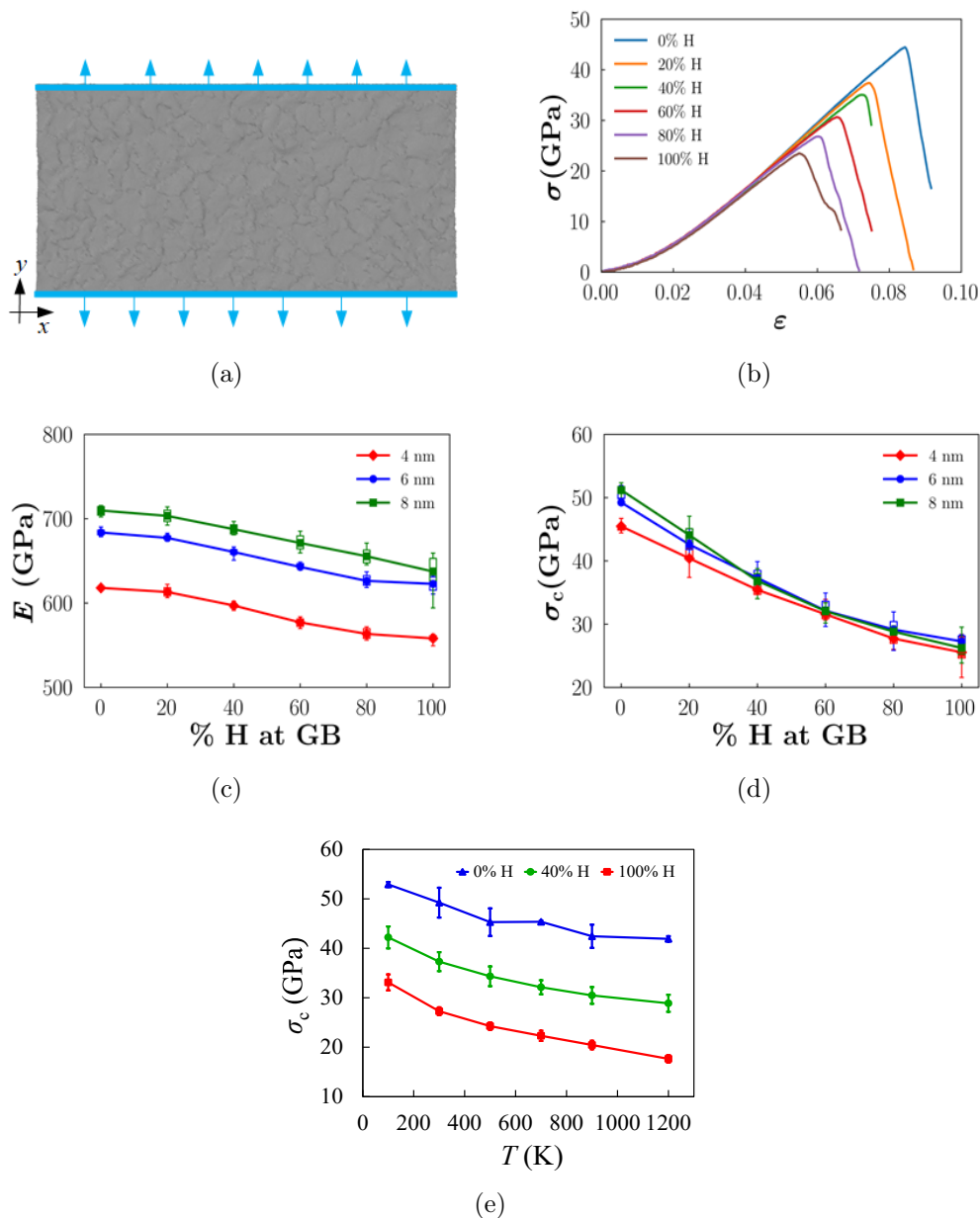


Figure 7.4: (a) A polycrystalline graphene sheet under tensile loading, (b) The stress–strain plot of a polycrystalline graphene with effective grain size 4 nm and hydrogen concentration ranging from 0 to 100% at 300 K, (c) Young’s modulus of polycrystalline graphene sheet, (d) strength of polycrystalline graphene sheet versus grain boundary hydrogen concentration, and (e) impact of temperature on the strength of polycrystalline graphene sheet with average grain size 6 nm.

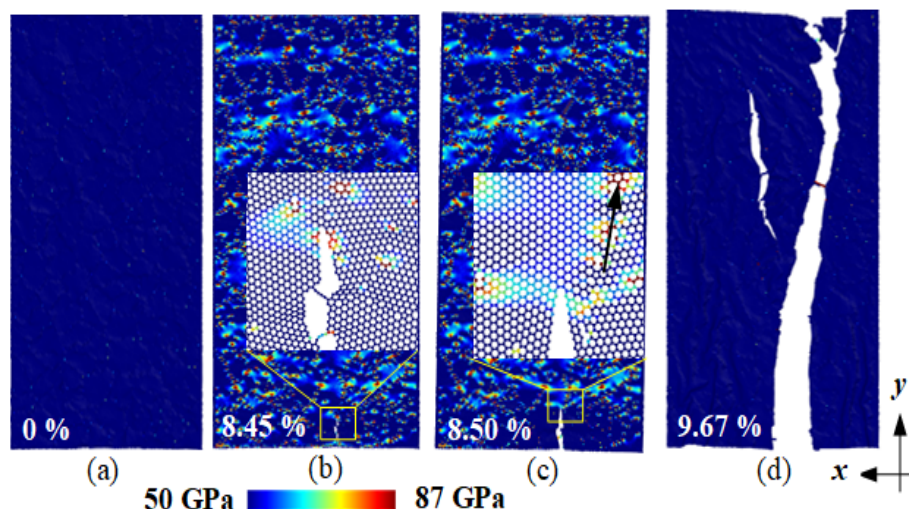


Figure 7.5: Crack initiation and propagation in a polycrystalline graphene with average grain size 4 nm without hydrogenation. The image illustrates polycrystalline graphene sheet at (a) 0%, (b) 8.45%, (c) 8.50%, and (d) 9.67% strain (black arrow shows the direction of grain boundary).

which leads to a strain rate of  $10^9 \text{ s}^{-1}$ . In order to reduce the stress in the  $x$ -direction to zero, the graphene sheet is allowed to relax in the  $x$ -direction during the NPT equilibration. The loading is applied until cracks are developed and propagate in the graphene sheet by the failure of C–C or C–H bonds along the fractured surfaces. The virial stress is used to calculate the continuum stress from the MD simulations using Eq. (1.17).

## 7.4 Results

### 7.4.1 Mechanical properties

Molecular dynamic simulations are used to obtain the stress–strain relations of pristine graphene. Tensile loading is applied in the  $y$ -direction of uncracked pristine graphene sheets as shown in Fig. 7.3a. The stress–strain curves of the pristine graphene sheet are shown in Fig. 7.3b. When the loading is applied in the zigzag direction, the Young’s modulus and failure strength of graphene are predicted respectively to be  $853.3 \pm 0.9 \text{ GPa}$ , and  $79.7 \pm 1.3 \text{ GPa}$ . On the other hand, if the loading is applied in the armchair direction, the Young’s modulus and failure strength are  $750.6$

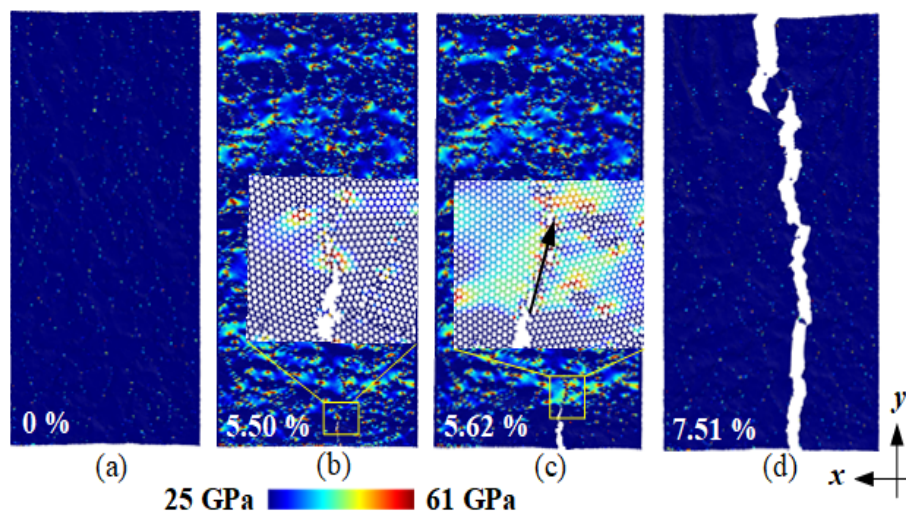


Figure 7.6: Crack initiation and propagation in a polycrystalline graphene sheet with average grain size 4 nm with 100% hydrogenation of its grain boundaries. The image illustrates polycrystalline graphene sheet at (a) 0%, (b) 5.50%, (c) 5.62%, and (d) 7.51% strain (black arrow shows the direction of grain boundary).

$\pm 0.4$  GPa, and  $81.3 \pm 1.3$  GPa, respectively. Similar results have been reported by the previous studies which employed MD simulations [353, 354, 355].

In the first set of simulations, uncracked polycrystalline sheets are subjected to tensile loading as shown in Fig. 7.4a. Polycrystalline sheets with three grain sizes of 4 nm, 6 nm, and 8 nm are considered. The hydrogen concentration on the grain boundaries varies from 0 to 100%. The stress–strain plot of polycrystalline graphene with effective grain size of 4 nm is plotted in Fig. 7.4b. The stress–strain plot is non-linear in the initial stage of the loading. Since the stress–strain curves of single grain graphene sheet does not show a nonlinear zone [12], the nonlinearity of the stress–strain curve of polycrystalline sheet is attributed to the out-of-plane deformations induced by the grain boundaries. During the initial stages of loading, the stretching of the graphene sheet leads to a reduction in the out-of-plane deformation of the graphene sheet and this appears as a nonlinear zone in stress–strain plot. After the out-of-plane deformations are fully stretched, the stress–strain curve becomes linear. A similar behavior has been observed in the previous studies [350, 343, 237].

By comparing the stress–strain curves of polycrystalline graphene sheet, it can be observed that as the hydrogen percentage of graphene grain boundaries increases, their Young’s modulus and strength reduces. The Young’s modulus  $E$  of polycrystalline sheets are plotted versus the grain boundaries hydrogen concentration in Fig. 7.4c. The Young’s modulus of graphene sheets is calculated using the slope of the linear portion of the stress–strain curves. The reduction in the Young’s modulus indicates that hydrogenation of graphene sheets reduces their stiffness. The strength of polycrystalline graphene sheets at different grain boundary hydrogenation percentage is plotted in Fig. 7.4d. These curves show that hydrogenation of grain boundaries reduces the strength of graphene sheets significantly; the strength of a polycrystalline sheet with 100% hydrogenation of grain boundaries is about half of the strength of the same polycrystalline sheet without hydrogenation.

The plots of Fig. 7.4c also indicate that polycrystalline grain size can significantly impact its Young’s modulus. Graphene sheets with smaller grain size have a lower Young’s modulus. This is because by reduction in the grain size the number of defects in graphene sheets increases. As shown in Fig. 7.4d, grain size also impact the strength of polycrystalline sheets without hydrogenation. Polycrystalline sheets with smaller grain size have lower strength. Previous study which employed MD reported similar results [344]. By increase in the hydrogenation percentage, the impact of grain size on the strength reduces and all the polycrystallines have nearly the same strength at 100% grain boundary hydrogenation.

The strength of polycrystalline graphene sheets with an average grain size of 6 nm at different temperatures is shown in Fig. 7.4e. The temperature is varied from 100 to 1200 K. It can be observed that with increase in temperature the strength of the polycrystalline graphene is decreasing. The impact of temperature on strength is more significant on polycrystalline sheets with higher hydrogenation percentage of their grain boundaries.

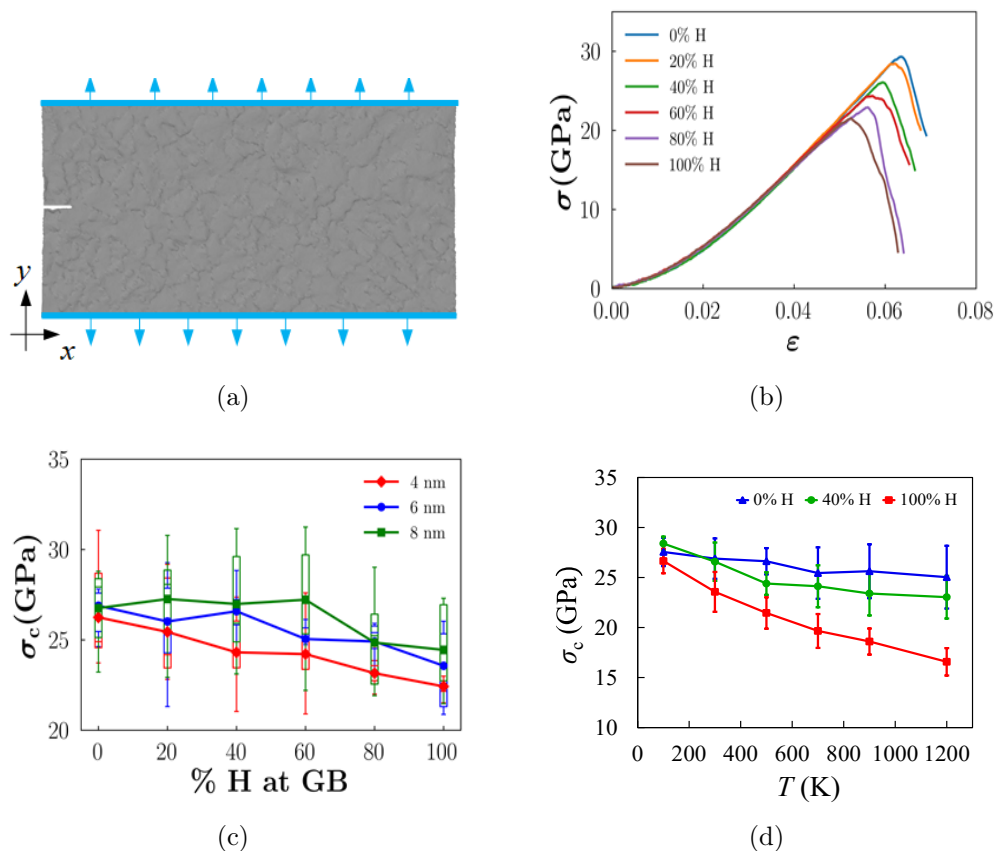


Figure 7.7: (a) A polycrystalline graphene sheet with an edge crack under tensile loading, (b) The stress–strain plot of a polycrystalline graphene with an edge crack and with effective grain size 4 nm and hydrogen concentration ranging from 0 to 100% at 300 K, (c) fracture strength of polycrystalline graphene, and (d) fracture strength of polycrystalline graphene sheets at different temperatures.

Increase in the tensile strain leads to the nucleation and growth of cracks in polycrystalline sheets. For the comparison purpose, the crack nucleation and growth in a polycrystalline sheet without hydrogenation and with 100% grain boundary hydrogenation are shown in Fig. 7.5 and Fig. 7.6, respectively. The initial relaxed structure of graphene sheet with average grain size of 4 nm is shown in Fig. 7.5a. The high stress points in this graph are at the location of grain boundary pentagon–heptagon defects. The stress contour plot at the strain of 8.45% is shown in Fig. 7.5b where the grain boundaries can be easily identified as high stress zones. At this strain, a crack nucleates at one of the high stress grain boundary defects. The inset image shows

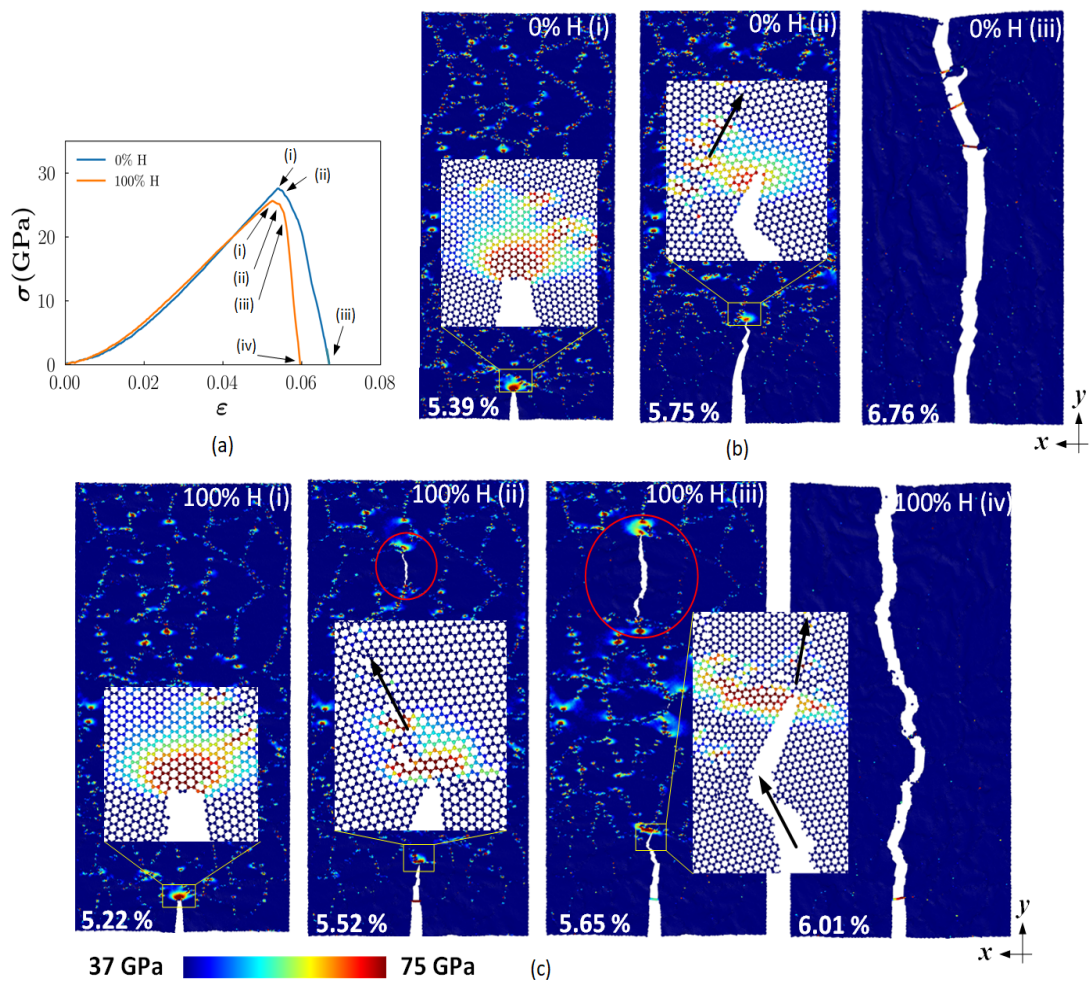


Figure 7.8: (a) Stress–Strain curves of polycrystalline graphene sheet with an edge crack with an average grain size of 6 nm with no hydrogenation and 100% hydrogenation, (b) Crack propagation path with no hydrogenation at (i) 5.39%, (ii) 5.75%, and (iii) 6.76% strain, (c) Crack propagation path with 100% hydrogenation at (i) 5.22%, (ii) 5.52%, (iii) 5.65%, and (iv) 6.01% strain (black arrow shows the direction of grain boundary).

that the edges of the newly created crack are in the zigzag direction and the crack tip is at one of the grain boundaries. By increase in the strain to 8.50%, the crack grows into the next grain along a zigzag path as is shown in Fig. 7.5c. By further increasing the tensile strain to 9.67%, the graphene sheets is split into two halves as is shown in Fig. 7.5d. The crack growth path is mainly intragranular and only a small portion of the crack path is along the grain boundaries.

The stress contour of the relaxed configuration of hydrogenated polycrystalline graphene sheet is shown in Fig. 7.6a. As expected, grain boundaries are associated with high stress zones in the relaxed state of the sheet. Cracks nucleate at the tensile strain of 5.5% which is significantly lower than the strain of 8.45% required to initiate a crack in the sheet without hydrogenation. The stress contour plot of the graphene sheet at the strain of 5.5% are shown in Fig. 7.6b. The stress values indicate that cracks develop in hydrogenated graphene sheets at a significantly lower stress. As can be seen, the crack nucleates close to one of the high stress zones of one of the grain boundaries. By increase in the tensile strain to 5.62%, the crack grows along the grain boundary as shown in Fig. 7.6c. This is in contrast with the intragranular crack path observed for graphene sheet without hydrogenation. Finally, by increasing the strain to 7.51%, the crack grows and split the graphene sheet as shown in Fig. 7.6d. The crack path on a hydrogenated graphene sheet, is a combination of intergranular and intragranular path which indicates that the presence of hydrogen atoms lead to a reduction of the fracture energy of grain boundaries [5].

#### 7.4.2 Fracture properties

To study fracture properties of hydrogenated polycrystalline graphene sheets, an edge crack of length 6 nm is generated in the polycrystalline sheets by removing a few layers of carbon atoms as shown in Fig. 7.7a. The pre-cracked sheet is subjected to tensile loading as described in the previous section. The stress-strain curves of a pre-cracked polycrystalline graphene sheet with average grain size of 4 nm are

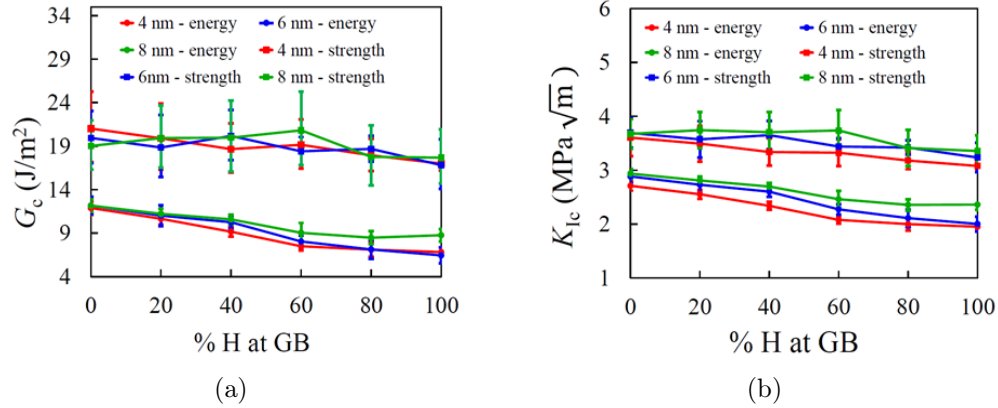


Figure 7.9: Fracture properties of polycrystalline graphene sheet. (a) critical energy release rate, and (b) critical stress intensity factor of polycrystalline graphene sheet versus hydrogenation percentage of grain boundaries.

shown in Fig. 7.7b. The stress–strain curves are used to plot the fracture strength of polycrystalline sheets at different hydrogenation percentage in Fig. 7.7c. It can be seen that by increase in the hydrogenation percentage the critical stress  $\sigma_c$  of graphene sheets reduces. In comparison with graphene sheets with no initial crack (Fig. 7.4d), the reduction in the strength of pre–cracked graphene sheets is less significant.

Comparing the strength of polycrystallines with different average grain size shows that the grain size does not affect the strength of pre–cracked polycrystalline sheets. The impact of temperature on the fracture stress of pre–cracked polycrystalline graphene sheets is studied. The fracture stress of polycrystalline sheets with an average grain size of 6 nm at different temperatures are shown in Fig. 7.7d. Similar to the trend observed in Fig. 7.4e, by increasing the temperature the strength of graphene sheets reduces. The effect of temperature is more pronounced on the strength of polycrystalline sheets with higher hydrogenation percentage.

The stress–strain curves and crack propagation path in a pre–cracked polycrystalline graphene sheet with average grain size of 6 nm at 0% and 100% hydrogenation are shown in Fig. 7.8. The atomic structure and stress contour of polycrystalline graphene without hydrogenation at three different strains are shown in Fig. 7.8b.

The peak stress occurs at the strain of 5.39% where the crack propagation has not occurred yet. With increase of the strain to 5.75% an intragranular crack propagation is observed. Finally, the crack grows across the entire graphene sheet width at the strain of 6.76%.

The structure and stress contour plots of polycrystalline graphene with 100% hydrogenation of grain boundaries at four different strain levels are shown in Fig. 7.8c. At 100% hydrogenation, the peak stress occurs at the strain of 5.22% which is slightly less than that of the graphene sheet without hydrogenation. At the strain of 5.52% the crack has propagated and arrested at one of the grain boundaries. As can be seen in the encircled zone, a new crack has initiated at one of the high stressed grain boundary. Further increase of the tensile strain to 5.65% leads to an intergranular crack growth. The second crack also grows simultaneously. Finally at 6.01% these two cracks coalesce and a complete failure of polycrystalline graphene is observed. A significant portion of crack growth in this case occurs along the grain boundaries which is a result of the hydrogen embrittlement of grain boundaries.

#### 7.4.2.1 Fracture energy

According to the Griffith's energy balance theorem, cracks propagate when the reduction in the potential energy of the system due to the crack growth is larger or equal to the increase in the surface energy of the system due to the creation of new surfaces. The change in the potential energy of the system  $\Delta U$  can be calculated using

$$\Delta U = U_f - U_i, \quad (7.1)$$

where  $U_f$  denotes the potential energy of the fully cracked system and  $U_i$  represents the potential energy of the relaxed system before the application of tensile strains.

The critical energy release rate  $G_c$  of the system can be calculated using

$$G_c = \frac{\Delta U}{t\Delta a} \quad (7.2)$$

where  $t$  is the thickness of the graphene sheet which is equal to 3.35 Å and  $\Delta a$  is the change in the crack length. The critical energy release rate can also be estimated using the critical stress  $\sigma_c$  which represents the peak stress before the crack growth occurs [356]

$$G_c = \frac{\sigma_c^2 a \pi}{E} \quad (7.3)$$

where  $a$  is the length of the initial edge crack and  $E$  is the Young's modulus of polycrystalline graphene sheet. The energy release rate can be used to obtain the critical stress intensity factor using  $K_{Ic} = \sqrt{G_c E}$ .

The critical energy release rate and stress intensity factor of polycrystalline graphene sheets are plotted in Fig. 7.9a and b. The  $G_c$  and  $K_{Ic}$  estimated using the fracture strength are respectively in the range of 21 - 17 J/m<sup>2</sup> and 3.7 - 3.1 MPa√m. On the other hand, the critical energy release rate and stress intensity factor estimated using the change in potential energy are respectively between 12 - 6 J/m<sup>2</sup> and 2.9 - 2.0 MPa√m which are lower than the values calculated using the fracture strength. The discrepancy is due to the fact that the dissipated energy is not considered in the potential energy approach while the fracture strength includes the dissipated energy [343].

The plots of Fig. 7.9 show that the increase in the hydrogenation percentage causes a reduction in both  $K_{Ic}$  and  $G_c$ . These figures also show that hydrogenation effects on the critical stress intensity factor is more significant than its impact on the strength of polycrystalline graphene sheet. This indicates that although after hydrogenation the strength of sheets does not reduce significantly, but they become more brittle. The plots of Fig. 7.9 also indicate that grain size does not impact the critical energy

release rate and stress intensity factor of polycrystalline graphene.

## 7.5 Conclusion

We studied the mechanical and fracture properties of polycrystalline graphene sheet with hydrogenated grain boundaries. With increase in the hydrogenation percentage the stiffness of the polycrystalline graphene sheets significantly reduced. The fracture strength of graphene sheets are not significantly affected by the hydrogenation. On the other hand, hydrogenation reduces the critical stress intensity factor of polycrystalline sheets. Hydrogenation also impact the crack growth path. At low hydrogenation percentage, cracks prefer intragranular growth path while as the hydrogenation percentage of grain boundaries increases, more portion of the crack growth occurs along the grain boundaries.

## CHAPTER 8: A Novel Approach for Studying Crack Propagation in Polycrystalline Graphene Using Machine Learning Algorithms

The advancement in prominent technologies such as quantum computing, energy storage, renewable energies, and biotechnology depends on the development of nanomaterials with exceptional properties. Graphene excellent thermal [13, 14, 15], electronic [16, 17, 18], optical [357, 358] and mechanical [9, 10, 11, 12] properties make it an excellent candidate for various applications including field effect transistors [19, 20, 21], supercapacitors [22, 23, 24, 25], nano composites [26, 27, 28, 29, 30], electro mechanical sensors [31, 32, 33], and optical devices [34, 35].

Large area polycrystalline sheets are often necessary for industrial applications. The most widely used technique for production of large graphene sheets is chemical vapor deposition (CVD) [76, 77, 78, 79]. The CVD-grown graphene sheets are generally polycrystalline [80, 81], composed of grains of different orientations seamed together at the grain boundaries. Polycrystalline graphene sheets can have different physical and mechanical properties than graphene [359, 222, 360, 342], to ensure the structural integrity of graphene based devices, it is necessary to understand the mechanical and fracture properties of polycrystalline graphene.

Atomic level modeling techniques such as density functional theory (DFT) [361, 12, 362, 363, 364, 365, 366, 367, 368] or molecular dynamics (MD) simulations [345, 369, 146, 114, 370, 371, 2, 372, 320, 346, 3, 373, 5, 347, 1, 374, 117, 348, 119] have been widely used in studying the properties of nanomaterials including graphene. Although these methods provide accurate predictions of the properties of graphene, they are computationally intensive, specially when several simulations should be conducted to account for the statistical variability of the micro structure of polycrystalline

graphene.

Artificial intelligence techniques, particularly machine learning (ML) and deep learning (DL), are becoming valuable tools in modeling mechanical properties of materials [375, 376, 377, 378, 379]. This is due to their ability to serve as lower-order surrogates to approximate higher-fidelity models, which significantly reduces the computational time. Despite the broad application and wide influence of ML, limited research has been conducted in using ML for predicting crack propagation in materials. Understanding the crack growth behavior is important in both scientific and industrial context and is essential to prolong the life of industrial products. Moore et al. [380] used data obtained from finite-discrete element model to develop an ML model using random forest and decision tree to predict dynamic fracture in brittle materials. Schwarzer et al. [381] implemented recurrent graph convolution neural networks to predict crack growth in brittle materials. Pierson et al. [382] used convolutional neural network to predict fatigue crack path in polycrystalline alloy. Wang et al. [383] developed a machine learning model using temporal independent convolutional neural network and bidirectional long short-term memory network to capture crack path in brittle materials. These studies [381, 382, 383] use continuum level data to predict fracture using machine learning. Since brittle fracture occurs as a result of bond breaking at atomic level, a machine learning method which can predict fracture mechanics using the data obtained from the microscopic process of bond breaking at atomic scale can be valuable toward the material design at nanoscale. More recently, Hsu et al. [384] used the data obtained from molecular dynamics to construct a convolutional LSTM model to predict the brittle fracture of a simple Lennard-Jones material. They examined different crystal orientations and also studied crack growth on bicrystalline materials.

This paper seeks to go beyond existing methods by developing a machine learning method for predicting the growth of cracks on realistic polycrystalline graphene

sheets. Simulation data obtained from high-fidelity molecular dynamic models are used to build the data set to train and test the machine learning model. We use a convolutional network to extract the microstructure of the fracturing polycrystalline graphene and a bidirectional recurrent neural network is adapted to predict the sequential growth of the crack.

### 8.1 Polycrystalline graphene sheet

Polycrystalline graphene sheet with dimensions of  $40 \times 20$  nm and with effective grain size of 3 to 9 nm has been considered. The effective grain size  $l_e$  of polycrystalline sheets is defined as  $\sqrt{\frac{A}{n_g}}$  where  $A$  is the surface area of graphene sheet and  $n_g$  is the number of grains in the sheet.

Theoretical studies and high-resolution images produced by transmission electron microscopy (HR-TEM) have shown that graphene grain boundaries are mainly comprised of pentagon-heptagon defects [81, 338, 233, 5]. In this paper, we use the algorithm proposed by Shekawat *et al.* [344] to generate polycrystalline graphene sheets with realistic grain boundaries composed of only pentagon-heptagon defects. In this methodology, the grain centers are randomly chosen and the Voronoi diagram associated with the grain centroids represents the polycrystalline structure. The grain orientations are also chosen randomly. The grain orientation  $\theta$  is defined based on the angle between a zigzag direction  $zz$  in the grain and the  $x$ -axis as is shown in Fig. 8.1. Due to the six-fold symmetry of graphene lattice, the orientation angle  $\theta$  of each grain is between  $0^\circ$  and  $60^\circ$ . By assigning a random crystalline orientation to each grain (Voronoi cell) a polycrystalline structure with random misorientation angles between grains is generated.

The arrangement of carbon atoms in grains and along the grain boundaries are obtained by first generating a triangular lattice dual to the graphene lattice of each grain and then using the centroidal Voronoi tessellation [351] to relax the atom positions along the grain boundaries. The grain boundaries obtained at this stage are

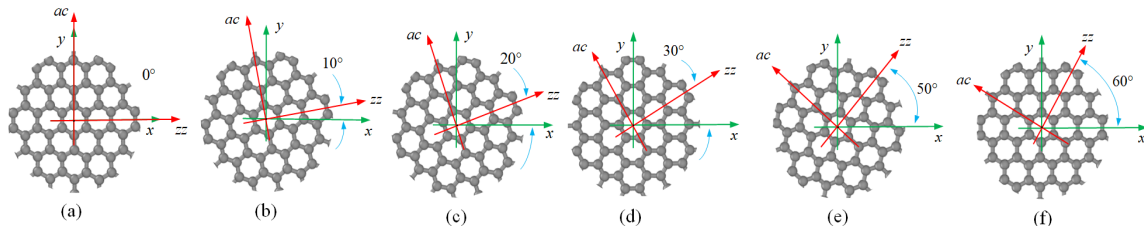


Figure 8.1: Graphene grains with different misorientation angles (a)  $0^\circ$ , (b)  $10^\circ$ , (c)  $20^\circ$ , (d)  $30^\circ$ , (e)  $50^\circ$ , and (f)  $60^\circ$ .

made up of only pentagon–heptagon pairs (Stone–Wales defects). The position of the atoms are fine tuned by minimizing the energy of system using the conjugate gradient method and subjecting the polycrystalline graphene sheet to an annealing process. During annealing the polycrystalline graphene sheets are heated in such a way that the crystalline part of the sheet is unaffected but the grain boundary regions are allowed to break and reform C–C bonds. After cooling down, the polycrystalline sheet has a more stable structure and a lower energy [352] with grain boundaries composed of only pentagon–heptagon defects separated by hexagonal rings.

After creating polycrystalline sheets, an edge cracks with width of 0.7 nm and length of 4 nm is created in each sheet by removing few rows of carbon atoms. The energy minimization process using the conjugate gradient method followed by the annealing process is conducted using LAMMPS molecular dynamics package [91]. The REBO2 (REBO2+S) potential has been employed to describe the C–C interactions [97]. REBO2 is a more advanced version of REBO potential which is capable of accurately modeling the fracture process in graphene sheet. Equations of motion of the system are integrated through velocity–Verlet algorithm with a time step size of 0.1 fs. In this approach, first the initial structure of graphene sheet is optimized by employing the conjugate gradient technique. The system is heated up to 250 K using the Berendsen thermostat within a time period of 1 ps followed by an equilibration stage within an NPT ensemble for another 1 ps. The graphene sheet temperature is then increased in an NPT ensemble up to 2500 K in steps of 250 K and each step lasts

for a time period of 2 ps. After the heating stage, the system is quenched to 1 K for 15 ps. Finally the system is further equilibrated at 1 K for a period of 10 ps. Examples of polycrystalline sheets generated using the prescribed algorithm are presented in Fig. 8.2. In this paper, to take into account the randomness of the polycrystalline structure and grain orientations, 100 polycrystalline graphene sheets are created for each effective grain size.

## 8.2 Tensile loading

After preparing the initial structure of graphene sheet, the temperature of the model is increased to 300 K. The graphene sheet temperature is scaled up to 300 K by using the Berendsen thermostat within a time period of 5 ps. The system is equilibrated within an NPT ensemble for 5 ps at 300 K.

The graphene sheet is subjected to a tensile strain in the  $y$ -direction as shown in Fig. 8.3a. To apply tensile loading on the graphene sheet, a few layers of atoms in the top and bottom edges are constrained in the  $y$  and  $z$ -directions while they are allowed to move in the  $x$ -direction. The tensile strain is applied in the  $y$ -direction in increments of  $10^{-7}$ . Each step of strain increment is accompanied by a step of NPT equilibration for 0.1 fs which leads to a strain rate of  $10^9 \text{ s}^{-1}$ . In order to reduce the stress in the  $x$ -direction to zero, the graphene sheet is allowed to relax in the  $x$  direction during the NPT equilibration. The tensile loading is applied until the initial edge crack propagates to the other side of graphene sheet. The virial stress is used to calculate the continuum stresses from the MD simulations using Eq. (1.17).

The stress contour plot of the polycrystalline sheets are presented in Fig. 8.2. The contour plots show that the presence of grain boundary defects induces stress concentrations in the relaxed polycrystalline graphene sheet. Previous studies have shown that such high stress points serve as crack nucleation [6] sites and can reduce the strength of polycrystalline sheet in comparison with pristine graphene sheets [342, 222, 359].

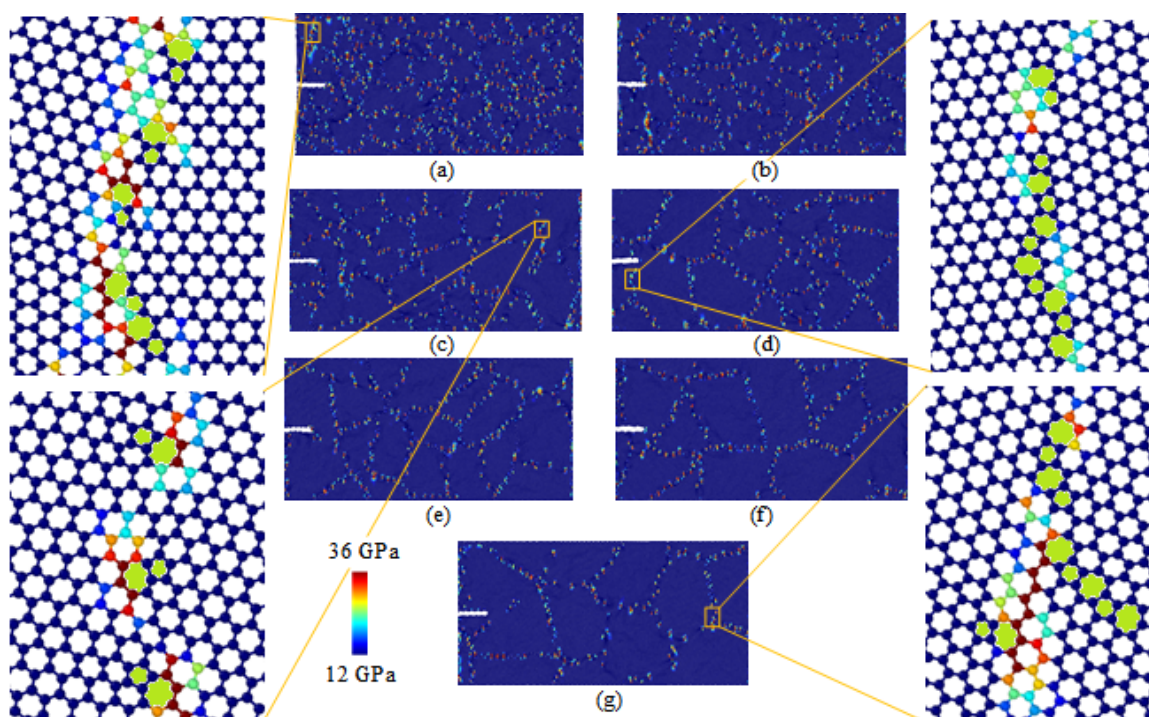


Figure 8.2: Polycrystalline graphene sheets with initial edge cracks and average grain sizes changing from 3 nm to 9 nm (colored based on the  $y$ - component of stress). Zoomed in images shows the grain boundaries which are made up of chain of pentagon–heptagon defects. (a) 3 nm, (b) 4 nm, (c) 5 nm, (d) 6 nm, (e) 7 nm, (f) 8 nm and (g) 9 nm.

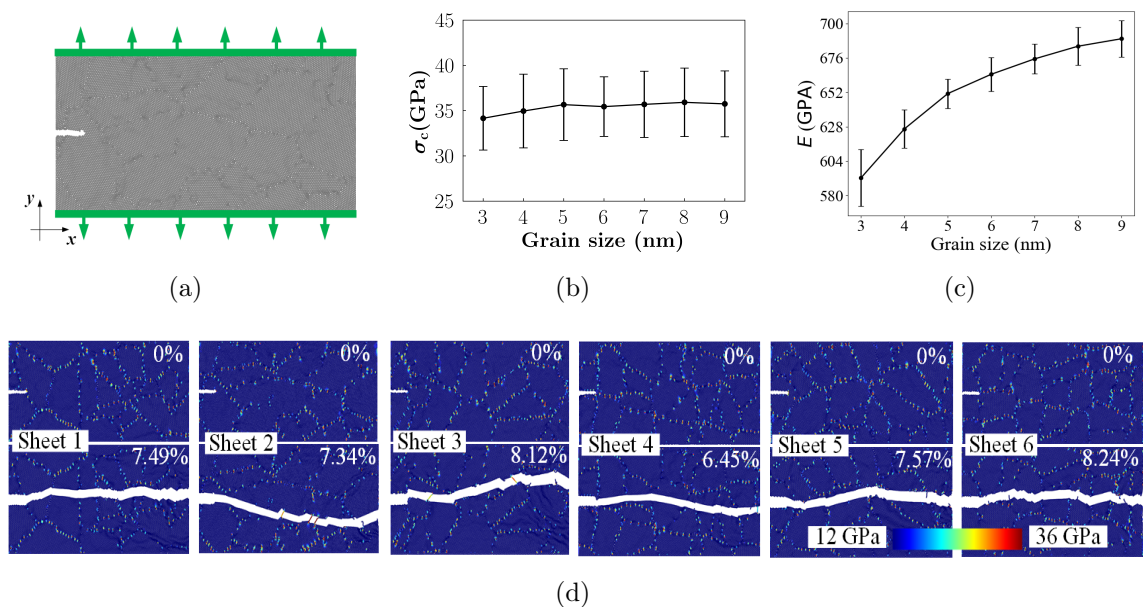


Figure 8.3: The fracture process in precracked polycrystalline graphene sheet. (a) Tensile loading applied in the  $y$ -direction, (b) effect of grain size on the strength of the polycrystalline graphene sheet, (c) effect of grain size on the Young's modulus of the polycrystalline graphene sheet, and (d) the crack path in 6 different polycrystalline graphene sheets with an average grain size of 6 nm. The contour plots show the  $y$ -component of stress in polycrystalline graphene sheet with initial crack at 0% strain (top image) and with fully grown crack (bottom image).

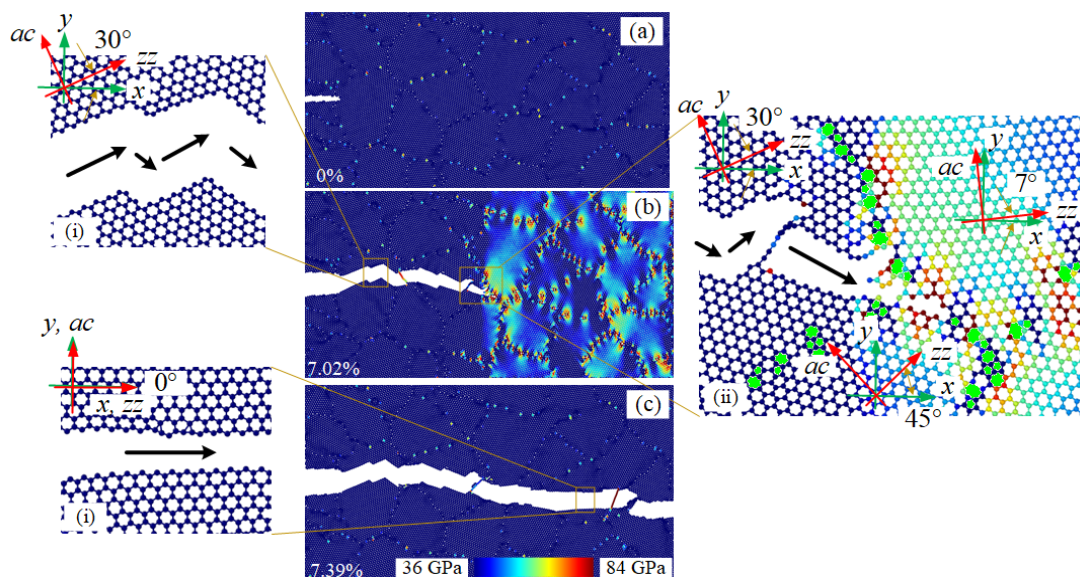


Figure 8.4: Crack growth in polycrystalline graphene sheets with average grain size 5 nm at strains (a) 0%, (b) 7.02%, and (c) 7.39%. The contour plots show the  $y$ -component of stress (black arrow shows crack path).

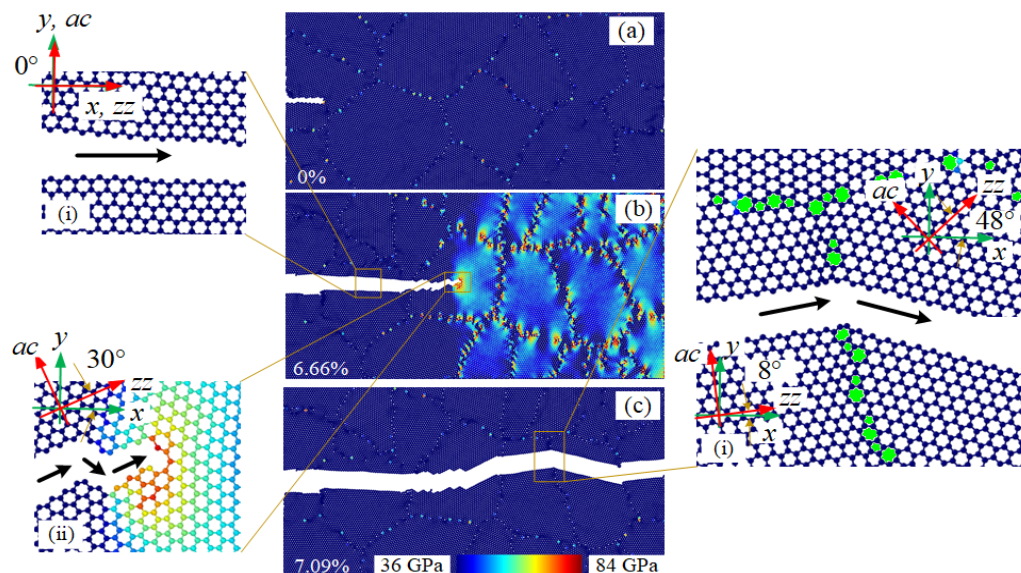


Figure 8.5: Crack growth in polycrystalline graphene sheets with average grain size 7 nm at strains (a) 0%, (b) 6.66%, and (c) 7.09%. The contour plots show the  $y$ -component of stress (black arrow shows crack path).

### 8.3 Results

#### 8.4 Fracture process from Molecular Dynamics Simulations

Tensile loading is applied in the  $y$ -direction of the precracked polycrystalline graphene sheet as shown in Fig. 8.3a. The tensile strength of polycrystalline sheets versus their effective grain sizes is plotted in Fig. 8.3b. It can be observed that the grain size does not affect the strength of pre-cracked graphene sheets. The Young's modulus of pre-cracked polycrystalline graphene sheet is plotted in Fig. 8.3c. This graph shows that the polycrystalline sheets with larger effective grain sizes have higher Young's modulus.

The initial configuration of the polycrystalline graphene sheets and their final configuration when the crack is fully developed along the width of graphene sheet are shown in Fig. 8.3d. The crack path is unique for each sheet and depends on the orientation of the individual grains and atomic structure of grain boundaries along the crack path.

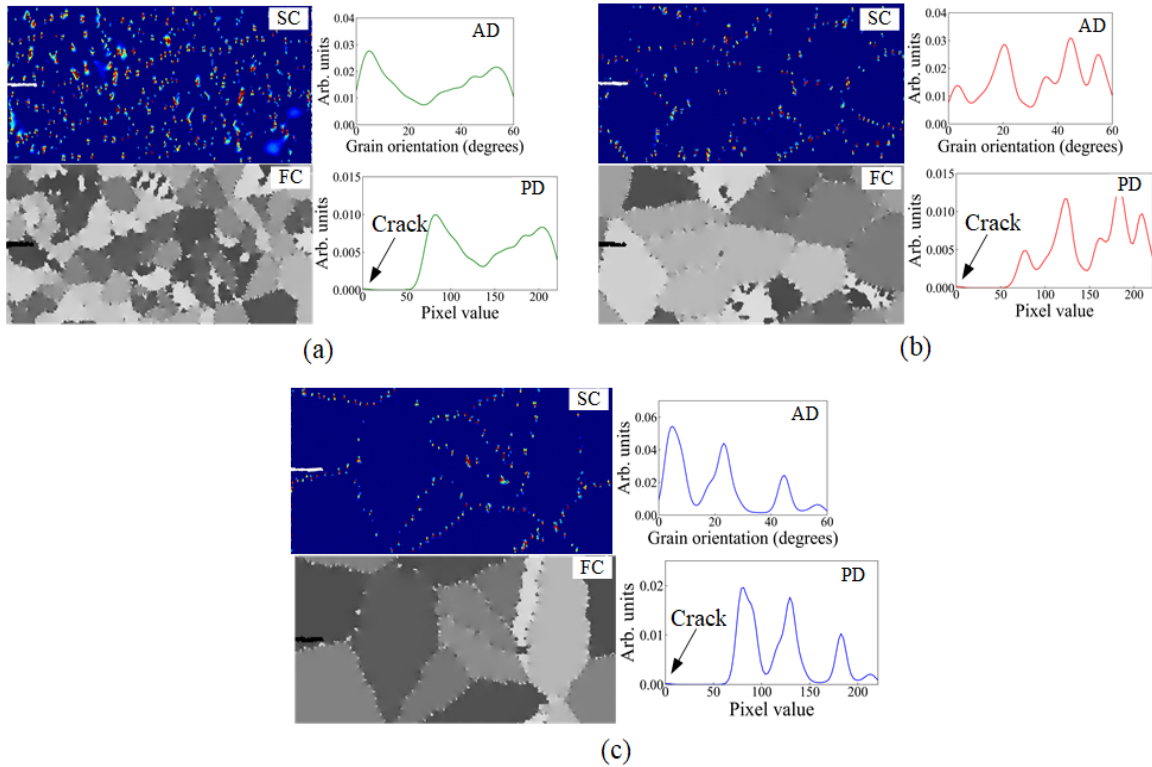


Figure 8.6: Initial configurations of polycrystalline graphene sheet. Image SC shows stress contour plots of relaxed polycrystalline graphene sheet and FC presents the grey scale image based on the grain orientation. The grey scale image is used as input to the machine learning model. The graph AD shows the density of atoms for each grain orientation and the graph PD represents the density of pixels per a given orientation. (a) Average grain size 3 nm, (b) average grain size 6 nm, and (c) average grain size 9 nm.

The crack propagation path and factors affecting it are further investigated in Fig. 8.4 and 8.5 where the cracks in two polycrystalline sheets at different strain levels are presented. The crack path in a grain with  $30^\circ$  orientation angle is shown in Fig. 8.4b(i),b(ii) and 8.5b(ii). It can be seen that when the grain orientation is  $30^\circ$ , the crack grows along the zigzag direction. The growth path is not necessarily straight but the crack can kink to grow along different zigzag directions. The crack path remains straight in grains with other orientation angles, crack grows along a zigzag direction without kinking. For example when the crack reaches a grain with  $0^\circ$  misorientation angle, it grows along a zigzag direction perpendicular to the loading direction as shown in Fig. 8.4c(i) and 8.5b(i). The crack path when the crack tip

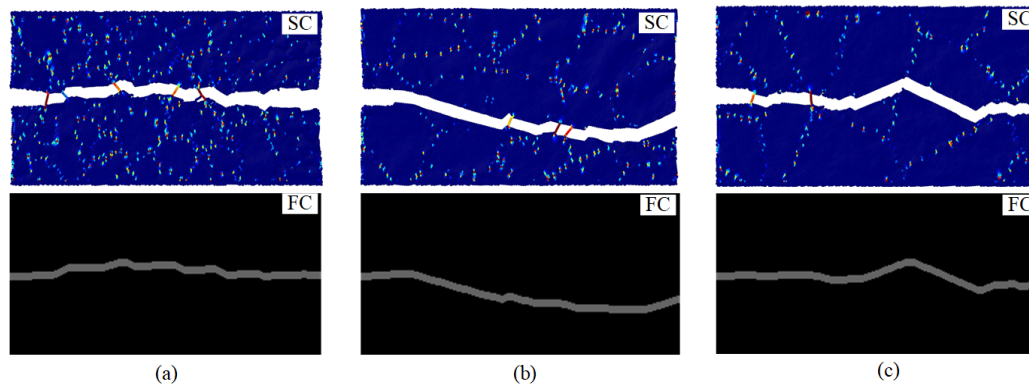


Figure 8.7: Polycrystalline graphene sheet showing the fully grown crack. Image SC shows the contour plot of stress distribution and FC shows the gray scale image of fully grown crack which is used as output of the ML model. (a) Average grain size 3 nm, (b) average grain size 6 nm, and (d) average grain size 9 nm.

reached the grain boundary between two grains with orientation angles of  $7^\circ$  and  $45^\circ$  is shown in Fig. 8.4b(ii). As shown, after reaching the grain boundary, the crack grows along the grain boundary creating an intergranular crack path. On the other hand when the crack grows in a grain with orientation angle of  $8^\circ$ , after reaching a grain boundary with misorientation angle of  $48^\circ$  degree, the crack kinks to grow along a zigzag direction in the adjacent grain with orientation angle of  $48^\circ$  as shown in Fig. 8.5c(i).

These results show that the crack propagation path in polycrystalline graphene sheet is determined by the grain orientation and grain boundary atomic structure. The cracks growth within each grain is along a zigzag direction in that grain. When the crack reaches a grain boundary, it will propagate to the next grain by kinking at the grain boundary or it grows along the grain boundary. Therefore, in predicting the crack growth path using a machine learning model, features such as grain orientations, grain boundaries misorientation angles and their atomic structure are of importance.

## 8.5 Fracture process from Machine learning model

High-fidelity atomistic modeling is computationally intensive. Computational cost of atomistic simulations grows quickly with number of atoms in the system. Our

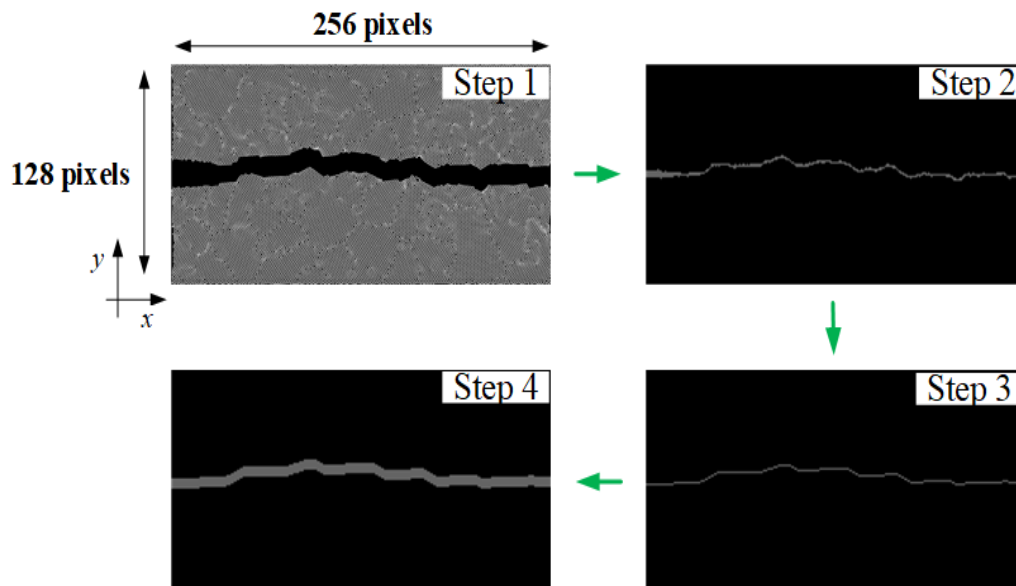


Figure 8.8: The process used to generate output images with  $128 \times 256$  pixels. Step 1 shows the image of polycrystalline graphene with fully grown crack. Step 2 presents the image with information of only the fully grown crack. Step 3 presents the approximated fully grown crack with width of 1 pixel. Step 4 gives the fully grown crack with width of 6 pixels.

polycrystalline graphene sheet contains about 32000 atoms. We run each molecular dynamics (MD) simulation on 8 processors. It takes 7–8 hours for the tensile modeling of polycrystalline sheets to complete.

To make quick and accurate predictions of crack path while avoiding the high computational costs associated with molecular dynamic simulations, we propose a deep learning model which is a combination of convolutional neural network (CNN) and bidirectional recurrent neural network (Bi-RNN). The source code of deep learning model is built in keras [385].

One of the challenging tasks in creating machine learning models is the generation of the data set required for training the model. The data set is constructed by conducting tensile loading simulations on 700 different polycrystalline graphene sheets with an effective grain size changing from 3–9 nm. Our data set is composed of input and output images  $(X, y)$  with dimensions of  $128 \times 256$  pixels. The input image

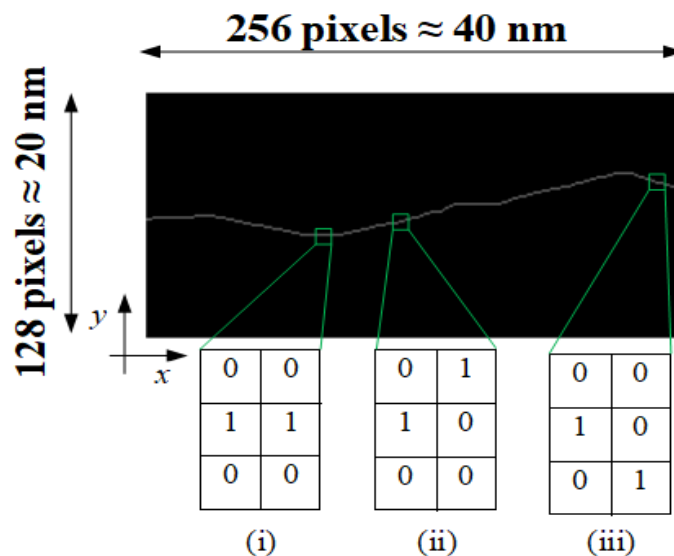


Figure 8.9: Image of fully grown crack showing pixel values of crack propagating in (i) straight and (ii),(iii) diagonal direction.

$X$  represents the relaxed atomic structure of the polycrystalline sheet and the output image  $y$  represents the graphene sheet after splitting into two halves, hence the output image  $y$  includes the path of fully developed crack. The data set is split into training, validation, and test data sets with 560, 70, and 70 simulations in each data set respectively. The training and validation data sets are used to train the model. The test set is not involved in the process of training the machine learning model. In the next section the methodology employed to prepare the input and output images used in the data set is presented

### 8.5.1 Data Preparation

Grayscale images of the initial configuration of polycrystalline graphene sheet with  $128 \times 256$  pixels are used as the input images. Polyhedral template matching (PTM) method [386] implemented in LAMMPS is used to obtain the lattice orientation of the local structure of each atom. The pixel value associated with each atom is assigned based on the local lattice orientation at that atom. Hence, the pixel value of each grains represents its orientation angle; grains with different orientation angle have

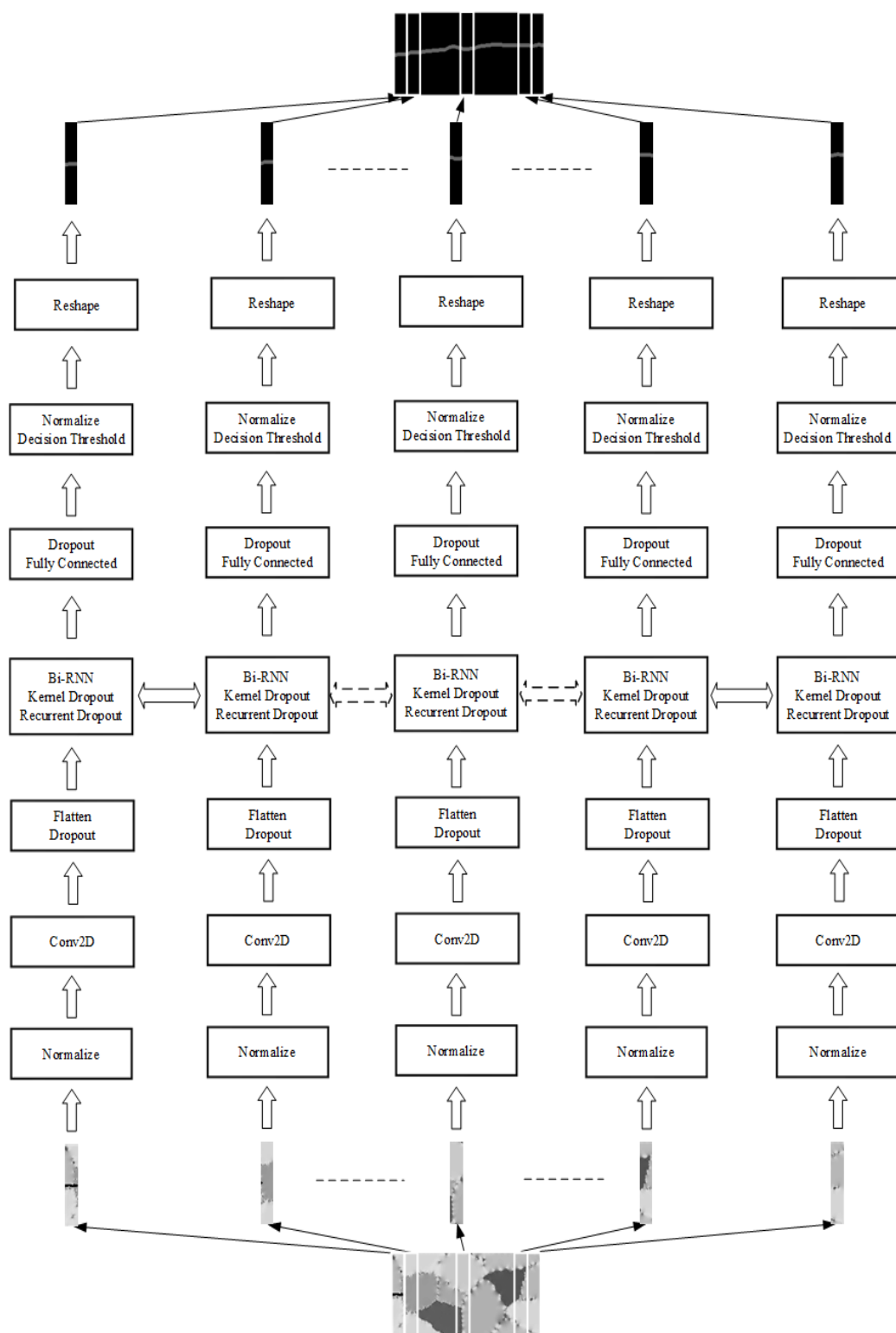


Figure 8.10: Process flow to predict fully grown crack in polycrystalline graphene sheet.

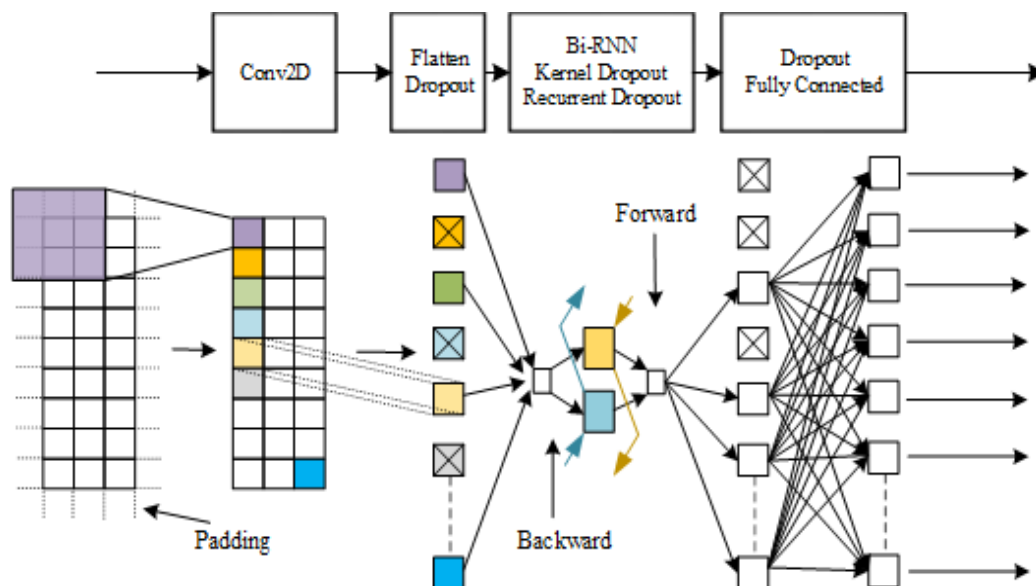


Figure 8.11: Machine learning architecture used for processing a slice of the image.

different colors in the input greyscale image.

The initial atomic structure of polycrystalline graphene sheets and their corresponding greyscale images are shown in Fig. 8.6. The colored contour plots show the atomic level stress distribution in the polycrystalline graphene sheet. In the colored images the grain boundaries can be recognized as points with high stress concentration. The grey scale images of polycrystalline graphene sheets used as the input to the machine learning model are shown in Fig. 8.6, where the color of each grain is assigned based on the orientation of the grain. The orientation of the grains changes from  $0^\circ$  to  $60^\circ$ . A pixel value of 68 is assigned to the grains with  $0^\circ$  orientation angle and a pixel value of 221 is assigned to grains with  $60^\circ$  orientation angle. A pixel value of zero is assigned to the crack path. To ensure that the pixel values of the greyscale image can accurately represent the grain orientations, the distribution of atom orientations is compared with the distribution of pixel values in the two graphs presented with each sub-figure in Fig. 8.6. By comparing these graphs it can be seen that the ratio of atoms with a certain orientation to all the atoms (atom percentage) is in good agreement with ratio of pixels with a certain value to the total number of pixels

in the image (pixel percentage). The similarity between these two graphs indicates that the greyscale image includes accurate information about the microstructure of the polycrystalline sheet.

The output image contains the path of fully grown crack. The original images generated using the atom positions and their corresponding greyscale images with only information of fully grown crack are shown in Fig. 8.7. The output image pixel values are zeros and ones. The crack path is represented with pixel values equal to one and everywhere else has a zero pixel value.

The steps followed to generate the output images from the MD simulations are shown in Fig. 8.8, which is containing only the information of fully grown crack. As shown in step 1 of Fig. 8.8, the coordinates of the atoms obtained from the MD simulations are used to create an image of the graphene sheet with fully grown crack. In step 2, the information regarding the microstructure of graphene sheet are eliminated so the image only contains the information regarding the crack path. In the next step, the width of the crack path is reduced to 1 pixel and the crack path is approximated by taking the moving average of the  $y$  position of the pixels containing the crack information. In the last step the width of the crack is increased to six pixels.

We use the length of the fully grown crack to quantitatively assess the quality of the ML predictions. Image processing modules of *python* programming language has been employed to measure the crack in the polycrystalline graphene sheet. Polycrystalline graphene sheets of dimensions  $20 \times 40$  nm are mapped into images of size  $128 \times 256$  pixels as shown in Fig. 8.9. Hence, each pixel in the image corresponds to a length of  $\frac{5}{32}$  nm in  $x$  and  $y$  directions. The image shown in Fig. 8.8 in step 3 with crack width one pixel is used to evaluate the length of the fully grown crack. As shown in Fig. 8.9, the crack can propagate in horizontal directions or can grow upward or downward in diagonal ways. If crack advances along a horizontal path as shown in the Fig. 8.9(i), then crack advances by a length of  $\frac{5}{32}$  nm per pixel. If crack advances

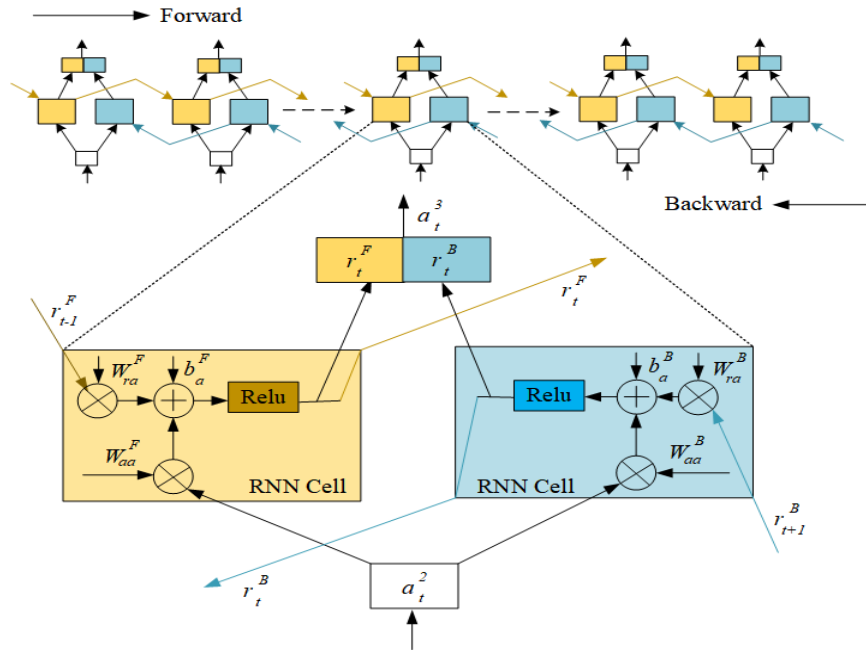


Figure 8.12: Bidirectional recurrent neural network showing the forward and backward recurrent neural network (RNN) cells.

in the diagonal path as shown in Fig. 8.9(ii) and (iii), then the crack advances by a length of  $\frac{5}{32}\sqrt{2}$  nm. In this way using image processing techniques, the entire length of the fully grown crack in the polycrystalline graphene sheet can be evaluated.

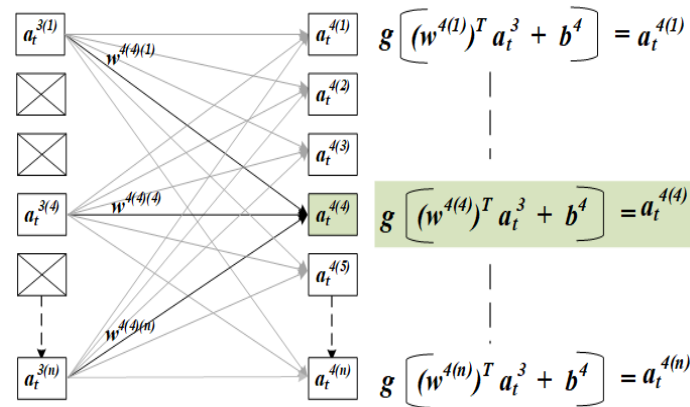


Figure 8.13: Fully connected layer of the machine learning model

### 8.5.2 Machine Learning Model

As discussed in the previous section the training data consists of the images of size  $128 \times 256$ . The input  $X$  of the training set is the grey scale image of initial configuration of the polycrystalline graphene sheet. The output of the training set contains the information of the fully grown crack.

The structure of the machine learning model implemented to predict the crack propagation path in polycrystalline graphene is shown in Fig. 8.10. The proposed machine learning model is a series of convolution (Conv2D), bidirectional recurrent neural network (Bi-RNN), and fully connected (FC) layers. The Convolution and fully connected layers are to extract geometric features like grain orientation, grain boundaries, and crack path. The Bi-RNN transfers the sequential information regarding the crack location and microstructure details and predicts the crack growth direction. As shown in Fig. 8.10, the input and output images are divided into slices. The size of each slice of input and output image is  $128 \times 3$  pixels. All the slices of input image is fed simultaneously to the machine learning architecture as shown in Fig. 8.10. The corresponding slices at the output layer contains the information of the crack.

More details on the structure of each layer is provided in Fig. 8.11. As the first step in using the input data, the pixel values are normalized using  $p = P/221$ , where  $p$  is the normalized pixel value and  $P$  is the pixel value before normalization. The normalized input image is passed on to a Conv2D with a learnable filter size of  $3 \times 3$ . To keep the original image size, one extra layer of pixels is added to around the slice image to. The output of convolution layer is reshaped from  $128 \times 3$  to  $384 \times 1$ . The data is passed on to the bidirectional recurrent neural network layer with an output with size of  $768 \times 1$ . The data is further passed on to a FC layer with sigmoid activation function [387]. The final image is obtained by reshaping the data to  $256 \times 3 \times 1$ . The binary-cross-entropy is used as the loss function of the model. Adam

optimizer method is used to optimize model parameters and reduce the loss [388]. Further details about each layer is presented in the followings.

### 8.5.2.1 Convolution layer

A  $3 \times 3$  kernel is used in the convolution layer. To keep the size of output and input image the same, the input image is padded on the sides with one layer of zeros. In this layer rectified linear activation function (ReLU) [387] is employed. ReLU  $g(z_t^1)$  is defined by

$$g(z_t^1) = \begin{cases} z_t^1 & z_t^1 \geq 0 \\ 0 & z_t^1 < 0 \end{cases} \quad (8.1)$$

where  $z_t^1 = a_t^0 * W^1 + b^1$ . In this equation, the convolution operator is denoted by  $*$ , the padded input slice of image received from the previous layer is denoted by  $a_t^0$  where  $t$  sequentially varies from 1 to  $T$ . Here  $T = 85$  is total number of slices in a given image.  $W^1$  is a  $3 \times 3$  convolution kernel and  $b^1$  is the bias parameter. The output obtained from the convolution layer  $a_t^1 = g(z_t^1)$  is reshaped from  $128 \times 3$  to  $384 \times 1$ . The reshaped output  $a_t^2$  is further passed on to the bidirectional recurrent neural network, after dropping out 50% of the data.

### 8.5.2.2 Bidirectional recursive neural network layer

The basic structure of the bidirectional recurrent neural network is shown in Fig. 8.12. Bidirectional recurrent neural networks are capable of transferring the data in both forward and backward direction, hence they exploit the past and future context by processing the input images in both directions.

A cell of the Bi-RNN is a combination of the two recurrent neural network (RNN) cells as shown in Fig. 8.12. The orange RNN cell transfers the data forward whereas the blue RNN cell transfers the data backward. The operation principle of both RNN cells is the same. Unlike convolutional and fully connected layers, the RNN cell has an internal state which allows it to memorize the information. As shown in Fig. 8.12,

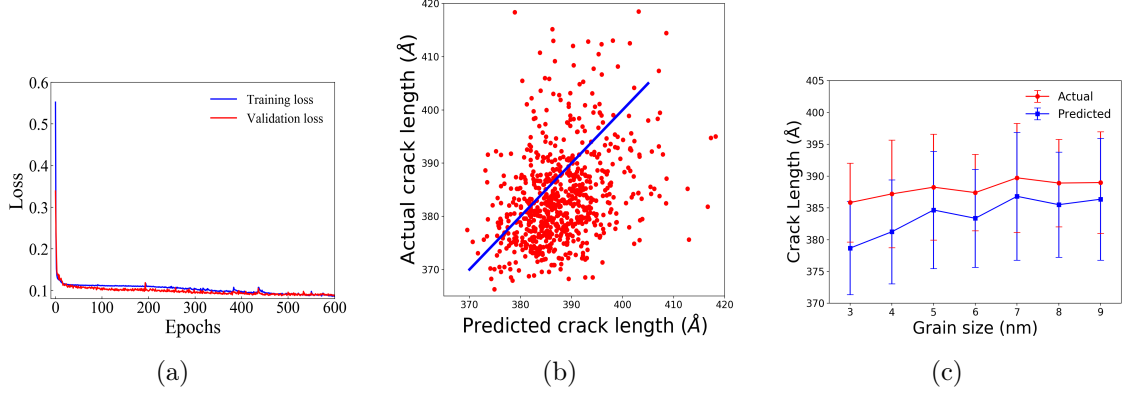


Figure 8.14: (a) Machine learning model loss curve, (b) crack length comparison from MD and machine learning model, (c) crack length versus grain size plots from MD and ML model.

bidirectional RNNs compute a forward hidden layer output  $r_t^F$  by iterating through all the input image slices from  $t = 1, \dots, T$  and compute a backward hidden layer output  $r_t^B$  by iterating through the image slices from  $t = T, \dots, 1$ . The two outputs are combined to compute one single output for the Bi-RNN cell using the following equations

$$\begin{aligned}
 r_t^F &= g(W_{aa}^F a_t^2 + W_{ra}^F r_{t-1}^F + b_a^F) \\
 r_t^B &= g(W_{aa}^B a_t^2 + W_{ar}^B r_{t+1}^B + b_a^B) \\
 a_t^3 &= \{r_t^F; r_t^B\}
 \end{aligned} \tag{8.2}$$

where  $g$  is the ReLU function defined in Eq. (8.1),  $a_t^3$  is the output of the Bi-RNN layer and has a shape of  $768 \times 1$ .  $W_{aa}^F$ ,  $W_{ra}^F$ ,  $W_{aa}^B$ ,  $W_{ra}^B$ ,  $W_r^F$ , and  $W_r^B$  are the weight matrices, and  $b_a^F$ , and  $b_a^B$  denote the forward, backward and output biases respectively. Dropout and L2 regularization have been employed to prevent overfitting. Dropout regularization has been applied to the inputs of the RNN cell and recurrent state. 50% of the input data  $a_t^2$  is dropped out for both forward and backward RNN cells. Furthermore, 10% of the forward and backward recurrent states  $r_{t-1}^F$ ,  $r_{t+1}^B$  are also dropped out.

### 8.5.2.3 Fully connected layer

The output of the Bi-RNN layer is passed on to the fully connected layer (FC) while 10% of the data received from the Bi-RNN layer is dropped out to avoid overfitting. Fig. 8.13 shows the fully connected layer to process one slice of image in our machine learning architecture. The output of the fully connected layer is given by

$$a_t^4 = g((W^4)^T a_t^3 + b^4) \quad (8.3)$$

where  $g$  is sigmoid function,  $W^4$  is the weight matrices, and  $b^4$  is the bias term. The fully connected layer has an output in the form of a  $384 \times 1$  vector. The output vector is normalized by dividing with it's maximum value  $a_t^5 = \frac{a_t^4}{\max(a_t^4)}$ . The values of the vector  $a_t^5$  is converted to zeros and ones using a decision threshold of 0.8 and reshaped to a  $128 \times 3$  matrix. The output matrix is composed of zeros and ones with the pixels representing crack have a value of one.

### 8.5.2.4 Loss function

The loss function employed in our ML model is binary-cross entropy. An L2 regularization is applied to avoid overfitting by penalizing the kernel and recurrent weight matrices. With L2 regularization on kernel and recurrent weights, the loss function  $L$  of all time steps is given by

$$L(\hat{y}, y) = \sum_{t=1}^T L(\hat{y}^t, y^t) + \lambda_1 (R_k^F + R_k^B) + \lambda_2 (R_r^F + R_r^B) + \lambda_3 F_k \quad (8.4)$$

where  $\lambda_1 = 5 \times 10^{-7}$  and  $\lambda_2 = 5 \times 10^{-7}$  are respectively kernel and recurrent regularization parameters of Bi-RNN layer and  $\lambda_3 = 5 \times 10^{-7}$  is kernel regularization parameter of the fully connected layer.  $R_k^F$ ,  $R_k^B$ ,  $R_r^F$ ,  $R_r^B$  and  $F_k$  are the sum of the squares of  $W_{aa}^F$ ,  $W_{aa}^B$ ,  $W_{ra}^F$ ,  $W_{ra}^B$  and  $W^4$  matrices.  $L(\hat{y}^t, y^t)$  represents the loss function

for each slice of image and is given by

$$L(\hat{y}^t, y^t) = \frac{1}{N}(-y^t \log \hat{y}^t - (1 - y^t) \log(1 - \hat{y}^t)) \quad (8.5)$$

where  $\hat{y}^t$  is the slice of image of predicted crack,  $y^t$  is the slice of image of actual crack, and  $N = 540$  is the number of samples in the training set.

Due to the randomness in the dropout and weight initialization, the machine learning model has been trained 20 different times. The model with the best training and validation loss is adopted for testing on test data. The proposed machine learning model is used to predict the crack path in polycrystalline graphene sheet. In the next section we will compare the crack path predicted by the proposed machine learning model and MD simulations.

#### 8.5.2.5 Predictions of Machine Learning Model

Plots of training and validation loss functions versus the number of epoch for learning rate  $\eta = 4 \times 10^{-4}$  are shown in Fig. 8.14a. It can be observed that training and validation loss values are decreasing with increase in the number of epochs. The validation and training loss have similar trend and values indicating that there over or underfitting is not occurring in the machine learning model.

The crack lengths obtained from the proposed machine learning model and MD simulations are compared in Fig. 8.14b and Fig. 8.14c. It can be observed that in general the crack lengths predicted by the machine learning model are in good agreement with those obtained from molecular dynamics. The difference between the two crack lengths become smaller as the average grain size of polycrystalline sheets increases. This is due to the fewer number of grain boundaries in the domain which cause less kinking in the crack growth path.

Our machine learning model is able to predict the crack propagation path on the test set. A select number of input images of polycrystalline sheets and the predicted

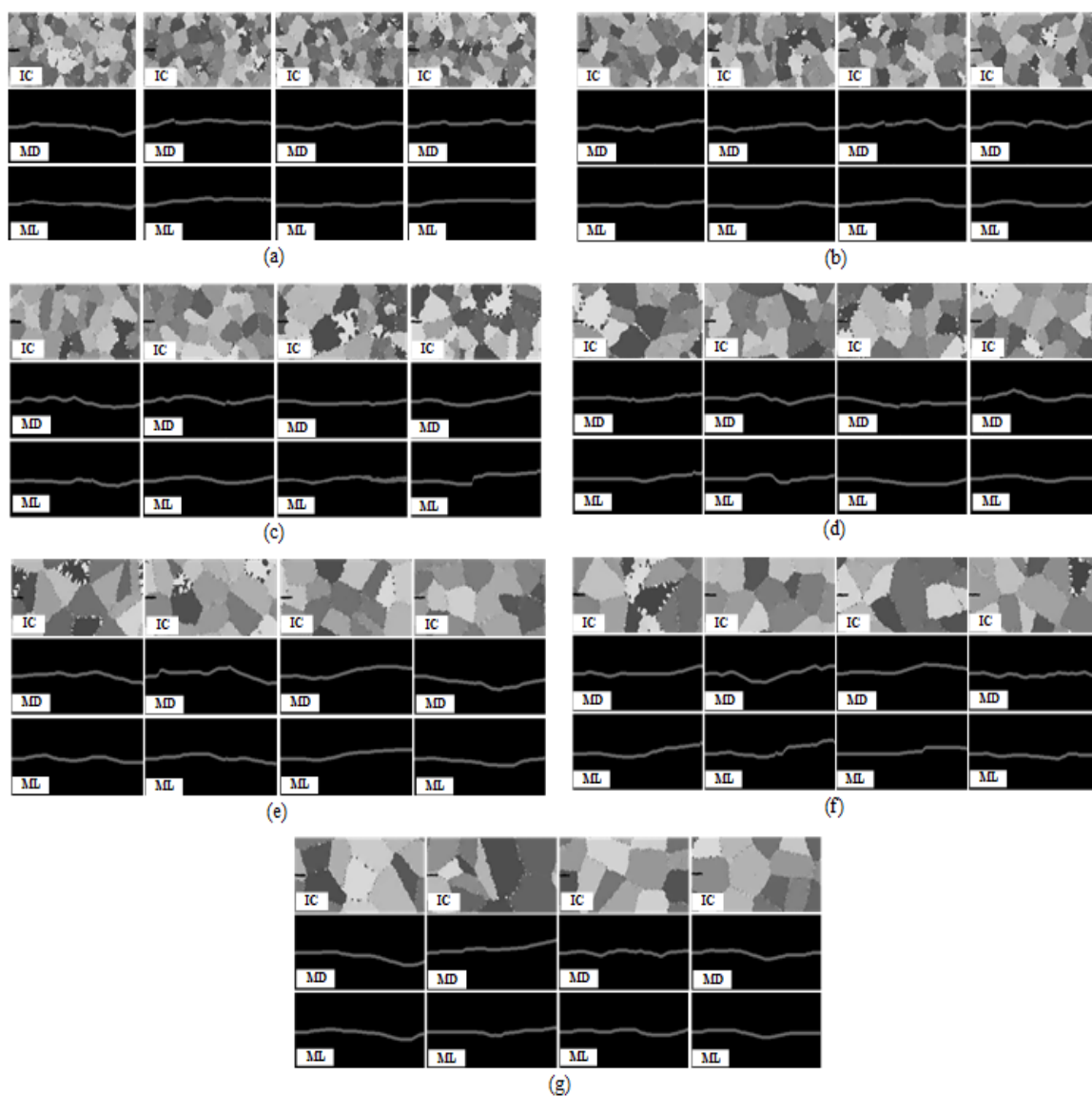


Figure 8.15: Crack propagation path obtained from MD simulations and machine learning model in polycrystalline graphene sheets with average grain sizes (a) 3 nm, (b) 4 nm, (c) 5 nm, (d) 6 nm, (e) 7 nm, (f) 8 nm, and (g) 9 nm. Greyscale image IC shows the initial configuration of the graphene sheet colored based on grain orientation, MD presents the fully grown crack obtained from MD simulations, and ML shows the fully grown crack predicted by machine learning model. These images are not used in the training process of the machine learning model.

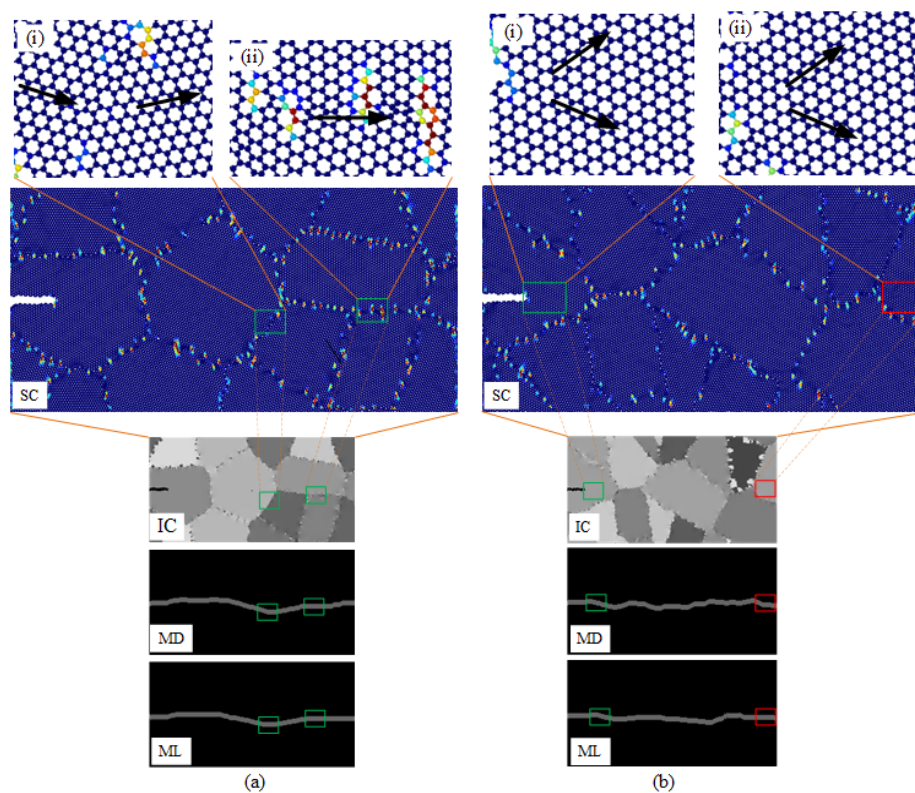


Figure 8.16: Crack propagation path obtained from MD simulations and machine learning model in polycrystalline graphene sheets with average grain sizes (a) 9 nm, and (b) 8 nm. Image SC shows the contour plots based on  $y$ -component of stress, image IC shows the initial configuration of the graphene sheet colored based on grain orientation, MD gives the fully grown crack obtained from MD simulations, and ML shows the fully grown crack predicted by machine learning model. These images are not used in the training process of the machine learning model.

crack paths by molecular dynamics and proposed ML model are shown in Fig. 8.15. It can be observed that in general the predicted crack path by the ML model is in good agreement with the MD simulations. The ML model can detect the grain boundaries and the crack kinks when it reaches a grain boundary to grow along a zigzag path in the next grain or to grow along the grain boundary as are shown in Fig. 8.16a. Hence, model is able to capture both intragranular and intergranular crack growth.

On the other hand, the machine learning model sometimes struggles to predict the crack path correctly if the grain orientation is close to  $30^\circ$ . An example of this is shown in Fig. 8.16b. This is due to the presence of two zigzag directions for crack

growth in grains with orientation close to  $30^\circ$  as shown in Fig. 8.16b(i) and b(ii). Since the crack growth path is not unique for such grains, in some cases ML model predicts correctly but in some cases ML model predicts the bisector line of these directions as the growth path. But when there is only one best possible crack growth direction, as shown in the zoomed-in images Fig. 8.16a, it can predict the crack propagation path.

## 8.6 Conclusion

In this paper a machine learning model based on the convolutional neural network and bidirectional recurrent neural network is proposed to predict the fracture evolution in polycrystalline graphene. Molecular dynamic simulations conducted on realistic models of polycrystalline sheet were used to obtain the data required to train and test the model. Important features such as grain orientation and the location of grain boundary is automatically extracted by the CNN and used in predicting the crack path by Bi-RNN. The proposed machine learning model was able to predict the crack path on polycrystalline graphene sheet with high accuracy and provides the results instantaneously.

## CHAPTER 9: Summary

RNEMD method has been employed to study thermal behavior of h-BN nanoribbon and C<sub>3</sub>N nanotubes. Kapitza conductance of the grain boundary and effective thermal conductivity of the h-BN nano ribbon has been evaluated. Our results showed that Kapitza conductance of grain boundary and effective thermal conductivity of h-BN nanoribbon decreases with increase in misorientation angle. Ballistic to diffusive transition length, dispersion curves, density of states, and thermal conductivity of C<sub>3</sub>NNT and CNT has been calculated. MD simulations indicated that thermal conductivity and ballistic to diffusive transition length of C<sub>3</sub>NNT are lower than that of the CNT.

MD simulations are used to study the thermo-mechanical properties of graphene-like two dimensional material with focus on MoS<sub>2</sub> and graphene nano sheets. Our simulations indicated that MoS<sub>2</sub> and graphene fails through brittle crack propagation. Griffith theory fails at nanoscale cracks of MoS<sub>2</sub>. Quantized fracture mechanics showed better results than Inglis theory at sharper cracks in MoS<sub>2</sub>. Environmental molecules like H<sub>2</sub> and O<sub>2</sub> can react with graphene and eventually accelerate the failure process. Our results showed that due to stress corrosion cracking, crack can grow in monocrystalline graphene in the presence of O<sub>2</sub> molecules. Sub-critical cracking may occur in strained graphene sheet in the presence of O<sub>2</sub> molecules. Extracted traction separation laws of the hydrogenated grain boundaries of bicrystalline graphene sheet. Fracture properties significantly depend on the hydrogen adsorption site at the grain boundaries of the bicrystalline graphene. Our results indicated that crack propagation path in polycrystalline graphene changes from intragranular to intergranular with increase in hydrogenation at the grain boundaries. Hydrogenation of grain bound-

aries degrades the bicrystalline and polycrystalline graphene, eventually reducing the strength and fracture toughness.

Advanced machine learning models have been developed for rapid prediction of the fracture process in polycrystalline graphene sheet. Data from the MD simulations has been used to train the ML model. Optimally trained ML model is capable of predicting the fully grown crack in polycrystalline graphene sheet instantaneously. Thus reducing the computational cost by several folds.

## REFERENCES

- [1] M. S. R. Elapolu and A. Tabarraei, “Kapitza conductance of symmetric tilt grain boundaries of monolayer boron nitride,” *Computational Materials Science*, vol. 144, pp. 161–169, 2018.
- [2] M. S. R. Elapolu, A. Tabarraei, A. Reihani, and A. Ramazani, “Phononic thermal transport properties of  $c_3n$  nanotubes,” *Nanotechnology*, vol. 31, no. 3, p. 035705, 2019.
- [3] M. S. R. Elapolu, A. Tabarraei, X. Wang, and D. E. Spearot, “Fracture mechanics of multi-layer molybdenum disulfide,” *Engineering Fracture Mechanics*, 2019.
- [4] M. S. R. Elapolu and A. Tabarraei, “An atomistic study of the stress corrosion cracking in graphene,” *The Journal of Physical Chemistry A*, vol. 124, no. 35, pp. 7060–7070, 2020.
- [5] M. S. R. Elapolu and A. Tabarraei, “Atomistic simulation based cohesive zone law of hydrogenated grain boundaries of graphene,” *The Journal of Physical Chemistry C*, 2020.
- [6] M. S. R. Elapolu and A. Tabarraei, “Mechanical and fracture properties of polycrystalline graphene with hydrogenated grain boundaries,” *The Journal of Physical Chemistry C*, 2021.
- [7] M. S. R. Elapolu, M. I. R. Shishir, and A. Tabarraei, “A novel approach for studying crack propagation in polycrystalline graphene using machine learning algorithms.” 2021.
- [8] K. S. Novoselov, A. K. Geim, S. V. Morozov, D. Jiang, Y. Zhang, S. V. Dubonos, I. V. Grigorieva, and A. A. Firsov, “Electric field effect in atomically thin carbon films,” *Science*, vol. 306, pp. 666–669, 2004.
- [9] C. Lee, X. Wei, J. W. Kysar, and J. Hone, “Measurement of the elastic properties and intrinsic strength of monolayer graphene,” *science*, vol. 321, no. 5887, pp. 385–388, 2008.
- [10] F. Liu, P. Ming, and J. Li, “Ab initio calculation of ideal strength and phonon instability of graphene under tension,” *Physical Review B*, vol. 76, no. 6, p. 064120, 2007.
- [11] D. Akinwande, C. J. Brennan, J. S. Bunch, P. Egberts, J. R. Felts, H. Gao, R. Huang, J.-S. Kim, T. Li, Y. Li, *et al.*, “A review on mechanics and mechanical properties of 2d materials—graphene and beyond,” *Extreme Mechanics Letters*, vol. 13, pp. 42–77, 2017.

- [12] A. Tabarraei, S. Shadalou, and J.-H. Song, “Mechanical properties of graphene nanoribbons with disordered edges,” *Computational Materials Science*, vol. 96, pp. 10–19, 2015.
- [13] A. A. Balandin, S. Ghosh, W. Bao, I. Calizo, D. Teweldebrhan, F. Miao, and C. N. Lau, “Superior thermal conductivity of single-layer graphene,” *Nano letters*, vol. 8, no. 3, pp. 902–907, 2008.
- [14] S. Ghosh, I. Calizo, D. Teweldebrhan, E. P. Pokatilov, D. L. Nika, A. A. Balandin, W. Bao, F. Miao, and C. N. Lau, “Extremely high thermal conductivity of graphene: Prospects for thermal management applications in nanoelectronic circuits,” *Applied Physics Letters*, vol. 92, no. 15, p. 151911, 2008.
- [15] Z. Guo, D. Zhang, and X.-G. Gong, “Thermal conductivity of graphene nanoribbons,” *Applied physics letters*, vol. 95, no. 16, p. 163103, 2009.
- [16] K. I. Bolotin, K. J. Sikes, Z. Jiang, M. Klima, G. Fudenberg, J. e. Hone, P. Kim, and H. Stormer, “Ultrahigh electron mobility in suspended graphene,” *Solid state communications*, vol. 146, no. 9-10, pp. 351–355, 2008.
- [17] K. Novoselov, S. Morozov, T. Mohinddin, L. Ponomarenko, D. Elias, R. Yang, I. Barbolina, P. Blake, T. Booth, D. Jiang, *et al.*, “Electronic properties of graphene,” *physica status solidi (b)*, vol. 244, no. 11, pp. 4106–4111, 2007.
- [18] A. C. Neto, F. Guinea, N. M. Peres, K. S. Novoselov, and A. K. Geim, “The electronic properties of graphene,” *Reviews of modern physics*, vol. 81, no. 1, p. 109, 2009.
- [19] B. Zhan, C. Li, J. Yang, G. Jenkins, W. Huang, and X. Dong, “Graphene field-effect transistor and its application for electronic sensing,” *Small*, vol. 10, no. 20, pp. 4042–4065, 2014.
- [20] S. Kim, J. Nah, I. Jo, D. Shahrjerdi, L. Colombo, Z. Yao, E. Tutuc, and S. K. Banerjee, “Realization of a high mobility dual-gated graphene field-effect transistor with al 2 o 3 dielectric,” *Applied Physics Letters*, vol. 94, no. 6, p. 062107, 2009.
- [21] M. C. Lemme, T. J. Echtermeyer, M. Baus, and H. Kurz, “A graphene field-effect device,” *IEEE Electron Device Letters*, vol. 28, no. 4, pp. 282–284, 2007.
- [22] Y. Wang, Z. Shi, Y. Huang, Y. Ma, C. Wang, M. Chen, and Y. Chen, “Supercapacitor devices based on graphene materials,” *The Journal of Physical Chemistry C*, vol. 113, no. 30, pp. 13103–13107, 2009.
- [23] Y. B. Tan and J.-M. Lee, “Graphene for supercapacitor applications,” *Journal of Materials Chemistry A*, vol. 1, no. 47, pp. 14814–14843, 2013.

- [24] C. Liu, Z. Yu, D. Neff, A. Zhamu, and B. Z. Jang, "Graphene-based supercapacitor with an ultrahigh energy density," *Nano letters*, vol. 10, no. 12, pp. 4863–4868, 2010.
- [25] Z. Yang, J. Tian, Z. Yin, C. Cui, W. Qian, and F. Wei, "Carbon nanotube-and graphene-based nanomaterials and applications in high-voltage supercapacitor: a review," *Carbon*, vol. 141, pp. 467–480, 2019.
- [26] R. J. Young, I. A. Kinloch, L. Gong, and K. S. Novoselov, "The mechanics of graphene nanocomposites: a review," *Composites Science and Technology*, vol. 72, no. 12, pp. 1459–1476, 2012.
- [27] J. Du and H.-M. Cheng, "The fabrication, properties, and uses of graphene/polymer composites," *Macromolecular Chemistry and Physics*, vol. 213, no. 10-11, pp. 1060–1077, 2012.
- [28] Z. Zhao, P. Bai, W. Du, B. Liu, D. Pan, R. Das, C. Liu, and Z. Guo, "An overview of graphene and its derivatives reinforced metal matrix composites: Preparation, properties and applications," *Carbon*, 2020.
- [29] A. H. Mashhadzadeh, A. Fereidoon, and M. G. Ahangari, "Experimental and multiscale quantum mechanics modeling of the mechanical properties of pvc/graphene nanocomposite," *Journal of Composite Materials*, vol. 54, no. 29, pp. 4575–4590, 2020.
- [30] A. H. Mashhadzadeh, A. Fereidoon, and M. G. Ahangari, "Combining density functional theory-finite element multi-scale method to predict mechanical properties of polypropylene/graphene nanocomposites: Experimental study," *Materials Chemistry and Physics*, vol. 201, pp. 214–223, 2017.
- [31] J. S. Bunch, A. M. Van Der Zande, S. S. Verbridge, I. W. Frank, D. M. Tanenbaum, J. M. Parpia, H. G. Craighead, and P. L. McEuen, "Electromechanical resonators from graphene sheets," *Science*, vol. 315, no. 5811, pp. 490–493, 2007.
- [32] Z. H. Khan, A. R. Kermany, A. Öchsner, and F. Iacopi, "Mechanical and electromechanical properties of graphene and their potential application in mems," *Journal of Physics D: Applied Physics*, vol. 50, no. 5, p. 053003, 2017.
- [33] C. S. Boland, U. Khan, G. Ryan, S. Barwich, R. Charifou, A. Harvey, C. Backes, Z. Li, M. S. Ferreira, M. E. Möbius, *et al.*, "Sensitive electromechanical sensors using viscoelastic graphene-polymer nanocomposites," *Science*, vol. 354, no. 6317, pp. 1257–1260, 2016.
- [34] M. Hossain, S. Muktaadhir, and M. M. Rana, "Multi-structural optical devices modeling using graphene tri-layer sheets," *Optik*, vol. 127, no. 15, pp. 5841–5851, 2016.

- [35] P. C. Sarker, M. M. Rana, and A. K. Sarkar, “A simple fdtd approach for the analysis and design of graphene based optical devices,” *Optik*, vol. 144, pp. 1–8, 2017.
- [36] R. S. Pease, “An x-ray study of boron nitride,” *Acta Crystallographica*, vol. 5, no. 3, pp. 356–361, 1952.
- [37] T. Ishii, T. Sato, Y. Sekikawa, and M. Iwata, “Growth of whiskers of hexagonal boron nitride,” *Journal of Crystal Growth*, vol. 52, pp. 285–289, 1981.
- [38] R. T. Paine and C. K. Narula, “Synthetic routes to boron nitride,” *Chemical Reviews*, vol. 90, no. 1, pp. 73–91, 1990.
- [39] K. Watanabe, T. Taniguchi, and H. Kanda, “Direct-bandgap properties and evidence for ultraviolet lasing of hexagonal boron nitride single crystal,” *Nature materials*, vol. 3, no. 6, p. 404, 2004.
- [40] Y. Kubota, K. Watanabe, O. Tsuda, and T. Taniguchi, “Deep ultraviolet light-emitting hexagonal boron nitride synthesized at atmospheric pressure,” *Science*, vol. 317, no. 5840, pp. 932–934, 2007.
- [41] M. Silly, P. Jaffrennou, J. Barjon, J.-S. Lauret, F. Ducastelle, A. Loiseau, E. Obraztsova, B. Attal-Tretout, and E. Rosencher, “Luminescence properties of hexagonal boron nitride: Cathodoluminescence and photoluminescence spectroscopy measurements,” *Physical Review B*, vol. 75, no. 8, p. 085205, 2007.
- [42] L. Boldrin, F. Scarpa, R. Chowdhury, and S. Adhikari, “Effective mechanical properties of hexagonal boron nitride nanosheets,” *Nanotechnology*, vol. 22, no. 50, p. 505702, 2011.
- [43] Q. Peng, W. Ji, and S. De, “Mechanical properties of the hexagonal boron nitride monolayer: Ab initio study,” *Computational Materials Science*, vol. 56, pp. 11–17, 2012.
- [44] A. Nag, K. Raidongia, K. P. Hembram, R. Datta, U. V. Waghmare, and C. Rao, “Graphene analogues of bn: novel synthesis and properties,” *ACS nano*, vol. 4, no. 3, pp. 1539–1544, 2010.
- [45] M. Topsakal, E. Aktürk, and S. Ciraci, “First-principles study of two-and one-dimensional honeycomb structures of boron nitride,” *Physical Review B*, vol. 79, no. 11, p. 115442, 2009.
- [46] H. Zhou, J. Zhu, Z. Liu, Z. Yan, X. Fan, J. Lin, G. Wang, Q. Yan, T. Yu, P. M. Ajayan, and J. M. Tour, “High thermal conductivity of suspended few-layer hexagonal boron nitride sheets, nano research,” *Nano Research*, vol. 7, no. 8, pp. 1232–1240, 2014.

- [47] I. Jo, M. T. Pettes, J. Kim, K. Watanabe, T. Taniguchi, Z. Yao, and L. Shi, "Thermal conductivity and phonon transport in suspended few-layer hexagonal boron nitride," *Nano Letters*, vol. 13, no. 2, pp. 550–554, 2013.
- [48] A. Tabarraei, "Thermal conductivity of monolayer hexagonal boron nitride nanoribbons," *Computational Materials Science*, vol. 108, pp. 66–71, 2015.
- [49] A. Tabarraei and X. Wang, "Anomalous thermal conductivity of monolayer boron nitride," *Applied Physics Letters*, vol. 108, no. 18, p. 181904, 2016.
- [50] C. R. Dean, A. F. Young, I. Meric, C. Lee, L. Wang, S. Sorgenfrei, K. Watanabe, T. Taniguchi, P. Kim, K. L. Shepard, and J. Hone, "Boron nitride substrates for high-quality graphene electronics," *Nature Nanotechnology*, vol. 5, no. 10, pp. 722–726, 2010.
- [51] R. Decker, Y. Wang, V. W. Brar, W. Regan, H.-Z. Tsai, Q. Wu, W. Gannett, A. Zettl, and M. F. Crommie, "Local electronic properties of graphene on a bn substrate via scanning tunneling microscopy," *Nano Letters*, vol. 11, no. 6, pp. 2291–2295, 2011.
- [52] J. Duan, X. Wang, X. Lai, G. Li, K. Watanabe, T. Taniguchi, M. Zebarjadi, and E. Y. Andrei, "High thermoelectric power factor in graphene/hbn devices," *PNAS*, vol. 113, no. 50, pp. 14272–14276, 2016.
- [53] J. Xue, J. Sanchez-Yamagishi, D. Bulmash, P. Jacquod, A. Deshpande, K. Watanabe, T. Taniguchi, P. Jarillo-Herrero, and B. J. LeRoy, "Scanning tunnelling microscopy and spectroscopy of ultra-flat graphene on hexagonal boron nitride," *Nature Materials*, vol. 10, no. 4, pp. 282–285, 2011.
- [54] S. K. Singhal, V. Kumar, K. Stalin, A. Choudhary, S. Teotia, G. B. Reddy, R. B. Mathur, S. P. Singh, and R. Pasricha, "Gold-nanoparticle-decorated boron nitride nanosheets: Structure and optical properties," *Part. Part. Syst. Charact.*, vol. 30, no. 5, pp. 445–452, 2013.
- [55] A. F. Khan, D. A. C. Brownson, E. P. Randviir, G. C. Smith, and C. E. Banks, "2d hexagonal boron nitride (2d-hbn) explored for the electrochemical sensing of dopamine," *Analytical Chemistry*, vol. 88, no. 19, pp. 9729–9737, 2016.
- [56] C. Zhi, Y. Bando, C. Tang, H. Kuwahara, and D. Golberg, "Large-scale fabrication of boron nitride nanosheets and their utilization in polymeric composites with improved thermal and mechanical properties," *Adv. Mater.*, vol. 21, no. 28, pp. 2889–2893, 2009.
- [57] K. Sato, H. Horibe, T. Shirai, Y. Hotta, H. Nakano, H. Nagai, K. Mitsuishi, and K. Watari, "Thermally conductive composite films of hexagonal boron nitride and polyimide with affinity-enhanced interfaces," *J. Mater. Chem.*, vol. 20, no. 14, pp. 2749–2752, 2010.

- [58] W.-L. Song, P. Wang, L. Cao, A. Anderson, M. J. Meziari, A. J. Farr, and Y.-P. Sun, "Polymer/boron nitride nanocomposite materials for superior thermal transport performance," *Angewandte Chemie International Edition*, vol. 51, no. 26, pp. 6498–6501, 2012.
- [59] C. Zhi, Y. Bando, T. Terao, C. Tang, H. Kuwahara, and D. Golberg, "Towards thermoconductive, electrically insulating polymeric composites with boron nitride nanotubes as fillers," *Advanced Functional Materials*, vol. 19, no. 12, pp. 1857–1862, 2009.
- [60] X. Li and H. Zhu, "Two-dimensional mos2: Properties, preparation, and applications," *Journal of Materiomics*, vol. 1, no. 1, pp. 33–44, 2015.
- [61] T. Li and G. Galli, "Electronic properties of mos2 nanoparticles," *The Journal of Physical Chemistry C*, vol. 111, no. 44, pp. 16192–16196, 2007.
- [62] B. W. Baugher, H. O. Churchill, Y. Yang, and P. Jarillo-Herrero, "Intrinsic electronic transport properties of high-quality monolayer and bilayer mos2," *Nano letters*, vol. 13, no. 9, pp. 4212–4216, 2013.
- [63] C. Ataca, H. Sahin, E. Akturk, and S. Ciraci, "Mechanical and electronic properties of mos2 nanoribbons and their defects," *The Journal of Physical Chemistry C*, vol. 115, no. 10, pp. 3934–3941, 2011.
- [64] K. F. Mak, C. Lee, J. Hone, J. Shan, and T. F. Heinz, "Atomically thin mos 2: a new direct-gap semiconductor," *Physical review letters*, vol. 105, no. 13, p. 136805, 2010.
- [65] A. Splendiani, L. Sun, Y. Zhang, T. Li, J. Kim, C.-Y. Chim, G. Galli, and F. Wang, "Emerging photoluminescence in monolayer mos2," *Nano letters*, vol. 10, no. 4, pp. 1271–1275, 2010.
- [66] B. Radisavljevic, A. Radenovic, J. Brivio, i. V. Giacometti, and A. Kis, "Single-layer mos2 transistors," *Nature nanotechnology*, vol. 6, no. 3, pp. 147–150, 2011.
- [67] R. Sundaram, M. Engel, A. Lombardo, R. Krupke, A. Ferrari, P. Avouris, and M. Steiner, "Electroluminescence in single layer mos2," *Nano letters*, vol. 13, no. 4, pp. 1416–1421, 2013.
- [68] O. Lopez-Sanchez, D. Lembke, M. Kayci, A. Radenovic, and A. Kis, "Ultrasensitive photodetectors based on monolayer mos2," *Nature nanotechnology*, vol. 8, no. 7, pp. 497–501, 2013.
- [69] H. M. Jeong, J. W. Lee, W. H. Shin, Y. J. Choi, H. J. Shin, J. K. Kang, and J. W. Choi, "Nitrogen-doped graphene for high-performance ultracapacitors and the importance of nitrogen-doped sites at basal planes," *Nano letters*, vol. 11, no. 6, pp. 2472–2477, 2011.

- [70] H. Wang, T. Maiyalagan, and X. Wang, "Review on recent progress in nitrogen-doped graphene: synthesis, characterization, and its potential applications," *Acs Catalysis*, vol. 2, no. 5, pp. 781–794, 2012.
- [71] Y. Shao, S. Zhang, M. H. Engelhard, G. Li, G. Shao, Y. Wang, J. Liu, I. A. Aksay, and Y. Lin, "Nitrogen-doped graphene and its electrochemical applications," *Journal of Materials Chemistry*, vol. 20, no. 35, pp. 7491–7496, 2010.
- [72] J. Mahmood, E. K. Lee, M. Jung, D. Shin, H.-J. Choi, J.-M. Seo, S.-M. Jung, D. Kim, F. Li, M. S. Lah, N. Parkd, H.-J. Shinc, J. H. Ohb, and J.-B. Baeka, "Two-dimensional polyaniline (c3n) from carbonized organic single crystals in solid state," *Proceedings of the National Academy of Sciences*, vol. 113, no. 27, pp. 7414–7419, 2016.
- [73] S. Yang, W. Li, C. Ye, G. Wang, H. Tian, C. Zhu, P. He, G. Ding, X. Xie, Y. Liu, *et al.*, "C<sub>3n</sub>-a 2d crystalline, hole-free, tunable-narrow-bandgap semiconductor with ferromagnetic properties," *Advanced Materials*, vol. 29, no. 16, p. 1605625, 2017.
- [74] F. Molani, S. Jalili, and J. Schofield, "A novel candidate for hydrogen storage: Ca-decorated zigzag c<sub>3n</sub> nanotube," *international journal of hydrogen energy*, vol. 41, no. 18, pp. 7431–7437, 2016.
- [75] E. Gao, S.-Z. Lin, Z. Qin, M. J. Buehler, X.-Q. Feng, and Z. Xu, "Mechanical exfoliation of two-dimensional materials," *Journal of the Mechanics and Physics of Solids*, vol. 115, pp. 248–262, 2018.
- [76] J. Yu, J. Li, W. Zhang, and H. Chang, "Synthesis of high quality two-dimensional materials via chemical vapor deposition," *Chemical science*, vol. 6, no. 12, pp. 6705–6716, 2015.
- [77] Z. Yan, J. Lin, Z. Peng, Z. Sun, Y. Zhu, L. Li, C. Xiang, E. L. Samuel, C. Kittrell, and J. M. Tour, "Toward the synthesis of wafer-scale single-crystal graphene on copper foils," *ACS nano*, vol. 6, no. 10, pp. 9110–9117, 2012.
- [78] L. Gan and Z. Luo, "Turning off hydrogen to realize seeded growth of subcentimeter single-crystal graphene grains on copper," *Acs Nano*, vol. 7, no. 10, pp. 9480–9488, 2013.
- [79] Z. Luo, S. Kim, N. Kawamoto, A. M. Rappe, and A. C. Johnson, "Growth mechanism of hexagonal-shape graphene flakes with zigzag edges," *Acs Nano*, vol. 5, no. 11, pp. 9154–9160, 2011.
- [80] P. Y. Huang, C. S. Ruiz-Vargas, A. M. Van Der Zande, W. S. Whitney, M. P. Levendorf, J. W. Kevek, S. Garg, J. S. Alden, C. J. Hustedt, Y. Zhu, *et al.*, "Grains and grain boundaries in single-layer graphene atomic patchwork quilts," *Nature*, vol. 469, no. 7330, pp. 389–392, 2011.

- [81] A. Hashimoto, K. Suenaga, A. Gloter, K. Urita, and S. Iijima, "Direct evidence for atomic defects in graphene layers," *Nature*, vol. 430, no. 7002, pp. 870–873, 2004.
- [82] A. L. Gibb, N. Alem, J.-H. Chen, K. J. Erickson, J. Ciston, A. Gautam, M. Linck, and A. Zettl, "Atomic resolution imaging of grain boundary defects in monolayer chemical vapor deposition-grown hexagonal boron nitride," *Journal of the American Chemical Society*, vol. 135, no. 18, pp. 6758–6761, 2013.
- [83] H. I. Rasool, C. Ophus, and A. Zettl, "Atomic defects in two dimensional materials," *Advanced materials*, vol. 27, no. 38, pp. 5771–5777, 2015.
- [84] M. V. Bracamonte, G. I. Lacconi, S. E. Urreta, and L. E. F. Foa Torres, "On the nature of defects in liquid-phase exfoliated graphene," *The Journal of Physical Chemistry C*, vol. 118, no. 28, pp. 15455–15459, 2014.
- [85] Y. Li, C. Yu, Y. Gan, P. Jiang, J. Yu, Y. Ou, D.-F. Zou, C. Huang, J. Wang, T. Jia, *et al.*, "Mapping the elastic properties of two-dimensional mos 2 via bimodal atomic force microscopy and finite element simulation," *npj Computational Materials*, vol. 4, no. 1, pp. 1–8, 2018.
- [86] H. Zhang, J. Huang, Y. Wang, R. Liu, X. Huai, J. Jiang, and C. Anfuso, "Atomic force microscopy for two-dimensional materials: A tutorial review," *Optics Communications*, vol. 406, pp. 3–17, 2018.
- [87] H. C. Schniepp, K. N. Kudin, J.-L. Li, R. K. Prud'homme, R. Car, D. A. Saville, and I. A. Aksay, "Bending properties of single functionalized graphene sheets probed by atomic force microscopy," *ACS nano*, vol. 2, no. 12, pp. 2577–2584, 2008.
- [88] G. Cao and H. Gao, "Mechanical properties characterization of two-dimensional materials via nanoindentation experiments," *Progress in Materials Science*, vol. 103, pp. 558–595, 2019.
- [89] Y. Zhang and C. Pan, "Measurements of mechanical properties and number of layers of graphene from nano-indentation," *Diamond and Related Materials*, vol. 24, pp. 1–5, 2012.
- [90] Z. Sha, Q. Wan, Q. Pei, S. Quek, Z. Liu, Y. Zhang, and V. Shenoy, "On the failure load and mechanism of polycrystalline graphene by nanoindentation," *Scientific reports*, vol. 4, no. 1, pp. 1–6, 2014.
- [91] S. Plimpton, "Fast parallel algorithms for short-range molecular dynamics," *Journal of computational physics*, vol. 117, no. 1, pp. 1–19, 1995.
- [92] J. Tersoff, "New empirical approach for the structure and energy of covalent systems," *Physical review B*, vol. 37, no. 12, p. 6991, 1988.

- [93] J. Tersoff, "Empirical interatomic potential for silicon with improved elastic properties," *Physical Review B*, vol. 38, no. 14, p. 9902, 1988.
- [94] T. Kumagai, S. Izumi, S. Hara, and S. Sakai, "Development of bond-order potentials that can reproduce the elastic constants and melting point of silicon for classical molecular dynamics simulation," *Computational materials science*, vol. 39, no. 2, pp. 457–464, 2007.
- [95] M. R. Murty and H. A. Atwater, "Empirical interatomic potential for si-h interactions," *Physical Review B*, vol. 51, no. 8, p. 4889, 1995.
- [96] T. Liang, S. R. Phillpot, and S. B. Sinnott, "Parametrization of a reactive many-body potential for mo-s systems," *Physical Review B*, vol. 79, no. 24, p. 245110, 2009.
- [97] L. Pastewka, P. Pou, R. Pérez, P. Gumbsch, and M. Moseler, "Describing bond-breaking processes by reactive potentials: Importance of an environment-dependent interaction range," *Physical Review B*, vol. 78, no. 16, p. 161402, 2008.
- [98] K. Chenoweth, A. C. T. Van Duin, and W. A. Goddard, "Reaxff reactive force field for molecular dynamics simulations of hydrocarbon oxidation," *The Journal of Physical Chemistry A*, vol. 112, no. 5, pp. 1040–1053, 2008.
- [99] H. M. Aktulga, J. C. Fogarty, S. A. Pandit, and A. Y. Grama, "Parallel reactive molecular dynamics: Numerical methods and algorithmic techniques," *Parallel Computing*, vol. 38, no. 4-5, pp. 245–259, 2012.
- [100] F. Müller-Plathe, "A simple nonequilibrium molecular dynamics method for calculating the thermal conductivity," *The Journal of Chemical Physics*, vol. 106, no. 14, pp. 6082–6085, 1997.
- [101] D. M. Heyes, "Pressure tensor of partial-charge and point-dipole lattices with bulk and surface geometries," *Physical Review B*, vol. 49, no. 2, p. 755, 1994.
- [102] T. W. Sirk, S. Moore, and E. F. Brown, "Characteristics of thermal conductivity in classical water models," *The Journal of chemical physics*, vol. 138, no. 6, p. 064505, 2013.
- [103] A. P. Thompson, S. J. Plimpton, and W. Mattson, "General formulation of pressure and stress tensor for arbitrary many-body interaction potentials under periodic boundary conditions," *The Journal of chemical physics*, vol. 131, no. 15, p. 154107, 2009.
- [104] L. Song, L. Ci, H. Lu, P. B. Sorokin, C. Jin, J. Ni, A. G. Kvashnin, D. G. Kvashnin, J. Lou, B. I. Yakobson, *et al.*, "Large scale growth and characterization of atomic hexagonal boron nitride layers," *Nano letters*, vol. 10, no. 8, pp. 3209–3215, 2010.

- [105] H. O. Pierson, "Boron nitride composites by chemical vapor deposition," *Journal of Composite Materials*, vol. 9, no. 3, pp. 228–240, 1975.
- [106] Y. Shi, C. Hamsen, X. Jia, K. K. Kim, A. Reina, M. Hofmann, A. L. Hsu, K. Zhang, H. Li, Z.-Y. Juang, M. S. Dresselhaus, L.-J. Li, and J. Kong, "Synthesis of few-layer hexagonal boron nitride thin film by chemical vapor deposition," *Nano Letters*, vol. 10, no. 10, pp. 4134–4139, 2010.
- [107] J. Philip, P. Hess, T. Feygelson, J. E. Butler, S. Chattopadhyay, K. H. Chen, and L. C. Chen, "Elastic, mechanical, and thermal properties of nanocrystalline diamond films," *Journal of Applied Physics*, vol. 93, no. 4, pp. 2164–2171, 2003.
- [108] Z. Wang, J. E. Alaniz, W. Jang, J. E. Garay, and C. Dames, "Thermal conductivity of nanocrystalline silicon: Importance of grain size and frequency-dependent mean free paths," *Nano Letters*, vol. 11, no. 6, pp. 2206–2213, 2011.
- [109] A. Bagri, S.-P. Kim, R. S. Ruoff, and V. B. Shenoy, "Thermal transport across twin grain boundaries in polycrystalline graphene from nonequilibrium molecular dynamics simulations," *Nano Letters*, vol. 11, no. 9, pp. 3917–3921, 2011.
- [110] A. Cao and J. Qu, "Kapitza conductance of symmetric tilt grain boundaries in graphene," *Journal of Applied Physics*, vol. 111, no. 5, p. 053529, 2012.
- [111] K. Kim, Z. Lee, W. Regan, C. Kisielowski, M. Crommie, and A. Zettl, "Grain boundary mapping in polycrystalline graphene," *ACS nano*, vol. 5, no. 3, pp. 2142–2146, 2011.
- [112] M. S. Elapolu and A. Tabarraei, "Impact of grain boundaries on the heat conductivity of mono-layer hexagonal boron nitride," in *ASME 2017 International Mechanical Engineering Congress and Exposition*, American Society of Mechanical Engineers Digital Collection, 2017.
- [113] J. Hu, X. Ruan, and Y. P. Chen, "Thermal conductivity and thermal rectification in graphene nanoribbons: a molecular dynamics study," *Nano letters*, vol. 9, no. 7, pp. 2730–2735, 2009.
- [114] X. Wang and A. Tabarraei, "Phonon thermal conductivity of monolayer MoS<sub>2</sub>," *Applied Physics Letters*, vol. 108, no. 19, p. 191905, 2016.
- [115] J.-W. Jiang, J.-S. Wang, and B. Li, "Young's modulus of graphene: a molecular dynamics study," *Physical Review B*, vol. 80, no. 11, p. 113405, 2009.
- [116] S. Zhao and J. Xue, "Mechanical properties of hybrid graphene and hexagonal boron nitride sheets as revealed by molecular dynamic simulations," *Journal of Physics D: Applied Physics*, vol. 46, no. 13, p. 135303, 2013.
- [117] X. Wang, A. Tabarraei, and D. E. Spearot, "Fracture mechanics of monolayer molybdenum disulfide," *Nanotechnology*, vol. 26, no. 17, p. 175703, 2015.

- [118] J.-W. Jiang, H. S. Park, and T. Rabczuk, "Molecular dynamics simulations of single-layer molybdenum disulphide (mos2): Stillinger-weber parametrization, mechanical properties, and thermal conductivity," *Journal of Applied Physics*, vol. 114, no. 6, p. 064307, 2013.
- [119] A. Tabarraei, X. Wang, and D. Jia, "Effects of hydrogen adsorption on the fracture properties of graphene," *Computational Materials Science*, vol. 121, pp. 151–158, 2016.
- [120] M. I. Petrescu and M.-G. Balint, "Structure and properties modifications in boron nitride. Part I: Direct polymorphic transformations mechanisms," *U.P.B. Sci. Bull.*, vol. 69, no. 1, pp. 35–42, 2007.
- [121] T.-H. Liu, G. Gajewski, C.-W. Pao, and C.-C. Chang, "Structure, energy, and structural transformations of graphene grain boundaries from atomistic simulations," *Carbon*, vol. 49, no. 7, pp. 2306–2317, 2011.
- [122] S. Plimpton, "Fast parallel algorithms for short-range molecular dynamics," *Journal of Computational Physics*, vol. 117, no. 1, pp. 1–19, 1995.
- [123] A. Kinacı, J. B. Haskins, C. Sevik, and T. Çağın, "Thermal conductivity of bn-c nanostructures," *Phys. Rev. B*, vol. 86, no. 11, p. 115410, 2012.
- [124] C. Sevik, A. Kinaci, J. B. Haskins, and T. Çağın, "Characterization of thermal transport in low-dimensional boron nitride nanostructures," *Phys. Rev. B*, vol. 84, no. 8, p. 085409, 2011.
- [125] E. T. Swartz and R. O. Pohl, "Thermal boundary resistance," *Rev. Mod. Phys.*, vol. 61, no. 3, pp. 605–668, 1989.
- [126] P. K. Schelling, S. R. Phillpot, and P. Keblinski, "Kapitza conductance and phonon scattering at grain boundaries by simulation," *Journal of Applied Physics*, vol. 95, no. 11, pp. 6082–6091, 2004.
- [127] P. G. Klemens, "Theory of thermal conduction in thin ceramic films," *International Journal of Thermophysics*, vol. 22, no. 1, pp. 265–275, 2001.
- [128] P. K. Schelling, S. R. Phillpot, and P. Keblinski, "Comparison of atomic-level simulation methods for computing thermal conductivity," *Phys. Rev. B*, vol. 65, no. 14, p. 144306, 2002.
- [129] P. Keblinski, S. R. Phillpot, D. Wolf, and H. Gleiter, "On the thermodynamic stability of amorphous intergranular films in covalent materials," *Journal of the American Ceramic Society*, vol. 80, no. 3, pp. 717–732, 1997.
- [130] D. Nika, E. Pokatilov, A. Askerov, and A. Balandin, "Phonon thermal conduction in graphene: Role of umklapp and edge roughness scattering," *Physical Review B*, vol. 79, no. 15, p. 155413, 2009.

- [131] I. Frank, D. M. Tanenbaum, A. M. van der Zande, and P. L. McEuen, “Mechanical properties of suspended graphene sheets,” *Journal of Vacuum Science & Technology B: Microelectronics and Nanometer Structures Processing, Measurement, and Phenomena*, vol. 25, no. 6, pp. 2558–2561, 2007.
- [132] F. Scarpa, S. Adhikari, and A. S. Phani, “Effective elastic mechanical properties of single layer graphene sheets,” *Nanotechnology*, vol. 20, no. 6, p. 065709, 2009.
- [133] P. Avouris, “Graphene: electronic and photonic properties and devices,” *Nano letters*, vol. 10, no. 11, pp. 4285–4294, 2010.
- [134] X. Dang, H. Dong, L. Wang, Y. Zhao, Z. Guo, T. Hou, Y. Li, and S.-T. Lee, “Semiconducting graphene on silicon from first-principles calculations,” *ACS nano*, vol. 9, no. 8, pp. 8562–8568, 2015.
- [135] M. Y. Han, B. Özyilmaz, Y. Zhang, and P. Kim, “Energy band-gap engineering of graphene nanoribbons,” *Physical review letters*, vol. 98, no. 20, p. 206805, 2007.
- [136] D. K. Samarakoon and X.-Q. Wang, “Tunable band gap in hydrogenated bilayer graphene,” *ACS nano*, vol. 4, no. 7, pp. 4126–4130, 2010.
- [137] Z. Luo, S. Lim, Z. Tian, J. Shang, L. Lai, B. MacDonald, C. Fu, Z. Shen, T. Yu, and J. Lin, “Pyridinic n doped graphene: synthesis, electronic structure, and electrocatalytic property,” *Journal of Materials Chemistry*, vol. 21, no. 22, pp. 8038–8044, 2011.
- [138] X. Zhou, W. Feng, S. Guan, B. Fu, W. Su, and Y. Yao, “Computational characterization of monolayer  $c_3n$ : A two-dimensional nitrogen-graphene crystal,” *Journal of Materials Research*, vol. 32, no. 15, pp. 2993–3001, 2017.
- [139] B. Mortazavi, “Ultra high stiffness and thermal conductivity of graphene like  $C_3N$ ,” *Carbon*, vol. 118, pp. 25–34, 2017.
- [140] M. Eslami, M. Moradi, and R. Moradi, “Dft investigation of hydrogen adsorption on the  $c_3n$  nanotube,” *Vacuum*, vol. 133, pp. 7–12, 2016.
- [141] J. Hales and A. S. Barnard, “Thermodynamic stability and electronic structure of small carbon nitride nanotubes,” *Journal of Physics: Condensed Matter*, vol. 21, no. 14, p. 144203, 2009.
- [142] S. Jalili, F. Molani, M. Akhavan, and J. Schofield, “Role of defects on structural and electronic properties of zigzag  $c_3n$  nanotubes: a first-principle study,” *Physica E: Low-dimensional Systems and Nanostructures*, vol. 56, pp. 48–54, 2014.
- [143] H. Wang, H. Wu, and J. Yang, “ $C_3n$ : a two dimensional semiconductor material with high stiffness, superior stability and bending poisson’s effect,” *arXiv preprint arXiv:1703.08754*, 2017.

- [144] A. Bagri, S.-P. Kim, R. S. Ruoff, and V. B. Shenoy, "Thermal transport across twin grain boundaries in polycrystalline graphene from nonequilibrium molecular dynamics simulations," *Nano letters*, vol. 11, no. 9, pp. 3917–3921, 2011.
- [145] M. Alaghemandi, E. Algaer, M. C. Böhm, and F. Müller-Plathe, "The thermal conductivity and thermal rectification of carbon nanotubes studied using reverse non-equilibrium molecular dynamics simulations," *Nanotechnology*, vol. 20, no. 11, p. 115704, 2009.
- [146] A. Tabarraei and X. Wang, "Anomalous thermal conductivity of monolayer boron nitride," *Applied Physics Letters*, vol. 108, no. 18, p. 181904, 2016.
- [147] A. Cao and J. Qu, "Kapitza conductance of symmetric tilt grain boundaries in graphene," *Journal of Applied Physics*, vol. 111, no. 5, p. 053529, 2012.
- [148] A. Tabarraei, "Thermal conductivity of monolayer hexagonal boron nitride nanoribbons," *Computational Materials Science*, vol. 108, pp. 66–71, 2015.
- [149] E. N. Koukaras, G. Kalosakas, C. Galiotis, and K. Papagelis, "Phonon properties of graphene derived from molecular dynamics simulations," *Scientific reports*, vol. 5, p. 12923, 2015.
- [150] B. Mortazavi and S. Ahzi, "Thermal conductivity and tensile response of defective graphene: A molecular dynamics study," *Carbon*, vol. 63, pp. 460–470, 2013.
- [151] A. Tabarraei and X. Wang, "A molecular dynamics study of nanofracture in monolayer boron nitride," *Materials Science and Engineering: A*, vol. 641, pp. 225–230, 2015.
- [152] S. G. Volz and G. Chen, "Molecular-dynamics simulation of thermal conductivity of silicon crystals," *Physical Review B*, vol. 61, no. 4, p. 2651, 2000.
- [153] J.-H. Zou and B.-Y. Cao, "Phonon thermal properties of graphene on h-bn from molecular dynamics simulations," *Applied Physics Letters*, vol. 110, no. 10, p. 103106, 2017.
- [154] P. Schelling, S. Phillpot, and P. Keblinski, "Phonon wave-packet dynamics at semiconductor interfaces by molecular-dynamics simulation," *Applied Physics Letters*, vol. 80, no. 14, pp. 2484–2486, 2002.
- [155] S.-c. Wang, X.-g. Liang, X.-h. Xu, and T. Ohara, "Thermal conductivity of silicon nanowire by nonequilibrium molecular dynamics simulations," *Journal of Applied Physics*, vol. 105, no. 1, p. 014316, 2009.
- [156] A. Kınacı, J. B. Haskins, C. Sevik, and T. Çağın, "Thermal conductivity of bn-c nanostructures," *Physical Review B*, vol. 86, no. 11, p. 115410, 2012.

- [157] C. Sevik, A. Kinaci, J. B. Haskins, and T. Çağın, “Characterization of thermal transport in low-dimensional boron nitride nanostructures,” *Physical Review B*, vol. 84, no. 8, p. 085409, 2011.
- [158] H. Berendsen, “Hjc berendsen, jpm postma, wf van gunsteren, a. dinola, and jr haak, j. chem. phys. 81, 3684 (1984).,” *J. Chem. Phys.*, vol. 81, p. 3684, 1984.
- [159] F. Müller-Plathe, “A simple nonequilibrium molecular dynamics method for calculating the thermal conductivity,” *The Journal of chemical physics*, vol. 106, no. 14, pp. 6082–6085, 1997.
- [160] A. Cao and J. Qu, “Size dependent thermal conductivity of single-walled carbon nanotubes,” *Journal of Applied Physics*, vol. 112, no. 1, p. 013503, 2012.
- [161] J. Turney, A. McGaughey, and C. Amon, “Assessing the applicability of quantum corrections to classical thermal conductivity predictions,” *Physical Review B*, vol. 79, no. 22, p. 224305, 2009.
- [162] S.-c. Wang, X.-g. Liang, and X.-h. Xu, “Thermal conductivity of silicon nanowire by nonequilibrium molecular dynamics simulations,” in *ASME 2008 First International Conference on Micro/Nanoscale Heat Transfer*, pp. 1155–1161, American Society of Mechanical Engineers, 2008.
- [163] A. S. Henry and G. Chen, “Spectral phonon transport properties of silicon based on molecular dynamics simulations and lattice dynamics,” *Journal of Computational and Theoretical Nanoscience*, vol. 5, no. 2, pp. 141–152, 2008.
- [164] L. T. Kong, “Phonon dispersion measured directly from molecular dynamics simulations,” *Computer Physics Communications*, vol. 182, no. 10, pp. 2201–2207, 2011.
- [165] L. D. Landau and E. M. Lifshitz, “Physique statistique,” 1984.
- [166] V. Tewary, “Green-function method for lattice statics,” *Advances in Physics*, vol. 22, no. 6, pp. 757–810, 1973.
- [167] L. T. Kong, G. Bartels, C. Campaña, C. Denniston, and M. H. Müser, “Implementation of green’s function molecular dynamics: An extension to lammmps,” *Computer Physics Communications*, vol. 180, no. 6, pp. 1004–1010, 2009.
- [168] T. Schneider and E. Stoll, “Molecular-dynamics study of a three-dimensional one-component model for distortive phase transitions,” *Physical Review B*, vol. 17, no. 3, p. 1302, 1978.
- [169] B. Dünweg and W. Paul, “Brownian dynamics simulations without gaussian random numbers,” *International Journal of Modern Physics C*, vol. 2, no. 03, pp. 817–827, 1991.

- [170] L. Lindsay, D. Broido, and N. Mingo, "Lattice thermal conductivity of single-walled carbon nanotubes: Beyond the relaxation time approximation and phonon-phonon scattering selection rules," *Physical Review B*, vol. 80, no. 12, p. 125407, 2009.
- [171] A. Reihani, A. Soleimani, S. Kargar, V. Sundararaghavan, and A. Ramazani, "Graphyne nanotubes: Materials with ultralow phonon mean free path and strong optical phonon scattering for thermoelectric applications," *The Journal of Physical Chemistry C*, 2018.
- [172] M. Asheghi, K. Kurabayashi, R. Kasnavi, and K. Goodson, "Thermal conduction in doped single-crystal silicon films," *Journal of applied physics*, vol. 91, no. 8, pp. 5079–5088, 2002.
- [173] N. Yang, G. Zhang, and B. Li, "Ultralow thermal conductivity of isotope-doped silicon nanowires," *Nano letters*, vol. 8, no. 1, pp. 276–280, 2008.
- [174] J. Zou, D. Kotchetkov, A. Balandin, D. Florescu, and F. H. Pollak, "Thermal conductivity of gan films: Effects of impurities and dislocations," *Journal of applied physics*, vol. 92, no. 5, pp. 2534–2539, 2002.
- [175] M. Chhowalla, H. S. Shin, G. Eda, L.-J. Li, K. P. Loh, and H. Zhang, "The chemistry of two-dimensional layered transition metal dichalcogenide nanosheets," *Nature chemistry*, vol. 5, no. 4, p. 263, 2013.
- [176] M. Chhowalla, Z. Liu, and H. Zhang, "Two-dimensional transition metal dichalcogenide (tmd) nanosheets," *Chemical Society Reviews*, vol. 44, no. 9, pp. 2584–2586, 2015.
- [177] S. Bertolazzi, J. Brivio, and A. Kis, "Stretching and breaking of ultrathin mos<sub>2</sub>," *ACS nano*, vol. 5, no. 12, pp. 9703–9709, 2011.
- [178] A. Kis, D. Mihailovic, M. Remskar, A. Mrzel, A. Jesih, I. Piwonski, A. J. Kulik, W. Benoît, and L. Forró, "Shear and young's moduli of mos<sub>2</sub> nanotube ropes," *Advanced Materials*, vol. 15, no. 9, pp. 733–736, 2003.
- [179] S. Wang, Z. Qin, G. S. Jung, F. J. Martin-Martinez, K. Zhang, M. J. Buehler, and J. H. Warner, "Atomically sharp crack tips in monolayer mos<sub>2</sub> and their enhanced toughness by vacancy defects," *ACS nano*, vol. 10, no. 11, pp. 9831–9839, 2016.
- [180] T. H. Ly, J. Zhao, M. O. Cichocka, L.-J. Li, and Y. H. Lee, "Dynamical observations on the crack tip zone and stress corrosion of two-dimensional mos<sub>2</sub>," *Nature communications*, vol. 8, p. 14116, 2017.
- [181] S.-Q. Yang, W.-L. Tian, Y.-H. Huang, P. Ranjith, and Y. Ju, "An experimental and numerical study on cracking behavior of brittle sandstone containing two non-coplanar fissures under uniaxial compression," *Rock Mechanics and Rock Engineering*, vol. 49, no. 4, pp. 1497–1515, 2016.

- [182] E. Meyer, "Atomic force microscopy," *Progress in surface science*, vol. 41, no. 1, pp. 3–49, 1992.
- [183] C. R. Blanchard, "Atomic force microscopy," *The chemical educator*, vol. 1, no. 5, pp. 1–8, 1996.
- [184] G. Pharr and W. Oliver, "Measurement of thin film mechanical properties using nanoindentation," *Mrs Bulletin*, vol. 17, no. 7, pp. 28–33, 1992.
- [185] S. Suresh and A. Giannakopoulos, "A new method for estimating residual stresses by instrumented sharp indentation," *Acta Materialia*, vol. 46, no. 16, pp. 5755–5767, 1998.
- [186] P. Zhang, L. Ma, F. Fan, Z. Zeng, C. Peng, P. E. Loya, Z. Liu, Y. Gong, J. Zhang, X. Zhang, *et al.*, "Fracture toughness of graphene," *Nature communications*, vol. 5, p. 3782, 2014.
- [187] M. Dewapriya and S. Meguid, "Atomistic modeling of out-of-plane deformation of a propagating griffith crack in graphene," *Acta Mechanica*, vol. 228, no. 9, pp. 3063–3075, 2017.
- [188] R. C. Cooper, C. Lee, C. A. Marianetti, X. Wei, J. Hone, and J. W. Kysar, "Nonlinear elastic behavior of two-dimensional molybdenum disulfide," *Physical Review B*, vol. 87, no. 3, p. 035423, 2013.
- [189] H. Bao, Y. Huang, Z. Yang, Y. Sun, Y. Bai, Y. Miao, P. K. Chu, K. Xu, and F. Ma, "Molecular dynamics simulation of nano-crack propagation in single-layer mos2 nanosheets," *The Journal of Physical Chemistry C*, 2017.
- [190] A. A. Griffith and M. Eng, "Vi. the phenomena of rupture and flow in solids," *Phil. Trans. R. Soc. Lond. A*, vol. 221, no. 582-593, pp. 163–198, 1921.
- [191] F. Wypych and R. Schöllhorn, "1t-mos 2, a new metallic modification of molybdenum disulfide," *Journal of the Chemical Society, Chemical Communications*, no. 19, pp. 1386–1388, 1992.
- [192] A. Stukowski, "Visualization and analysis of atomistic simulation data with ovito—the open visualization tool," *Modelling and Simulation in Materials Science and Engineering*, vol. 18, no. 1, p. 015012, 2009.
- [193] D. Tromans and J. Meech, "Fracture toughness and surface energies of covalent minerals: theoretical estimates," *Minerals engineering*, vol. 17, no. 1, pp. 1–15, 2004.
- [194] N. M. Pugno and R. S. Ruoff, "Quantized fracture mechanics," *Philosophical Magazine*, vol. 84, no. 27, pp. 2829–2845, 2004.
- [195] P. Marcus, *Corrosion mechanisms in theory and practice*. CRC Press, 2011.

- [196] A. King, G. Johnson, D. Engelberg, W. Ludwig, and J. Marrow, "Observations of intergranular stress corrosion cracking in a grain-mapped polycrystal," *Science*, vol. 321, no. 5887, pp. 382–385, 2008.
- [197] R. Gangloff, "Hydrogen assisted cracking of high strength alloys," tech. rep., DTIC Document, 2003.
- [198] T. Michalske and S. Freiman, "A molecular mechanism for stress corrosion in vitreous silica," *Journal of the American Ceramic Society*, vol. 66, no. 4, pp. 284–288, 1983.
- [199] N. Das, K. Suzuki, Y. Takeda, K. Ogawa, and T. Shoji, "Quantum chemical molecular dynamics study of stress corrosion cracking behavior for fcc Fe and Fe-Cr surfaces," *Corrosion Science*, vol. 50, no. 6, pp. 1701–1706, 2008.
- [200] P. Arnoux, "Atomistic simulations of stress corrosion cracking," *Corrosion Science*, vol. 52, no. 4, pp. 1247–1257, 2010.
- [201] R. Matsumoto, S. Taketomi, S. Matsumoto, and N. Miyazaki, "Atomistic simulations of hydrogen embrittlement," *International Journal of Hydrogen Energy*, vol. 34, no. 23, pp. 9576–9584, 2009.
- [202] A. Barnoush and H. Vehoff, "In situ electrochemical nanoindentation: A technique for local examination of hydrogen embrittlement," *Corrosion Science*, vol. 50, no. 1, pp. 259–267, 2008.
- [203] M. Xu, A. Tabarraei, J. T. Paci, J. Oswald, and T. Belytschko, "A coupled quantum/continuum mechanics study of graphene fracture," *International journal of fracture*, vol. 173, no. 2, pp. 163–173, 2012.
- [204] B. Zhang, L. Mei, and H. Xiao, "Nanofracture in graphene under complex mechanical stresses," *Applied Physics Letters*, vol. 101, no. 12, p. 121915, 2012.
- [205] M.-Q. Le and R. C. Batra, "Single-edge crack growth in graphene sheets under tension," *Computational Materials Science*, vol. 69, pp. 381–388, 2013.
- [206] M. Dewapriya, R. Rajapakse, and A. Phani, "Atomistic and continuum modelling of temperature-dependent fracture of graphene," *International Journal of Fracture*, vol. 187, no. 2, pp. 199–212, 2014.
- [207] Y. Hwangbo, C.-K. Lee, S.-M. Kim, J.-H. Kim, K.-S. Kim, B. Jang, H.-J. Lee, S.-K. Lee, S.-S. Kim, J.-H. Ahn, *et al.*, "Fracture characteristics of monolayer CVD-graphene," *Scientific Reports*, vol. 4, p. 4439, 2014.
- [208] M. Topsakal, S. Cahangirov, and S. Ciraci, "The response of mechanical and electronic properties of graphene to the elastic strain," *Applied Physics Letters*, vol. 96, no. 9, p. 091912, 2010.

- [209] H. C. Schniepp, J.-L. Li, M. J. McAllister, H. Sai, M. Herrera-Alonso, D. H. Adamson, R. K. Prud'homme, R. Car, D. A. Saville, and I. A. Aksay, "Functionalized single graphene sheets derived from splitting graphite oxide," *The Journal of Physical Chemistry B*, vol. 110, no. 17, pp. 8535–8539, 2006.
- [210] H. Yang, X. Huang, W. Liang, A. C. Van Duin, M. Raju, and S. Zhang, "Self-weakening in lithiated graphene electrodes," *Chemical Physics Letters*, vol. 563, pp. 58–62, 2013.
- [211] L. R. Radovic, "Active sites in graphene and the mechanism of  $\text{CO}_2$  formation in carbon oxidation," *Journal of the American Chemical Society*, vol. 131, no. 47, pp. 17166–17175, 2009.
- [212] X. Huang, H. Yang, A. C. T. Van Duin, K. J. Hsia, and S. Zhang, "Chemo-mechanics control of tearing paths in graphene," *Physical Review B*, vol. 85, no. 19, p. 195453, 2012.
- [213] R. Kane, *Environmentally Assisted Cracking: Predictive Methods for Risk Assessment and Evaluation of Materials, Equipment, and Structures*, vol. 1401. Astm International, 2000.
- [214] H. Zhao and N. R. Aluru, "Temperature and strain-rate dependent fracture strength of graphene," *Journal of Applied Physics*, vol. 108, no. 6, p. 064321, 2010.
- [215] Z. Bai, L. Zhang, and L. Liu, "Bombarding graphene with oxygen ions: combining effects of incident angle and ion energy to control defect generation," *The Journal of Physical Chemistry C*, vol. 119, no. 47, pp. 26793–26802, 2015.
- [216] P. Keblinski, S. R. Phillpot, D. Wolf, and H. Gleiter, "Amorphous structure of grain boundaries and grain junctions in nanocrystalline silicon by molecular-dynamics simulation," *Acta materialia*, vol. 45, no. 3, pp. 987–998, 1997.
- [217] A. R. Khoei and M. S. Khorrami, "Mechanical properties of graphene oxide: A molecular dynamics study," *Fullerenes, Nanotubes and Carbon Nanostructures*, vol. 24, no. 9, pp. 594–603, 2016.
- [218] Q. X. Pei, Y. W. Zhang, and V. B. Shenoy, "A molecular dynamics study of the mechanical properties of hydrogen functionalized graphene," *Carbon*, vol. 48, no. 3, pp. 898–904, 2010.
- [219] T. Watanabe, B. Ni, S. R. Phillpot, P. K. Schelling, and P. Keblinski, "Thermal conductance across grain boundaries in diamond from molecular dynamics simulation," *Journal of Applied Physics*, vol. 102, no. 6, p. 063503, 2007.
- [220] M. A. Tschopp, D. E. Spearot, and D. L. McDowell, "Atomistic simulations of homogeneous dislocation nucleation in single crystal copper," *Modelling and Simulation in Materials Science and Engineering*, vol. 15, no. 7, p. 693, 2007.

- [221] H. Zhang, A. F. Fonseca, and K. Cho, "Tailoring thermal transport property of graphene through oxygen functionalization," *The Journal of Physical Chemistry C*, vol. 118, no. 3, pp. 1436–1442, 2014.
- [222] B. Mortazavi and G. Cuniberti, "Atomistic modeling of mechanical properties of polycrystalline graphene," *Nanotechnology*, vol. 25, no. 21, p. 215704, 2014.
- [223] Y. Li, S. Wang, Q. Wang, and M. Xing, "Enhancement of fracture properties of polymer composites reinforced by carbon nanotubes: A molecular dynamics study," *Carbon*, vol. 129, pp. 504–509, 2018.
- [224] D. Porezag, T. Frauenheim, T. Köhler, G. Seifert, and R. Kaschner, "Construction of tight-binding-like potentials on the basis of density-functional theory: Application to carbon," *Physical Review B*, vol. 51, p. 12947, 1995.
- [225] H. J. C. Berendsen, J. P. M. Postma, W. F. van Gunsteren, A. DiNola, and J. R. Haak, "Molecular dynamics with coupling to an external bath," *The Journal of Chemical Physics*, vol. 81, no. 8, pp. 3684–3690, 1984.
- [226] B. D. Jensen, K. E. Wise, and G. M. Odegard, "Simulation of the elastic and ultimate tensile properties of diamond, graphene, carbon nanotubes, and amorphous carbon using a revised reaxff parametrization," *The Journal of Physical Chemistry A*, vol. 119, no. 37, pp. 9710–9721, 2015.
- [227] B. D. Jensen, K. E. Wise, and G. M. Odegard, "The effect of time step, thermostat, and strain rate on reaxff simulations of mechanical failure in diamond, graphene, and carbon nanotube," *Journal of Computational Chemistry*, vol. 36, no. 21, pp. 1587–1596, 2015.
- [228] K. Sendt and B. S. Haynes, "Density functional study of the reaction of  $\text{O}_2$  with a single site on the zigzag edge of graphene," *Proceedings of the Combustion Institute*, vol. 33, no. 2, pp. 1851–1858, 2011.
- [229] C. Goringe, D. Bowler, and E. Hernández, "Tight-binding modelling of materials," *Reports on Progress in Physics*, vol. 60, p. 1447, 1997.
- [230] C. Herrero, R. Ramírez, and E. Hernández, "Hydrogen and muonium in diamond: A path-integral molecular dynamics simulation," *Physical Review B*, vol. 73, p. 245211, 2006.
- [231] T. Anderson, *Fracture mechanics: fundamentals and applications*. CRC press, 2005.
- [232] B. Hourahine, B. Aradi, V. Blum, F. Bonafe, A. Buccheri, C. Camacho, C. Cevallos, M. Deshayé, T. Dumitrică, A. Dominguez, *et al.*, "Dftb+, a software package for efficient approximate density functional theory based atomistic simulations," *The Journal of Chemical Physics*, vol. 152, no. 12, p. 124101, 2020.

- [233] T.-H. Liu, G. Gajewski, C.-W. Pao, and C.-C. Chang, "Structure, energy, and structural transformations of graphene grain boundaries from atomistic simulations," *Carbon*, vol. 49, no. 7, pp. 2306–2317, 2011.
- [234] W. H. Brito, R. Kagimura, and R. H. Miwa, "Hydrogenated grain boundaries in graphene," *Applied Physics Letters*, vol. 98, no. 21, p. 213107, 2011.
- [235] P. A. Denis and F. Iribarne, "Comparative study of defect reactivity in graphene," *The Journal of Physical Chemistry C*, vol. 117, no. 37, pp. 19048–19055, 2013.
- [236] A. Verma, A. Parashar, and M. Packirisamy, "Tailoring the failure morphology of 2d bicrystalline graphene oxide," *Journal of Applied Physics*, vol. 124, no. 1, p. 015102, 2018.
- [237] N.-N. Li, Z.-D. Sha, Q.-X. Pei, and Y.-W. Zhang, "Hydrogenated grain boundaries control the strength and ductility of polycrystalline graphene," *The Journal of Physical Chemistry C*, vol. 118, no. 25, pp. 13769–13774, 2014.
- [238] D. C. Elias, R. R. Nair, T. M. G. Mohiuddin, S. V. Morozov, P. Blake, M. P. Halsall, A. C. Ferrari, D. W. Boukhvalov, M. I. Katsnelson, A. K. Geim, and K. S. Novoselov, "Control of graphene's properties by reversible hydrogenation: evidence for graphane," *Science*, vol. 323, no. 5914, pp. 610–613, 2009.
- [239] J. S. Burgess, B. R. Matis, J. T. Robinson, F. A. Bulat, F. K. Perkins, B. H. Houston, and J. W. Baldwin, "Tuning the electronic properties of graphene by hydrogenation in a plasma enhanced chemical vapor deposition reactor," *Carbon*, vol. 49, no. 13, pp. 4420–4426, 2011.
- [240] J. Zhou, Q. Wang, Q. Sun, X. S. Chen, Y. Kawazoe, and P. Jena, "Ferromagnetism in semihydrogenated graphene sheet," *Nano letters*, vol. 9, no. 11, pp. 3867–3870, 2009.
- [241] A. I. Shkrebtii, E. Heritage, P. McNelles, J. L. Cabellos, and B. S. Mendoza, "Graphene and graphane functionalization with hydrogen: electronic and optical signatures," *physica status solidi c*, vol. 9, no. 6, pp. 1378–1383, 2012.
- [242] J. Son, S. Lee, S. J. Kim, B. C. Park, H.-K. Lee, S. Kim, J. H. Kim, B. H. Hong, and J. Hong, "Hydrogenated monolayer graphene with reversible and tunable wide band gap and its field-effect transistor," *Nature communications*, vol. 7, p. 13261, 2016.
- [243] G. I. Barenblatt, *The mathematical theory of equilibrium cracks in brittle fracture*, vol. 7. Elsevier, 1962.
- [244] G. I. Barenblatt, "The formation of equilibrium cracks during brittle fracture. general ideas and hypotheses. axially-symmetric cracks," *Journal of Applied Mathematics and Mechanics*, vol. 23, no. 3, pp. 434–444, 1959.

- [245] D. S. Dugdale, "Yielding of steel sheets containing slits," *Journal of the Mechanics and Physics of Solids*, vol. 8, no. 2, pp. 100–104, 1960.
- [246] P. H. Geubelle and J. S. Baylor, "Impact-induced delamination of composites: a 2d simulation," *Composites Part B: Engineering*, vol. 29, no. 5, pp. 589–602, 1998.
- [247] H. D. Espinosa and P. D. Zavattieri, "A grain level model for the study of failure initiation and evolution in polycrystalline brittle materials. part i: Theory and numerical implementation," *Mechanics of Materials*, vol. 35, no. 3-6, pp. 333–364, 2003.
- [248] X.-P. Xu and A. Needleman, "Numerical simulations of fast crack growth in brittle solids," *Journal of the Mechanics and Physics of Solids*, vol. 42, no. 9, pp. 1397–1434, 1994.
- [249] V. Tvergaard and J. W. Hutchinson, "The relation between crack growth resistance and fracture process parameters in elastic-plastic solids," *Journal of the Mechanics and Physics of Solids*, vol. 40, no. 6, pp. 1377–1397, 1992.
- [250] Y. J. Wei and L. Anand, "Grain-boundary sliding and separation in polycrystalline metals: application to nanocrystalline fcc metals," *Journal of the Mechanics and Physics of Solids*, vol. 52, no. 11, pp. 2587–2616, 2004.
- [251] H. Tan, C. Liu, Y. Huang, and P. H. Geubelle, "The cohesive law for the particle/matrix interfaces in high explosives," *Journal of the Mechanics and Physics of Solids*, vol. 53, no. 8, pp. 1892–1917, 2005.
- [252] Y. Freed and L. Banks-Sills, "Crack growth resistance of shape memory alloys by means of a cohesive zone model," *Journal of the Mechanics and Physics of Solids*, vol. 55, no. 10, pp. 2157–2180, 2007.
- [253] I. Scheider, "Micromechanical based derivation of traction-separation laws for cohesive model simulations," *Procedia Engineering*, vol. 1, no. 1, pp. 17–21, 2009.
- [254] I. Scheider, "Derivation of separation laws for cohesive models in the course of ductile fracture," *Engineering Fracture Mechanics*, vol. 76, no. 10, pp. 1450–1459, 2009.
- [255] E. Farmand-Ashtiani, D. Alanis, J. Cugnoni, and J. Botsis, "Delamination in cross-ply laminates: Identification of traction–separation relations and cohesive zone modeling," *Composites Science and Technology*, vol. 119, pp. 85–92, 2015.
- [256] S.-K. Chien, Y.-T. Yang, and C.-K. Chen, "Influence of hydrogen functionalization on thermal conductivity of graphene: Nonequilibrium molecular dynamics simulations," *Applied Physics Letters*, vol. 98, no. 3, p. 033107, 2011.

- [257] S. Xiong and G. Cao, “Molecular dynamics simulations of mechanical properties of monolayer  $\text{mos}_2$ ,” *Nanotechnology*, vol. 26, no. 18, p. 185705, 2015.
- [258] J.-L. Zang, Q. Yuan, F.-C. Wang, and Y.-P. Zhao, “A comparative study of young’s modulus of single-walled carbon nanotube by cpmd, md and first principle simulations,” *Computational Materials Science*, vol. 46, no. 3, pp. 621–625, 2009.
- [259] V. Yamakov, E. Saether, D. R. Phillips, and E. H. Glaessgen, “Molecular-dynamics simulation-based cohesive zone representation of intergranular fracture processes in aluminum,” *Journal of the Mechanics and Physics of Solids*, vol. 54, no. 9, pp. 1899–1928, 2006.
- [260] X. W. Zhou, J. A. Zimmerman, E. D. Reedy Jr, and N. R. Moody, “Molecular dynamics simulation based cohesive surface representation of mixed mode fracture,” *Mechanics of Materials*, vol. 40, no. 10, pp. 832–845, 2008.
- [261] L. Guin, J. L. Raphanel, and J. W. Kysar, “Atomistically derived cohesive zone model of intergranular fracture in polycrystalline graphene,” *Journal of Applied Physics*, vol. 119, no. 24, p. 245107, 2016.
- [262] H. Krull and H. Yuan, “Suggestions to the cohesive traction–separation law from atomistic simulations,” *Engineering Fracture Mechanics*, vol. 78, no. 3, pp. 525–533, 2011.
- [263] C. R. Dandekar and Y. C. Shin, “Effect of porosity on the interface behavior of an  $\text{al}_2\text{o}_3$ –aluminum composite: A molecular dynamics study,” *Composites Science and Technology*, vol. 71, no. 3, pp. 350–356, 2011.
- [264] B. Paliwal and M. Cherkaoui, “An improved atomistic simulation based mixed-mode cohesive zone law considering non-planar crack growth,” *International Journal of Solids and Structures*, vol. 50, no. 20-21, pp. 3346–3360, 2013.
- [265] P. M. Anderson, J. P. Hirth, and J. Lothe, *Theory of Dislocations*. Cambridge University Press, 2017.
- [266] O. V. Yazyev and S. G. Louie, “Topological defects in graphene: Dislocations and grain boundaries,” *Physical Review B*, vol. 81, no. 19, p. 195420, 2010.
- [267] A. Hillerborg, M. Mod er, and P.-E. Petersson, “Analysis of crack formation and crack growth in concrete by means of fracture mechanics and finite elements,” *Cement and concrete research*, vol. 6, no. 6, pp. 773–781, 1976.
- [268] C.-T. Sun and Z. H. Jin, *Fracture Mechanics*. Academic Press, 2011.
- [269] C. Shet and N. Chandra, “Analysis of energy balance when using cohesive zone models to simulate fracture processes,” *J. Eng. Mater. Technol.*, vol. 124, no. 4, pp. 440–450, 2002.

- [270] B. Lawn, *Fracture of Brittle Solids*. Cambridge University Press, 1993.
- [271] J. A. Zimmerman, E. B. WebbIII, J. J. Hoyt, R. E. Jones, P. A. Klein, and D. J. Bammann, “Calculation of stress in atomistic simulation,” *Modelling and simulation in materials science and engineering*, vol. 12, no. 4, p. S319, 2004.
- [272] N. C. Admal and E. B. Tadmor, “A unified interpretation of stress in molecular systems,” *Journal of elasticity*, vol. 100, no. 1-2, pp. 63–143, 2010.
- [273] Y. Li, D. Datta, and Z. Li, “Anomalous mechanical characteristics of graphene with tilt grain boundaries tuned by hydrogenation,” *Carbon*, vol. 90, pp. 234–241, 2015.
- [274] F. Bonaccorso, L. Colombo, G. Yu, M. Stoller, V. Tozzini, A. C. Ferrari, R. S. Ruoff, and V. Pellegrini, “Graphene, related two-dimensional crystals, and hybrid systems for energy conversion and storage,” *Science*, vol. 347, no. 6217, 2015.
- [275] S. Kumar, N. McEvoy, H.-Y. Kim, K. Lee, N. Peltekis, E. Rezvani, H. Nolan, A. Weidlich, R. Daly, and G. S. Duesberg, “Cvd growth and processing of graphene for electronic applications,” *physica status solidi (b)*, vol. 248, no. 11, pp. 2604–2608, 2011.
- [276] P. Avouris and C. Dimitrakopoulos, “Graphene: synthesis and applications,” *Materials today*, vol. 15, no. 3, pp. 86–97, 2012.
- [277] M. Zhong, D. Xu, X. Yu, K. Huang, X. Liu, Y. Qu, Y. Xu, and D. Yang, “Interface coupling in graphene/fluorographene heterostructure for high-performance graphene/silicon solar cells,” *Nano Energy*, vol. 28, pp. 12–18, 2016.
- [278] N. N. Rosli, M. A. Ibrahim, N. A. Ludin, M. A. M. Teridi, and K. Sopian, “A review of graphene based transparent conducting films for use in solar photovoltaic applications,” *Renewable and Sustainable Energy Reviews*, vol. 99, pp. 83–99, 2019.
- [279] E. P. Randviir, D. A. Brownson, and C. E. Banks, “A decade of graphene research: production, applications and outlook,” *Materials Today*, vol. 17, no. 9, pp. 426–432, 2014.
- [280] V. Tozzini and V. Pellegrini, “Prospects for hydrogen storage in graphene,” *Physical Chemistry Chemical Physics*, vol. 15, no. 1, pp. 80–89, 2013.
- [281] G. Dimitrakakis, E. Tylianakis, and G. Froudakis, “Pillared graphene: a new 3-d network nanostructure for enhanced hydrogen storage,” *Nano letters*, vol. 8, no. 10, pp. 3166–3170, 2008.
- [282] J. Li, Z. Shan, and E. Ma, “Elastic strain engineering for unprecedented materials properties,” *MRS Bulletin*, vol. 39, no. 2, pp. 108–114, 2014.

- [283] V. M. Pereira and A. C. Neto, "Strain engineering of graphene's electronic structure," *Physical review letters*, vol. 103, no. 4, p. 046801, 2009.
- [284] C. Si, Z. Sun, and F. Liu, "Strain engineering of graphene: a review," *Nanoscale*, vol. 8, no. 6, pp. 3207–3217, 2016.
- [285] R. Roldán, A. Castellanos-Gomez, E. Cappelluti, and F. Guinea, "Strain engineering in semiconducting two-dimensional crystals," *Journal of Physics: Condensed Matter*, vol. 27, no. 31, p. 313201, 2015.
- [286] Z. Dai, L. Liu, and Z. Zhang, "Strain engineering of 2d materials: issues and opportunities at the interface," *Advanced Materials*, vol. 31, no. 45, p. 1805417, 2019.
- [287] K. R. Pyun and S. H. Ko, "Graphene as a material for energy generation and control: Recent progress in the control of graphene thermal conductivity by graphene defect engineering," *Materials Today Energy*, vol. 12, pp. 431–442, 2019.
- [288] K. Chu, J. Wang, Y.-p. Liu, and Z.-r. Geng, "Graphene defect engineering for optimizing the interface and mechanical properties of graphene/copper composites," *Carbon*, vol. 140, pp. 112–123, 2018.
- [289] Y. Wang, S. Chen, and X. Ruan, "Tunable thermal rectification in graphene nanoribbons through defect engineering: a molecular dynamics study," *Applied Physics Letters*, vol. 100, no. 16, p. 163101, 2012.
- [290] S. Yadav, Z. Zhu, and C. V. Singh, "Defect engineering of graphene for effective hydrogen storage," *International journal of hydrogen energy*, vol. 39, no. 10, pp. 4981–4995, 2014.
- [291] H. Zhang and R. Lv, "Defect engineering of two-dimensional materials for efficient electrocatalysis," *Journal of Materiomics*, vol. 4, no. 2, pp. 95–107, 2018.
- [292] G. Bottari, M. Á. Herranz, L. Wibmer, M. Volland, L. Rodríguez-Pérez, D. M. Guldi, A. Hirsch, N. Martín, F. D'Souza, and T. Torres, "Chemical functionalization and characterization of graphene-based materials," *Chemical Society Reviews*, vol. 46, no. 15, pp. 4464–4500, 2017.
- [293] D. Boukhvalov and M. Katsnelson, "Chemical functionalization of graphene with defects," *Nano letters*, vol. 8, no. 12, pp. 4373–4379, 2008.
- [294] T. Kuila, S. Bose, A. K. Mishra, P. Khanra, N. H. Kim, and J. H. Lee, "Chemical functionalization of graphene and its applications," *Progress in Materials Science*, vol. 57, no. 7, pp. 1061–1105, 2012.
- [295] D. Boukhvalov and M. Katsnelson, "Chemical functionalization of graphene," *Journal of Physics: Condensed Matter*, vol. 21, no. 34, p. 344205, 2009.

- [296] M. Seifert, J. E. Vargas, M. Bobinger, M. Sachsenhauser, A. W. Cummings, S. Roche, and J. A. Garrido, “Role of grain boundaries in tailoring electronic properties of polycrystalline graphene by chemical functionalization,” *2D Materials*, vol. 2, no. 2, p. 024008, 2015.
- [297] J. Xu, G. Yuan, Q. Zhu, J. Wang, S. Tang, and L. Gao, “Enhancing the strength of graphene by a denser grain boundary,” *ACS nano*, vol. 12, no. 5, pp. 4529–4535, 2018.
- [298] J. Wu and Y. Wei, “Grain misorientation and grain-boundary rotation dependent mechanical properties in polycrystalline graphene,” *Journal of the Mechanics and Physics of Solids*, vol. 61, no. 6, pp. 1421–1432, 2013.
- [299] Y. I. Jhon, S.-E. Zhu, J.-H. Ahn, and M. S. Jhon, “The mechanical responses of tilted and non-tilted grain boundaries in graphene,” *Carbon*, vol. 50, no. 10, pp. 3708–3716, 2012.
- [300] H. Ghasemi, A. Rajabpour, and A. Akbarzadeh, “Tuning thermal conductivity of porous graphene by pore topology engineering: Comparison of non-equilibrium molecular dynamics and finite element study,” *International Journal of Heat and Mass Transfer*, vol. 123, pp. 261–271, 2018.
- [301] N. Wei, L. Xu, H.-Q. Wang, and J.-C. Zheng, “Strain engineering of thermal conductivity in graphene sheets and nanoribbons: a demonstration of magic flexibility,” *Nanotechnology*, vol. 22, no. 10, p. 105705, 2011.
- [302] T. Ma, Z. Liu, J. Wen, Y. Gao, X. Ren, H. Chen, C. Jin, X.-L. Ma, N. Xu, H.-M. Cheng, *et al.*, “Tailoring the thermal and electrical transport properties of graphene films by grain size engineering,” *Nature communications*, vol. 8, no. 1, pp. 1–9, 2017.
- [303] J. Y. Kim, J.-H. Lee, and J. C. Grossman, “Thermal transport in functionalized graphene,” *ACS nano*, vol. 6, no. 10, pp. 9050–9057, 2012.
- [304] Y. Zeng, C.-L. Lo, S. Zhang, Z. Chen, and A. Marconnet, “Dynamically tunable thermal transport in polycrystalline graphene by strain engineering,” *Carbon*, vol. 158, pp. 63–68, 2020.
- [305] G. Barbarino, C. Melis, and L. Colombo, “Effect of hydrogenation on graphene thermal transport,” *Carbon*, vol. 80, pp. 167–173, 2014.
- [306] S. Chen, A. L. Moore, W. Cai, J. W. Suk, J. An, C. Mishra, C. Amos, C. W. Magnuson, J. Kang, L. Shi, *et al.*, “Raman measurements of thermal transport in suspended monolayer graphene of variable sizes in vacuum and gaseous environments,” *ACS nano*, vol. 5, no. 1, pp. 321–328, 2011.

- [307] Y. Wang, H. Zhan, Y. Xiang, C. Yang, C. M. Wang, and Y. Zhang, "Effect of covalent functionalization on thermal transport across graphene–polymer interfaces," *The journal of physical chemistry C*, vol. 119, no. 22, pp. 12731–12738, 2015.
- [308] T. Sreeprasad and V. Berry, "How do the electrical properties of graphene change with its functionalization?," *Small*, vol. 9, no. 3, pp. 341–350, 2013.
- [309] F. Guinea, "Strain engineering in graphene," *Solid State Communications*, vol. 152, no. 15, pp. 1437–1441, 2012.
- [310] W. Wei and X. Qu, "Extraordinary physical properties of functionalized graphene," *Small*, vol. 8, no. 14, pp. 2138–2151, 2012.
- [311] S. Park, M. A. Shehzad, M. F. Khan, G. Nazir, J. Eom, H. Noh, and Y. Seo, "Effect of grain boundaries on electrical properties of polycrystalline graphene," *Carbon*, vol. 112, pp. 142–148, 2017.
- [312] F. Banhart, J. Kotakoski, and A. V. Krasheninnikov, "Structural defects in graphene," *ACS nano*, vol. 5, no. 1, pp. 26–41, 2011.
- [313] R. Grantab, V. B. Shenoy, and R. S. Ruoff, "Anomalous strength characteristics of tilt grain boundaries in graphene," *Science*, vol. 330, no. 6006, pp. 946–948, 2010.
- [314] G.-H. Lee, R. C. Cooper, S. J. An, S. Lee, A. Van Der Zande, N. Petrone, A. G. Hammerberg, C. Lee, B. Crawford, W. Oliver, *et al.*, "High-strength chemical-vapor-deposited graphene and grain boundaries," *science*, vol. 340, no. 6136, pp. 1073–1076, 2013.
- [315] B. Zheng and G. X. Gu, "Tuning the graphene mechanical anisotropy via defect engineering," *Carbon*, vol. 155, pp. 697–705, 2019.
- [316] S. Mukherjee, R. Alicandri, and C. V. Singh, "Strength of graphene with curvilinear grain boundaries," *Carbon*, vol. 158, pp. 808–817, 2020.
- [317] A. H. Mashhadzadeh, M. G. Ahangari, A. Dadrasi, and M. Fathalian, "Theoretical studies on the mechanical and electronic properties of 2d and 3d structures of beryllium-oxide graphene and graphene nanobud," *Applied Surface Science*, vol. 476, pp. 36–48, 2019.
- [318] M. Dewapriya, R. Rajapakse, and N. Nigam, "Influence of hydrogen functionalization on the fracture strength of graphene and the interfacial properties of graphene–polymer nanocomposite," *Carbon*, vol. 93, pp. 830–842, 2015.
- [319] S. S. Sharma, B. B. Sharma, and A. Parashar, "Mechanical and fracture behavior of water submerged graphene," *Journal of Applied Physics*, vol. 125, no. 21, p. 215107, 2019.

- [320] M. I. R. Shishir and A. Tabarraei, “A molecular dynamic study of nano-fracture of c3n,” in *ASME International Mechanical Engineering Congress and Exposition*, vol. 59469, p. V009T11A051, American Society of Mechanical Engineers, 2019.
- [321] L. Yi, Z. Yin, Y. Zhang, and T. Chang, “A theoretical evaluation of the temperature and strain-rate dependent fracture strength of tilt grain boundaries in graphene,” *Carbon*, vol. 51, pp. 373–380, 2013.
- [322] Y. Anno, Y. Imakita, K. Takei, S. Akita, and T. Arie, “Enhancement of graphene thermoelectric performance through defect engineering,” *2D Materials*, vol. 4, no. 2, p. 025019, 2017.
- [323] H. Karamitaheri, N. Neophytou, M. Pourfath, R. Faez, and H. Kosina, “Engineering enhanced thermoelectric properties in zigzag graphene nanoribbons,” *Journal of Applied Physics*, vol. 111, no. 5, p. 054501, 2012.
- [324] W. Zhao, Z. Guo, J. Cao, and J. Ding, “Enhanced thermoelectric properties of armchair graphene nanoribbons with defects and magnetic field,” *AIP Advances*, vol. 1, no. 4, p. 042135, 2011.
- [325] L. M. Sandonas, R. Gutierrez, A. Pecchia, A. Dianat, and G. Cuniberti, “Thermoelectric properties of functionalized graphene grain boundaries,” *J. Self-Assembly Mol. Electron*, vol. 3, pp. 1–20, 2015.
- [326] J. Choi, N. D. Tu, S.-S. Lee, H. Lee, J. S. Kim, and H. Kim, “Controlled oxidation level of reduced graphene oxides and its effect on thermoelectric properties,” *Macromolecular Research*, vol. 22, no. 10, pp. 1104–1108, 2014.
- [327] T. Li, A. D. Pickel, Y. Yao, Y. Chen, Y. Zeng, S. D. Lacey, Y. Li, Y. Wang, J. Dai, Y. Wang, *et al.*, “Thermoelectric properties and performance of flexible reduced graphene oxide films up to 3,000 k,” *Nature Energy*, vol. 3, no. 2, pp. 148–156, 2018.
- [328] H. Zhang, C. Lazo, S. Blügel, S. Heinze, and Y. Mokrousov, “Electrically tunable quantum anomalous hall effect in graphene decorated by 5 d transition-metal adatoms,” *Physical review letters*, vol. 108, no. 5, p. 056802, 2012.
- [329] I. I. Klimovskikh, M. M. Otrokov, V. Y. Voroshnin, D. Sostina, L. Petaccia, G. Di Santo, S. Thakur, E. V. Chulkov, and A. M. Shikin, “Spin–orbit coupling induced gap in graphene on pt (111) with intercalated pb monolayer,” *ACS nano*, vol. 11, no. 1, pp. 368–374, 2017.
- [330] C. Weeks, J. Hu, J. Alicea, M. Franz, and R. Wu, “Engineering a robust quantum spin hall state in graphene via adatom deposition,” *Physical Review X*, vol. 1, no. 2, p. 021001, 2011.

- [331] R. Balog, B. Jørgensen, L. Nilsson, M. Andersen, E. Rienks, M. Bianchi, M. Fanetti, E. Lægsgaard, A. Baraldi, S. Lizzit, *et al.*, “Bandgap opening in graphene induced by patterned hydrogen adsorption,” *Nature materials*, vol. 9, no. 4, pp. 315–319, 2010.
- [332] J. García-Lastra, “Strong dependence of band-gap opening at the dirac point of graphene upon hydrogen adsorption periodicity,” *Physical Review B*, vol. 82, no. 23, p. 235418, 2010.
- [333] F. Gargiulo, G. Autès, N. Virk, S. Barthel, M. Rösner, L. R. Toller, T. O. Wehling, and O. V. Yazyev, “Electronic transport in graphene with aggregated hydrogen adatoms,” *Physical review letters*, vol. 113, no. 24, p. 246601, 2014.
- [334] K. M. McCreary, A. G. Swartz, W. Han, J. Fabian, and R. K. Kawakami, “Magnetic moment formation in graphene detected by scattering of pure spin currents,” *Physical review letters*, vol. 109, no. 18, p. 186604, 2012.
- [335] E. Cadelano, P. L. Palla, S. Giordano, and L. Colombo, “Elastic properties of hydrogenated graphene,” *Physical Review B*, vol. 82, no. 23, p. 235414, 2010.
- [336] Q. Peng, C. Liang, W. Ji, and S. De, “A theoretical analysis of the effect of the hydrogenation of graphene to graphane on its mechanical properties,” *Physical Chemistry Chemical Physics*, vol. 15, no. 6, pp. 2003–2011, 2013.
- [337] R. Ansari, M. Mirnezhad, and H. Rouhi, “Mechanical properties of fully hydrogenated graphene sheets,” *Solid State Communications*, vol. 201, pp. 1–4, 2015.
- [338] K. Kim, Z. Lee, W. Regan, C. Kisielowski, M. Crommie, and A. Zettl, “Grain boundary mapping in polycrystalline graphene,” *ACS nano*, vol. 5, no. 3, pp. 2142–2146, 2011.
- [339] B. Mortazavi, M. Pötschke, and G. Cuniberti, “Multiscale modeling of thermal conductivity of polycrystalline graphene sheets,” *Nanoscale*, vol. 6, no. 6, pp. 3344–3352, 2014.
- [340] H. Liu, Y. Lin, and S. Luo, “Grain boundary energy and grain size dependences of thermal conductivity of polycrystalline graphene,” *The Journal of Physical Chemistry C*, vol. 118, no. 42, pp. 24797–24802, 2014.
- [341] P. Wu, S. Quek, Z. Sha, Z. Dong, X. Liu, G. Zhang, Q. Pei, and Y. Zhang, “Thermal transport behavior of polycrystalline graphene: A molecular dynamics study,” *Journal of applied physics*, vol. 116, no. 20, p. 204303, 2014.
- [342] J. Kotakoski and J. C. Meyer, “Mechanical properties of polycrystalline graphene based on a realistic atomistic model,” *Physical Review B*, vol. 85, no. 19, p. 195447, 2012.

- [343] G. Jung, Z. Qin, and M. J. Buehler, “Molecular mechanics of polycrystalline graphene with enhanced fracture toughness,” *Extreme Mechanics Letters*, vol. 2, pp. 52–59, 2015.
- [344] A. Shekhawat and R. O. Ritchie, “Toughness and strength of nanocrystalline graphene,” *Nature communications*, vol. 7, no. 1, pp. 1–8, 2016.
- [345] M. Dewapriya, A. S. Phani, and R. Rajapakse, “Influence of temperature and free edges on the mechanical properties of graphene,” *Modelling and Simulation in Materials Science and Engineering*, vol. 21, no. 6, p. 065017, 2013.
- [346] Z. Qin, G. S. Jung, M. J. Kang, and M. J. Buehler, “The mechanics and design of a lightweight three-dimensional graphene assembly,” *Science advances*, vol. 3, no. 1, p. e1601536, 2017.
- [347] H. Attariani, S. E. Rezaei, and K. Momeni, “Mechanical property enhancement of one-dimensional nanostructures through defect-mediated strain engineering,” *Extreme Mechanics Letters*, vol. 27, pp. 66–75, 2019.
- [348] X. Nie, L. Zhao, S. Deng, Y. Zhang, and Z. Du, “How interlayer twist angles affect in-plane and cross-plane thermal conduction of multilayer graphene: A non-equilibrium molecular dynamics study,” *International Journal of Heat and Mass Transfer*, vol. 137, pp. 161–173, 2019.
- [349] Z.-L. Li, Z.-M. Li, H.-Y. Cao, J.-H. Yang, Q. Shu, Y.-Y. Zhang, H. Xiang, and X. Gong, “What are grain boundary structures in graphene?,” *Nanoscale*, vol. 6, no. 8, pp. 4309–4315, 2014.
- [350] T. Zhang, X. Li, S. Kadkhodaei, and H. Gao, “Flaw insensitive fracture in nanocrystalline graphene,” *Nano letters*, vol. 12, no. 9, pp. 4605–4610, 2012.
- [351] C. Ophus, A. Shekhawat, H. Rasool, and A. Zettl, “Large-scale experimental and theoretical study of graphene grain boundary structures,” *Physical Review B*, vol. 92, no. 20, p. 205402, 2015.
- [352] M. Becton, X. Zeng, and X. Wang, “Computational study on the effects of annealing on the mechanical properties of polycrystalline graphene,” *Carbon*, vol. 86, pp. 338–349, 2015.
- [353] Z. Xu, “Graphene nano-ribbons under tension,” *Journal of computational and Theoretical nanoscience*, vol. 6, no. 3, pp. 625–628, 2009.
- [354] I. V. Lebedeva, A. S. Minkin, A. M. Popov, and A. A. Knizhnik, “Elastic constants of graphene: Comparison of empirical potentials and dft calculations,” *Physica E: Low-dimensional Systems and Nanostructures*, vol. 108, pp. 326–338, 2019.

- [355] E. Aparicio, E. Tangarife, F. Munoz, R. Gonzalez, F. Valencia, C. Careglio, and E. Bringa, “Simulated mechanical properties of finite-size graphene nanoribbons,” *Nanotechnology*, vol. 32, no. 4, p. 045709, 2020.
- [356] “Chapter 2 - griffith theory of fracture,” in *Fracture Mechanics* (C. Sun and Z.-H. Jin, eds.), pp. 11–24, Boston: Academic Press, 2012.
- [357] L. Falkovsky, “Optical properties of graphene,” in *Journal of Physics: conference series*, vol. 129, p. 012004, IOP Publishing, 2008.
- [358] D. Prezzi, D. Varsano, A. Ruini, A. Marini, and E. Molinari, “Optical properties of graphene nanoribbons: The role of many-body effects,” *Physical Review B*, vol. 77, no. 4, p. 041404, 2008.
- [359] H. I. Rasool, C. Ophus, W. S. Klug, A. Zettl, and J. K. Gimzewski, “Measurement of the intrinsic strength of crystalline and polycrystalline graphene,” *Nature communications*, vol. 4, no. 1, pp. 1–7, 2013.
- [360] M. I. R. Shishir and A. Tabarraei, “Molecular dynamics simulation based cohesive zone representation of intergranular fracture processes in bicrystalline graphene,” in *ASME International Mechanical Engineering Congress and Exposition*, vol. 84607, p. V012T12A028, American Society of Mechanical Engineers, 2020.
- [361] R. Rasuli, M. Ahadian, *et al.*, “Mechanical properties of graphene cantilever from atomic force microscopy and density functional theory,” *Nanotechnology*, vol. 21, no. 18, p. 185503, 2010.
- [362] R. Faccio, P. A. Denis, H. Pardo, C. Goyenola, and A. W. Mombrú, “Mechanical properties of graphene nanoribbons,” *Journal of Physics: Condensed Matter*, vol. 21, no. 28, p. 285304, 2009.
- [363] R. A. Soler-Crespo, W. Gao, P. Xiao, X. Wei, J. T. Paci, G. Henkelman, and H. D. Espinosa, “Engineering the mechanical properties of monolayer graphene oxide at the atomic level,” *The journal of physical chemistry letters*, vol. 7, no. 14, pp. 2702–2707, 2016.
- [364] M. Mirnezhad, R. Ansari, M. Seifi, H. Rouhi, and M. Faghihnasiri, “Mechanical properties of graphene under molecular hydrogen physisorption: an ab initio study,” *Solid State Communications*, vol. 152, no. 10, pp. 842–845, 2012.
- [365] B. Chakraborty, P. Ray, N. Garg, and S. Banerjee, “High capacity reversible hydrogen storage in titanium doped 2d carbon allotrope  $\psi$ -graphene: Density functional theory investigations,” *International Journal of Hydrogen Energy*, vol. 46, no. 5, pp. 4154–4167, 2021.
- [366] N. Dimakis, F. A. Flor, A. Salgado, K. Adjibi, S. Vargas, and J. Saenz, “Density functional theory calculations on transition metal atoms adsorbed on graphene monolayers,” *Applied Surface Science*, vol. 421, pp. 252–259, 2017.

- [367] B. Mortazavi, M. Shahrokhi, M. Raeisi, X. Zhuang, L. F. C. Pereira, and T. Rabczuk, "Outstanding strength, optical characteristics and thermal conductivity of graphene-like bc3 and bc6n semiconductors," *Carbon*, vol. 149, pp. 733–742, 2019.
- [368] A. H. Mashhadzadeh, M. Fathalian, M. G. Ahangari, and M. Shahavi, "Dft study of ni, cu, cd and ag heavy metal atom adsorption onto the surface of the zinc-oxide nanotube and zinc-oxide graphene-like structure," *Materials Chemistry and Physics*, vol. 220, pp. 366–373, 2018.
- [369] Y. Liu, Y. Bian, A. Chernatynskiy, and Z. Han, "Effect of grain boundary angle on the thermal conductivity of nanostructured bicrystal zno based on the molecular dynamics simulation method," *International Journal of Heat and Mass Transfer*, vol. 145, p. 118791, 2019.
- [370] A. Verma and A. Parashar, "Molecular dynamics based simulations to study failure morphology of hydroxyl and epoxide functionalised graphene," *Computational Materials Science*, vol. 143, pp. 15–26, 2018.
- [371] H. Ying, A. Moore, J. Cui, Y. Liu, D. Li, S. Han, Y. Yao, Z. Wang, L. Wang, and S. Chen, "Tailoring the thermal transport properties of monolayer hexagonal boron nitride by grain size engineering," *2D Materials*, vol. 7, no. 1, p. 015031, 2019.
- [372] S. Zhao, Y. Zhang, J. Yang, and S. Kitipornchai, "Significantly improved interfacial shear strength in graphene/copper nanocomposite via wrinkles and functionalization: A molecular dynamics study," *Carbon*, vol. 174, pp. 335–344, 2021.
- [373] W. Ning, Y. Chen, K. Cai, Y. Zhang, Q. Pei, J.-C. Zheng, Y.-W. Mai, and J. Zhao, "Unusual thermal properties of graphene origami crease: A molecular dynamics study," *Green Energy & Environment*, 2020.
- [374] H. Ghasemi, B. Abraham, J. Rutledge, and H. Yazdani, "Mechanical properties of c3n nanotubes," *Diamond and Related Materials*, vol. 109, p. 108090, 2020.
- [375] Z. Qi, N. Zhang, Y. Liu, and W. Chen, "Prediction of mechanical properties of carbon fiber based on cross-scale fem and machine learning," *Composite Structures*, vol. 212, pp. 199–206, 2019.
- [376] Z. Zhang, Y. Hong, B. Hou, Z. Zhang, M. Negahban, and J. Zhang, "Accelerated discoveries of mechanical properties of graphene using machine learning and high-throughput computation," *Carbon*, vol. 148, pp. 115–123, 2019.
- [377] M. Pathan, S. Ponnusami, J. Pathan, R. Pitisongsawat, B. Erice, N. Petrinic, and V. Tagarielli, "Predictions of the mechanical properties of unidirectional fibre composites by supervised machine learning," *Scientific reports*, vol. 9, no. 1, pp. 1–10, 2019.

- [378] X. Wang, D. Han, Y. Hong, H. Sun, J. Zhang, and J. Zhang, "Machine learning enabled prediction of mechanical properties of tungsten disulfide monolayer," *ACS omega*, vol. 4, no. 6, pp. 10121–10128, 2019.
- [379] F.-Z. Dai, B. Wen, Y. Sun, H. Xiang, and Y. Zhou, "Theoretical prediction on thermal and mechanical properties of high entropy (zr<sub>0.2</sub>hf<sub>0.2</sub>ti<sub>0.2</sub>nb<sub>0.2</sub>ta<sub>0.2</sub>)c by deep learning potential," *Journal of Materials Science & Technology*, vol. 43, pp. 168–174, 2020.
- [380] B. A. Moore, E. Rougier, D. O'Malley, G. Srinivasan, A. Hunter, and H. Viswanathan, "Predictive modeling of dynamic fracture growth in brittle materials with machine learning," *Computational Materials Science*, vol. 148, pp. 46–53, 2018.
- [381] M. Schwarzer, B. Rogan, Y. Ruan, Z. Song, D. Y. Lee, A. G. Percus, V. T. Chau, B. A. Moore, E. Rougier, H. S. Viswanathan, *et al.*, "Learning to fail: Predicting fracture evolution in brittle material models using recurrent graph convolutional neural networks," *Computational Materials Science*, vol. 162, pp. 322–332, 2019.
- [382] K. Pierson, A. Rahman, and A. D. Spear, "Predicting microstructure-sensitive fatigue-crack path in 3d using a machine learning framework," *JOM*, vol. 71, no. 8, pp. 2680–2694, 2019.
- [383] Y. Wang, D. Oyen, W. G. Guo, A. Mehta, C. B. Scott, N. Panda, M. G. Fernández-Godino, G. Srinivasan, and X. Yue, "Stressnet-deep learning to predict stress with fracture propagation in brittle materials," *npj Materials Degradation*, vol. 5, no. 1, pp. 1–10, 2021.
- [384] Y.-C. Hsu, C.-H. Yu, and M. J. Buehler, "Using deep learning to predict fracture patterns in crystalline solids," *Matter*, vol. 3, no. 1, pp. 197–211, 2020.
- [385] F. Chollet *et al.*, "Keras," 2015.
- [386] P. M. Larsen, S. Schmidt, and J. Schiøtz, "Robust structural identification via polyhedral template matching," *Modelling and Simulation in Materials Science and Engineering*, vol. 24, no. 5, p. 055007, 2016.
- [387] X. Glorot, A. Bordes, and Y. Bengio, "Deep sparse rectifier neural networks," in *Proceedings of the fourteenth international conference on artificial intelligence and statistics*, pp. 315–323, JMLR Workshop and Conference Proceedings, 2011.
- [388] D. P. Kingma and J. Ba, "Adam: A method for stochastic optimization," *arXiv preprint arXiv:1412.6980*, 2014.